HEAT TRANSFER, OIL LUBRICATION AND MOULD TAPERS IN STEEL BILLETS CASTING MACHINES

By

Sanjay Chandra

B.Tech, Institute of Technology, Banaras Hindu University, India, 1983

A THESIS SUBMITTED IN PARTIAL FULFILLMENT OF THE REQUIREMENTS FOR THE DEGREE OF DOCTOR OF PHILOSOPHY

in

THE FACULTY OF GRADUATE STUDIES

(Department of Metals and Materials Engineering)

We accept this thesis as conforming

to the required standard

THE UNIVERSITY OF BRITISH COLUMBIA

May 1992

In presenting this thesis in partial fulfilment of the requirements for an advanced degree at the University of British Columbia, I agree that the Library shall make it freely available for reference and study. I further agree that permission for extensive copying of this thesis for scholarly purposes may be granted by the head of my department or by his or her representatives. It is understood that copying or publication of this thesis for financial gain shall not be allowed without my written permission.

Department of METALS AND MATERIALS ENGG.

The University of British Columbia
Vancouver, Canada

Date 13th July 1992

DE-6 (2/88)

ABSTRACT

This study examines in detail the factors that influence mould-billet interaction and heat transfer during the continuous casting of steel billets. In an extensive three-year project, major industrial trials were held in three Canadian steel plants involving in each case an operating mould instrumented with arrays of thermocouples to record mould wall and mould cooling water temperatures. Additionally, load cells were installed between the mould housing and the oscillator table to record mould-billet interaction. Linear variable displacement transducers were attached to the mould wall in order to monitor mould displacement. Measurements were made under different casting conditions - steel grades, types and flow rates of lubricating oils and mould tapers - and were recorded on a computer controlled data acquisition system. The liquid steel surface in the mould was also filmed during casting.

Two existing mathematical models of the mould were modified and used to calculate the axial heat flux profiles and the dynamic distortion of the mould during service. A two-dimensional, finite-difference, heat-flow, mathematical model of the billet was developed to simulate solidification and shrinkage as a function of axial position in the mould. The coefficient of thermal contraction of steel was estimated as a function of steel carbon content and temperature from experimental data in the literature on the lattice parameter of δ and γ unit cells; this was particularly important to model the shrinkage of low-carbon steels. It has been shown that in theory, the low-carbon steels ($C < 0.15\%$) should experience the largest contraction due to δ - γ phase transformation; but in practice, they shrink less because heat transfer to the mould is low compared to higher carbon grades. A computer programme was developed to analyse the load cell response as a function of

mould displacement. Finally billet samples collected during the trials were metallographically examined to study the different aspects of the solidification in the mould e.g., cracks, oscillation mark depth and rhomboidity.

The most important result of the research work has been the finding that the heat transfer in the mould is significantly influenced by the taper of the mould wall in the meniscus region. A high initial taper (2.5-3.0%/m) in the meniscus region can compensate for the outward bulging of the mould wall during operation preventing it from acquiring a *negative taper*. This absence of negative taper has been shown to decrease mould-billet interaction during the negative strip period thereby leading to a decrease in the heat extracted in the meniscus region. This finding has been corroborated by an analysis of the load cell signals. It has been shown unambiguously that, for high mould heat transfer, a shallow initial taper of the mould, that permits the wall to acquire a bulged shape, is required. High heat transfer in the mould is likely to result in adverse lubrication condition for casting high-carbon steel billets.

Filming of the steel surface has shown that *only some* of the lubricating oil flowing down the mould wall reaches below the meniscus while the remainder collects on the liquid steel surface and burns. As a result an increase in the flow rate of the oil is not reflected in a commensurate increase in lubrication or heat transfer. In fact the industrial trials have clearly revealed that the existing flow rate of oil at all three plants could be reduced at least by half without any visible deleterious effect on billet quality.

It has also been possible to link various sensor signals to the generation of defects in the billet, in particular to the formation of off-corner internal cracks, transverse depressions and billet rhomboidity. This together with the linkages between mould heat transfer and operating variables now makes it possible to conceive of a control system consisting of an instrumented mould and an expert system that not only can asses billet quality on-line but can also initiate corrective action by changing operating conditions that alter the heat transfer in the mould.

Table of Contents

LIST OF TABLES

LIST OF FIGURES

LIST OF SYMBOLS

k_s	Thermal conductivity of steel, kW/m°C.
T	Temperature, °C.
t	Time below meniscus, s.
ρ	Density of steel, kg/m^3.
C_p	Heat capacity of steel, J/kg°C.
T_p	Pouring temperature °C.
T_l	Liquidus temperature of steel, °C.
T_s	Solidus temperature of steel, °C.
x, y, z	Transverse directions, m.
X, Y	Width and thickness of billet, m.
q_o	Heat flux from the surface of billet to the mould, kW/m^2.
V_δ	Specific volume of delta unit cell, cm^3/g.
V_γ	Specific volume of gamma unit cell, cm^3/g.
$a^T_{\delta_c}$	Lattice parameter of delta iron at temperature T and carbon content C, angstroms.
$a^T_{\gamma_c}$	Lattice parameter of gamma iron at temperature T and carbon content C, angstroms.

X_c Carbon content of delta phase, atomic percent.

W_c Carbon content of gamma phase, weight percent.

M_T Dimension of the mould wall at the top of the mould, m.

M_B Dimension of the mould wall at the bottom of the mould, m.

M_L Total length of the mould, m.

K_m Thermal conductivity of mould, kW/m°C.

ρ_m Density of mould, kg/m^3.

C_{pm} Specific heat of mould, J/kg°C.

ρ_w Density of water, kg/m^3.

V_w Velocity of cooling water in channel, m/s.

d_w Water channel gap width, m.

C_{pw} Specific heat of water, J/kg°C.

T_w Temperature of water, °C.

h_w Heat-transfer coefficient at the mould/cooling water interface, kW/m^{2}°C.

Q_{FC} Forced convection heat flux.

Q_{FD}	Heat flux in the fully developed nucleate boiling region.
Q_{TR}	Heat flux in the transition region between the point of incipient and the fully developed nucleate boiling.
Q_{FN}	Heat flux at the inception of boiling.
Q_{ϕ}	Heat flux at the inception of boiling using the equation for fully developed boiling region.
μ	Viscosity of fluid, N.s/m^2.
σ	Surface tension of liquid/ vapour interface, N/m.
C_{sf}	Emperical constant that depends on the nature of the heating surface/fluid combination.
g	Gravitational acceleration m/s^2.
h_{fc}	Forced convection heat-transfer coefficient.
T_{sat}	Saturation temperature of water °C.

Subscripts

f	fluid.
l	liquid.
m	mould.
v	saturated vapour.
w	water.

ACKNOWLEDGEMENT

I would like to express my sincere thanks to my supervisors, Professors I.V. Samarasekera and J.K. Brimacombe, for their invaluable guidance and advice during the course of the research work. Mr. Ian Bakshi organised the industrial trials at the three steel plants and his role in this and other areas of the work is deeply appreciated. The assistance of Mr. Robert Hapke and Mr. Neil Walker in the instrumentation of the moulds and the metallographic examinations of the billets is sincerely appreciated. I would also like to thank Mr. Walker for his help in printing the photographs used in the thesis.

I am grateful to the management of TATA STEEL for granting me the necessary study leave to complete my thesis.

Finally, I would like to thank the manufacturers of the mould at Company C; their poor machining helped create ideal conditions for high mould heat transfer!

CHAPTER 1 : INTRODUCTION

The continuous casting of steel billets involves the pouring of molten steel at a controlled rate into a water-cooled copper mould and the continuous withdrawal of a partially solidified billet as shown in Figure 1.1. The withdrawal of the steel strand is aided by the oscillation of the mould and a constant supply of a lubricating oil onto the mould wall. The mould extracts heat and freezes a solid shell which thickens progressively as it moves down the mould. As a result of the cooling, the solid shell shrinks and pulls away from the mould wall thereby opening up an air gap. Heat transfer from the molten steel to the mould wall takes place, as shown in Figure 1.2, by the following five steps in series [1]

(i) Convection in the liquid steel pool.

(ii) Conduction in the solid shell.

(iii) Conduction and, to a lesser extent, radiation across the air gap

(iv) Conduction in the mould wall.

(v) Convection at the mould-cooling water interface.

Heat transfer from molten steel to the walls of the continuous casting mould is controlled, in large part, by conduction across the air gap. In the upper region of the mould the air gap is considerably less than a millimeter wide but, in many cases, accounts for as much as 80-90% of the total resistance to heat flow [2]. To compensate for the billet shrinkage, the mould walls are tapered inwardly; the resulting reduction in the air gap improves the rate of mould heat extraction and decreases the surface temperature of the billet at the mould exit, thereby reducing the tendency of the billet surface to reheat [3-5] and form sub-surface cracks. Lack of sufficient taper, additionally, can lead to the formation of off-corner cracks. On the other hand, an excessive taper can cause difficulty in the withdrawal of the strand [3,6] which promotes mould wear [3,7] and, in extreme cases, causes the billet to jam in the mould [1].

The quantification of the strand-mould gap is thus a primary step towards defining mould taper. The gap is, however, a complex function of several variables and its width changes in both the longitudinal and transverse directions which renders it extremely difficult to characterize. The shrinkage of the billet is affected significantly by the grade of steel being cast, particularly the low carbon grades where the contraction accompanying the solid-state transformation from the delta to austenite phase must be taken into account. Another factor contributing to the complexity of the analysis is the distortion of the mould which can be significant [8].

Mould oscillation is probably the most outstanding feature of the conventional casting process with an upright (curved or straight) mould. Historically mould oscillation was applied for the first time in 1949 on two pilot plants constructed independently by S. Junghans and I. Rossi [9,10]. This technique helped to minimize casting problems and surface defects due to shell sticking which were typical in continuous casting with a stationary mould . Consequently mould oscillation was adopted, with little delay, on further installations.

The oscillation is typically sinusoidal and for some period of the downstroke, the mould velocity is faster than the strand withdrawal speed. This period is referred to as *negative strip* (t_N) and when this is expressed as a fraction of the total period of oscillation it is called *NSR* (negative strip ratio). Some aspects of mould oscillation are shown in Figure 1.3. Oscillation of the mould leads to the formation of '*oscillation marks*' which give the billet surface a rough appearance. The solidification structure beneath an oscillation mark - on account of the locally reduced heat transfer - is much coarser than the subsurface structure between the marks [11] as shown in Figure 1.4. The negative-strip time is known to correlate strongly, as shown in Figure 1.5 with the depth of oscillation marks [12]. This has, of course, to be balanced against the positive effect that mould oscillation has on preventing shell sticking.

Traditionally *oil* has been used as a *lubricant* for casting small sized billets while slab and bloom moulds have been lubricated by mould powders. In the case of billets the liquid lubricant is pumped to the top of the mould into an oil channel from which it weeps through a narrow slot onto the hot mould face. The velocity of the oil down the mould wall is dictated by the oil feed rate and the viscosity which is a function of the mould wall temperature [13]. Proper lubrication by oil is essential to ensure good billet quality in terms of surface defects and cracks. Additionally the presence of oil at and below the meniscus is likely to affect heat transfer rates in the mould and is an important factor in billet shrinkage and, therefore, mould taper. On the other hand, excessive oil flow is uneconomical and contributes to the formation of pinholes on the billet surface. Originally oils for mould-strand lubrication were derived from animal and vegetable sources; however, more recently, mineral oils, are being utilised in mould lubrication.

The continuous casting process has been established worldwide due to its higher yield, enhanced productivity and more uniform quality compared to the conventional ingot casting process. As much as 65% of the current steel production in the world is continuously cast whilst in Japan this figure exceeds 90%. Significant savings in energy can be realised if the continuously cast steel is directly hot charged into the reheat furnace prior to rolling [14]; but for direct charging to be successful it is necessary to produce good quality billets.

After nearly two decades of research at UBC it has been conclusively shown that heat transfer and solidification in the water-cooled mould are of prime importance to billet quality. In view of the fact that steel has low ductility and mechanical strength close to the solidus temperature [15,16], it is not surprising to note that a wide variety of casting problems, ranging from breakouts to shape defects, are directly related to the events in the mould. Thus mould-strand interaction controls billet quality to a large extent.

The present work was undertaken to understand the various factors that influence mould-strand interaction. With the experience at UBC of organising numerous successful plant trials, measurement of mould wall temperature and mould-billet friction forces were carried out on operating moulds at *three different steel plants* in Canada. Data was collected under a variety of operating conditions and then processed through several mathematical models developed for the purpose. Predictions from the models were verified by several independent observations including examination of surfaces and internal structures of billets collected during plant trials. Dramatically different mould-heat transfer rates observed at the three plants could be successfully linked to the shape of the distorted mould during service.

This study has led to a very comprehensive understanding of the factors that influence mould heat transfer and thereby has laid the grounds for the design of mould tapers to cast a wide range of steel grades. It has also been possible to identify an important property of mould lubricating oils necessary for proper lubrication and to recommend oil flow rate. Furthermore, signals from sensors attached to the mould have been related to the formation of defects in the billet. With the knowledge of the various operating variables and their impact on mould heat transfer the foundation has been laid for the design of a control system capable of identifying and correcting billet defects during casting.

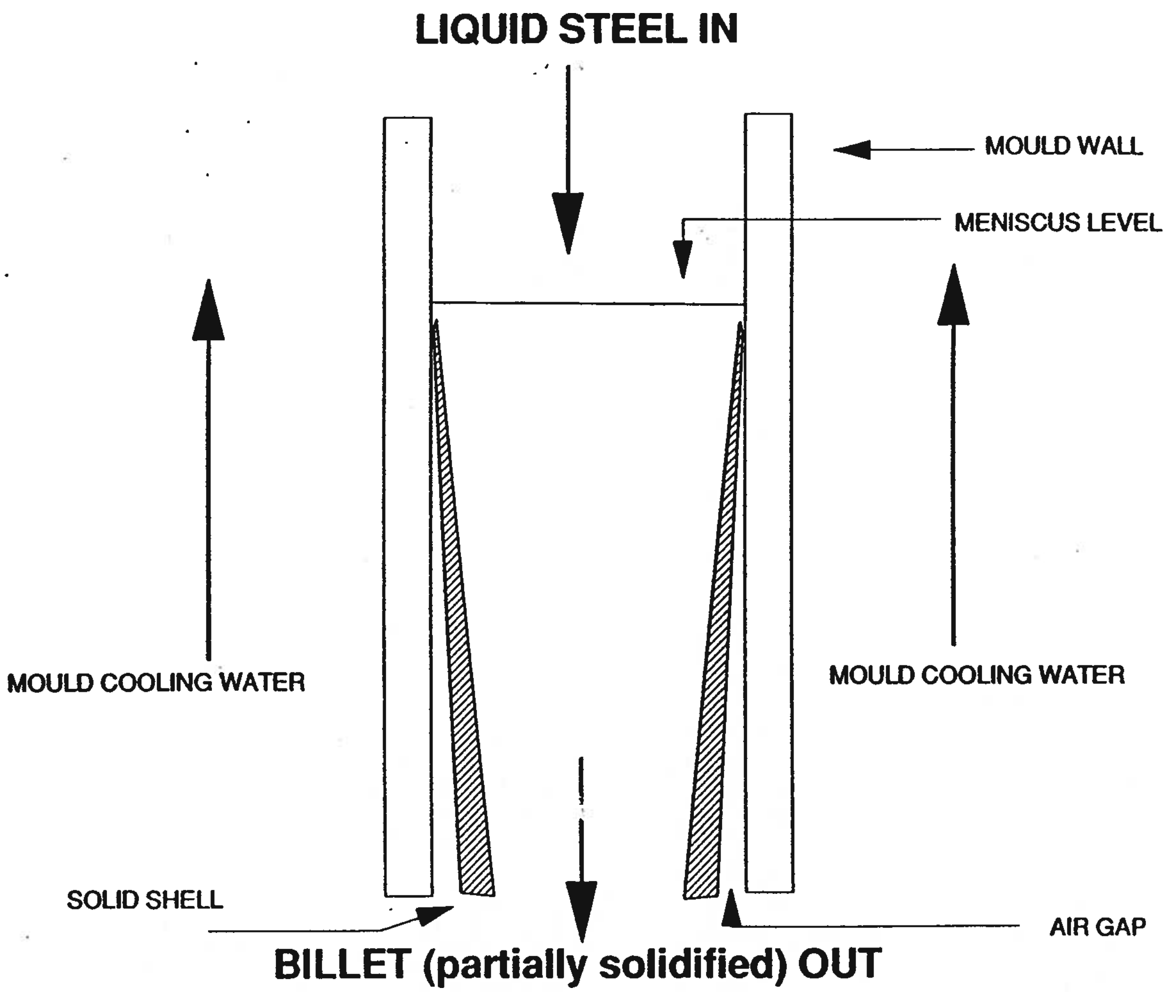

FIGURE 1.1 Schematic diagram of a casting set-up for the continuous casting of steel billets.

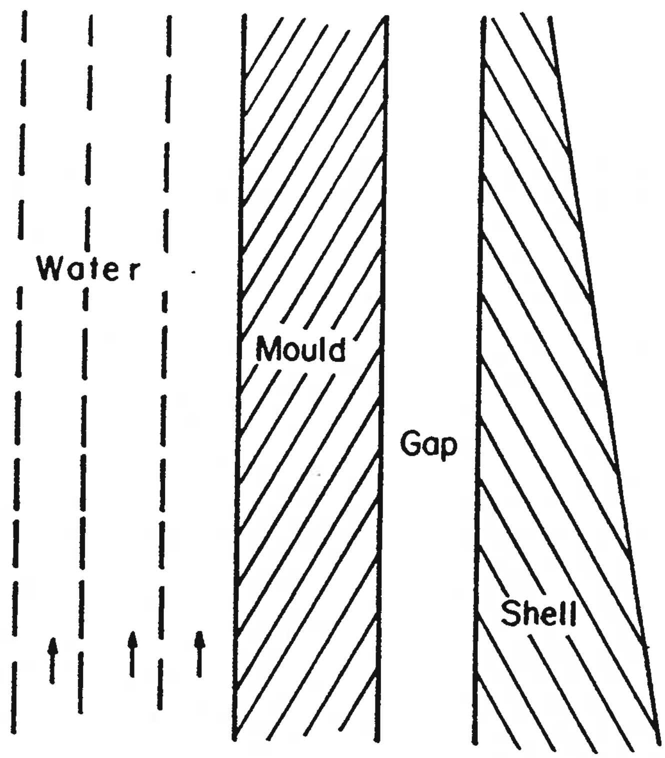

FIGURE 1.2 Schematic diagram of heat removal in a continuous casting machine.

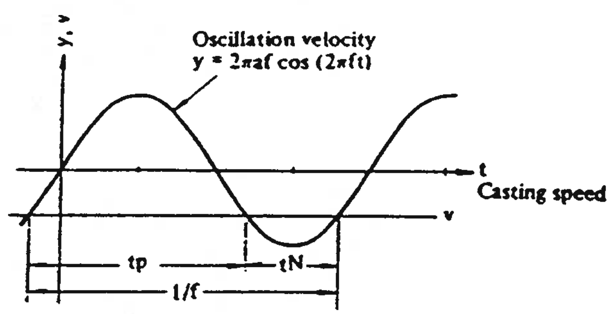

$t_p = \arccos(-v/2\pi af)/\pi f$

$t_N = 1/f - tp$

$NSR = (2f\,t_N) \times 100\ (\%)$

FIGURE 1.3 Sinusoidal oscillation cycle of the mould.

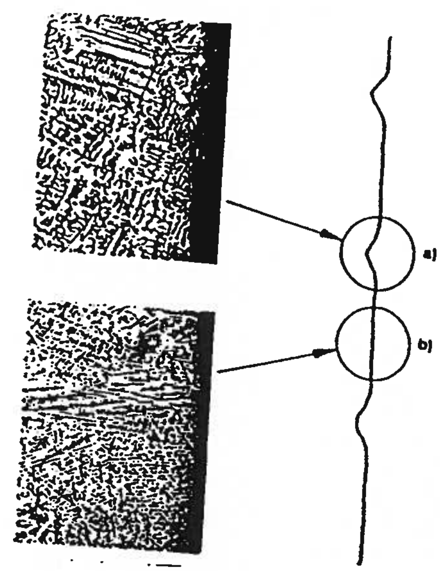

FIGURE 1.4 The effect of cooling rate on billet microstructure.

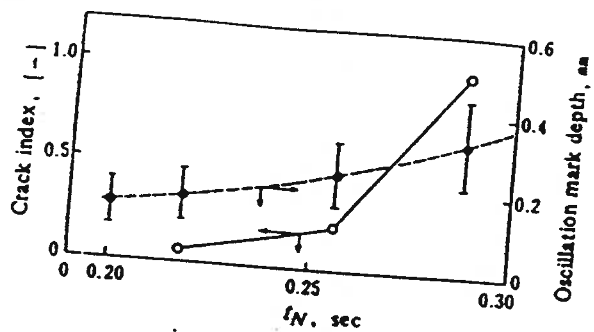

FIGURE 1.5 Relationship between negative strip time and the depth of oscillation marks.

Chapter 2 : LITERATURE REVIEW

This chapter gives an overview of the knowledge available in the literature on billet quality and mould-billet interaction. Notwithstanding the many years that billet casting has been practiced, the mechanism of oil lubrication has never been examined in detail. While there is a rich collection of literature on mould-strand interaction in slab casting, such is not the case in the field of oil lubrication in billets. There are a few minor references to lubrication in the billet mould but it is clear that these are not based on rigorous analysis. Not surprisingly then some of the conclusions are contradictory.

2.1 Thermomechanical Behaviour of the Mould

The billet mould is one of simple design - a copper tube having a wall thickness of 12-18 mm and constrained within a steel jacket with water flowing through the annulus as shown in Figure 2.1. The copper tube is secured in the mould assembly by spilt plates fitting into slots close to the top of all four mould tube faces. The mould has been the subject of extensive research by Samarasekera and Brimacombe [17-22]. The following paragraphs summarize their findings.

The temperature distribution in the wall of a billet casting mould depends on the amount of heat extracted from the solidifying billet, the rate at which it is conducted through the mould wall and the rate of heat transfer to the cooling water. During the casting operation the mould distorts and changes shape in response to internally generated thermal stresses. Distortion of the mould, only part of which is permanent (plastic), arises from the combination of the differential thermal expansion due to non-uniform heating of the mould wall, the restraint of the free expansion of the copper by the mould support system and the geometric configuration of the mould itself. Thus the mould tube bulges where it is hottest near the meniscus to give a *negative outward taper* as opposed to the normal inward taper. Furthermore, the bulge in the mould is not static but changes dynamically in response to mould temperature variations caused by metal level fluctuation and, in some cases, by nucleate boiling in the cooling channel.

The variables that influence the magnitude of the bulge, and its position relative to the top of the mould are cooling water velocity, metal level fluctuation, position of the mould tube constraint relative to the top of the mould, and the type of the constraint. It has been found that a four-sided constraint to support the mould tube within the housing is superior to a two-sided constraint. As regards cooling water velocity, it has been established that a drop in its value leads to an increase in both the magnitude of the negative taper below the metal level and the peak distortion.

With the aid of mathematical models, based on data collected in industrial trials, Brimacombe, Samarasekera and co-workers have been able to link mould distortion and dynamic mould wall movement due to nucleate boiling to several mould-related quality problems such as rhomboidity, non-uniform oscillation mark depth, etc. The impact that mould-strand interaction has on billet quality is covered in a subsequent section.

While the effect of several operating variables on the distortion of the mould has been established by Brimacombe, Samarasekera and co-workers, the impact of a few other variables have not been quantified. Thus the effect on mould distortion, of casting low-carbon billets as opposed to high-carbon billets has not been established. Similarly, the impact that the pre-existing mould taper may have on the shape the mould acquires during service, is an area that needs further investigation.

2.2 Mould Lubrication with Oil

As mentioned earlier, oils used for mould-strand lubrication were originally derived from animal and vegetable sources. Occasionally, mineral oil is blended with vegetable oil and used during casting. There are a multitude of physical and chemical tests which yield useful information on the characteristics of lubricating oils. Some of the most common tests are outlined below.

(a) The *Carbon Residue* of a lubricating oil is the amount of deposit, in percentage by weight, left after evaporation and pyrolysis of the oil under certain prescribed conditions.

(b) The *Flash Point* of an oil is the temperature at which the oil releases enough vapor to ignite when an open flame is applied while the temperature at which vapors are released rapidly enough to sustain combustion is called the *Fire Point*. For any specific product, both flash and fire points will vary depending on the apparatus and the heating rate. The flash point of oils varies with viscosity - higher viscosity oils have higher flash points.

(c) The *Pour Point* of a lubricating oil is the lowest temperature at which it will pour or flow when it is chilled without disturbance under prescribed conditions. Most oils contain some dissolved wax and, as an oil is chilled, this wax begins to separate as crystals that interlock to form a rigid structure which traps the oil in small pockets preventing it from flowing.

(d) Probably the single most important property of a lubricating oil is its *viscosity*. Viscosity can be determined by measuring the force required to overcome fluid friction in a film of known dimensions. Viscosity determined in this way is called *dynamic* or *absolute viscosity* with units of poise (P) or Pascal seconds (Pa s). Dynamic viscosity is a function only of the internal friction of a fluid. *Kinematic viscosity* combines the effect of oil density and viscosity and can be obtained from division of dynamic viscosity of an oil with its density giving units of Stokes (St) or square millimeters per second (mm^2/s). The viscosity of any fluid changes with temperature - increasing as the temperature is decreased.

A good lubricant, apart from the properties discussed above, needs to be non-toxic and not smoke excessively when used.

2.2.1 Mechanism of lubrication

Three common modes of lubrication encountered in operation of an industrial process where two metallic surfaces slide past each other are *hydrodynamic* (thick film or fluid), *boundary layer* and *mixed lubrication* [23].

In *hydrodynamic* or *fluid lubrication* the surfaces in relative motion are separated by a lubricant layer of appreciable thickness and under "ideal" conditions there is no wear of the solid surface. The thickness of the film is approximately one order of magnitude larger than the roughness of either surface. The resistance to motion is due entirely to the viscosity of the interposed lubricant layer and the coefficient of friction encountered are in the range 0.001 - 0.002.

If the sliding speeds are low or the loads are high then it is often impossible to obtain fluid lubrication and the thick lubricant layer breaks down leading to *boundary layer lubrication.* In this mode the surfaces are separated by a lubricant film of only a few molecular dimension and under this condition the friction is influenced by the nature of the underlying surface as well as by the chemical constitution of the lubricant. The bulk viscosity plays little or no part in the frictional behaviour and the coefficient of friction encountered is in the range 0.1 - 0.4.

Mixed lubrication becomes operative under conditions when the film thickness is reduced from 10 to 3 times the height of the asperities on the surface and the coefficient of friction increases from 0.001 to 0.4.

In the case of boundary layer lubricants, addition of a small amount of fatty acid to mineral oils significantly lowers friction values [24]. This has generally been attributed to the adherence of the fatty acid to the surface of the metal substrate. It has been shown that the fatty acid molecules orient themselves with the carbonyl groups at the solid surface. This results in the formation on the surface of a film of fatty acid molecules all attached to the surface as shown in Figure 2.2. These layers actually isolate the surface of the two metals and thereby reduce friction. The forces of adhesion are strong enough to resist removal of the fatty acid and there are indications that a chemical reaction actually takes place at the surface resulting in the formation of a soap film that is chemically bound to the metal surface.

Indirect evidence of the formation of a soap film can be observed from the fact that fatty acids are most effective as friction reducers where the nature of the metal permits a definite chemical reaction. Table 2.1 shows that non-reactive surfaces are almost unaffected by fatty acids as compared to more reactive surfaces. Another piece of indirect evidence is that the temperature at which the lubricant film breaks down is considerably higher than the melting point of the fatty acid temperature and corresponds approximately to the stage at which metallic soap, formed by chemical reaction, softens and melts. It has been found that the greater the number of carbon atoms and the longer the molecule, the lower the coefficient of friction. This is expected as the longer hydrocarbon chains would provide more effective separation of the two surfaces.

2.2.2 Factors affecting mould friction

2.2.2.1 Oil flow rate and oil type

The only published work on the effect of *oil flow rate* on lubrication is that of Brendzy [13]. In an industrial trial with a mould instrumented by load cells, Brendzy showed that the reduction of oil flow (from 54 ml/min to 24 ml/min) for three different types of lubricant studied resulted in increased interaction between the strand and mould as shown in Figure 2.3. That such an interaction could be seen regardless of the oil type or the effect of carbon is an indication of how strongly friction is affected by flow rate. This enhanced interaction, however, did not seem to have any significant effect on billet quality. The relevance of the different regions of the sensor signal is explained in a subsequent section.

It has been shown [13] that the three oils under study exhibited a different degree of lubrication at the same flow rate. It has been suggested that this may, in part, be a reflection of the differences in the fatty acid content of the different lubricants. Additionally, the lubrication by these oils showed a varying degree of dependency on flow rate. However, as changes in the lubricant type could not be separated from the changes in the grade of steel cast, this finding remains inconclusive. Furthermore, in light of the prevailing high temperatures during continuous casting, it is unrealistic to expect that the amount of fatty acid in the oils, can significantly alter the performance of lubricants.

2.2.2.2 Steel grade

Mairy et al. [25] have shown that the lubrication is different with each steel grade and that, at least in case of *slab casting*, the flux practice must be adapted to the different steel grades. It was shown by them that steels with 0.13% carbon produce lower friction signals than those with 0.40% carbon. This has been attributed to the peritectic transformation in low-carbon steels giving rise to maximum contraction and non-uniform shell growth. It is debatable, however, if the shrinkage of low-carbon steels would necessarily be higher than high-carbon grades. While there is an "extra" contraction in low carbon grades arising from the δ to γ phase transformation, the heat transfer for these grades is known to be low. Without carrying out appropriate calculations, it is difficult to say which factor dominates.

Singh and Blazek [26] plotted mould friction as a function of carbon content of steel, Figure 2.3, from their work on an experimental caster. The stationary experimental mould was lubricated by Swift 1011 oil at 8.5 ml/min. While acknowledging a wide variation in values the authors concluded that steel with a high carbon content (more than 0.4%) tended to have lower mould friction which they attributed to the higher carbon in steels acting as a lubricant. The low friction value for the 0.1 % carbon steel (compared to lower carbon grades) was thought to be related to the amount of rippling on the surface of the billet.

Since Singh and Blazek have not discussed how friction measurements were carried out and in light of their "experimental mould", it is difficult to comment on how much of their results apply to an industrial caster. In any case a recent work at Hoogovens, Holland [27], where an operating mould was instrumented by accelerometers, has shown that higher friction values were obtained while casting low-carbon grade steel billets. This result contradicts that obtained by Singh and Blazek. The higher friction values for low-carbon grades have been explained [27] on the basis of larger contact area of the billet with the mould arising out of a smaller shrinkage for these grades.

2.2.2.3 Mould taper

Komatsu et al. [28] have studied mould friction on a small scale experimental caster using mould powder as a lubricant and found that excess tensile stress is applied to the solidified shell by a tapered mould during positive stripping periods. It will be shown in a subsequent section that the heat flux in the mould which governs the magnitude of solid shell contraction, is taper dependent.

2.3 Heat Transfer in the Mould

In its simplest form, the transfer of heat from the liquid steel to the mould cooling water takes place by conduction through the solid shell, across the billet-mould gap and through the mould wall followed by convection at the mould cooling water interface, as was explained in the previous chapter. From the heat transfer point of view, the mould can be divided into two zones [29] : an upper region in which heat extraction can be influenced by factors altering the gap width or gap conductivity like taper, mould distortion, lubricant type and flow rate, and a lower region of gap and shell resistance dominance in which the heat extraction can be influenced by factors like casting speed (alters the shell thickness) and taper (changes gap). The influence of the lubricating medium on the heat transfer is examined in the following section.

2.3.1 Effect of oil on heat flux

To lubricate the mould with oil, an oil film is created on the mould wall. This oil film flows down to the meniscus and pyrolyses in contact with the steel meniscus. Part of the oil escapes as gas while the rest may be pushed into the gap between the mould and the solidifying shell during the downstroke of the mould oscillation [27,30]. Mould powders, on the other hand, melt and wet the steel, with the extent of wetting being controlled by interfacial forces. The difference in behaviour between the two types of lubricant gives rise to different patterns of heat extraction. A plot of specific heat-flux profiles (total heat extracted per unit weight) for an oil and two different mould fluxes is shown in Figure 2.5. Klipov et al. [31] have reported that the oil heat flux is greater than the powder in the upper part of the mould by 15-20% while it is the reverse in the lower part of the mould by 20-25%. The higher upper-mould heat flux with oil is probably on account of a hydrogen-rich atmosphere (from the pyrolysis of oil) between the shell and the mould which increases the thermal conductivity of the gap. In the lower part of the mould spray water is believed to penetrate and decompose in the mould/strand gap to from a hydrogen-rich gas [32]. Taylor [32] suggests that oil wets the strand surface more effectively than a high melting point powder and reduces the production of hydrogen.

There are some difficulties in understanding the explanations offered by the authors above. Firstly, it is well known that heat transfers in billet casting (using oil) are higher than those obtained in slab casting (using powders) and secondly, it is unclear how a layer of oil can "wet" the steel strand which is at a temperature in excess of 1100 °C.

2.3.2 Effect of mould powders on heat flux

Singh and Blazek carried out experiments in a continuous casting mould with horizontal water passages [33]. They found, using mould powder as a lubricant, that

(i) In the case of low-carbon steel (C = 0.10%) the heat transfer increased just below the meniscus but decreased thereafter as shown in Figure 2.6.

(ii) In the case of high-carbon steel (C = 0.40%) the heat transfer was significantly lower over the entire mould length as shown in Figure 2.7.

The behaviour of low-carbon steel is believed to be caused by the molten flux filling in the 'ripples' on the steel skin just below the meniscus thereby increasing the thermal conductivity of the gap. In the lower regions of the mould the ferrostatic force, in the opinion of the authors, causes the steel shell to be in contact with the mould wall and the presence of the molten flux then acts as an insulator. In case of high-carbon steels, the authors suggest that the billet surface, being smooth, are in good contact with the mould wall and the introduction of the mould flux causes the latter to behave as an insulator thereby decreasing heat transfer. It needs to be mentioned, however, that these experiments were on a stationary mould the length of which was almost half that of a typical industrial mould (0.8 m).

2.3.3 Effect of steel grade on heat flux

Several researchers [17,34] have reported a drop in the heat transfer rate while casting steels with carbon content of around 0.10%. This reduction is thought to stem from the large volume shrinkage accompanying the δ to γ phase transformation for these grades of steel. The phase change and the resulting shrinkage occur when the solid shell of the billet is thin causing the billet surface to ripple. The increased surface roughness of the billet locally increases the mould-billet gap causing a drop in the heat transfer from the billet to the mould.

2.3.4 Mould taper

As mentioned in the previous chapter, in the case of billets, some researchers have observed that mould taper improves heat transfer [3,4] and also decreases the surface temperature at the strand exit [5], presumably because it reduces the gap width over the lower region of the mould. However, details of the actual measurements are not available and it is difficult to guess whether heat transfer measurements were carried out with a systematic change in mould tapers. In the case of continuous casting of slabs, mould design, in particular the taper of the narrow plates [34,35], is known to influence the heat transfer in the mould. Deshimaru et al. [34] have enhanced heat extraction rates near the corner by using a plate with a higher taper at the corner. Wolf [36] has shown that the heat flux in the mould is enhanced with increase in the taper of the narrow face as shown in Table 2.2.

2.4 Mould-Friction Measuring Devices

Friction in the continuous casting mould has been monitored by several techniques. In almost all cases there is little knowledge on the exact nature of the friction forces so that usually a relative measure of the friction is made, making it difficult to compare results from different sources. In addition, certain devices employ measuring techniques from which the effect of friction cannot be cleanly separated.

2.4.1 Accelerometers

Short et al. [36] replaced linear variable displacement transducers (LVDTs) used for routine checking of mould oscillation with *accelerometers* as the latter were found to be simpler and more sensitive than the LVDTs and, additionally, could be used as an indicator of mould friction. These researchers blended esters with commercially available mould lubricating oils to optimize wetting behaviour, mould heat transfer and mould friction. Their experience shows that good mechanical stability of the oscillator is required to avoid interference with what they called "metallurgical effects of solidification" in the mould. They found that commercial oils could be blended with esters to lower friction in the mould to levels obtained with powder lubrication. No further details are available on their work.

More recently, Stel et al. [27] have also used accelerometers to measure mould friction. Their work complements the results obtained by Brendzy [13].

2.4.2 Strain gauges

Yamanaka et al. [37] have measured the frictional forces in their experimental caster by mounting *strain gauges* on the centre rod which pulls the solidified shell. Wolf [38] refers to a similar technique where the net frictional force was measured by piezo-quartz transducers mounted on the mould support. The observed increase in frictional force at higher casting speed was attributed to a decrease in mould flux thickness in the mould-shell gap. Foussal et al. [39] positioned strain gauges on the coupling rod of a mould and found that the signal generated was periodic although a difference in phase exists between mould displacement and mould friction. In the case of the Japanese workers, the frictional force was found to lag behind the mould displacement by 90 degrees at slow casting speeds (1.2 m/min). However, this phase difference became negligible at high casting speeds. They attributed this behaviour to the rheological characteristics of mould flux. In the case of the French workers, it is the mould displacement which lags behind the friction force for which they offer no explanation.

The apparent contradiction in the observation of the two researchers reinforces the importance of the location at which installation strain gauges are installed and the difficulties of simulating the actual behaviour of the mould in a laboratory. Furthermore, it is unclear what exactly is meant by "lag" or "lead" of the friction signal over the mould displacement signal.

2.4.3 Load cells

The third and probably the most popular method of monitoring mould friction has been the use of *load cells*. Several researchers have used load cells mounted on the mould oscillating table [13,25,40-43], of which Brendzy's [13] work conducted on (industrial) billet moulds, is the only one that discusses the results obtained in some detail.

Komatsu's [40] measured, the friction force in terms of the difference in apparent mould weight and mould inertia weight and found it to decrease along a straight line during casting and to be higher for tapered moulds. Additionally the friction force during the negative strip period decreased as the NSR decreased.

Gloor [41] has developed a commercial mould friction measuring system (MFM) that employs a load cell mounted on the connecting rod between the eccentric drive and the short-lever oscillation mechanism. Data acquisition and evaluation by a computer equipped with special hardware and software makes it possible to calculate and deliver the friction values virtually in real time. His work shows that boron-alloyed steel (C = 0.19%) has a substantially higher friction than a 0.48% carbon steel when cast on the same strand, with the same mould at casting speeds of 1.8 m/min and 1.5 m/min respectively.

Mairy and Wolf [25] studied the friction acting on a slab mould and found that friction forces were much higher and tended to fluctuate more when oil was used as the lubricant instead of powder. This observation is similar to that of Short et al. [35] in their investigation of lubricants in billet casting. Additionally, 0.12 % carbon steels yielded a significantly higher friction level than that for lower carbon (0.08%, 0.06%) when consecutively cast with the same mould powder. Stel et al. [27] have also reported higher friction forces when billets are cast with oils rather than with mould flux.

Brendzy [13], in an industrial trial, placed load cells between a mould housing and the oscillator table. Linear Variable Displacement Transducers (LVDTs) were placed on the mould table to record the oscillation characteristics of the mould system. A copper mould and mould cooling water were instrumented with an array of thermocouples. In view of the detailed nature of their work and its relevance to the current proposal their results are described in somewhat greater detail in the next section.

2.5 Load Cell Response and its Analysis

As mentioned earlier, a billet mould with an empirically designed parabolic taper (4.9%/m in the meniscus region, 1.8%/m in the middle of the mould and 0.8%/m toward the end of the mould) was instrumented with load cells placed between the mould housing and oscillator table to measure loading on the mould during casting. LVDTs were located on the mould table to record the oscillation displacement of the mould system.

A typical load cell profile is shown in Figure 2.8. The response of the load cells is periodic and consists of two distinct modes of mould-strand interaction in each oscillation cycle. The first occurs during the upstroke and the second during the downstroke. The minimum loads (valleys) vary at a low frequency while the maximum loads (peaks) remain relatively constant. Additionally the nature of the peaks is distinctly different from that of the valleys. While the minimas exhibit a relatively smooth appearance, the maxima are broader and appear jagged. This phenomena has also been observed by Stel et al. [27].

It was further seen that as the mould moves downwards (as indicated by the LVDT signals), there is a sudden decrease in the compressive load as the negative-strip period begins. This decrease continues smoothly until the maximum downward velocity of the mould is reached at which point the load begins to increase. During upstroke the load cells signals exhibit a slip-stick behaviour.

By superimposing the casting speed on the load cell response Brendzy showed (Figure 2.9) that there was a clear relationship between the variation of the minimum load and the casting speed. It was seen that minimum load increases as casting speed increases and decreases as the speed decreases. This visual correlation was subsequently verified through regression analysis. The load maxima, on the other hand, were found to be a function of oil type and flow rate. In an interesting analysis of the load cell data, it was postulated that the variation of the maximum loads (as seen for low carbon grades, in Figure 2.10) were a manifestation of binding. This conclusion was subsequently corroborated by an examination of surface of the billet cast during the test period.

2.6 Mould-Strand Interaction and Billet Quality

Of the fundamental processes taking place during the casting of steel, heat transfer and solidification in the water-cooled mould are among the most important. It is recognised that a wide variety of casting problems, ranging from breakouts to shape defects and surface quality, are related directly to events in the mould. Clearly then mould-strand interaction controls billet quality to a large extent. Some of the common defects in billets that can be traced to adverse mould strand interactions are discussed below.

2.6.1 Oscillation Marks

Several mechanisms have been proposed to explain the formation of oscillation marks in billets. Conceptually these can be divided into the following two categories :

(i) The solidifying shell at the meniscus "sticks" to the mould wall such that on the upstroke of the mould, the shell ruptures allowing liquid steel to partially fill the gap created. Subsequently with the mould moving downwards, there is a period of "healing" when the ruptured shell reforms [32,44-49].

(ii) The billet mould distorts during operation so as to acquire a negative taper at the meniscus. During downstroke the distorted mould jams down on the solidified shell causing it to buckle leading to the formation of an oscillation mark [17] as shown in Figure 2.11.This mechanism can adequately explain the effect of several operating variables like mould cooling water flow rate, mould wall thickness and mould material on the depth of oscillation marks. Further, recent work [13] involving load cells has confirmed the interaction of the mould and the billet during the negative-strip period. Strong support for this mechanism has also been seen in the work of Stel et al. [27], who have observed a sudden decrease in mould acceleration in the middle of negative strip period. The authors explain this by considering the interaction between a negatively tapered mould with the billet surface during the negative strip period. The obstruction of the mould movement by the strand causes a drop in the downward acceleration of the mould.

There is general consensus that factors enhancing meniscus solidification promote formation of oscillation marks and that the pitch of these marks can be obtained by dividing the casting speed with mould oscillation frequency.

2.6.2 Transverse Depression and Transverse Cracks.

A mechanism for the formation of transverse depression has been proposed by Samarasekera and Brimacombe [29] as shown in Figure 2.12. Here a schematic representation of a longitudinal section of the billet in the mould is shown and, owing to inadequate shrinkage of the billet or/and excessive taper of the mould, the billet binds in the mould and the solid shell is then subjected to two opposing forces - a withdrawal force pulling it downward and a friction force, on account of binding, resisting withdrawal. Under these conditions, the solid shell behaves somewhat like a specimen in a tensile test and forms a "neck" in the ductile section adjacent to the surface region. This "neck" is what is seen as a transverse depression on the surface of the billet. The less ductile regions of the shell, close to the solidification front, may break open forming a transverse crack at the base of the depression.

2.6.3 Billet Rhomboidity and Internal Cracks.

Two of the most common mould-related quality problems encountered in billet casting are rhomboidity and longitudinal corner cracks as shown in Figures 2.13 and 2.14. Detailed research by Samarasekera, Brimacombe and co-workers [18] has established that surface cracks and shape defects are related. Indirect evidence of this also appears in work by other researchers who have shown that when rhomboidity is reduced through corrective measures for adverse mould conditions, it also leads to a reduction in the severity of longitudinal corner cracks [50-53]. Further when the two defects occur together, the cracks tend to appear at the obtuse-angle corners of the rhomboid billet [49,50]. When the cracks form in the absence of rhomboidity they are usually a result of improper corner radius [3,54] or mould distortion and wear [50,51].

By analysing heat flux data obtained from industrial trials with several mathematical models, Samarasekera and Brimacombe [18] have shown that low mould cooling water velocities lead to intermittent boiling asynchronously on different mould faces. The result is that the different faces of the billet cool at unequal rates which causes nonuniform shrinkage and rhomboidity as the colder faces contract more than hotter faces (which may even expand if the surfaces reheat). Further the situation may be aggravated by the mould itself assuming a rhomboidal shape in response to the asynchronous nature of intermittent boiling of the mould cooling water.

The dynamic billet rhomboidity may give rise to longitudinal cracks at the obtuse-angle corners of the shell because a tensile strain acting parallel to the diagonal joining the acute-angle corners is generated at the solidification front as shown in Figure 2.15. Tensile strains may also be generated at the solidification front due to surface reheating if the obtuse-angle corner of the billet pulls away from the mould, thereby creating a locally wide corner gap and reducing heat flow to the mould. Depending on the crack depth, the extent of reheating, and the magnitude of the tensile strains generated by the ensuing shrinkage of the shell as it cools deeper in the mould, the crack may penetrate to the surface and become a visible defect at the corner. In extreme cases this could lead to a breakout.

The proposed mechanism is consistent with several plant observations listed below.

(i) The simultaneous occurrence of longitudinal corner cracks and billet rhomboidity.

(ii) Change in the orientation of billet rhomboidity during a cast.

(iii) The presence of longitudinal crack at the obtuse angle corners.

(iv) The interdendritic nature of the crack [50,55,56].

(v) Greater severity of these defects in steels containing 0.18% - 0.25% carbon [51,57] and higher carbon (> 0.4%) grades [52,58].

(High heat transfer rate during the casting of high-carbon grade billets is likely to cause the water to boil while the low ductility of steels with carbon content between 0.18% and 0.25% may play an important role in the formation of cracks).

(vi) The improvement in billet quality with reduction in mould cooling water flow rates in high-carbon grades to levels lower than that maintained for lower carbon steels [58].

(As the water velocity is reduced, boiling becomes more vigorous and less intermittent, such that cooling is more uniform around the periphery of the mould, and rhomboid conditions are less likely).

(vii) The increase in severity of rhomboidity with decrease in section size [51].

(Smaller size billets (100-130 mm square) are sometimes cast through moulds that have wall thickness of 6-9.5 mm compared to 12.7 mm wall thickness for larger billets (150-180 mm square). Thinner mould walls would cause the water to boil leading to rhomboidity in small billets).

(viii) Reduction in rhomboidity by machining horizontal serrations on the outside surface of the mould wall in contact with the cooling water [57].

(The roughness of the outside wall promotes sustained boiling and effectively eliminates the boiling hysteresis that triggers thermal cycling in the mould wall and causes intermittent boiling in the cooling channel).

The mechanism proposed above may be too crude to explain the important effect of the other variables such as corner radius, superheat and casting speed on rhomboidity and longitudinal corner cracks. There is one common factor linking these variables viz., all affect corner shell thickness. It is probable that a thinner corner shell (on account of increased casting speed, higher superheat and increased corner radius) may simply be more susceptible to surface cracking in the zone of intermittent boiling because they are considerably hotter, and cracks can more easily propagate to the surface.

Off-squareness can be linked to the spray cooling as well. It has been observed by Bommaraju et al. [59] that the obtuse angle corners of off-square billets usually had the deepest oscillation marks, and hence reduced local heat extraction in the mould, relative to other areas around the periphery of the billet. Under such conditions these corners, emerging from the mould, would be thin and hot, as is often observed in the spray chambers of continuous casting machines, Cracks could form most easily adjacent to these corners owing to the locally weakened shell. On the other hand, corners with shallow oscillation mark experience higher heat extraction in the mould and would have thicker and cooler solid shell at the exit of the mould. Thus the solid shell profile of such a billet at the bottom of the mould may be as shown in Figure 2.16. The off-squareness at the exit from the mould cannot exceed that of the mould itself but, once the billet reaches the spray, the cooling of the shell again would be non-uniform due to the varying shell thickness. The differential contraction can then cause the billet to assume a rhomboid shape.

2.6.4 Off-Corner Internal Cracks

In a study on mould behaviour and billet solidification, Bommaraju et al. [59] found that internal cracks were observed within 15 mm from any corner at a depth of 5 mm from the surface in many of the transverse billet sections. The authors postulated that deep oscillation marks form in the off-corner regions and locally reduce heat extraction and shell growth. Towards the exit of the mould where the mould-billet gap is large especially with an empirically designed single taper, bulging and subsequent hinging of a face or faces of the billet in the off-corner regions would take place. This would result in the generation of tensile strains at the solidification front in the off corner regions leading to internal cracks as shown in Figure 2.17. Thus cracks can form and continue growing inwards following the solidification front, as it advances, as long as the strain is maintained. Based on this mechanism, off-corner cracks should appear at the sites that have the deepest oscillation marks as was found by the authors.

Thus the achievement of uniform, shallow oscillation marks should reduce the incidence and severity of off-corner cracks. Also measures to minimize shell bulging in the lower region of the mould should decrease the cracking problem. Thus a properly tapered mould could have a beneficial effect by reducing the mould-billet gap.

2.6.5 Pinholes

Donaldson [60], in his examination into the quality of billets, found that pinholes occur more frequently on the sides of the billets than at the corners and that the pinholes have a tendency to form in zones. Excessive lubricant has often been thought to promote the formation of pinholes. The oil pyrolyzes due to the elevated temperatures providing excess hydrogen responsible for creating pinholes. Recently researchers have related pinholes to the oxygen content of the liquid steel [27]. Other researchers, like Brown [61] have shown that the presence of excess moisture in the ladle or tundish and high tapping temperature may cause pickup of the hydrogen and nitrogen which would also lead to pinholes.

Table 2.1 Coefficient of friction at room temperature [24].

Surfaces	Clean	Paraffin Oil	Paraffin Oil + 1% Lauric Acid	
Nickel	0.7	0.3	0.28	Non-reactive
Chromium	0.4	0.3	0.3	
Platinum	1.2	0.28	0.25	
Silver	1.4	0.8	0.7	
Glass	0.9	—	0.4	
Copper	1.4	0.3	0.08	Reactive
Cadmium	0.5	0.45	0.05	
Zinc	0.6	0.2	0.04	
Magnesium	0.6	0.5	0.08	
Iron	1.0	0.3	0.2	Less reactive
Aluminum	1.4	0.7	0.3	

Table 2.2 Effect of taper of the narrow face of a slab mould on the average heat flux in the mould [36].

Taper (%/m)	0	1.5	2.2	2.6
Mould heat flux (kcal/m²min)	15 008	16 704	19 575	*

*Strand is sticking in the mould.

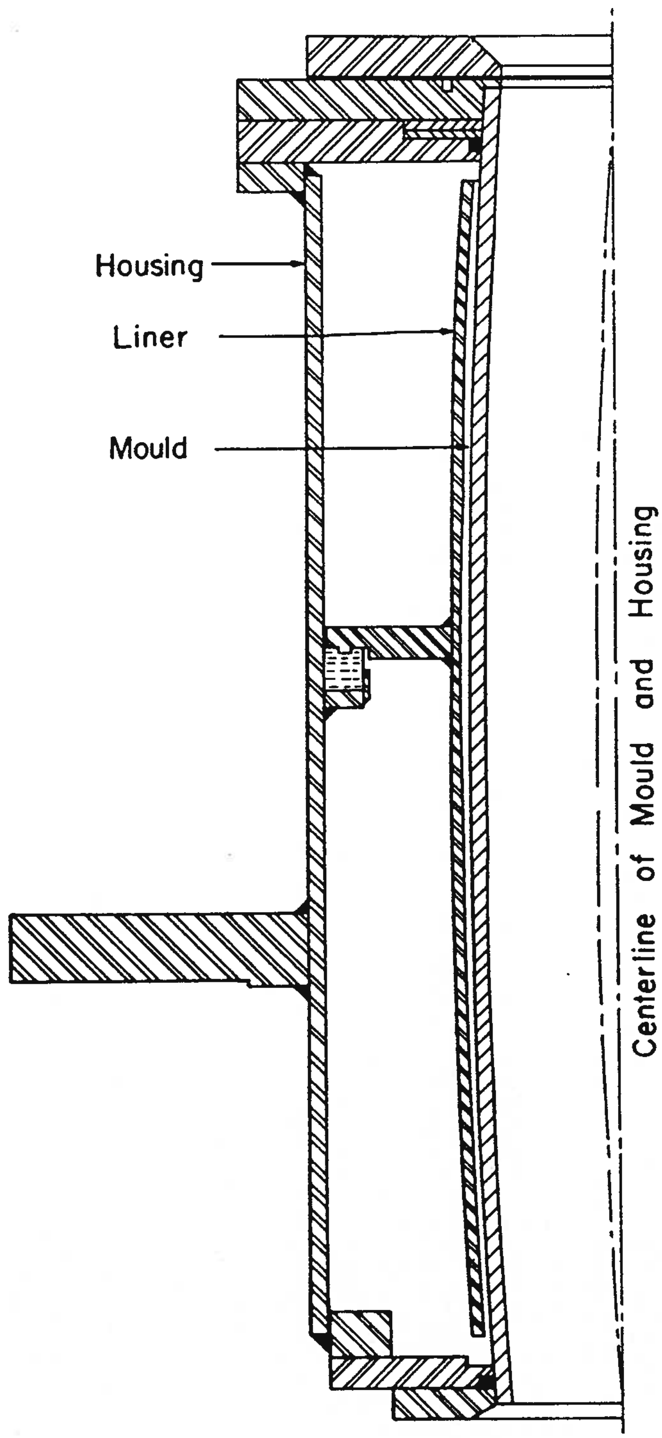

Figure 2.1 Schematic diagram of a typical mould used for continuous casting of steel billets.

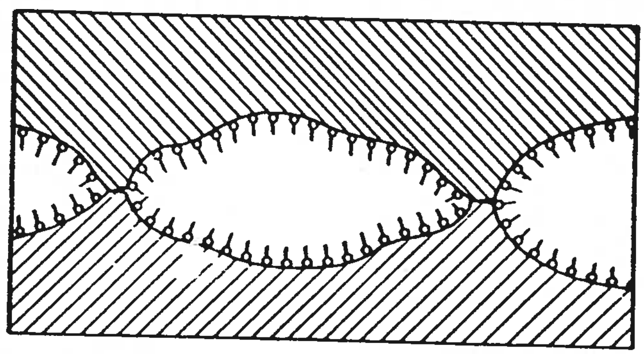

Figure 2.2 Schematic diagram of fatty acid molecules adhering to the solid surface [24].

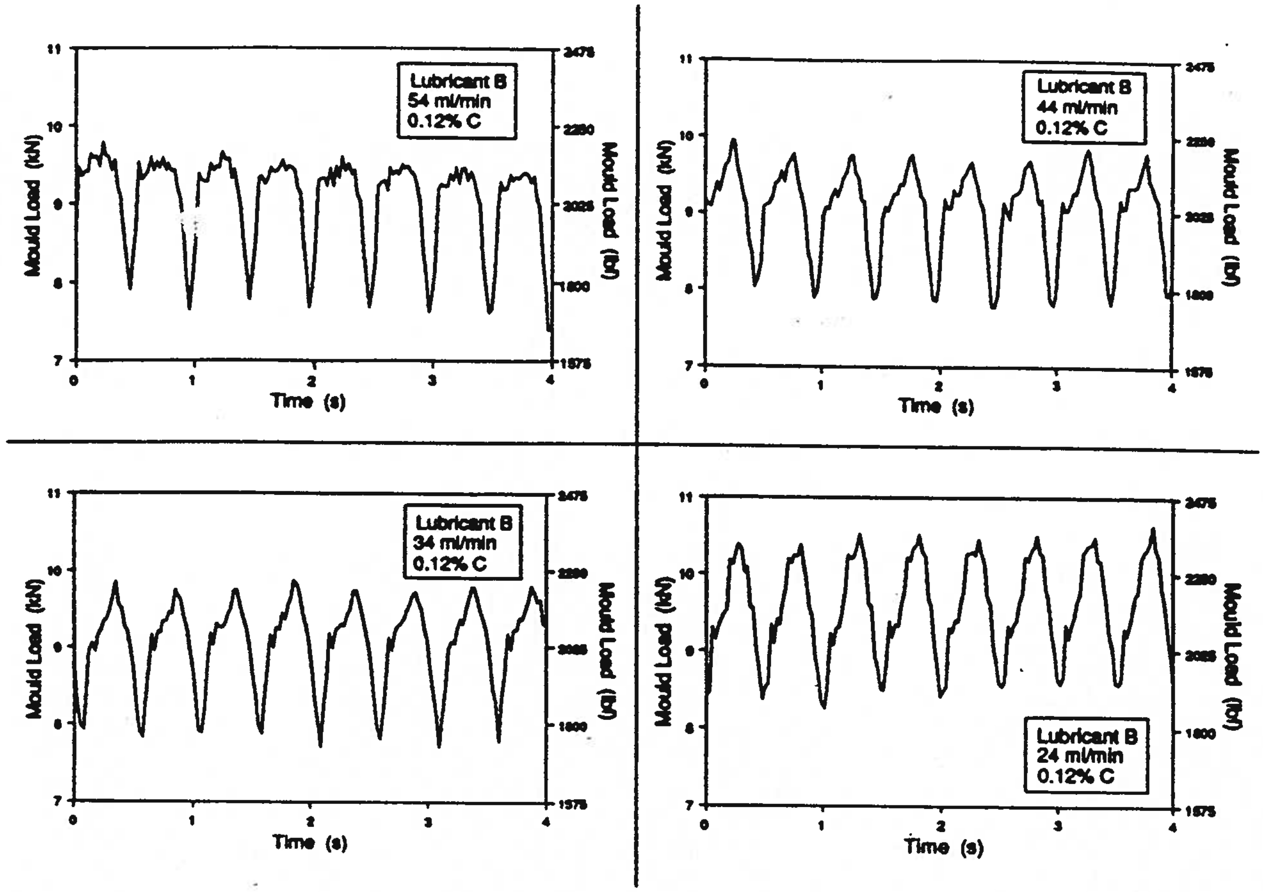

Figure 2.3 Load cell response at different flow rates of mould lubricant B during casting of low-carbon billets [13].

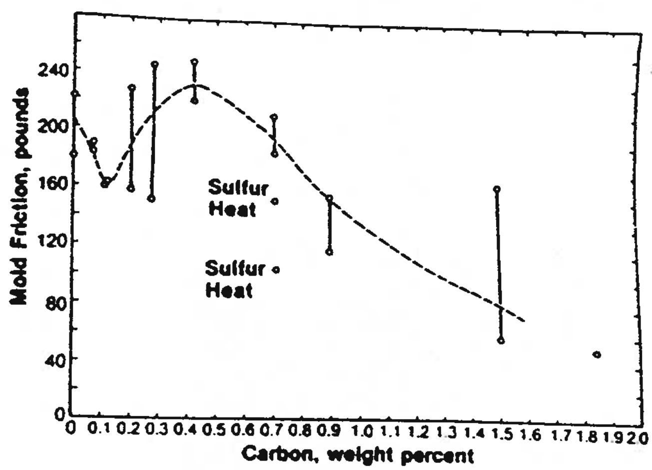

Figure 2.4 Effect of carbon content of steel on mould fricition during continuous casting of steel billets. Data obtained using an "experimental" mould lubricated by Swift 1011 oil at 8.5 ml/min [26].

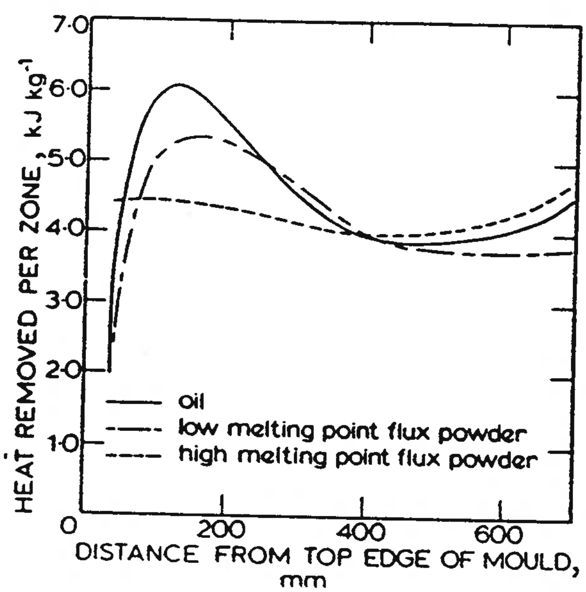

Figure 2.5 Specific heat extraction as a function of distance from the top of the mould for different lubricants [31].

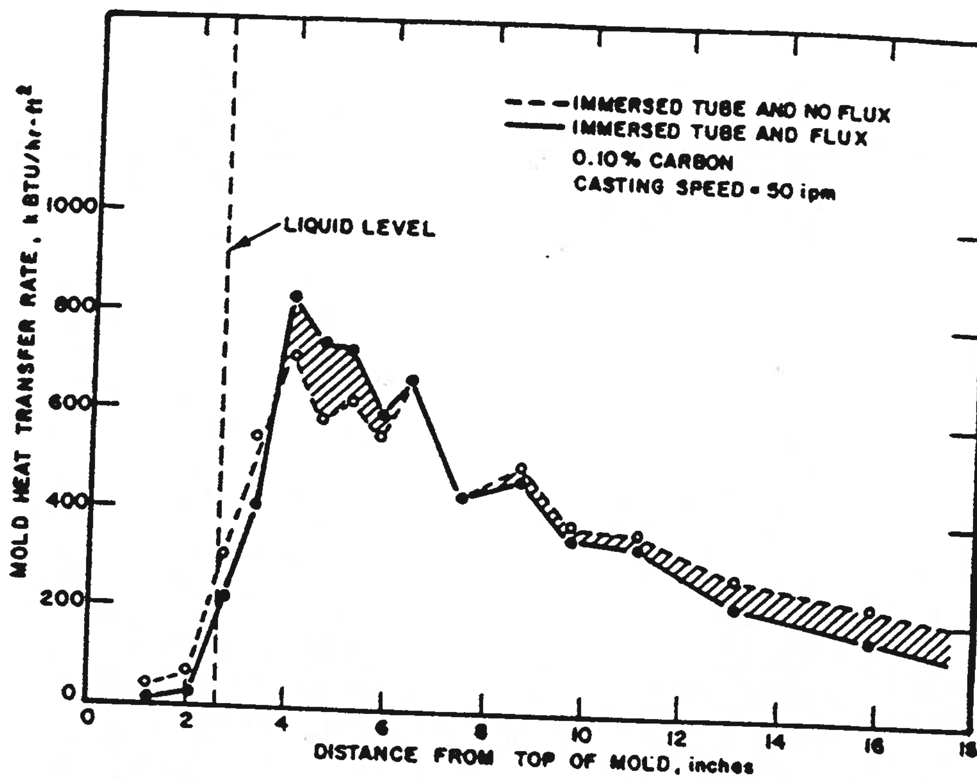

Figure 2.6 Effect of mould flux on the heat-flux profile for low carbon steel [33].

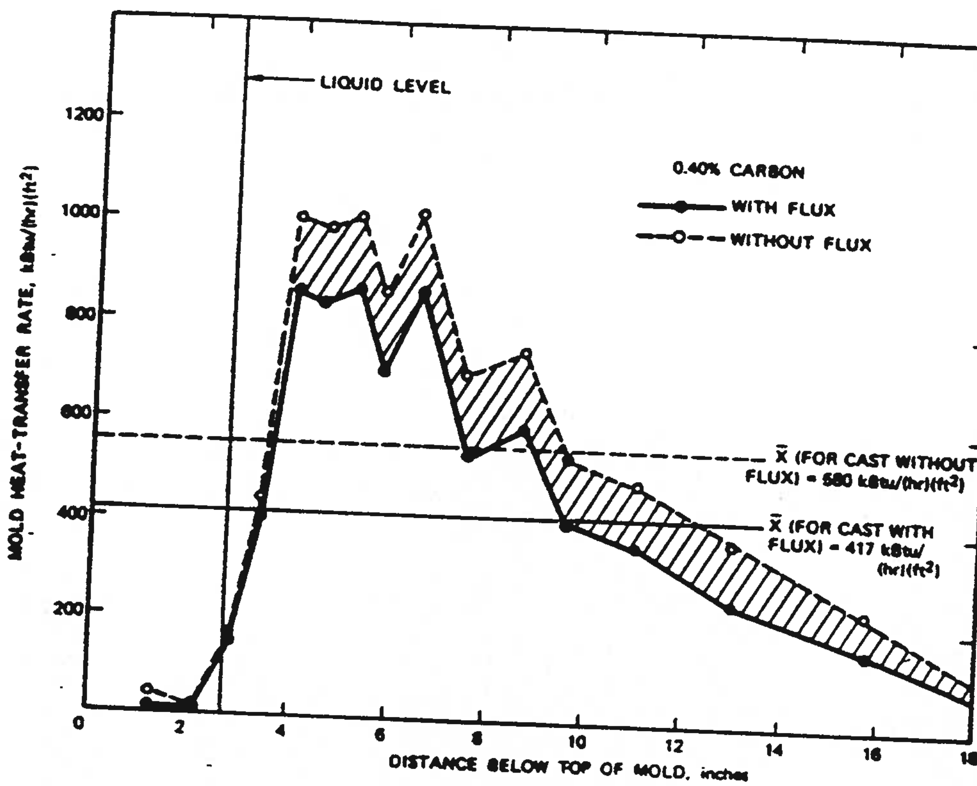

Figure 2.7 Effect of mould flux on the heat-flux profile for high-carbon steel [33].

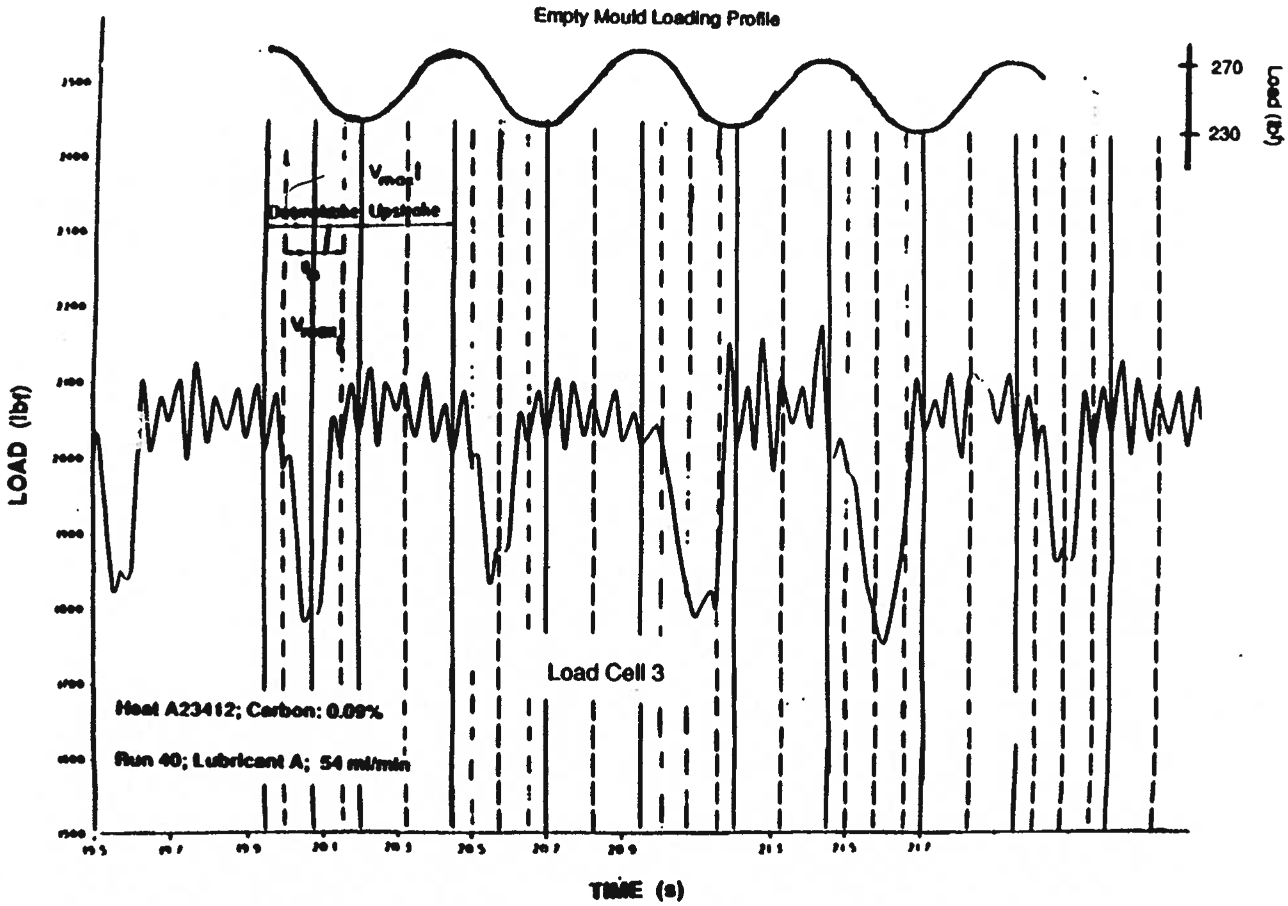

Figure 2.8 A typical load cell profile [13].

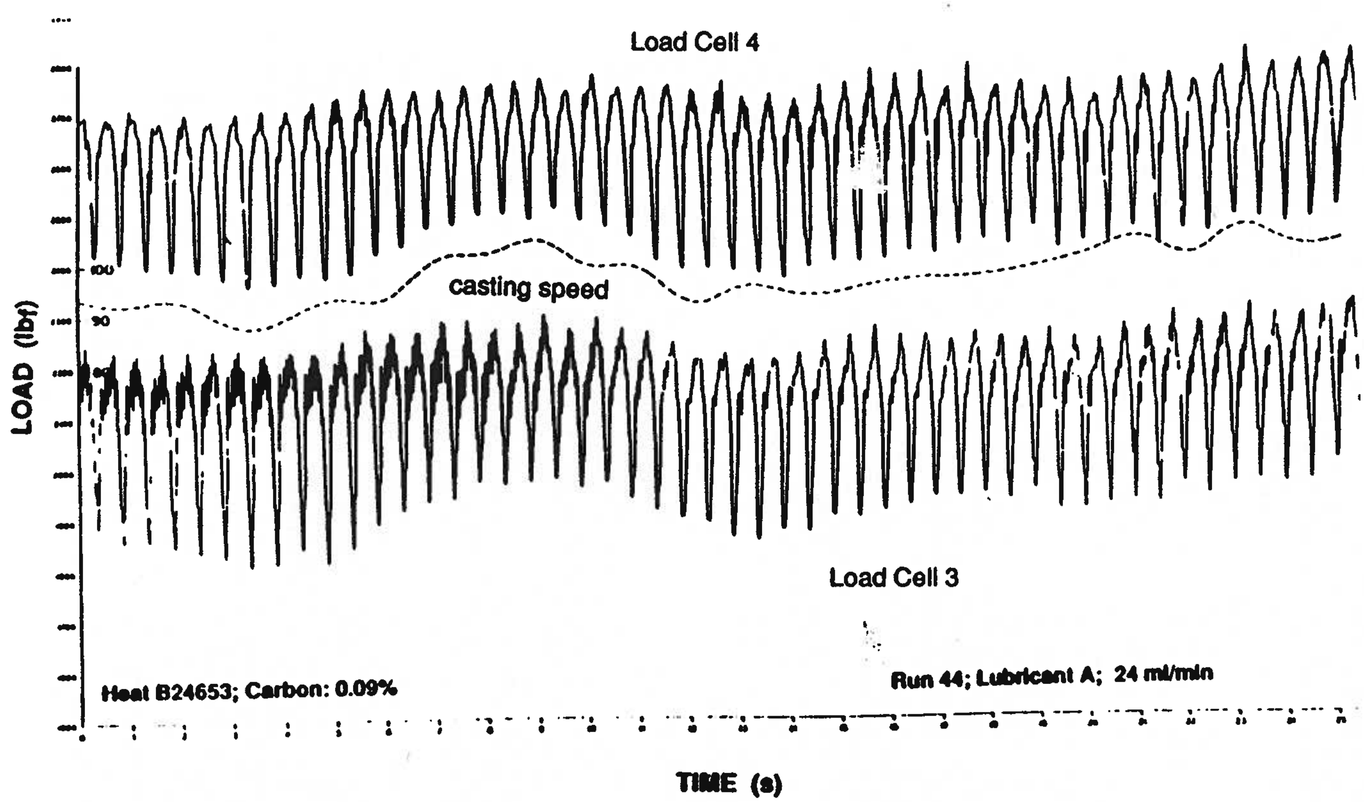

Figure 2.9 Change in the minimum load with casting speed [13].

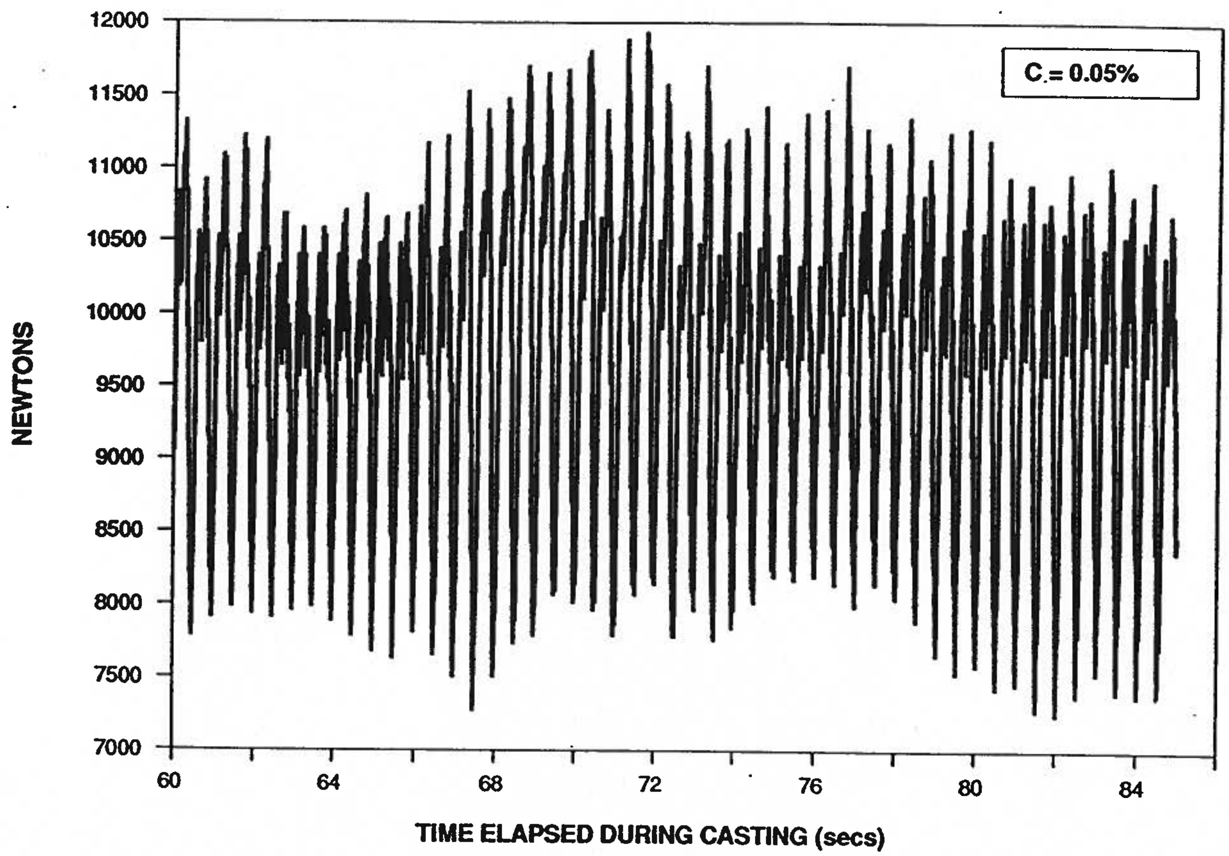

Figure 2.10 Load cell response for a billet binding in the mould [13].

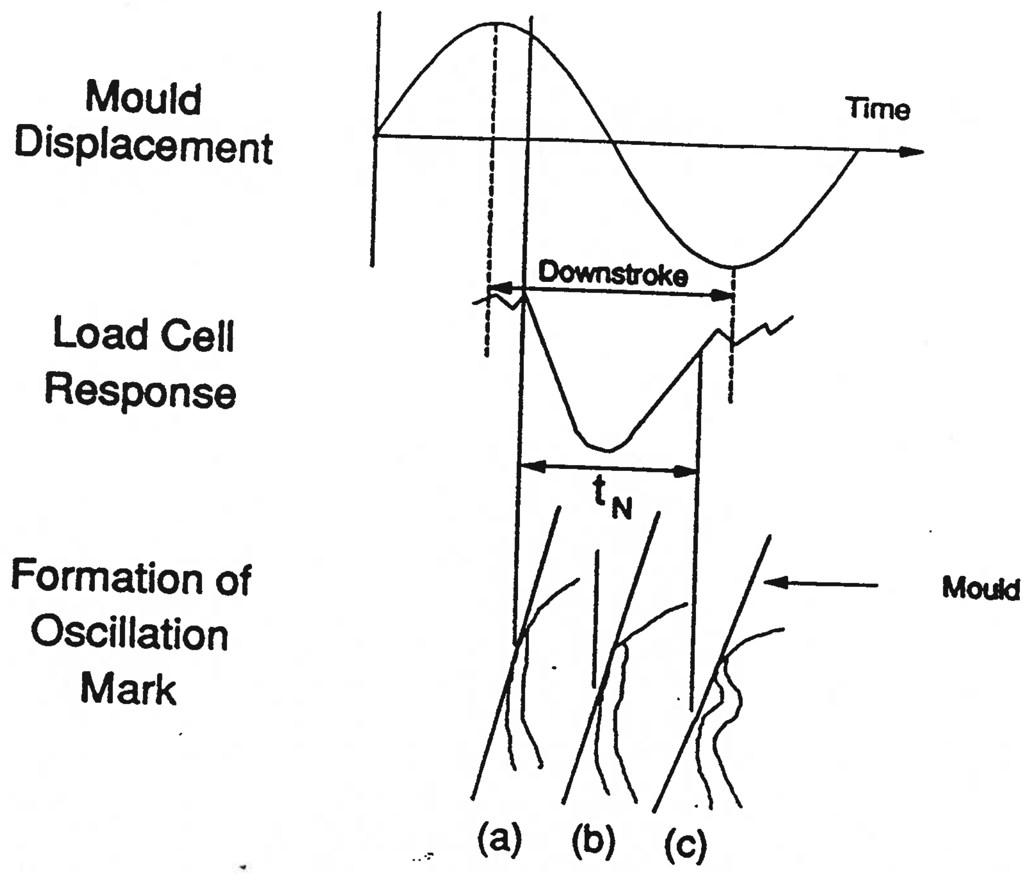

Figure 2.11 Mechanism for the formation of an oscillation mark due to interaction of the mould with the billet during negative strip period [13].

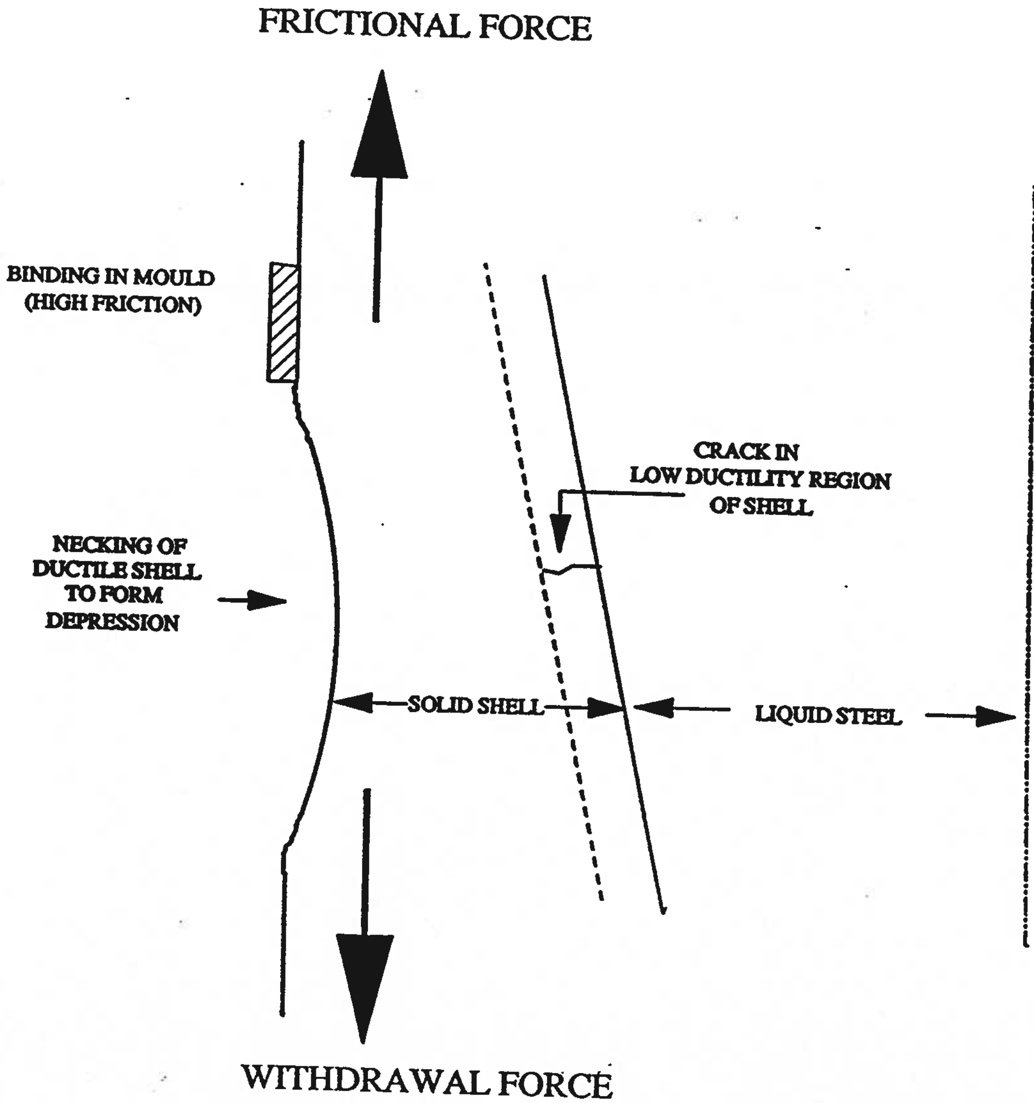

Figure 2.12 Mechanism for the formation of transverse depressions and transverse cracks (not to scale) [29].

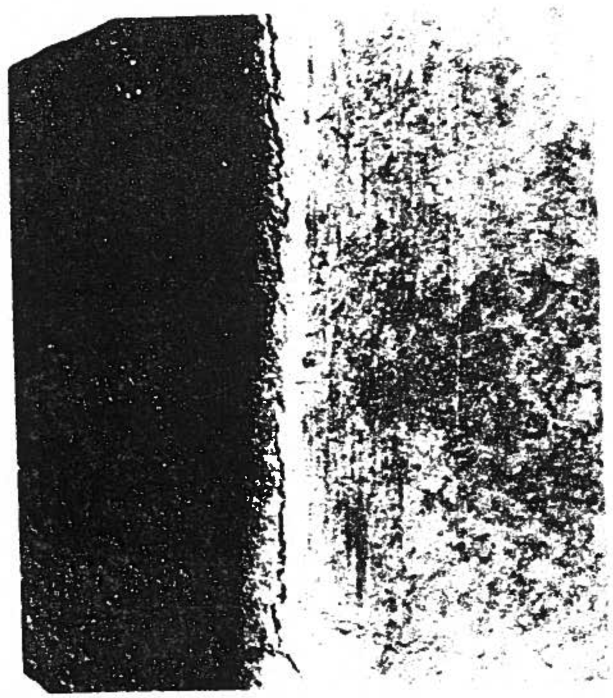

Figure 2.13 Longitudinal corner cracks in continuously cast steel billets [18].

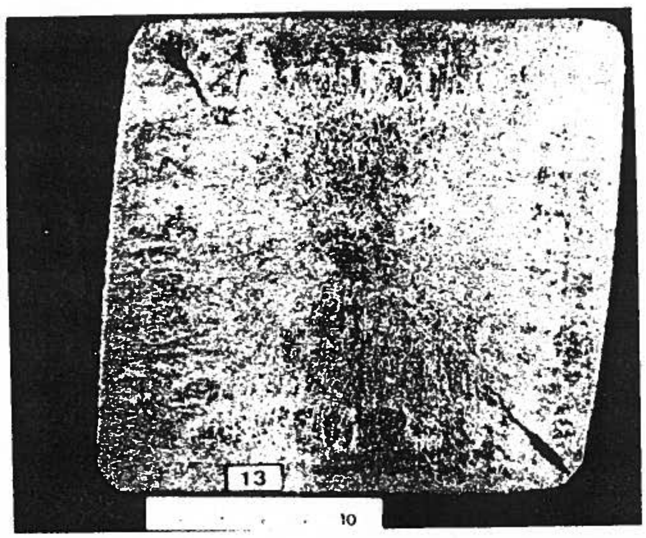

Figure 2.14 Off-squareness in continuously cast steel billets [18].

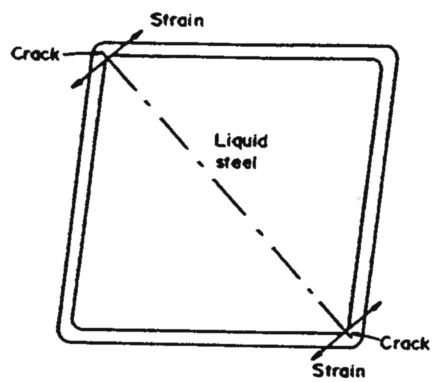

Figure 2.15 Schematic diagram showing the formation of sub-surface crack on the diagonal at the obtuse-angle corners of a off-square billet [18].

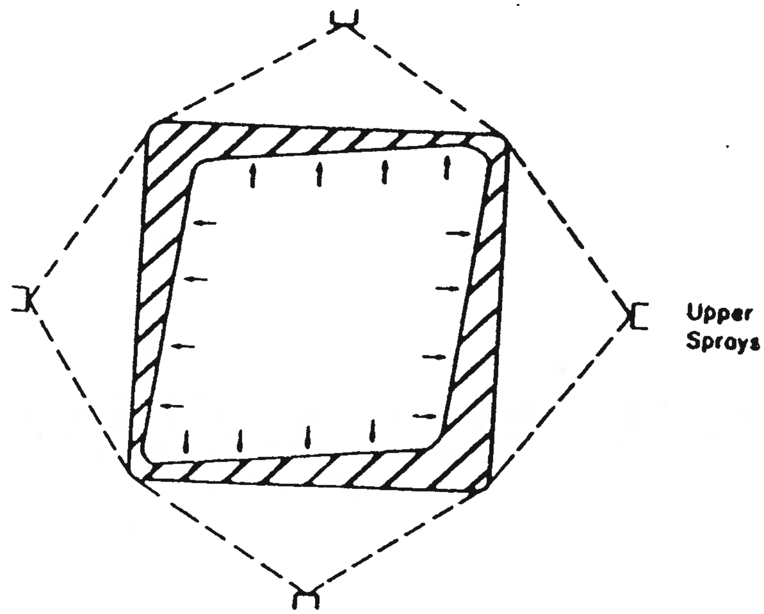

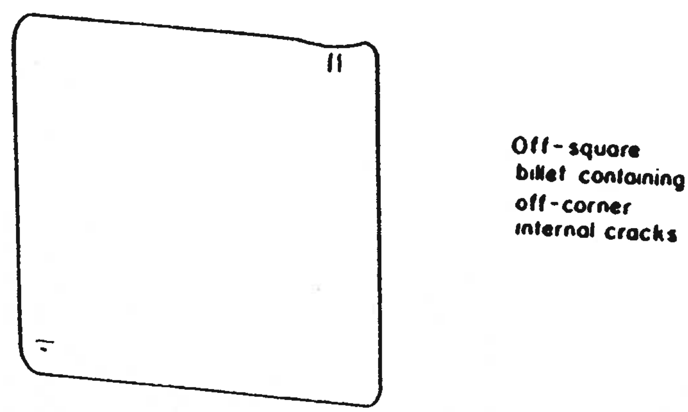

Figure 2.16 Schematic diagram showing billet with non-uniform shell thickness being distorted into off-square shape by spray cooling [59].

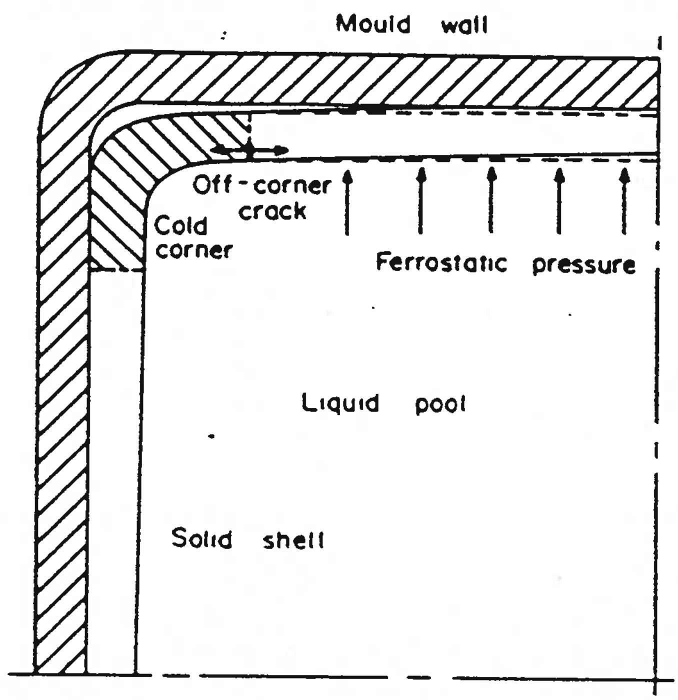

Figure 2.17 Schematic diagram showing the generation of an internal crack due to bulging of the billet shell in the mould and a hinging action in the off-corner region [59].

Chapter 3 : SCOPE AND OBJECTIVES OF THE PRESENT WORK

As has been discussed in the previous chapters the genesis of quality problems of the billet lies in the mould. Though sketchy in details, it is clear from the chapter on literature review, that research workers are in consensus that heat transfer and lubrication in the mould are the most crucial parameters that control billet quality.

It is also clear that, owing to dissimilar shrinkage characteristics of different grades of steel, there cannot be a universal mould taper through which all grades of steel can be successfully cast. Furthermore, while the need for a lubricating oil is well established, little is known about the influence the various properties of oil have on lubrication and heat transfer.

Considering the complicated nature of the continuous casting process and the interplay of various components of the casting machine it is highly unlikely that any useful knowledge can be gained from laboratory experiments. Clearly plant trials, in which operating moulds can be instrumented by sensors, need to be carried out. It was felt that the measurement of mould temperature and mould-billet friction forces would reveal the effect of various variables on mould-billet interaction and provide insight into design of mould taper for different grades of steel

With a view to ultimately understand variables that affect mould taper design and the role of oil in mould lubrication, three plant trials in which operating moulds were instrumented by thermocouples and load cells, were organised. It was hoped that the analysis of the data collected from trials would be able to fulfill the following objectives :

[1] To determine the mechanism by which heat is extracted in the mould as well as determine the heat extraction rate for a range of steel grades.

[2] To modify and use a mathematical model of the mould wall capable of calculating heat-flux profile down the mould wall.

[3] To develop a mathematical model to simulate the solidification of steel and its shrinkage as a function of its position in the mould.

[4] To develop a computer program to analyse load cell signals as a function of mould displacement.

[5] To ultimately specify *oil flow rates* and *mould tapers* necessary to successfully cast a wide variety of steel grades.

[6] To link sensor signals to formation of defects in the billet.

Chapter 4 : EXPERIMENTAL

Plant trials were conducted at three plants identified as Companies B, C and E. In order to systematically study the effects of various operating parameters, it was decided to collect mould temperature and mould-billet friction data for different grades of steels. For each grade of steel, data was collected at least at three different flow rates of the mould lubricating oil. A total of six different types of oils were used - four vegetable based oils and two mineral oils. The oils were chosen so as to give a range of boiling points, eg. the mineral oils have low boiling point (< 200 °C) while the boiling points of vegetable oils are higher. In order to asses the impact, if any, of the fatty acid content of the oil a High Erucic Acid oil (HEAR), was used. Data could be collected for billets with carbon contents ranging from 0.05% to 0.80%. For some period of the trial, the oscillation frequency of the mould was changed from the one normally used. The details of the trials and the equipments used to collect data are discussed below.

4.1 Pre-Trial Preparations

In preparation for the trial the condition of the mould system was determined at each of the three plants. To this end, a series of checks were made on the oscillator, mould water flow, mould oil distribution system and mould design. Additionally the three companies were responsible for checking the machine alignment and monitoring the quality of the mould water carefully to ensure that it met desired standards.

4.1.1 Retrofit of mould housing

At Company B and C, the original mould constraint system had consisted essentially of two keeper plates which fitted into slots machined into the straight sides of the mould wall. This is the same system that has been extensively studied and found to result in non-uniform distortion around the mould periphery and subsequent billet quality problem [62], particularly if a shallow metal level

(<100 mm) is maintained. Therefore, the constraint system was changed to one incorporating tight-toleranced four-sided constraints, known to be superior from a billet-quality stand point [63]. This required the manufacturing of new split plates and the cutting of new slots on the four mould wall faces. The tolerances achieved by custom machining to match the split plates to mould tube slots was less than 0.076 mm. Similar work had to done on the top plates at Company E.

A new oil plate was also manufactured, prior to the trials, based on the UBC Oil Distribution System [64]. This system ensures uniform oil flow on all faces of the mould wall. Finally, recesses were machined into the mould housing to accommodate the load cells and several holes were drilled and tapped in the housing wall for thermocouple wires to pass through.

4.2 Measurement of Mould Wall Temperature

Brimacombe, Samarasekera and co-workers have, for the last two decades, successfully instrumented operating moulds with thermocouples to measure mould wall temperatures [8,13,17,19]. The same time-tested technique of thermocouple installation was adopted in the present work.

The installation procedure, in its simplest form, consists of drilling holes through the steel baffle tube and the copper mould wall such that when the thermocouple wire is inserted, the tip of the thermocouple rests approximately mid-way between the hot and the cold faces of the mould. Care is taken to ensure that all the holes that are drilled are at the mid-face of the mould and to the same depth in the mould wall. A flat bottom drill is used to flatten the drilled hole which is then tapped using a bottom tap to ensure threading to the bottom of the hole. The hole depth is measured and recorded.

Single wire, Type T (Copper-Constantan) intrinsic thermocouple, is used to measure mould wall temperature. A bead is created on the Constantan (55% Cu - 45% Ni) thermocouple wire (diameter = 0.81 mm) by using a TIG welding machine. The bead is filed to produce a flat foot like end approximately 0.30-0.40 mm thick. Heat shrinkable tube (1.6 mm in diameter) is then shrunk onto the bare Constantan wire. This wire is then inserted through the baffle into the mould wall and held in place by a threaded copper plug screwed into the copper mould. Use of silicone sealent ensures a water tight fit. Shielded copper wires are joined with the Constantan wire in the water chamber and the former is then connected to the Data Acquisition System by bringing out the wires through holes cut in the mould housing. The mould is pressure tested to ensure that there are no water leaks. To monitor the bulk inlet, the bulk outlet and the outlet water temperature at each face of the mould two wire, type T thermocouple were used. The temperature of the data acquisition or junction box (cold junction temperature) was measured by a mercury-in-glass thermometer. A schematic diagram of the set up is shown in Figure 4.1. All thermocouple wires were tested for continuity and calibrated.

Type T thermocouple can be used to measure temperature from -270 °C to 400 °C and the use of an intrinsic thermocouple ensures that the arrangement has a low thermal inertia. The time taken by a 1 mm Constantan wire on a copper substrate to reach 95% of the steady state e.m.f is of the order of micro-seconds [65].

4.3 Measurement of Mould-Billet Friction Forces

Brendzy in her thesis [13] has described in detail the installation procedure for the load cells for measurement of mould-billet friction forces and the same method was followed.

The load cell is a transducer that converts a load acting on it into an analog electrical signal. This conversion is achieved by the physical deformation of strain gauges which are bonded to the load cell button and wired in a Wheatstone bridge configuration. Weight applied to the load cell through compression produces a deflection of the button which introduces strain to the gauges. The strain produces an electrical resistance change proportional to the load. The load cells are of the LCG series (of OMEGA) and capable of withstanding 44.5 KN of compressive loading. The cells are 38.1 mm in diameter and have a total height of 15.8 mm and are shown in Figure 4.2. Manufacturers specifications indicate that these can handle 150% of the full scale load, operate accurately in temperatures up to 121 °C and a have repeatability value of +/- 0.05% of full scale (~ 22.7 N).

The load cells were calibrated prior to use on an Instron machine. The 10 volts power supply necessary for the excitation of the load cell was obtained by connecting three 6 volts batteries in series. The resulting 18 volts supply was stepped down to 10 volts via a self compensating voltage circuit designed to maintain a constant output voltage. Filters were placed in the circuit to eliminate any noise pick up in the 10 volts line.

The load cells were positioned between the mould housing and the mould oscillator table as shown in Figures 4.3 and 4.4. Four circular recesses were machined into the mould housing plate into each of which a load cell was placed. Due to the coarse threads on the hold down bolts, which connect the housing to the oscillating table, a bolt spring assembly was designed to control the initial torquing load on the load cell. As the mould housing was lowered onto the oscillating table, the load cell positioner was turned until the load cell button contacted the oscillating table. The bolts were then tightened until the spring became fully compressed.

4.4 Measurement of Mould Displacement

To record mould displacement, linear variable differential transformers (also called linear variable displacement transducers) were used.

The LVDT is an electromechanical device that produces an electrical output proportional to the displacement of a separate moveable core. It consists of a primary coil and two secondary coils symmetrically spaced on a cylindrical frame as shown in Figure 4.5. A free-moving, od-shaped magnetic core inside the coil assembly provides a path for the magnetic flux linking the coils. When the primary coil is energized by an external ac source, voltages are induced in the two secondary coils. These are connected series opposing so that the voltages are of opposite polarity. Therefore, the net output of the transducers is the difference between these voltages, which is zero when the core is at the centre or null position. When the core is moved from the null position, the induced voltage in the coil towards which the core is moved increases, while the induced voltage in the opposite coil decreases. This action produces a differential voltage output that varies linearly with changes in core position.

The LVDTs' are attached to the housing in such a way that they register the movement of the mould. Since it is not necessary to know the absolute displacement of the mould, the LVDTs' do not have to be calibrated on the oscillator. It is only necessary to ensure that the full range movement of the LVDT, when in use, is within the linear output range of the circuitry.

Two Daytronic (model 3130) signal conditioners were used to operate the LVDTs. The LVDTs' were calibrated to provide an output of 2.5 volts per 10 mm displacement.

4.5 Other Miscellaneous Measurements

4.5.1 Casting Speed

The signal from the withdrawal roll tachometer which is proportional to the casting speed, was used to record the casting speed. The signal from the tachometer is typically 0-40 or 0-200 volts D.C and was stepped down (0-20 millivolts) and filtered for any electrical noise (8 or 45 Hz) before being sent to the data acquisition system. The calibration of the signal was done on site by measuring the output voltage relative to the casting speed gauge and adjusting a variable resistor so as to produce a convenient ratio (e.g 10 mv = 100 ipm).

4.5.2 Metal Level

The 4-20 milliampere signal from the metal level controller was modified to produce a 0-10 millivolt output before it was connected to the data acquisition setup. This signal was calibrated by lowering a steel billet into the mould and measuring the output signal for different lengths of the test billet in the mould.

4.5.3 Internal Dimensions of the Mould

To measure the internal mould dimensions (taper trace) of a continuous casting billet mould an apparatus consisting of 3 LVDTs and a 10 turn potentiometer are assembled and calibrated in such a way as to enable a constant measurement of the mould profile as the equipment is passed through the mould. Taper traces are thus obtained for three locations on each mould wall. The accuracy of the measurements are +/- 0.024 mm.

4.5.4 Filming of the steel surface

The meniscus region of the steel surface was filmed by a hand held camcorder focussed on the steel surface in the mould. It was thus possible to see and record the motion of the oil down the mould wall.

4.6 Data Acquisition

4.6.1 EXP-16

Metrabyte's Universal Expansion Interface, Model No EXP-16, is an expansion multiplexer / amplifier system as shown in Figure 4.6 that can be used with any data acquisition system.

Each EXP-16 concentrates 16 differential analog input channels into one analog output channel and also provides signal amplification, filtering and conditioning. Additionally, the instrumentation amplifier provides gains of 0.5, 1, 2, 10, 50, 100 as well as programmable gain capability. The 16 differential input channels are selected by a solid state 4 bit TTL/CMOS compatible address. Provision is made on the board for filtering, attenuation and measuring current instead of voltage. All analog input connections are conveniently made on miniature screw connector strips. Cold-junction sensing and compensation circuitry as well as a biasing resistor for open thermocouple detection also exists in the system. The EXP-16 can be connected directly to

MetraByte's DAS-8 or sets of EXP-16s can be cascaded by identical cables to a total of 128 channels ($16 \times 8 = 128$) of standard voltage, 112 ($16 \times 7 = 112$) of thermocouple measurement. When used with DAS-8, channel selection is via the OP1-4 digital outputs of the DAS-8.

4.6.2 DAS-8

MetraByte's DAS-8 is an 8 channel, 12 bit high speed, A/D converter and timer/counter board, shown in Figure 4.7, for the IBM PC. The DAS-8 board is 5 inches long and can be fitted into a "half-slot" of a PC. All connections are made through a standard 37 pin D male connector that projects through the rear of the computer.

DAS-8 is a successive approximation A/D converter with sample/hold. The full scale input of each channel is ±5 volts with a resolution of 2.44 millivolts and the inputs are single ended with a common ground. The A/D conversion time is typically 25 microsecond (maximum 35 microsecond). The 8254 programmable counter timer which provides periodic interrupts for the A/D converter has 3 separate 16 bit down counter one of which is connected to the sub-multiple of the system clock and all the I/O functions of the remaining two are accessible to the user. Input frequencies of up to 2.5 MHz can be handled by the 8254. The 7 bits of TTL digital I/O provided are composed of one output port of 4 bits and one input port of 3 bits. Each output handles 5 standard TTL loads (8 mA sink current). A precision +10.00 v ($\pm 0.1 v$) reference voltage output is derived from the A/D converter reference. This output can source/sink 2 mA.

4.6.3 General

To ensure that ground loops are not created all signals were grounded at the source (mould). The shielding was also done appropriately by grounding all shields at one point (mould). The instrument end of the data acquisition setup was "floated" by the use of an isolation transformer. Electrical noise was inadvertently introduced in signals from the sensors at Company E making the task of data analysis extremely difficult. Figure 4.8 is a schematic diagram showing the main components of the data acquisition set up.

The computer based data acquisition system by controlled by Labtech Notebook Software from Laboratory Technologies Corporation, USA. The signals from the load cells and the LVDT's along with signals from a few selected thermocouples were sampled at 50 Hz for 120 seconds; thermocouple signals were collected at 1 Hz. for 600 seconds (10 min) and at 30 Hz. for 100 seconds.

After the completion of the trial all thermocouple wires were tested to identify those that had failed during operation.

4.7 Details of the Trials

This section summarises in the form of several tables the different conditions under which the data was collected at the three plants.

4.7.1 Casting machines and casting practice

The details of the casting machines and the moulds used in the control and test strands at each of the three Plants are shown in Tables 4.1 and 4.2. As can be seen in Table 4.1, the moulds at Companies B & C were square while the mould at Company E was rectangular. Shrouding of the steel stream between the mould and the tundish with nitrogen gas was carried out at all three companies to minimize oxygen pick up by the steel steam. Such a shrouding practice also decreases the chances of the mould lubricating oil burning on the mould wall above the meniscus. The negative strip time for the companies varied, under standard oscillation frequency between 0.13 - 0. 16 seconds. Table 4.2 is a comparison of the control and test strands at each of the three companies. The important features are the following

[a] *The test mould at Company B & E had steep upper tapers while the test mould at Company C was almost untapered near the meniscus.*

[b] All moulds except for the one used in the control strand at Company C were an alloy of Cu-Cr-Zr.

[c] The mould cooling water flow rate was in excess of 10 m/s in all three companies

[d] The test moulds at all three Companies were equipped with the UBC design oil distribution system.

4.7.2 Oils used in the trials

The properties of the various lubricating oils used in the trials are summarised in Table 4.3. As can be seen, the temperature at which 20% of the oil boils off is the lowest for the mineral oil Mineral_S (230 °C), and approximately 280 °C for the other oils. In addition HEAR oil has 45.2% of Erucic fatty acid which is well in excess of the value for the Erucic acid content of the other oils.

4.7.3 Thermocouple arrangements

The arrangement of the thermocouples in terms of their depth and axial position on the mould wall are given in Tables 4.4, 4.5 and 4.6 for Companies B, E & C respectively. At Company B thermocouples were installed on the inner curved wall (ICW), the right side wall (RSW; at both centre and off-centre locations) and the outer curved wall (OCW). At Company E & C thermocouples were mounted on the inner curved wall and the right side wall only. Additionally at Company E, five thermocouples (6 A,B,C,D,E) were placed at the meniscus level from one end to the other of the right side wall.

4.7.4 Chemical compositions and casting conditions of different heats

The chemical compositions of the heats monitored at the three plants are tabulated in Tables 4.7, 4.8 and 4.9 while the casting conditions for the same heats are shown in Tables 4.10, 4.11 and 4.12 for Companies B, E and C respectively.

At Company B (Table 4.7), data was collected for billets with carbon contents between 0.046% to 0.42%; at Company E from 0.17% to 0.89% (Table 4.8) and at Company C, the carbon contents of the billets were between 0.19% to 0.86% (Table 4.9).

At Company B data was collected, as shown in Table 4.10, with flow rates of oil varying between 24 - 53 ml/min. As shown in Table 4.11, at Company E, the oil flow rate was varied between 0ml/min (no oil) to 110 ml/min. Additionally the oscillation frequency of the mould was changed form the normal value of 170 cpm to 130 cpm. At Company C, the frequency of mould oscillation was changed, for selected heats, from 144 cpm to 96 cpm. Additionally, data was acquired for flow rates of oil varying between 0ml/min to 100 ml/min. To clearly identify the effect of oil flow rate on heat transfer, the flow rate of Canola oil was changed from 0 ml/min to 100 ml/min in the middle of a data collection sequence. Table 4.13 summarizes the different types of oil and the flow rates at which they were used at the three plants.

4.8 Laboratory Work

The billet samples collected during the plant trials were subjected to a rigorous inspection procedure which is outlined in the form of a flow chart in Figure 4.9.

Sulphur printing of transverse and longitudinal sections was carried out after the surfaces were ground, washed with soap and water and then dried. The printing was done on resin coated photographic paper which had been immersed for 3 to 4 minutes in a 4% sulphuric acid solution in water. The soaked paper was placed on the section, emulsion side down and rolled to ensure good contact and left there for approximately 4 minutes. The paper was removed, labeled, washed in water to remove the sulphuric acid, fixed and dried. Care was taken to orient the billet section with the ICW at the top of the paper.

Macro-etching was done after the completion of the sulphur printing. A solution of 50% HCL and 50% water was heated to 85 °C for around thirty minutes and then scrubbed to remove the black oxide. The surface was covered with glycerin to prevent rusting, photographed, washed in warm water, dried with alcohol and sprayed with a clear lacquer.

When the subsurface structure was to be examined an appropriately prepared sample was etched with a solution of 5% Picric acid in water at 80-85 °C.

The various kinds of inspections carried out can be broken into the following broad categories:

Dimensional checks	Internal inspection	Surface Inspection
(i) Distance between opposite faces	(i) Internal cracks	(i) Profilometer measurements of oscillation-mark depth
(ii) Off squareness	(ii) Inclusions	(ii) Longitudinal and transverse depressions
	(iii) Porosity	(iii) Surface cracks
	(iv) Cast structure	(iv) Bleeds, laps, pinholes and other surface imperfections

4.9 Analysis of Mould Temperature Measurement

4.9.1 Conversion of thermocouple measurement to mould wall temperatures

If the slope of the thermocouple voltage output versus the temperature curve (the Seebeck coefficient) is plotted against temperature it becomes quite obvious that the thermocouple is a non-linear device. It is thus necessary to fit a polynomial, as shown below, to convert the thermocouple voltage to temperature.

$$T = a_0 + a_1 x^1 + a_2 x^2 + a_3 x^3 + \ldots\ldots + a_n x^n$$

where T= temperature, x = thermocouple voltage, $a_0, a_1, \ldots\ldots\ldots\ldots a_n$ are coefficients unique to the type of the thermocouple and n is the order of the polynomial. The coefficients are available from Omega Temperature Measurement Handbook and Encyclopedia which notes that the accuracy for the type T thermocouple is +/- 0.5 °C if a 7th order polynomial is used. During the actual calculation of the polynomial an alternative form of it, as suggested by Horner, is used to speed up the calculation. This form, shown below, converts the time consuming exponentiation operation to one involving only multiplication.

$$T = a_0 + x(a_1 + x(a_2 + x(a_3 + x(a_4 + x(a_5 + x(a_6 + a_7 x))))))$$

A schematic diagram of the temperature measuring set up and the equivalent circuit to which it can be reduced is shown in the Figure 4.10. It needs to be noted that a second thermocouple is created by the junction of the Copper and Constantan wire in the water chamber and, as shown in the circuit, the voltage generated at this junction (V2) opposes the voltage being measured (V1). The measured voltage (VM) thus needs to be increased by V2 to get V1. The value of the opposing voltage (V2) is obtained by the two wire thermocouples used to measure the water temperature. An important point here is that the junction referred to above lies in the outlet water for the mould thermocouples that are above the plenum divider, and the inlet water for those thermocouples that are below the plenum. The reference junction temperature is, as mentioned before, measured by a mercury-in-glass thermometer place at the appropriate location. In keeping with the correct procedure, the reference junction temperature is converted to a voltage, added to the sum of VM and V1 and the resultant voltage is reconverted to a temperature value.

4.9.2 Data Filtration technique

Figure 4.11 is a flowchart showing the different stages through which the analysis of mould thermocouple data proceeds. The filtered thermocouple response is input to a mathematical model of the mould to obtain the axial heat-flux profile down the length of the mould and the temperature distribution in the mould wall. The latter is used in a elasto-plastic model of the mould to compute the distortion of the mould wall while the heat-flux profile is used in a heat flow model of the mould to calculate billet shrinkage profile and shell thickness. The details of the models are discussed in the next few chapters.

A typical (unfiltered) mould-thermocouple response is shown in Figure 4.12. The fluctuations in the temperature are believed to be caused largely by metal level variation in the mould due, in part, to casting speed change [17]. This is confirmed in Figure 4.13 where an increase in the metal level (metal level drops lower in the mould), is seen to cause a drop in the temperature sensed by the meniscus thermocouple. Clearly, such effects have to be isolated from the variation in temperature caused by strand-mould interaction and associated gap changes and the method of data-filtering has been explained in an earlier publication [17]. The first step is the identification of the thermocouple just above the meniscus (for Company B, it was found to be the second thermocouple, TC2, on the inner curved wall) at which signal fluctuations are predominantly due to metal level changes rather than strand-mould interaction. Each temperature recorded by TC2 corresponds to a particular metal level and, therefore, by isolating data (for all thermocouples) for only those time periods during which the temperature of TC2 is within a narrow range, it is possible to select data corresponding to a fixed metal level. With the availability of the casting speed signal it was also possible to further refine this process of data filtering by extracting data for time periods when temperatures recorded by TC2, as well as the casting speed, were both within a narrow range. It is thought that this stringent criteria of data extraction better reflects the effect of gap width on the thermocouple response. The extracted data was time averaged for each thermocouple to give temperature profiles for different heats.

To maintain consistency in data extraction from heat to heat the reference temperature and casting speed range were selected to be within 5 C° and 2 mm/s of the mean value recorded by TC2 and the casting speed sensor respectively.

4.10 Analysis of Load Cell Response

Since the load cell signal are sampled at 50 Hz. an enormous amount of data is collected even in a short period of 10 seconds. To be able to analyze the load signal correctly it is necessary to plot the same on a paper 1524 mm by 1224 mm - a size that cannot be handled by conventional plotters. Thus a special plotter was acquired to carry out the plotting and a software to do the same was developed. Also plotted alongside were the casting speed and metal level signals. With plots of signals from LVDTS, load cells and other related sensors all available on the same page, analysis of mould billet interaction could be carried out conveniently.

Consider Figure 4.14 which shows the various components of the mould oscillation. As explained by Brendzy [13], during the negative strip period of the down stroke the mould pushes on the billet and the billet pushes back thereby reducing the load sensed by the load cell. The shape of the load cell signal during the upstroke of the mould is important from the stand point of mould friction. It is imperative to break up the load cell signal into pre and post negative strip periods and analyse the load changes in those periods. A computer programme to do so was developed that identifies the beginning and end of negative strip periods in each oscillation cycle and calculates load changes in these periods. This calculation is carried out for the entire period for which the data has been collected. The output of the programme was so designed as to enable quick and easy comparison of load cell signals under different conditions. In particular the programme quantifies the following:

(1) The difference in load at the beginning and end of negative strip period.

(2) The maximum amount of decompression that the load cells experience during the negative strip period. This is the difference in the load at the start of the negative strip time and the minimum load attained during negative strip period.

(3) The percentage of the negative strip time for which the decompression of the load cell occurs. This is the time elapsed between start of negative strip period and the attainment of minimum load, expressed as a percentage of the negative strip period.

(4) The difference in the maximum load during the upstroke and the load at the beginning of the

negative strip time.

(1) - (3) are different ways of quantifying mould-billet interaction during the negative strip period while (4) is an indicator of friction during the upstroke of the mould. On account of differences in pre-loads of the load cells as well as the distribution of load between the bolts, O-rings, spring and the load cells at the three plants, it is not possible to compare absolute values of load across trials. This is overcome by the use of parameter (3) which only compares the time for which the load cell is decompressed.

Table 4.1 Details of the casting practice at Plants B, E, and C.

	COMPANY B	COMPANY E	COMPANY C
Machine type	Curved mould	Curved mould	Curved mould
Machine radius	7.9 m (26')	3.9 m (13')	7.9 m (26')
Mould Length	812.8 mm	812 mm	835 mm
Heat size	60 tonne	60 tonne	150 tonne
Sequence	Yes	Yes	Yes
Billet size	120 x 120 mm (4.7 x 4.7)	127 x 178 mm (5 x 7")	140 x 140 mm (5.5 x 5.5")
Nominal casting speed	2 - 2.5 m/min (80 - 100 ipm)	1.65 m/min (65 ipm)	1.90 m/min (75 ipm)
Reoxidation protection	N_2 shrouding	N_2 shrouding	N_2 shrouding
Oscillation type	Sinusoidal	Sinusoidal	Sinusoidal
Stroke length	9.5 mm (0.37")	6.4 mm (0.25")	11.2 mm (0.44")
Oscillation frequency	2 Hz. (120 cpm)	2.8 & 2.2 Hz. (170 & 130 cpm)	2.4 & 1.6 Hz. (144 & 96 cpm)
Negative strip time	0.15 s	0.12 & 0.13 s	0.16 & 0.19 s
Mould lead	2.1 mm	2.2 & 1.3 mm	5.3 & 3.0 mm

Table 4.2 Details of the test and control strands used in the trials at Plants B, E and C.

Features	COMPANY B		COMPANY E		COMPANY C	
	Test (# 3)	Control (# 2)	Test (# 4)	Control (# 6)	Test (# 4)	Control (# 5)
Material	Cu-Cr-Zr	Cu-Cr-Zr	Cu-Cr-Zr	Cu-Cr-Zr	Cu-Cr-Zr	DHP Cop-per
Thickness	12.7 mm	12.7 mm	19 mm	12.7 mm	16 mm	12.7 mm
Corner Radius	-	-	3.2 mm	3.2 mm	3.2 mm	4.8 mm
Construction	Tube	Tube	Reformed Tube	Reformed Tube	Tube	Tube
Mould Length	812.8 mm	812.8 mm	812 mm	812 mm	835 mm	835 mm
Mould Taper	Parabolic (4.9 at top and 0.8 %/m near end)	Parabolic (4.9 at top and 0.8 %/m near end)	Double (2.7 &, 0.8 %/m)	Triple (3.6, 0.9,0.55 %/m)	Multiple (0.4, 2.5, %/m etc.)	Double (1.4, 0.6 %/m)
Water Gap	4.76 mm	4.76 mm	3.2 mm	4.8 mm	3.2 mm	6.3 mm
Water Flow rate	11 m/s		44 l/s 18 m/s	44 l/s 12 m/s	28 l/s 12.4 m/s	31 l/s m/s
Constraint Type	Four-sided	Two-sided	Four-sided	Two-sided	Four-sided	Two-sided
Distribution System for Oil	UBC design	Conventional	UBC design	Conventional design	UBC design	Conventional
Oil Channel Vol	167 ml	120 ml	200 ml	140 ml	280 ml	90 ml
Oil Gap	0.41 mm	0.76 mm	0.38 mm	0.35 mm	0.38 mm	0.51 mm
Gasket Type	Cross	Conventional	Cross	Conventional	Cross	Conventional
No of Oil Lines	1	1	1	1	1	2
Gap Protector	No	No	Yes	No	Yes	No

Table 4.3 Property of various lubricating oils used in the trials at the three Plants.

	Canola	**HEAR**	**Mineral_S**	**Mineral_O**	**Soybean**	**51-LN**
Type of Oil	Vegetable	Vegetable	Mineral	Mineral	Vegetable	Vegetable
Viscosity (SUS) @38 °C	160	185	200	250	160	N.A
Flash Point (oC)	>315	>300	226	>320	327	227
Fire Point (°C)	>360	>350	252	N.A	343	N.A
Boiling Point (°C)						
Start	205	215	170	205	180	205
20%	280	280	230	270	275	300
50%	315	320	300	315	320	335
90%	335	335	330	335	335	350
Fatty Acid Contents						
Palmitic (c16:0)	5.3%	3.2%	2.9%	5.1%	9.9%	2.1%
Oleic (c18:1w9)	57.7%	14.9%	40.3%	22.1%	18.1%	47.3%
Linoleic (c18:2w6)	23.6%	15.1%	27.1%	65.5%	55.9%	24.6%
Linolenic (c18:3w3)	9.2%	9.3%	26.0%	2.7%	11.3%	18.3%
Eicosenoic (c20:1w9)	0.7%	8.2%	0.3%	0.3%	0.4%	0.6%
Erucic (c22:1w11)	0.3%	45.2%	0.1%	0.1%	0.1%	0.1%

Table 4.4 Depth and axial position of thermocouples used to monitor mould wall temperature at Company B.

T.C. No.	Distance from mould top (mm)	Hole Depth (mm)	T.C. No.	Distance from mould top (mm)	Hole Depth (mm)
ICW - Centreline			**Right Side - Centreline**		
1	85	7.44	1	85	6.17
2	100	5.87	2	100	6.12
3	114	5.77	3	116	6.10
4	130	5.715	4	131	6.15
5	146.5	5.61	5	145	6.10
6	170	5.715	6	170.5	5.94
7	195	5.84	7	196	5.84
8	220	6.02	8	221	5.89
9	243	6.35	9	246	5.87
10	312	6.25	10	313	5.89
11	342	5.89	11	343	6.07
12	372	5.77	12	373	5.92
13	402	5.64	13	403	6.02
14	452	5.79	14	453	6.07
15	505	6.35	15	503	5.97
16	552.5	5.59	16	553	5.92
17	603	5.74	17	603	6.09
18	712	5.69	18	703	6.35
Right Side - Off-centre			**OCW - Centreline**		
1	84	6.12	1	86	5.84
2	100	6.17	2	101	5.26
3	115	6.12	3	115	5.49
4	130	6.12	4	130	5.49
5	145	5.92	5	146	5.61
6	170	5.99	6	170	5.69
7	196	5.97	7	196	5.72
8	220	5.89	8	221	5.79
9	246	5.82	9	244	5.72
10	312	5.87	10	312	5.74
11	342	5.97	11	343	5.69
12	372	5.87	12	372	5.66
13	402	6.04	13	402	5.69
14	452	5.92	14	453	5.52
15	502.5	5.99	15	502.5	5.74
16	552.5	6.10	16	553	5.92
17	602	6.10	17	603	5.87
18	713	6.30	18	713	5.82

Table 4.5 Depth and axial position of thermocouples used to monitor mould wall temperature at Company E.

T.C. No.	Distance from mould top (mm)	Hole Depth (mm)	T.C. No.	Distance from mould top (mm)	Hole Depth (mm)
ICW - Centreline			Right Side - Centreline		
1	85	9.90	1	84.4	10.00
2	99	9.85	2	99	10.15
3	114	10.00	3	115	10.10
4	129	10.00	4	130	10.00
5	144	9.85	5	145	10.00
6 A	159	9.90	6 A	160	9.80
B	159	9.65	B	160	9.90
C	158	9.90	C	159	9.80
D	158	9.80	D	158	9.90
E	159	9.75	E	158	10.25
7	188	9.80	7	190	9.60
8	218	9.70	8	218	9.50
9	248	9.75	9	250	9.35
10	277	9.70	10	277	9.45
11	327	10.10	11	327	9.15
12	358	9.95	12	358	9.90
13	388	9.85	13	390	9.20
14	418	9.90	14	419	8.80
15	448	9.60	15	448	8.75
16	479	10.20	16	478	9.80
17	509	10.20	17	509	9.65
18	569	10.00	18	569	9.65
19	629	10.15	19	629	9.65
20	690	9.95	20	690	9.85
21	750	9.45	21	750	9.90

Table 4.6 Depth and axial position of thermocouples used to monitor mould wall temperature at Company C.

T.C. No.	Distance from mould top (mm)	Hole Depth (mm)	T.C. No.	Distance from mould top (mm)	Hole Depth (mm)
ICW - Centreline			**Right Side - Centreline**		
1	67	8.0	1	65	7.75
2	85	7.9	2	80	7.8
3	101	7.7	3	100	7.8
4	116	7.9	4	116	7.8
5	131	7.9	5	129	7.8
6	146	7.8	6	144	7.8
7	162	7.9	7	160	7.7
8	177	7.9	8	174	7.8
9	191	7.9	9	189	7.75
10	216	7.85	10	214	7.75
11	241	7.9	11	299	7.8
12	300	7.9	12	318	7.85
13	320	7.9	13	349	7.8
14	350	7.8	14	378	7.55
15	381	7.8	15	409	7.65
16	411	7.9	16	438	7.8
17	441	7.8	17	468	7.9
18	471	7.9	18	499	7.65
19	501	7.8	19	549	7.65
20	551	7.9	20	609	7.7
21	602	7.8	21	649	7.75
22	652	7.9	22	699	7.8
23	702	8.1	23	749	7.8
24	751	8.1			

Table 4.7 Chemical compositions of the heats monitored at Company B.

Heat No.	Grade	C (%)	Mn (%)	S (%)	P (%)	Si (%)	Cu (%)	Cr (%)	Ni (%)	Mo (%)	Nb (%)	V (%)	Sn (%)	Pb (%)	Zn (%)	Al (%)
B24636	1008	.046	.530	.038	.012	.160	.110	.070	.080	.020	-	-	.006	-	-	.004
B24637	1008	.040	.420	.039	.017	.120	.090	.070	.080	.020	-	-	.006	-	-	.004
B24368	1008	.068	.460	.026	.009	.140	.090	.040	.060	.020	-	-	.005	-	-	.003
B24369	1008	.045	.360	.022	.009	.080	.100	.030	.080	.020	-	-	.006	-	-	.003
B24640	1008	.035	.370	.026	.011	.090	.120	.040	.070	.020	-	-	.006	-	-	.004
B24641	1008	.041	.480	.020	.008	.090	.100	.030	.070	.020	-	-	.005	-	-	.004
B24642	1008	.043	.440	.020	.008	.120	.090	.030	.070	.020	-	-	.005	-	-	.003
B24643	1018	.170	.830	.018	.018	.200	.100	.080	.080	.020	-	-	.006	-	-	.004
B24644	1018	.180	.750	.013	.010	.240	.170	.070	.100	.020	-	-	.010	-	-	.005
B24645	1018	.180	.850	.018	.018	.280	.140	.070	.090	.020	-	-	.009	-	-	.005
B24646	1039	.400	.780	.015	.014	.240	.130	.100	.100	.020	-	-	.008	-	-	.005
B24647	1039	.420	.810	.019	.012	.210	.130	.100	.090	.020	-	-	.008	-	-	.004
A23408	1008	.051	.350	.021	.014	.100	.110	.040	.090	.020	-	-	.007	-	-	.004
B24649	1008	.050	.400	.020	.011	.110	.090	.070	.090	.010	-	-	.007	-	-	.005
A23409	1015	.150	.350	.026	.017	.100	.270	.070	.110	.020	-	-	.010	-	-	.004
B24650	1010	.120	.470	.018	.013	.100	.210	.050	.100	.020	-	-	.011	-	-	.004
A23412	1010	.090	.410	.025	.014	.120	.350	.060	.100	.020	-	-	.011	-	-	.004
B24653	1010	.094	.460	.020	.010	.110	.190	.040	.080	.020	-	-	.009	-	-	.004
B24654	1012	.120	.400	.022	.008	.100	.240	.050	.100	.020	-	-	.010	-	-	.004
A23413	1012	.120	.420	.020	.008	.120	.230	.040	.100	.020	-	-	.009	-	-	.004
B24655	1010	.110	.350	.023	.007	.080	.240	.040	.110	.020	-	-	.012	-	-	.004
B24657	4037	.400	.730	.018	.011	.240	.110	.070	.060	.021	-	-	.005	-	-	.004

Table 4.8 Chemical compositions of the heats monitored at Company E.

Heat No.	Grade	C (%)	Mn (%)	S (%)	P (%)	Si (%)	Cu (%)	Cr (%)	Ni (%)	Mo (%)	Nb (%)	V (%)	Sn (%)	Pb (%)	Zn (%)	Al (%)
26493	5160	.57	.79	.025	.010	.23	.09	.78	.05	.012	.003	.029	.007	.005	.002	.003
26494	5160	.57	.78	.029	.012	.22	.07	.77	.05	.011	.002	.026	.006	.003	.001	.003
26495	5160	.57	.82	.029	.008	.22	.08	.78	.06	.014	.000	.024	.006	.003	.002	.003
26501	1018	.21	.73	.025	.023	.23	.10	.08	.06	.011	.002	.002	.008	.004	.011	.003
26503	1018	.19	.85	.018	.007	.25	.11	.06	.05	.013	.002	.003	.007	.005	.010	.003
26504	1018	.17	.83	.021	.007	.24	.11	.07	.06	.014	.002	.002	.007	.007	.009	.003
26505	1018	.17	.79	.18	.010	.24	.11	.07	.06	.013	.002	.003	.008	.005	.007	.003
26507	1018	.18	.85	.024	.015	.19	.11	.14	.06	.023	.003	.004	.008	.006	.010	.003
26508	1146	.45	.85	.098	.008	.23	.12	.08	.06	.018	.003	.023	.008	.005	.006	.003
26509	1146	.44	.79	.101	.009	.21	.11	.09	.06	.012	.002	.021	.008	.004	.002	.002
26510	1090	.87	.95	.025	.014	.46	.11	.11	.06	.014	.023	.003	.008	.007	.001	.004
26511	1090	.86	.92	.028	.014	.47	.12	.10	.05	.011	.022	.003	.008	.005	.001	.004
26512	1090	.87	.86	.036	.016	.43	.12	.11	.05	.015	.019	.003	.007	.005	.002	.004
26514	1080	.83	.74	.022	.010	.21	.08	.08	.04	.009	.001	.021	.005	.003	.003	.002
26515	1080	.85	.75	.024	.010	.24	.07	.08	.04	.008	.002	.020	.005	.004	.002	.002
26516	1080	.85	.77	.025	.010	.23	.08	.09	.04	.011	.002	.020	.006	.005	.002	.003
26519	1080	.86	.75	.027	.013	.23	.09	.09	.04	.010	.003	.020	.006	.003	.001	.002
26520	1080	.89	.73	.028	.013	.23	.09	.10	.05	.012	.003	.022	.013	.009	.001	.003
26521	1080	.87	.73	.028	.010	.21	.08	.09	.05	.011	.003	.018	.006	.003	.001	.003
26535	1541	.40	1.44	.036	.018	.22	.11	.09	.05	.012	.002	.024	.007	.005	.001	.001
26538	1050	.54	.98	.029	.008	.22	.11	.11	.07	.013	.001	.003	.004	.003	.001	.016
26539	1050	.53	.98	.030	.008	.22	.09	.11	.05	.011	.001	.003	.005	.003	.001	.018
26540	1050	.52	1.04	.030	.009	.23	.10	.11	.06	.014	.001	.004	.006	.005	.001	.017
26541	1050	.51	1.00	.031	.010	.21	.10	.10	.06	.013	.001	.003	.005	.002	.001	.014
26555	1045	.46	.76	.028	.015	.26	.14	.10	.07	.013	.001	.004	.008	.003	.001	.003

Table 4.9 Chemical compositions of the heats monitored at Company C.

Heat No.	Grade	C (%)	Mn (%)	S (%)	P (%)	Si (%)	Cu (%)	Cr (%)	Ni (%)	Mo (%)	Nb (%)	V (%)	Sn (%)	Pb (%)	Zn (%)	Al (%)
D 6122	1045	.48	.72	.018	.007	.24	.16	.05	.05	.006	-	.025	.006	-	-	-
D 6123	1045	.49	.69	.018	.008	.24	.15	.05	.05	.006	-	.023	.007	-	-	-
C 7653	1045	.47	.73	.017	.014	.26	.11	.05	.04	.006	-	.023	.004	-	-	-
C 7654	1045	.46	.82	.018	.014	.29	.12	.08	.05	.005	-	.024	.007	-	-	-
C 7655	1045	.45	.72	.020	.014	.28	.18	.09	.05	.005	-	.022	.007	-	-	-
C 7658	5160	.57	.77	.024	.008	.17	.11	.79	.05	.047	-	.015	.006	-	-	-
C 7659	5160	.58	.81	.028	.013	.20	.14	.80	.05	.050	-	.016	.007	-	-	-
C 7660	5160	.57	.81	.025	.014	.19	.14	.85	.06	.059	-	.018	.009	-	-	-
C 7661	5160	.57	.81	.020	.014	.19	.13	.86	.07	.068	-	.018	.008	-	-	-
C 7663	1141	.38	1.42	.029	.020	.24	.11	.11	.03	.004	-	.027	.006	-	-	-
C 7664	L325	.21	.88	.024	.010	.28	.39	.89	.70	.011	-	.009	.009	-	-	-
A 28184	L325	.24	.88	.019	.019	.34	.46	.87	.62	.009	-	.010	.006	-	-	-
D 6131	1084	.86	.71	.027	.012	.24	.22	.10	.07	.013	-	.023	.008	-	-	-
A 28187	L20	.21	1.10	.026	.021	.21	.15	.07	.05	.007	-	.056	.007	-	-	-
A 28188	1045	.46	.69	.020	.021	.27	.13	.08	.04	.004	-	.024	.006	-	-	-
D 6135	1045	.46	.69	.020	.010	.24	.16	.05	.04	.004	-	.023	.006	-	-	-
A 28191	L17C	.21	.95	.020	.017	.18	.10	.06	.05	.009	-	.004	.006	-	-	-
A 28192	L17C	.19	.98	.015	.015	.19	.05	.05	.04	.008	-	.004	.003	-	-	-
A 28193	L17C	.19	1.00	.023	.016	.25	.27	.09	.06	.012	-	.004	.008	-	-	-
D 6143	L17C	.21	.98	.019	.008	.19	.14	.02	.05	.005	-	.003	.006	-	-	-

Table 4.10 Important casting conditions for the heats monitored at Company B.

Heat No.	Grade	C (%)	Oil Type	Flow Rate (ml/min)	Tundish Temp (°C)	Superheat (°C)	Billet No.
B24636	1008	.046	Soybean	53 53 53	1546 1538 1530	19 11 3	636-3-1 636-3-2 636-3-3
B24637	1008	.040	Soybean	53 53	1559 1541	41 23	637-3-3/2-3 637-3-8/2-8
B24638	1008	.068	Soybean	53 53	1579 1568	53 42	638-3-3/2-3 638-3-7/2-7
B24639	1008	.045	Soybean	53 53	1572 1549	43 20	639-3-3/2-3 639-3-7/2-7
B24640	1008	.035	Soybean	53 53	1594 1566	64 36	640-3-2 640-3-7/2-7
B24641	1008	.041	Soybean	53 53	1568 1567	39 38	641-3-3/2-3 641-3-7/2-7
B24642	1008	.043	Soybean	53 53	1567 1550	38 21	642-3-3/2-3 642-3-7/2-7
B24643	1018	.170	Soybean	53 53	1572 1582	58 68	643-3-3/2-3 643-3-7/2-7
B24644	1018	.180	Soybean	53 53	1555 1552	42 39	644-3-3/2-3 644-3-7/2-7
B24645	1018	.180	Soybean	53 53	1559 1539	47 27	645-3-3/2-3 645-3-7/2-7
B24646	1039	.400	Soybean	53 53	1548 1534	53 38	646-3-3/2-3 646-3-7/2-7
B24647	1039	.420	Soybean	53	1534	39	647-3-7/2-7
A23408	1008	.051	Soybean	53	1561	33	408-3-3/2-3
B24649	1008	.050	Soybean	53 40	1564	36	649-3-3/2-3

A23409	1015	.150	Soybean	40 30 20	1546 1538	28 20	409-3-3/2-3 409-3-6/2-6 409-3-8/2-8
B24650	1010	.120	Soybean	53	-	-	-
A23412	1010	.090	Mineral_S	53 44 34	1553 1553 1541	30 30 18	412-3-3/2-3 412-3-5/2-5 412-3-7/2-7
B24653	1010	.094	Mineral_S	34 24	1546 1561	23 38	653-3-3/2-3 653-3-7/2-7
B24654	1012	.120	51-LN	53 53	1557 1566	32 45	654-3-3/2-3 654-3-7/2-7
A23413	1012	.120	51-LN	44 34 24			
B24655	1010	.110	Soybean	53	1570	48	655-3-3/2-3
B24657	4037	.400	Soybean	53	1508	12	655-2-3

Table 4.11 Important casting conditions for the heats monitored at Company E.

Heat No.	Grade	C (%)	Oil Type	Flow Rate (ml/min)	Tundish Temp (°C)	Superheat (°C)	Billet No.
26493	5160	.57	Canola	65	1557	79	493-4-1/6-1
				45	1543	65	493-4-2/6-2
				Manual	1535	57	493-4-3/6-3
26494	5160	.57	Soybean	Manual	1541	63	494-4-1/6-1
26495	5160	.57	Soybean	Manual	1529	51	495-4-1/6-1
26501	1018	.21	Canola	65	1577	66	501-4-1/6-1
				45	1574	63	-
				25	1577	66	501-4-2/6-2
26503	1018	.19	Canola	65	1574	61	503-4-1/6-1
				45	1579	66	-
				25	1579	66	503-4-2/6-2
26504	1018	.17	HEAR	65	1568	54	504-4-1/6-1
				45	1568	52	-
				25	1563	49	504-4-2/6-2
26505	1018	.17	Soybean	65	1566	51	505-4-1/6-1
				45	1557	42	-
				25	1563	48	505-4-2/6-2
26507	1019	.17	Mineral_S	65	1574	61	507-4-1/6-1
				45	1566	53	-
				25	1566	53	507-4-2/6-2
26508	1146	.45	Mineral_S	110	1546	58	-
			Canola	65	1549	61	508-4-1/6-1
			Canola	45	1549	61	508-4-2/6-2
			Canola	25	1543	55	508-4-3/6-3
26509	1146	.44	HEAR	65	1549	60	509-4-1/6-1
				45	1543	54	509-4-2/6-2
				25	1541	52	509-4-3/6-3
26510	1090	.87	HEAR	65	1527	77	510-4-1/6-1
				45	1527	77	510-4-2/6-2
				25	1524	74	510-4-3/6-3
				< 25	1524	74	-
26511	1090	.86	Canola	65	1543	92	511-4-1/6-1
				45	1541	90	511-4-2/6-2
				25	1538	87	511-4-3/6-3
26512	1090	.87	Mineral_S	65	1527	77	512-4-1/6-1
				45	1541	91	512-4-2/6-2
				25	1538	88	512-4-3/6-3

26514	1080	.83	Mineral_S	65 45 25	1535 1529 1524	78 72 67	514-4-1/6-1 514-4-2/6-2 514-4-3/6-3
26515	1080	.85	Canola	65 45 25	1518 1518 1518	63 63 63	515-4-1/6-1 515-4-2/6-2 -
26516	1080	.85	HEAR	65 45 25	1527 1524 1521	72 69 66	516-4-1/6-1 516-4-2/6-2 516-4-3/6-3
26519	1080	.86	Soybean	65 45 25	1541 1535 1529	87 81 75	519-4-1/6-1 519-4-2/6-2 519-4-3/6-3
26520	1080	.89	Soybean	65* 45* 25*	1535 1527 1521	84 76 70	520-4-1/6-1 520-4-2/6-2 520-4-3/6-3
26521	1080	.87	Soybean	100* 100	1538 1532	85 79	521-4-1/6-1 521-4-2/6-2
26535	1541	.40	Soybean	65 45 25 100	1552 1549 1549 1543	62 59 59 53	535-4-1/6-1 535-4-2/6-2 535-4-3/6-3 -
26538	1050	.54	Soybean	65 45 25	1557 1557 1557	76 76 76	538-4-1/6-1 538-4-2/6-2 538-4-3/6-3
26539	1050	.53	Canola	65 45 25	1552 1549 1538	70 67 56	539-4-1/6-1 539-4-2/6-2 539-4-3/6-3
26540	1050	.52	HEAR	65 45 25	1535 1538 1535	53 56 53	540-4-1/6-1 540-4-2/6-2 540-4-3/6-3
26541	1050	.51	Soybean	65 45 25	1538 1538 1535	55 55 52	541-4-1/6-1 541-4-2/6-2 541-4-3/6-3
26555	1045	.46	Soybean Flux	65	1549 1535	61 47	555-4-1/6-1 555-6-2

* Oscillation Frequency changed to 130 osc/min.

Table 4.12 Important casting conditions for the heats monitored at Company C.

Heat No.	Grade	C (%)	Oil Type	Flow Rate (ml/min)	Tundish Temp (°C)	Superheat (°C)	Billet No.
D 6122	1045	0.48	Canola	70	1535	48	122-4/5-1
D 6123	1045	0.49	Canola	100 70 25	1541 1539 1537	54 52 50	123-4/5-1 123-4/5-2 123-4/5-3
C 7653	1045	0.47	Mineral_S	100 70 25	1536 1532 1532	47 44 44	653-4/5-1 653-4/5-2 653-4/5-3
C 7654	1045	0.46	HEAR	100 70 25	1540 1535 1534	52 49 48	654-4/5-1 654-4/5-2 654-4/5-3
C 7655	1045	0.45	Mineral_O	100 70 25	1522 1526 1520	33 37 31	655-4/5-1 655-4/5-2 655-4/5-3
C 7658	5160	0.57	Canola	100 70 25	1526 1524 1525	47 45 46	658-4/5-1 658-4/5-2 658-4/5-3
C 7659	5160	0.58	Mineral_S	100 70 25	1529 1517 1511	52 40 34	659-4/5-1 659-4-2 659-4-3
C 7660	5160	0.57	HEAR	100 70 25	1525 1525 1525	47 47 47	660-4/5-1 660-4/5-2 660-4/5-3
C 7661	5160	0.57	Mineral_O	100 70 25	1539 1530 1526	61 52 48	661-4/5-1 661-4/5-2 661-4/5-3
C 7663	1141	0.38	Canola	100 70 70 25	1508 1536 1535 1535	17 45 44 44	663-4/5-1 663-4/5-2 663-4/5-3 663-4/5-4

C 7664	L325	0.21	Canola	100 70 25	1541 1540 1538	36 35 33	664-4/5A,5B-1 664-4-2 664-4-3
A 82184	L325	0.24	Mineral_S	100 70 25	1525 1547 1551	23 45 49	184-4/5-1 184-4/5-2 184-4/5-3
D 6131	1084	0.86	Mineral_O	100 70 25	1514 1515 1510	61 62 57	131-4/5-1 131-4/5-2 131-4/5-3
A 28187	L20	0.21	HEAR	100 70 25	1573 1574 1574	64 64 65	187-4/5-1 187-4/5-2 187-4/5-3
A 28188	1045	0.46	HEAR	100* 70* 25* 0*	1547 1546 1546 1544	58 57 57 55	188-4/5-1* 188-4/5-2* 188-4/5-3*
D 6135	1045	0.46	Mineral_O	100* 70* 25*	1543 1540 1533	54 51 44	135-4/5-1* 135-4/5-2* 135-4/5-3*
A 28191	L17C	0.21	Canola	100 70 25	1559 1571 1565	59 60 54	191-4/5-1 191-4/5-2 191-4/5-3
A 28192	L17C	0.19	Mineral_S	70 100 25	1549 1549 1550	36 36 37	192-4/5-1 192-4/5-2 192-4/5-3
A 28193	L17C	0.19	HEAR	100 70 25	1560 1553 1540	50 43 30	193-4/5-1 193-4/5-2 193-4/5-3
D 6143	L17C	0.21	Mineral_O	100 70 25	1556 1550 1550	45 40 40	143-4/5-1 143-4/5-2 143-4/5-3

* Oscillation frequency changed to 96 from 144 osc/min.

Table 4.13 Summary of the types of oils and the flow rates at which they were used at the three Plants

PLANT B

Oil Type	Flow rate (ml/min)	Steel Grade
Mineral_S	54, 44, 34	1010
Soybean	40, 30, 20	1008, 1010, 1012, 1015,1039
51-LN	54,44,34,24	1008,1012,1018,4037

PLANT E

Oil Type	Flow rate (ml/min)	Steel Grade
Canola	65, 45, 25	1018, 1050, 1080, 1090, 1146, 5160
HEAR	65, 45, 25	1018, 1050, 1080, 1090, 1146
Mineral_S	65, 45, 25	1018, 1050, 1080, 1541, 5160
Soybean	65, 45, 25	1019, 1050, 1080, 1090, 1146

PLANT C

Oil Type	Flow rate (ml/min)	Steel Grade
Canola	100, 70, 25	1017, 1045, 1141, 5160, L325
HEAR	100, 70, 25	1017, 1045, 5160, L20, L325
Mineral_S	100, 70, 25	1017, 1045, 5160, L325
Mineral_O	100, 70, 25	1017, 1045, 1084, 1141, 5160

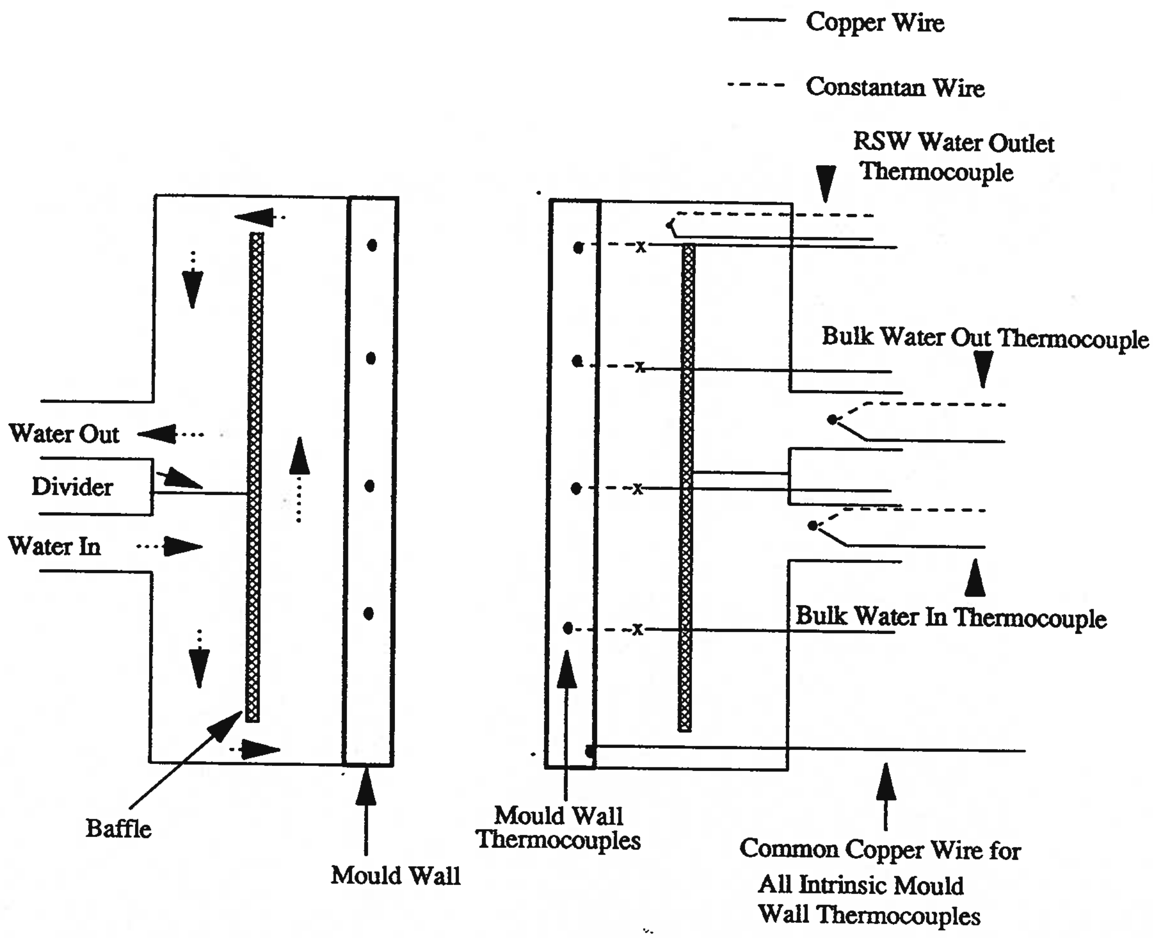

Figure 4.1 Schematic diagram of the set-up for measurement of mould wall and mould cooling water temperatures.

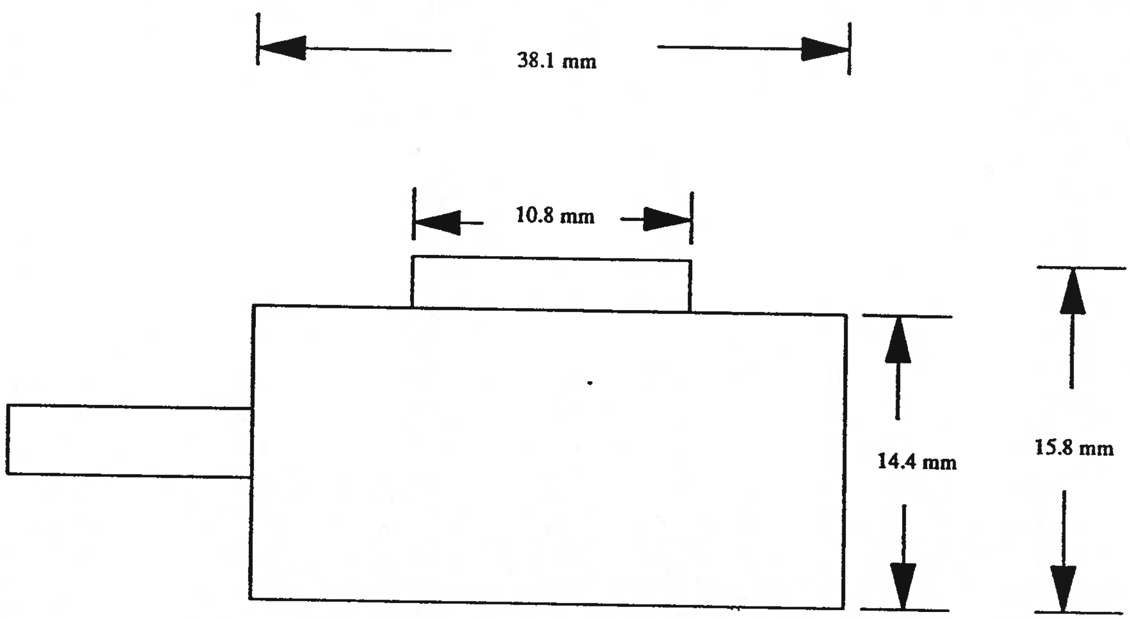

Figure 4.2 Schematic illustration of the load cell.

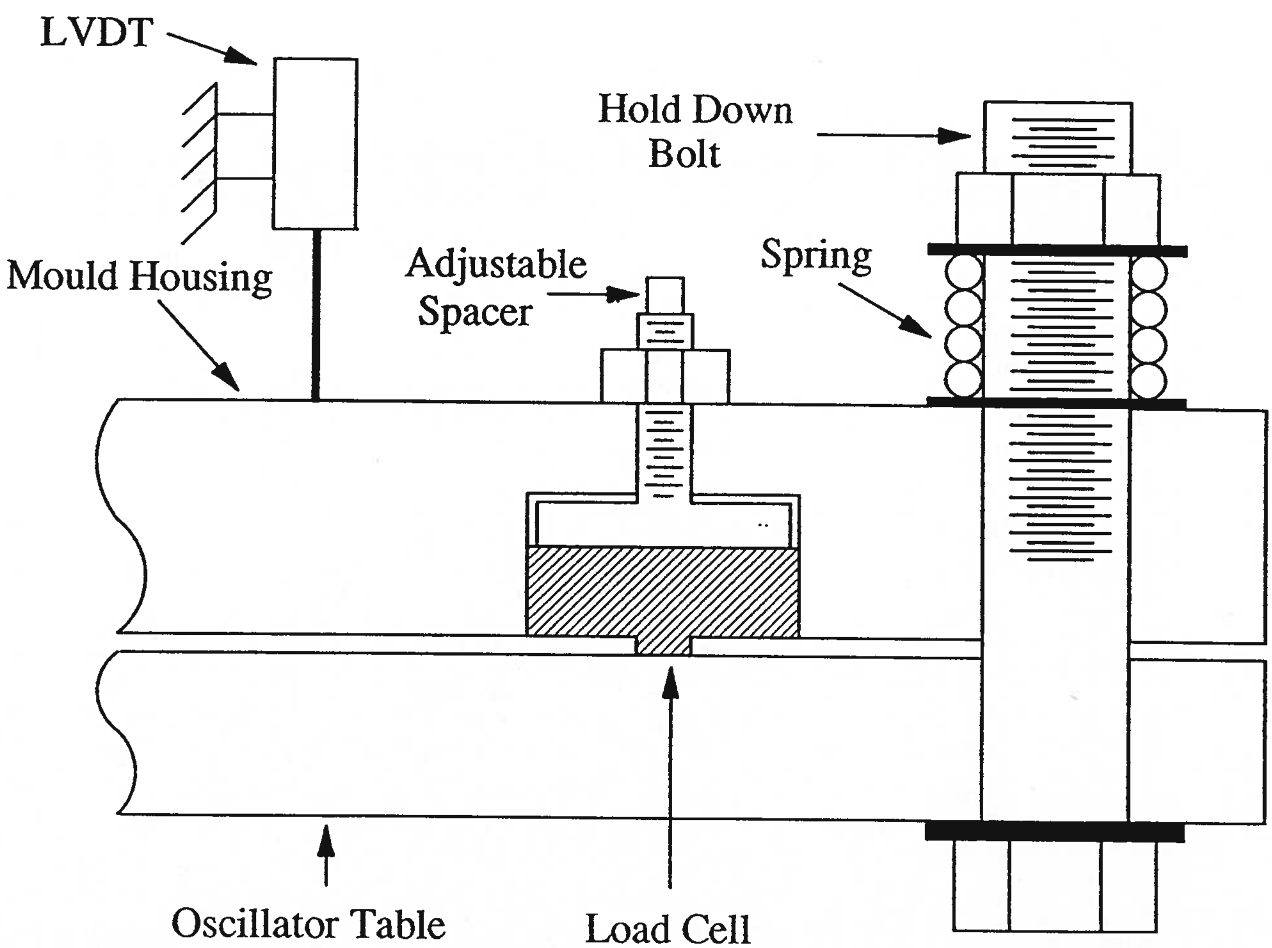

Figure 4.3 Schematic illustration of the positioning of the load cell between the mould housing and the mould oscillating table.

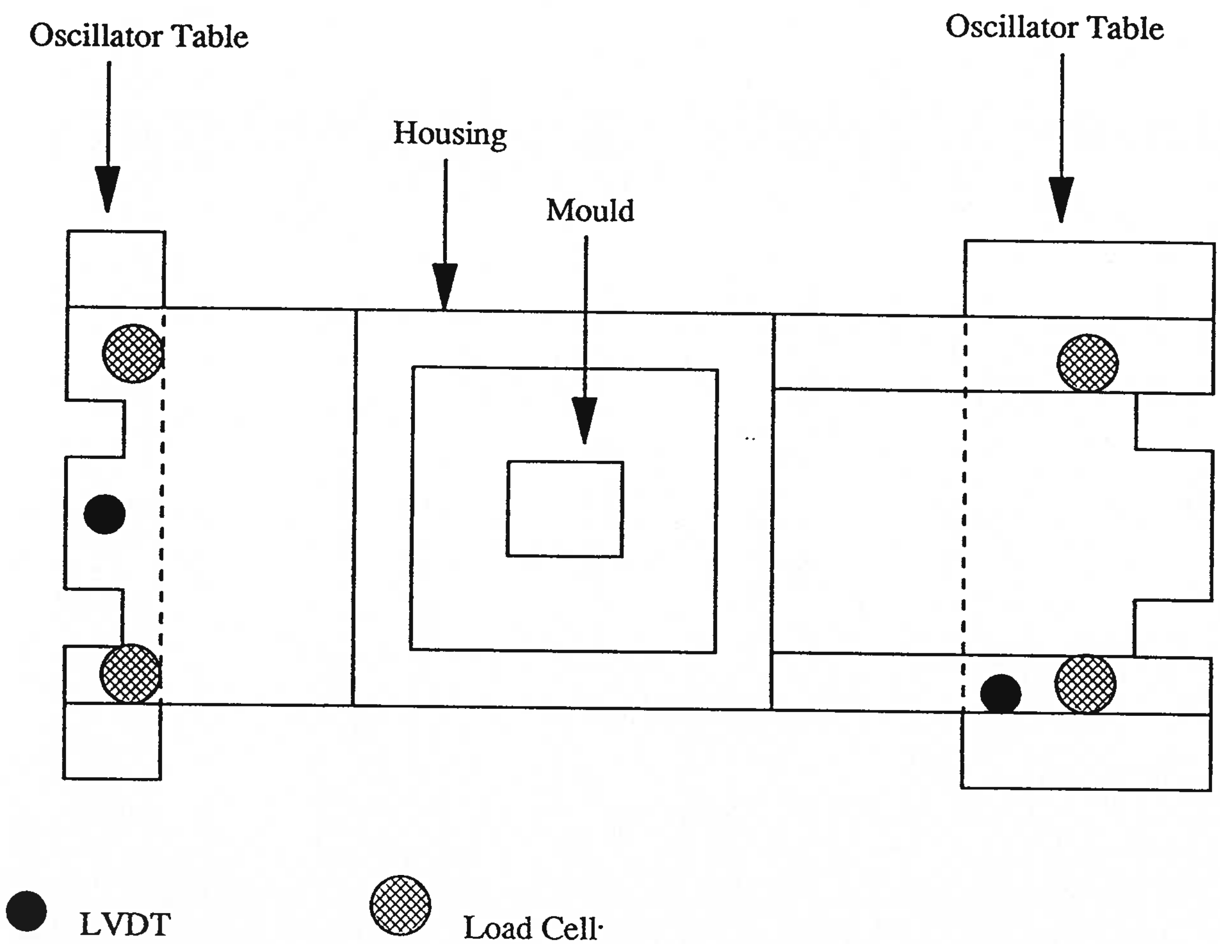

Figure 4.4 Schematic diagram showing the placement of LVDTs and load cells.

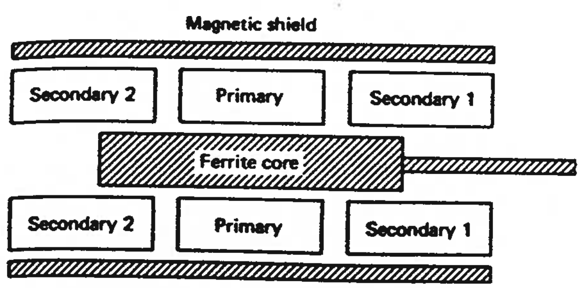

Figure 4.5 Schematic diagram of the construction of a LVDT.

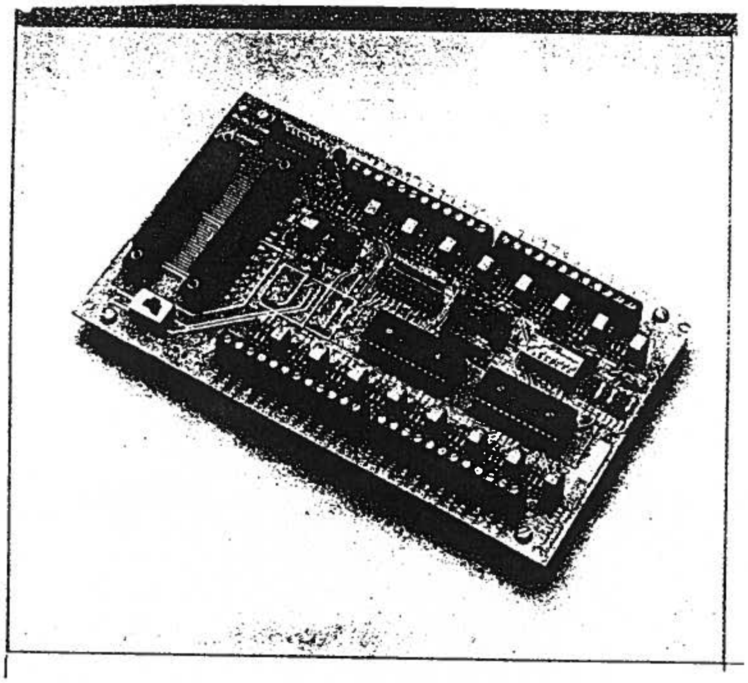

Figure 4.6 Photograph of MetraByte's Universal Expansion Interface; expnasion multiplexer/amplifier system.

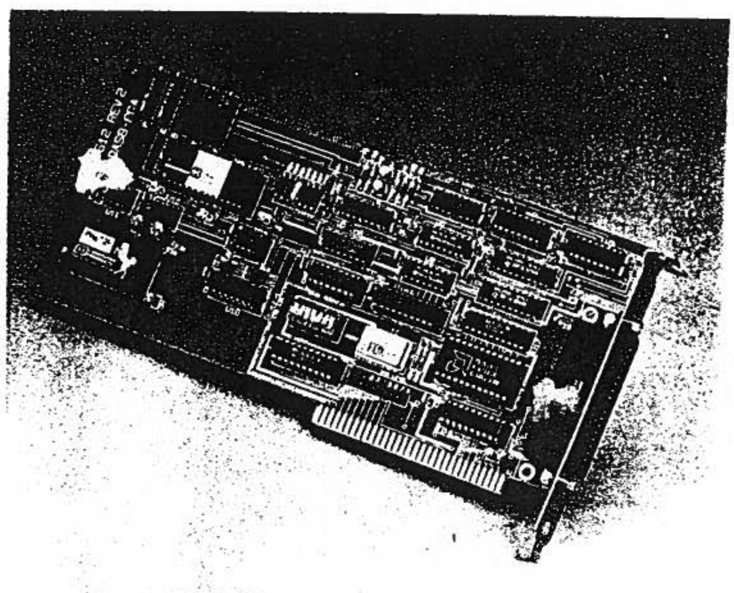

Figure 4.7 Photograph of the 8 channel high speed A/D converter and Timer counter interface from MetraByte.

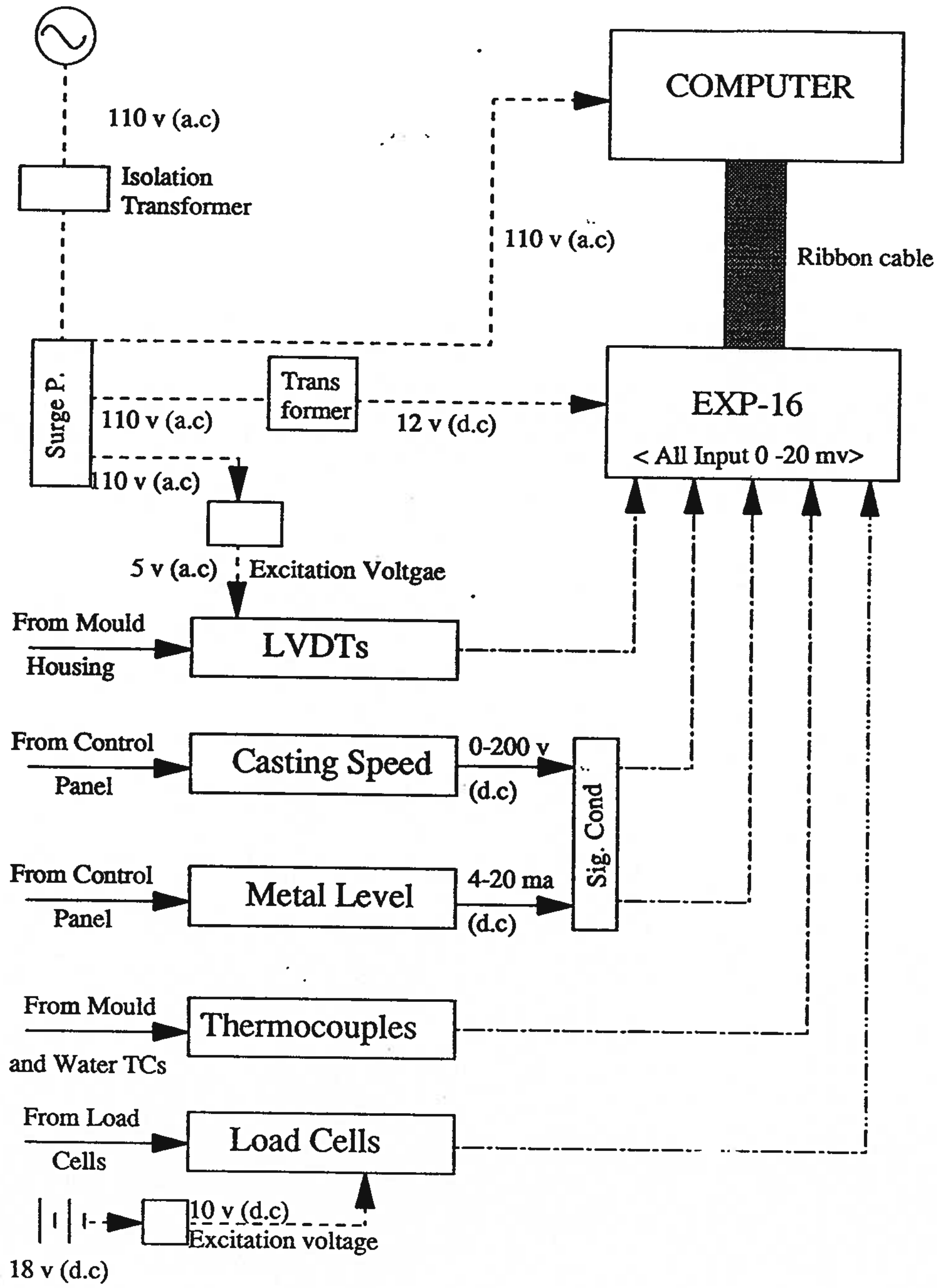

Figure 4.8 Schematic diagram showing the main parts of the data acquisition set-up.

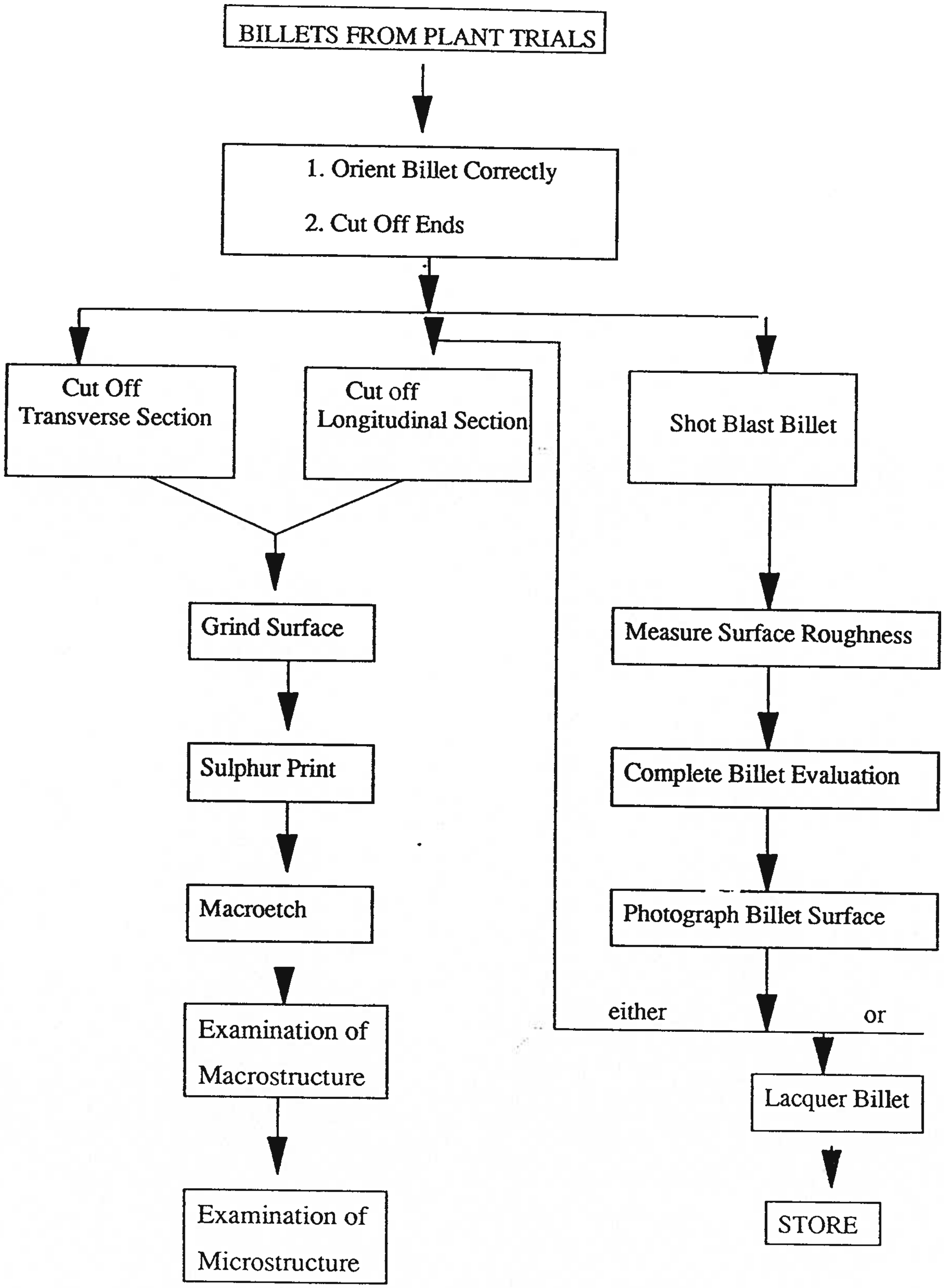

Figure 4.9 Flow chart of the billet inspection procedure

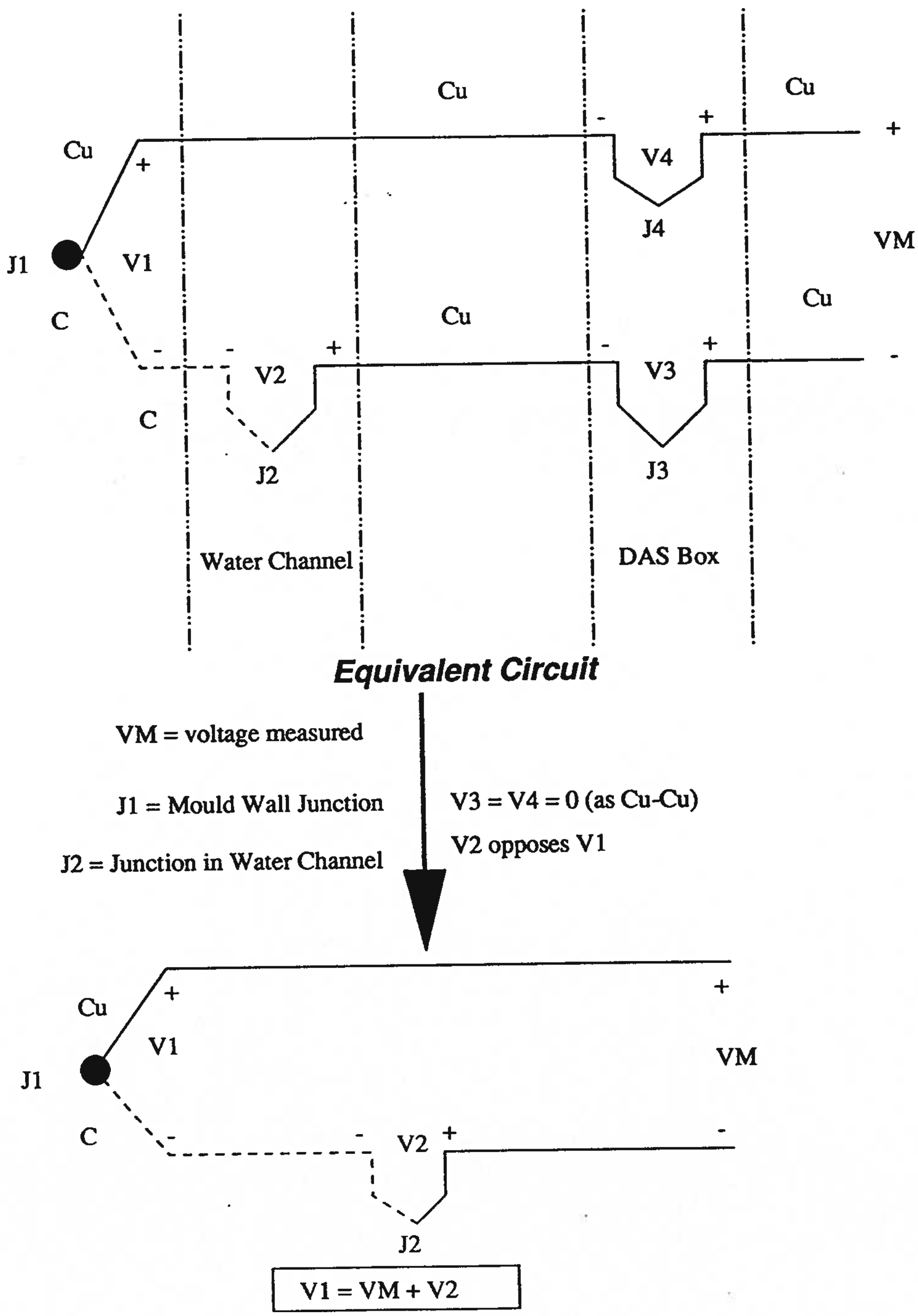

Figure 4.10 Circuit diagram of the thermocouple connection.

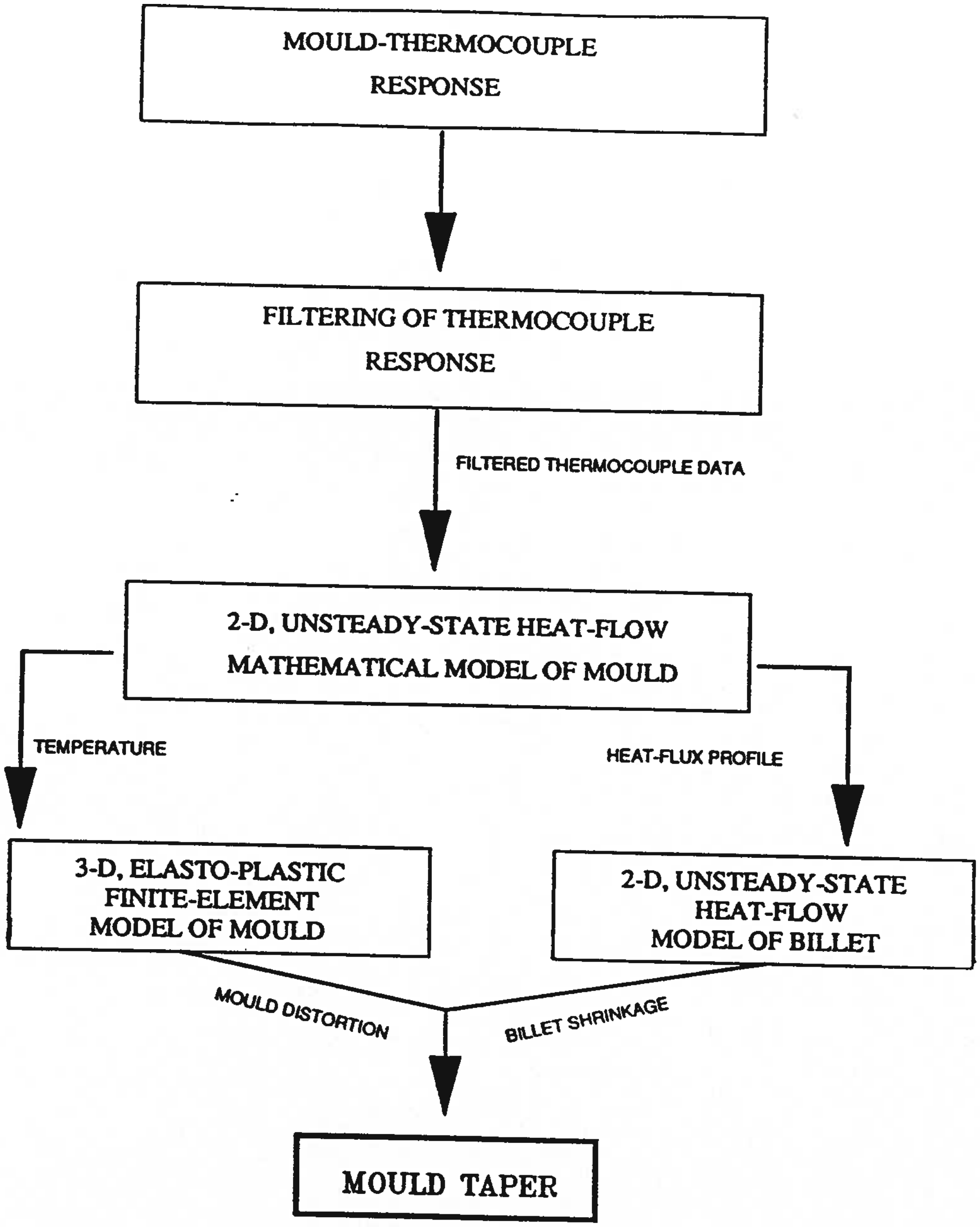

Figure 4.11 Flow chart showing the models used, and the steps involved, in the analysis of mould thermocouple data.

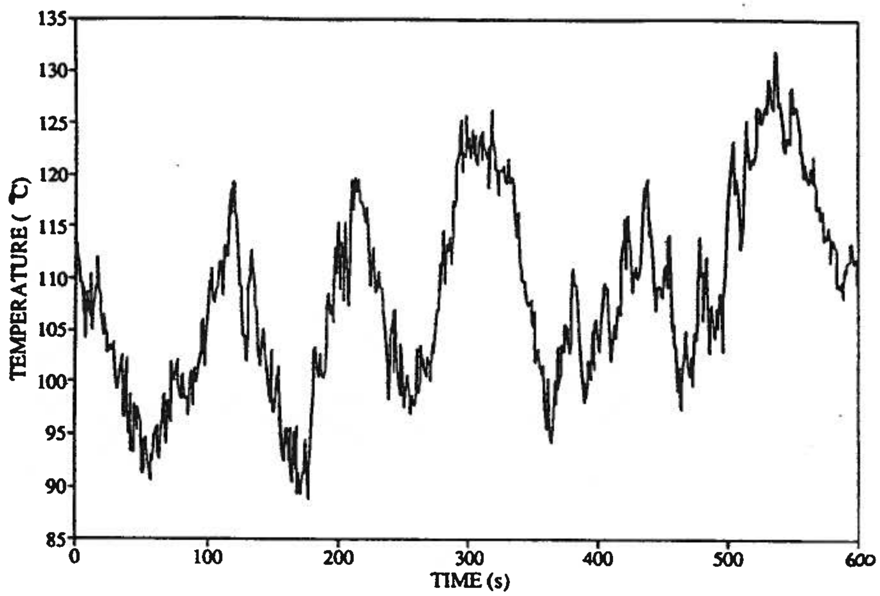

Figure 4.12 A typical unfiltered mould-thermocouple response at Company B.

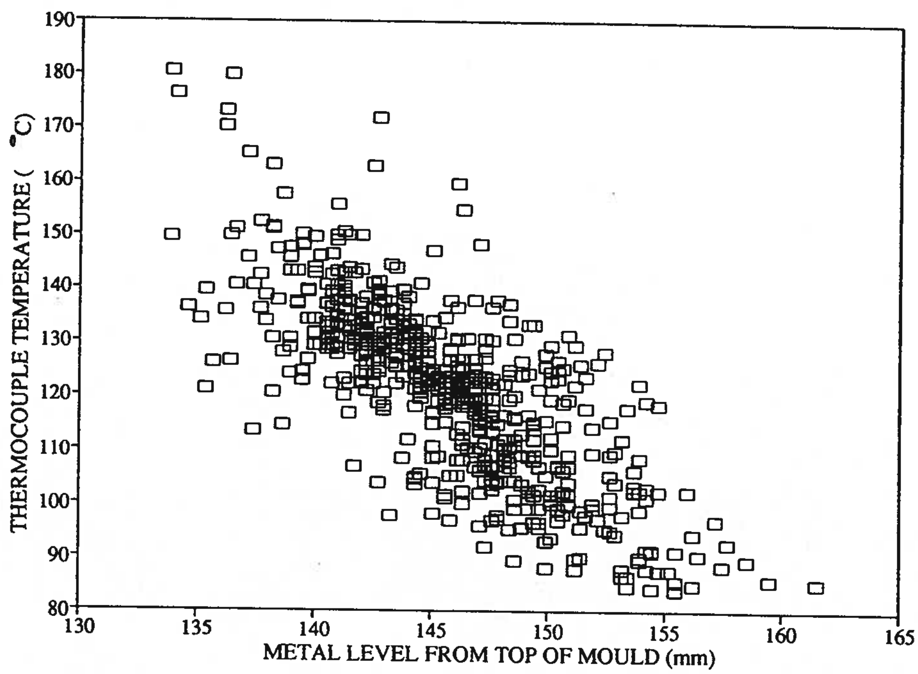

Figure 4.13 Effect of metal level fluctuation on the temperature recorded by the meniscus thermocouple.

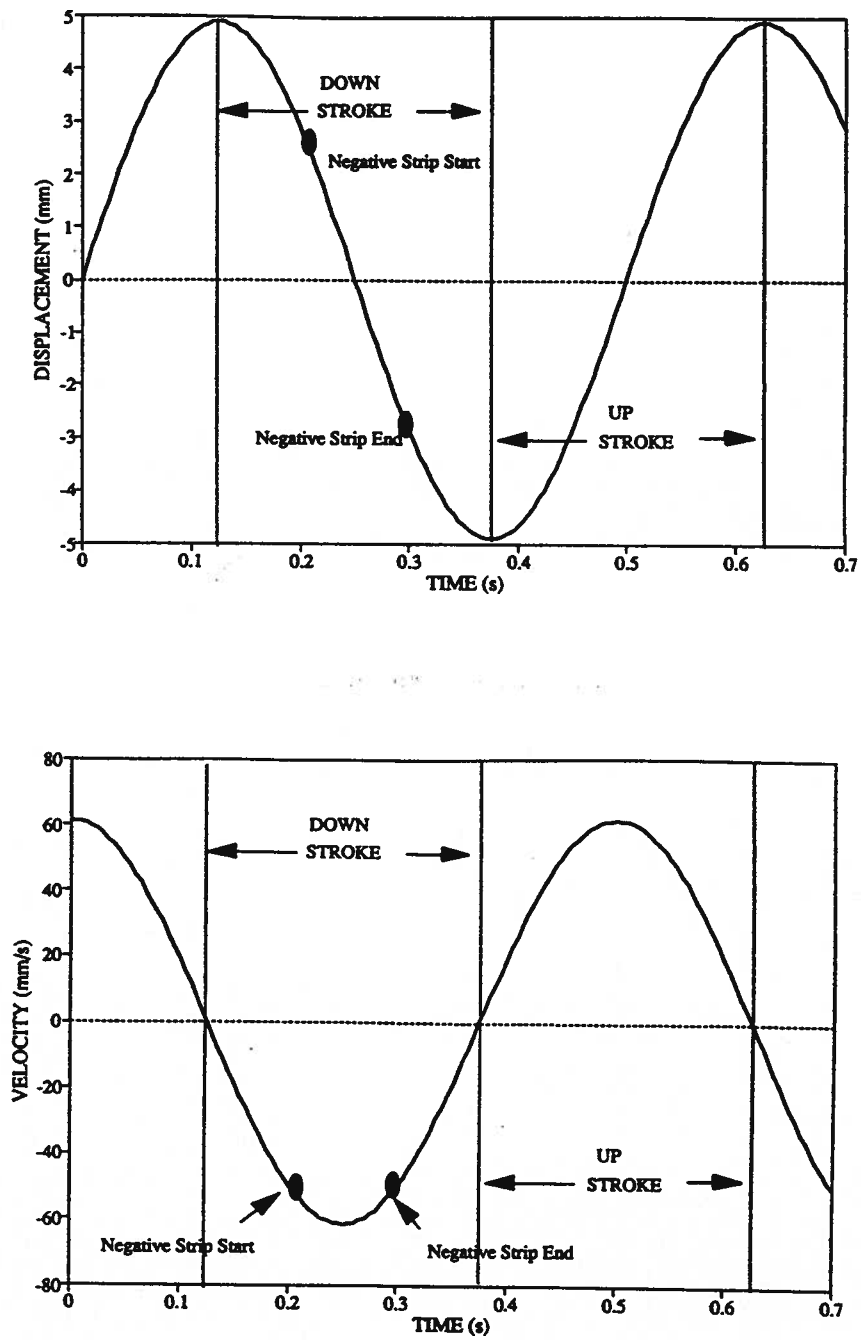

Figure 4.14 Various components of a mould oscillation cycle.

Chapter 5 : RESULTS OF PLANT TRIALS

In this chapter the raw data collected from the three plant trials is presented without subjecting the information to any major analysis. Thus the mould temperature and mould-billet friction forces are presented and a detailed explanation of the observations is, in most cases, deferred until the results of the various mathematical model calculations become available at the end of chapter 8.

5.1 Mould Temperature Data

The dependance of the mould temperature on important operating variables is discussed in the sections that follows. Typical unfiltered response of selected thermocouples are shown in Figure 5.1 while Figure 5.2 is a plot of the standard deviation of temperatures recorded. It needs to be kept in mind that the temperatures shown in this chapter are those recorded by the thermocouples which are located roughly in the middle of the mould wall. *Thus the temperature of the hot face of the mould, as calculated by mathematical models, would be significantly higher*. It also needs to be pointed out that in graphs in which the thermocouple temperatures have been plotted as a function of distance below the mould, the measurments were made at discrete points (at each thermocouple location), and lines have been drawn through the points.

5.1.1 Effect of carbon content

The effect of carbon content of the billet on the mould wall temperature is best seen in the graphs for Plant B where data was collected for heats with carbon contents ranging from 0.05% C to 0.42% C. Figure 5.3 shows the time-averaged axial temperature profile for heats with different carbon contents.

As was discussed in a previous Chapter, the low mould temperature for a 0.12% and 0.09% carbon heats are as reported by other workers [17,34]. The shrinkage accompanying the phase change from δ to γ, which occurs while the solid shell is very thin for 0.12% - 0.09% C, causes the billet surface to become rippled thereby increasing the local billet-mould gap. This leads to a drop in heat transfer and, therefore, mould wall temperatures.

5.1.2 Effect of oil type

Time-averaged mould wall temperatures are presented in Figures 5.2 through 5.7 from data collected during trials at Plant C. The mould wall temperatures are given for 4 different oils at two different flow rates for steel grades 1018 (Figures 5.4, 5.5) and 1045 (Figures 5.6, 5.7).

It can be seen from these figures that the vegetable based oils (Canola and HEAR) in general give somewhat higher mould temperatures than the mineral oils (Mineral_S and Mineral_O). The difference in temperature is most discernible at low flow rates and for the 1018 grade.

5.1.3 Effect of oil flow rate

At Plant C the flow rates of the oils could be changed in systematic manner for all the four oils tested. Time-averaged mould wall temperature measurements are presented for the three oils at three different flow rates in Figures 5.8 through 5.10. In the case of Canola oil the flow was turned down almost to zero and the effect is shown separately in Figure 5.11. Figure 5.12 shows the response of selected thermocouples as the flow rate of Canola oil is changed from 0 ml/min to 100 ml/min.

Preliminary observations indicate that the increased flow rate of oils leads to an increase in mould heat transfer mainly in the meniscus region. The effect is most pronounced with the mineral oil (Steelskin). It is thought that the enhancement of heat transfer is due to improved thermal conductivity of mould-billet gap on account of its hydrogen content arising from the breakdown of oil; higher flow rates of oil leading to increased hydrogen content in the gap. A point that needs to be noted is that *the largest enhancement in the mould wall temperature occurs when the oil flow* rate is changed from 0 ml/min (*no oil) to 25 ml/min (Figure 5.12)*. This increase in temperature is much higher than the increase that takes place when the flow rate of oil is changed from 25 ml/min to 100 ml/min.

5.1.4 Effect of oscillation frequency

The oscillation frequency of the mould was changed at Plant C from its normal value of 144 cpm to 96 cpm. The corresponding change in oscillation related parameters are summarized in Table 5.1 (note the slight increase in the negative strip period from 0.19 seconds to 0.16 seconds with a decrease in the oscillation frequency). The effect that this change in oscillation frequency has on the mould temperature is shown in Figure 5.13. It can be clearly seen from the above figure that there is an increase in the mould wall temperature with a decrease in the oscillation frequency. *This result at first glance seems to be at variance with what would be expected; an increase in the negative strip time (at lower oscillation frequency) should increase the oscillation mark depth of the billets thereby increasing the local air gap width leading to a decrease in heat transfer and mould wall temperature.*

5.1.5 Mould temperature at the three Plants

Figure 5.14 and 5.15 show the time averaged mould wall temperatures collected for the three plants while casting steel of the same grade. Even allowing for differences in mould wall thickness and the location of the thermocouples it can be clearly seen that the mould wall temperatures at Company C are the highest indicating a significant increase in mould heat transfer over the other two plants. *This issue, which is of prime importance, is investigated in detail in subsequent chapters.*

5.2 Mould-Billet Friction Forces

The manner in which the mould-billet friction forces are analysed has been discussed in the previous chapter and are summarised here. The analysis consists of :

(a) Observation of the shape of the load cell response curve.

(b) Computation of the percentage of the negative strip time for which decompression of the load cell takes place

(c) Computation of the load at the start and end of the negative strip period.

(d) Calculation of the difference in the maximum load attained during the upstroke and the load at the start of negative strip period.

Such a route of analysis is necessary because, as explained, in the previous chapter, the absolute loads cannot be compared across trials.

5.2.1 Effect of oil type and flow rate on load cell response

The analysis of the load cell response from Company B has been part of the research work of Brendzy [13]. As mentioned earlier, she had observed that the reduction of oil flow (from 54 ml/min to 24 ml/min) resulted in increased mould-strand interaction. Furthermore, there is some evidence in her work to suggest that different oils exhibited different degrees of lubricity at the same flow rate.

Load cell data from Company C, however, shows that there is no influence of either the type of oil or its flow rate on mould friction. Figure 5.16 through 5.23 which show the load cell response for the four oils at two flow rates for a 1045 grade steel clearly reveal the same general nature of the load cell response curve. Table 5.2 shows the other parameters used for comparing load cell response and clearly no dependance of oil type or oil flow rate can be discerned. *Furthermore, using Brendzy's analysis [13] of the up stroke part of the cycle it appears that there is a large amount of friction in this part of the stroke regardless of the types of oil or their flow rates.*

5.2.2 Effect of carbon content

Both Brendzy [13] and other researchers [25,26,27] have indicated that there is a dependance of the mould-billet friction forces on the carbon content of the steel being cast. Figure 5.24 - 5.26 show the load cell response while casting 1018, 1045 and 5160 steel grade and Table 5.3 summarizes the statistics of the load cell response in different periods of the mould displacement. The increased friction at lower carbons is clearly seen in the difference between the load at start of negative strip time and the minimum load recorded during the down stroke. This result is consistent with that obtained by Stel et al. [27].

5.2.3 Effect of mould oscillation frequency

The effect of mould oscillation frequency on the mould-billet friction is shown in Figures 5.27 (144 cpm) and 5.28 (96 cpm) for HEAR oil at 25 ml/min and in Figures 5.29 (144 cpm) and 5.30 (96 cpm) for HEAR oil at 100 ml/min for a 1045 grade steel. The corresponding statistics for the load cell response are presented in Table 5.4. There is a greater decompression of the load cells (more mould-billet interaction) at the lower oscillation frequency of 96 cpm as shown by the difference in load at the start of negative strip time and the minimum load recorded during the downstroke. The increased mould-billet interaction is also obvious from the duration of the decompression period which is about 80-85% of the negative strip period for the 96 cpm case against ~70 % for the 144 cpm case. (*The cross marks on the mould displacement curve for the above mentioned figures indicate the start and end of negative strip time while the open square corresponds to the end of load cell decompression. Thus the position of the open square marker relative to the other two markers is a measure of the percentage of the negative strip time for which the load cell is decompressed*).

5.2.4 Difference in the load cell signals from the three Plants

From the standpoint of mould-billet interaction during the negative period, there are major differences in the load cell signals from the three plants. Typical load cell signals for Plant B, E and C are shown in Figures 5.31, 5.32 and 5.33 and the statistics for the different parts of the oscillation cycle is presented in Table 5.5. A close examination of Figures 5.31, 5.32 and 5.33 shows that at both Plant B and E the decompression period of the load cell is only 50 - 55 % of the negative strip period while at Plant C it is clearly in excess of 70%. This analysis is seen somewhat better in Figures 5.34, 5.35 and 5.36 where the load cell response is shown for just one cycle for the three plants. (As mentioned in the previous section the position of the open square marker relative to the cross markers (Figure 5.31-5.33) is a measure of the percentage of the negative strip time for which the load cell is decompressed).

Clearly then, there is more mould-billet interaction at Plant C than at the other two plants.

5.3 Billet Quality Evaluation

Billets collected during the trials at the three plants were subjected to an extremely exhaustive quality evaluation details of which have been covered in the previous chapter. A total of 45, 85 and 49 billets from Plants B, E and C were cut and macro-etched. Since a description of the results of the quality evaluation would be too detailed only the main quality problems observed in the billets are discussed below.

5.3.1 Transverse depressions

After lightly shot blasting the billets from Company B to remove scale, surface inspection for cracks was carried out. A characteristic of the grades 1008, 1010 & 1012 was the presence of severe transverse depressions present along the billet surface. These depressions appeared on both the control and test strands. Figure 5.37 is a macro-etch of a longitudinal section of a 1008 grade steel which contrasts with the relatively smooth surface of a "high carbon" grade billet as shown in Figure 5.38.

Observations made by looking into the spray chamber during the casting of the low-carbon grades revealed visible jerking of the billet while exiting the mould. Thus prima-facie it would appear that the parabolic taper of the billet mould at Company B is too tight for these low-carbon grades. Severe binding in the mould can lead to the formation of transverse depressions and cracks as explained in a previous chapter.

5.3.2 Off-corner internal cracks

Off-corner internal cracks were present in billets from Company E & C and absent from billets from Company B. The depth of cracks beneath the surface at each of the eight off-corner sites (see Figure 5.39) was measured and an average depth was calculated for each steel grade. Furthermore, for each group, the percentage of billets that had cracks at a given site was also determined.

For Company E, the most serious quality problem in both the test and control strand billets, is the presence of off-corner internal cracks. A typical macro-etch of a 1090 grade billet showing typical off-corner, internal cracks is presented in Figure 5.40. Figures 5.41 to 5.45 show the average depth of crack at different sites for both the test and control strands for grades 1018, 1050, 1080, 1090 and 1146. Longitudinal off-corner depressions were frequently seen on the test and control strand billets and Figure 5.46 shows this finding in the form of a bar graph. The principal findings of the analysis are summarised below.

[1] Cracks are present randomly on all eight sites with no apparent selectivity.

[2] The cracks are deeper on the test strand billets than on the control strand

[3] The crack depths vary from 8-11 mm on the test strand.

[4] The severity of cracking is worse in the 1080, 1090 and 1146 grades, with all the billets examined containing a crack in at least one off-corner site. Of these three grades the resulfurized steels (1146) had off-corner internal cracks at six of the eight possible sites on both the test and control strands.

[5] Longitudinal off-corner depressions are observed on the straight faces that are not deformed by the withdrawal rolls.

The mechanism by which off-corner, internal cracks form has been discussed earlier. It involves bulging of one of the faces, invariably the wide face, accompanied by rotation of the corner

[59]. Longitudinal off-corner depressions could form by this mechanism off the corner adjacent to the bulged face. Cracks form close to the solidification front in the region of low ductility as a result of the tensile stresses generated at the off-corner by bulging of the wide face and on the adjacent off-corner due to the rotation of the corner. The depth of the crack beneath the surface is a measure of the shell thickness of the billet at the time the crack formed.

The depth of the crack (8-11 mm) is a vital evidence in the analysis of the formation of the crack. Utilising the shell growth profile from the results of the mathematical model, discussed in Chapter 8, it can be shown that, allowing for 20 % variation in shell thickness between the mid-face and the off-corner (with the latter being lower), the cracks are forming just below the mould. The occurrence of cracks in both the test and control strands for all grades suggests that they are more likely related to the bulging of the wide face below the mould. The greater propensity for cracking in the high carbon and resulphurized grades is because the shell thickness is lower at the mould exit on account of their longer freezing range. The depth of cracks for these grades is closer on average to 8-9 mm in the 1018 grade.

An important difference between the test and control strands lies in the average depth of cracks from the surface. It is clear that the cracks are on average 1-2 mm deeper on the test strand. Since the mechanism of cracking is undoubtedly the same on both strands, this observation suggests that the shell thickness at the bottom of the test strand is 1-2 mm greater than on the control strand. *This is important as it indicates greater heat transfer in the control strand mould.*

For Company C, Figure 5.47 is a typical macro-etched transverse section showing the presence of off-corner, internal cracks. Figures 5.48 - 5.52 show the average depth of cracks at different sites for both the test and control strands for grades 1018, 1045, 5160, 1084 and L325 respectively. Results of analysis done on billets from Company C are summarized below.

[1] Cracks are present randomly on all eight sites with no apparent selectivity.

[2] The severity of cracking correlates well with the off-squareness.

[3] The crack depths vary from 6-14 mm on the test strand.

[4] The cracks are most severe in the 5160, L-325 and 1084 billets in comparison to 1018 and 1045 billets.

[5] Longitudinal off-corner depressions are observed on all billets.

A detailed analysis for the cause of these cracks is left until a later section.

5.3.3 Midway cracks

In an analysis somewhat similar to the preceding section, the depth of cracks beneath the surface at each of the four locations (see Figure 5.39) were measured and an average depth was calculated for each steel grade. Furthermore, for each group, the percentage of billets that had cracks at a given location was also determined.

Figure 5.53 is a macro-etch of a transverse section of a billet from Company E showing typical midway cracks. Average depths of these midway cracks for grade 1018, 1050, 1080, 1090 and 1146 for Company E are shown in Figures 5.54 to 5.58. These cracks are seen on all grades and predominantly on the wide faces. In some cases the cracks appear to extend to the centreline.

A typical macro-etch, for Company C, of a transverse section containing midway cracks is shown in Figure 5.59. Details of the crack depths and percentage of the billets exhibiting midway cracks are presented in Figures 5.60 to 5.64. Thus it can be seen that the cracks appear most frequently in 1018, L-325 and 1084 grades as compared to 1045 and 5160 billets. There is little difference in crack frequency between the test and control strands and no discernible preference of the cracks to appear adjacent to a given billet face. Comparison of the crack depth to the shell profile (available from Chapter 8) reveals that the midway cracks are forming 2.5 to 3.0 m from the top of the mould. This location corresponds to the bottom of the sprays, as expected, which suggests that the sprays need to be redesigned to minimize surface reheat of the billets below the secondary cooling zone.

The length of the spray chamber (1.74 m), for example, is too short.

5.3.4 Surface roughness

A ready measure of the surface roughness of billets is available from the profilometer readings of the billet surface. These results are put on a firmer footing by combining them with visual observation of the billet surface.

5.3.4.1 Effect of carbon

The effect of carbon on the surface roughness of the billets is best seen at Company B where billets were collected for a wide range of carbons. Figures 5.65, 5.66 and 5.67 are photographs of the longitudinal section of billets from grades 1008, 1012 and 1039. The wrinkled surface of a 1012 grade stands out in direct contrast to the smoother surfaces of the other two grades. This difference in surface roughness is only expected as the phase change from δ to γ for the 1012 grade takes place very early in the solidification and the solid shell, being thin and thus unable to resist the stresses arising from the contraction accompanying the phase change, buckles giving rise to a "wrinkled" surface appearance. The phase change for the 1008 grade takes place after it has undergone significant amount of cooling and the solid shell is reasonably thick to withstand phase-change related stresses. The higher carbon grade, 1039, when below the solidus is in the γ phase and does not undergo δ to γ phase transformation.

5.3.4.2 Effect of oil type

At Company B there was no discernible effect of either the oil type or its flow rate on billet quality [13]. This conclusion is based on billet surface evaluation and profilometer measurements. However since changes in the oil type could not be separated from changes in carbon content of billets, this finding remains somewhat inconclusive.

At Company E, systematic changes were made to oil type and its flow rate and the results are discussed below. Figures 5.68 - 5.71 are graphs of oscillation mark depth of four 1018 billets cast with Canola, HEAR, Mineral_S and Soybean oils respectively. Figures 5.72 - 5.75 are the corresponding photographs of the surfaces of these billets. The billet cast with Canola clearly have the best appearance. The surface of the HEAR oil billet is considerably rougher whilst the billets cast with Mineral_S and Soybean lubricating oils have deeper and more irregular oscillation marks. The profilometer readings for the billets cast with Mineral_S and Soybean oils, further show that not only are the oscillation marks more uniform across the face but are also shallower and less sensitive to oil flow rate than with other oils. The oscillation-mark depths appear to be highly sensitive to flow rate with the Soybean oil, and are very non-uniform for Mineral_S oil. Notwithstanding the inherent superiority of Canola oil, there are occasional problems like sticking and bleeds.

The profilometer measurements of oscillation-mark depths of 1080 grade billets from Company E for the four oils, Canola, HEAR, Mineral_S and Soybean are shown in Figures 5.76 - 5.79 and the corresponding photographs in Figures 5.80 - 5.83. At a flow rate of 45 ml/min the oscillation marks on billets cast with Canola are slightly more uniform while the billets cast with Soybean appear to have bleeds and laps.

Profilometer measurement of 1090 grade billet cast at Company E with Canola, HEAR and Mineral_S are shown in Figures 5.84 - 5.86 and the corresponding photographs are shown in Figures 5.87 - 5.89. Neither the type of nor its flow rate appear to have any significant effect on the oscillation-mark depth except with Canola oil where there was a marked deterioration in uniformity at 65 ml/min.

The last set of billets from Company E is the one belonging to the 1146 grade and the profilometer measurement of oscillation mark depths are shown for Canola and HEAR oils in Figures 5.90 - 5.91. The depths of these marks are deeper than that observed on billets from grades 1018, 1080 or 1090. Furthermore these marks appear quite non-uniform in depth across the face of the billet. Corresponding photographs of billets are shown in Figures 5.92 - 5.93.

Figures 5.94 - 5.97 shows the oscillation-mark depths for 1018 grade billets from Company C cast with Canola, HEAR, Mineral_S and Mineral_O oils at different flow rates, and photographs of the billet surfaces cast at a flow rate of 25 ml/min are shown in Figures 5.98 - 5.101. At low flow rates it is clear that the billets cast with Canola oil have the best appearance with those cast with HEAR oil being relatively similar. The oscillation mark depth support this observation. With increasing flow rate the uniformity of the depth of oscillation marks deteriorates for both Canola and HEAR. This finding is in accordance with the observations made on billet from Company E.

The oscillation mark depth for 1045 grade billet from Company C cast with HEAR and Mineral_O oils is shown in Figures 5.102 - 5. 103 and the corresponding photographs are shown in Figures 5.104 - 5.105. No clear trend is discernible.

For the 5160 grade billets from Company C the oscillation mark depths for Canola, HEAR, Mineral_S and Mineral_O oils are presented in Figures 5.106 - 5.109. At oil flow rates of 25 ml/min the oscillation marks are shallower and more uniform when casting with Canola and Mineral_S whilst at flow rates of 100 ml/min Mineral_O performs the best.

5.3.4.3 Effect of oscillation frequency

The effect of oscillation frequency on oscillation mark depth can be seen for Company C by comparing the oscillation mark depth for 1045 grade billet cast at 96 cpm with HEAR oil (Figure 5.110) and Mineral_O oil (Figure 5.111) with Figures 5.102 and 5.103 which give the oscillation mark depth for 1045 grade billet with the same oils at 144 cpm. It is clear that for HEAR oil, at low flow rates, the oscillation marks are more non-uniform at a higher frequency while at high flow rates the differences are not significant. For the billets cast with Mineral_O oil no clear trends emerge.

The oscillation mark depth for 1080 grade billet cast at 130 cpm is given in Figure 5.112. This, when compared to the depths shown in Figure 5.83, reveals that at both high and low flow rates there is a slight decrease in the average depth of oscillation mark. At high flow rates the variability in oscillation-mark depth is higher.

5.3.5 Rhomboidity

Rhomboidity was determined by measuring the difference in the lengths between the two diagonals of a transverse section of a billet. In almost all cases rhomboidity was less than 1% in Companies B & E. In case of billets from Company C, the control strand had the most severely off-square billets of the 1018, 5160 and L-325 grades as shown in Figure 5.113. It is important to note that the mould cooling water velocity in the control strand is much lower than that in the test strand and there is a possibility that the cold face temperature of the control strand mould could exceed the boiling point of water at the prevailing pressure. This issue is investigated in greater detail in a subsequent chapter.

5.3.6 Other defects

Detailed examination of the billet surface revealed two defects that can be sources of problem while rolling steel billets.

5.3.6.1 Craze cracks

Craze cracks are a network of cracks usually up to 1 mm deep that can be revealed by macroetching billet surfaces. Earlier work at the Centre for Metallurgical Processing, UBC, had shown that increasing copper content of steel resulted in deeper, more interconnected cracks. This is consistent with studies done on bloom casting elsewhere [66]. It had also been found that an increase in the Ni/Cu ratio reduced the severity of the cracking.

The same phenomenon was found when transverse sections from Company C were macroetched. A typical example of craze cracking is shown in Figure 5.114. The cracking in its least severe form was observed to start at the corners of the inside radius, with the width of coverage increasing towards the centreline until the entire billet surface was affected. It was also observed that the other three billet surfaces exhibited similar behaviour, although to a lesser degree for a given copper content and Ni/Cu ratio.

To categorize the severity of cracking, a craze cracking index was formulated [67]. The index consists of measuring (in mm) the distance across the billet face that was affected by the cracking. It is then multiplied by a reduction factor based on the visual appearance of crack severity. This index is plotted versus copper, nickel, carbon content and nickel/copper ratio in Figures 5.115 to 5.118.

Importance of the Ni/Cu ratio can be seen when steel grades 1018 and L-325 are compared. The 1018 grade has a copper content ranging from 0.05% to 0.27% with craze cracking indices which vary with copper content. When the L-325 grade is examined, craze cracking indices are observed to be much lower in spite of the copper content being approximately 0.40%. It appears that the Ni/Cu ratio of 0.2-0.8 of the 1018 grade is inferior to the ratio of 1.3-1.8 in grade L-325.

5.3.6.2 Zipper marks

A new defect, termed "zipper marks" was observed on the surface of billets from Company E. This defect is generally associated with a bead of material trapped initially on the mould wall and Figures 5.119 and 5.120 show this defect for billets cast with Canola and Soybean oils respectively. Beading was generally observed on both the test and control strand billets. A control strand grade 1080 billet cast with Soybean oil as a lubricant was sectioned transversely through a bead and subjected to metallographic examination. Figure 5.121 is a macro-etch of the transverse section through the bead from which it is evident that the bead has solidified on the surface of the billet and in this instance is approximately 0.3 mm thick. An EDX analysis of the bead on the SEM indicated that the bead has the same composition as the billet. Thus the bead may be a result of micro-bleeding of the solidifying shell. This could be due to poor lubrication which causes tearing and bleeding. The bleeding problem appears to be most severe on high carbon billets which could be related to the long freezing range and the susceptibility of the shell to rupture. This defect was observed at both high and low flow rates with the four types of oils.

Table 5.1 Oscillation characteristics of the oscillator at Plant C for two different oscillation frequencies.

Oscillation Frequency (cpm,Hz)	Negative Strip Period (s)	Mould Lead (mm)
144, 2.4	0.16	5.4
96,1.6	0.19	3.1

Table 5.2 Difference in the maximum load attained during the upstroke and the load at the beginning of t_N while casting 1045 grade steel at Company C.

Type of oil	Load at flow rate of oil (25 ml/min) (N)	Load at flow rate of oil (100 ml/min) (N)
Canola	196	187
Mineral_S	178	169
HEAR	196	182
Mineral_O	n.a	209

Table 5.3 Difference in the maximum load attained during the upstroke and the load at the beginning of t_N while casting different steel grades at Company C.

Steel Grade	Load (N)
1018	240
1045	196
5160	196

Table 5.4 Decompression of the load cell during the negative strip period and the percentage of negative strip time for which this decompression lasts for two oscillation frequencies at Company C.

Oscillation frequency (cpm, Hz)	Load at 25 ml/min (N)	Load at 100 ml/min (N)	Period of decompression at 25 ml/min (%)	Period of decompression at 100 ml/min (%)
144	583	627	68	72
96	902	920	84	87

Table 5.5 Percentage of the negative strip time for which the load cell is decompressed (during negative strip period) at Company B, E and C while casting a 1018 grade steel.

Company	Period of decompression (%)
B	50
E	52
C	78

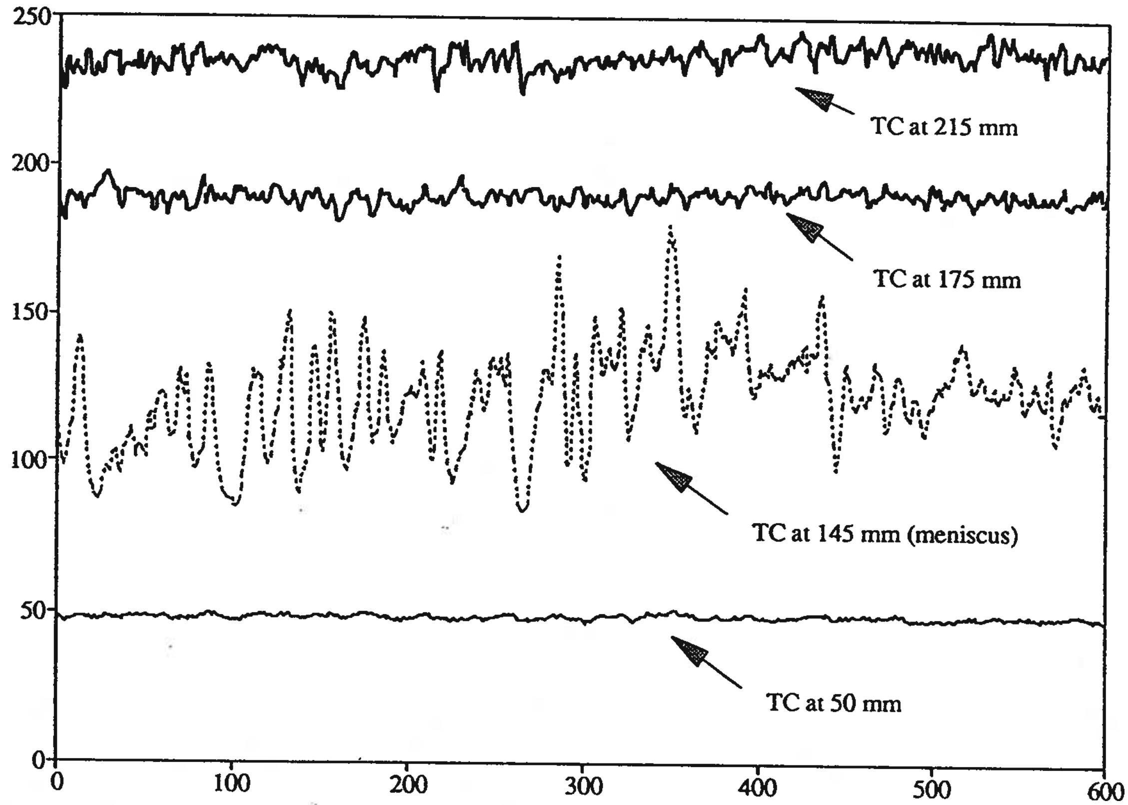

Figure 5.1 Unfiltered response of selected thermocouples at Company C while casting a 1045 grade billet.

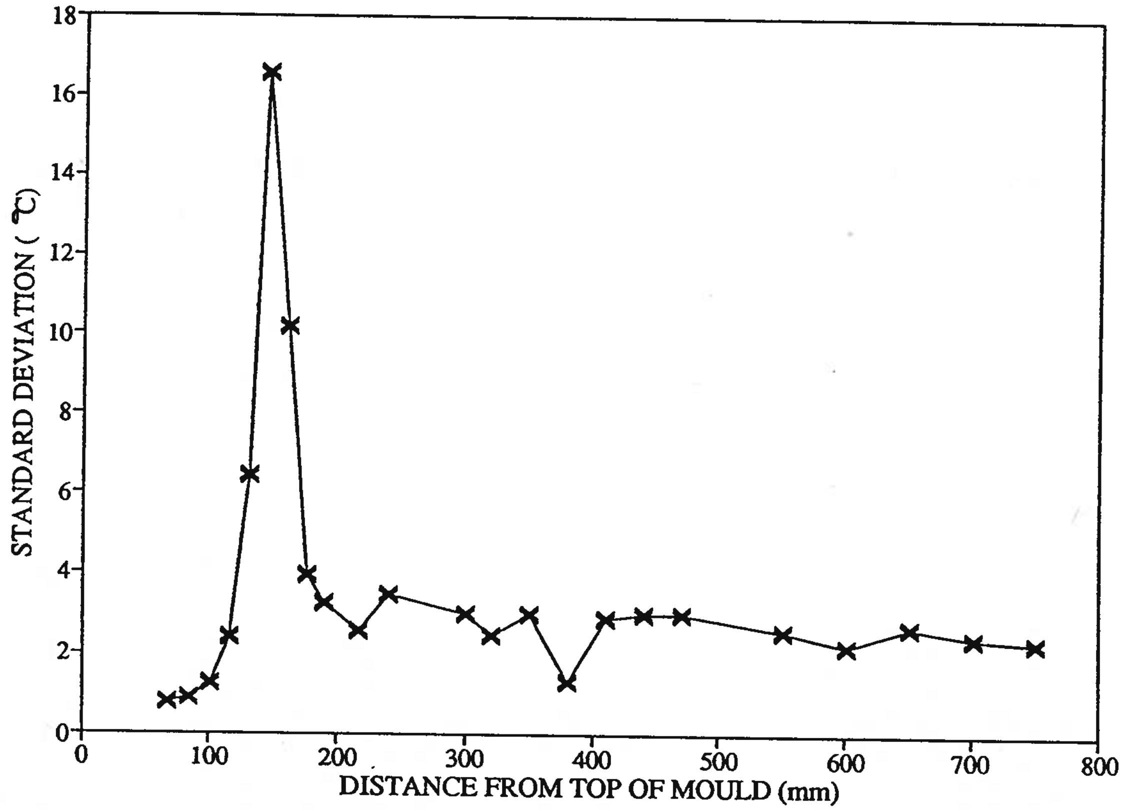

Figure 5.2 Typical standard deviation values for temperature data collected by thermcouples at Company C.

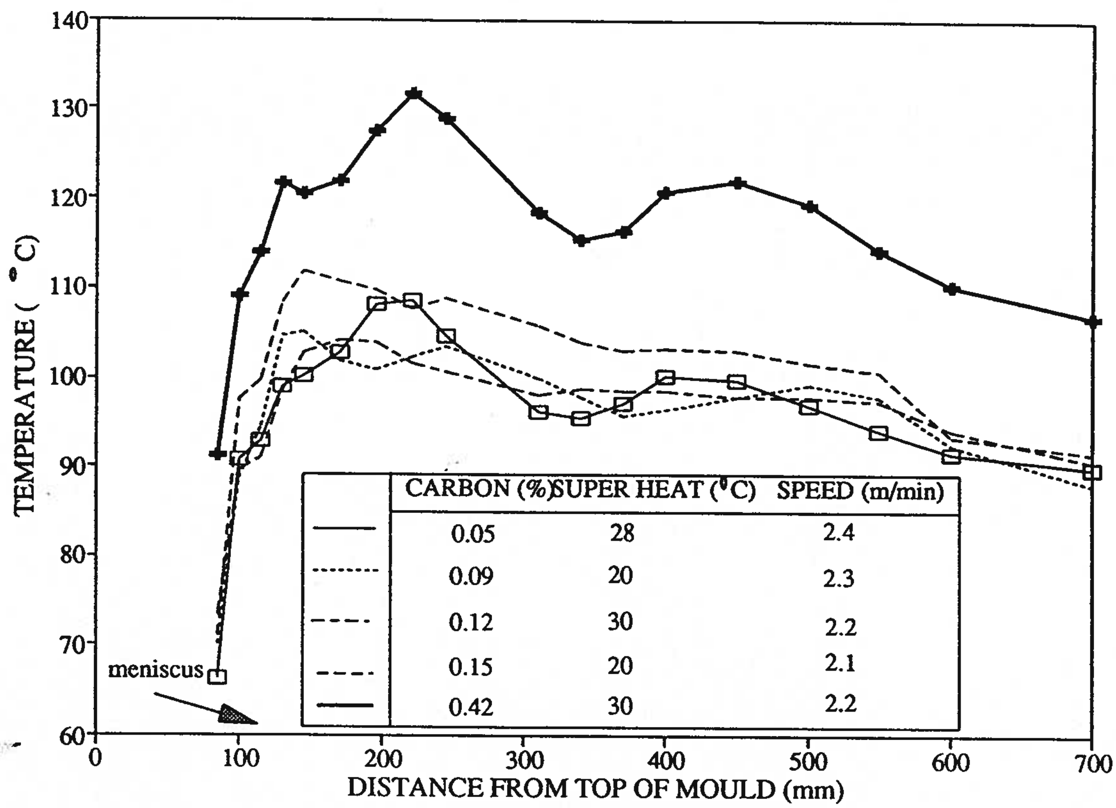

Figure 5.3 Time-averaged axial temperature profile for different carbon contents at Company B. (Note that the temperatures are those recorded by thermocouples located approximately midway between the cold and hot faces of the mould).

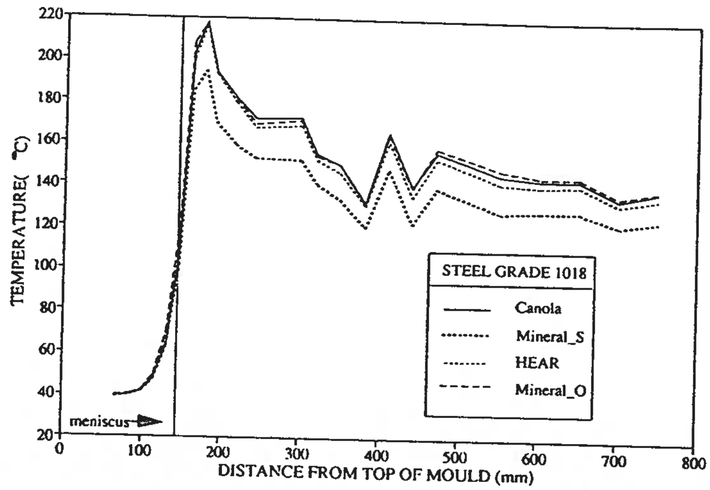

Figure 5.4 Time-averaged axial temperature profile for a 1018 grade of steel billets cast at 25 ml/min of Canola, Mineral_S, HEAR and Mineral_O lubricating oils at Company C. (Note that the temperatures are those recorded by thermocouples located approximately midway between the cold and hot faces of the mould).

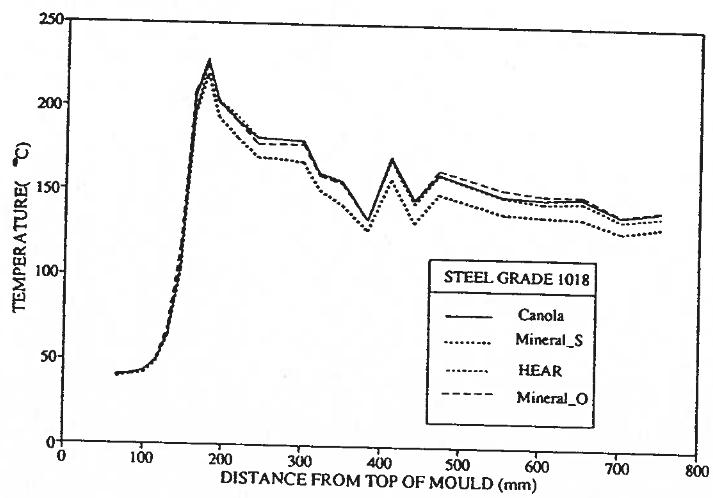

Figure 5.5 Time-averaged axial temperature profile for a 1018 grade of steel billets cast at 100 ml/min of Canola, Mineral_S, HEAR and Mineral_O lubricating oils at Company C. (Note that the temperatures are those recorded by thermocouples located approximately midway between the cold and hot faces of the mould).

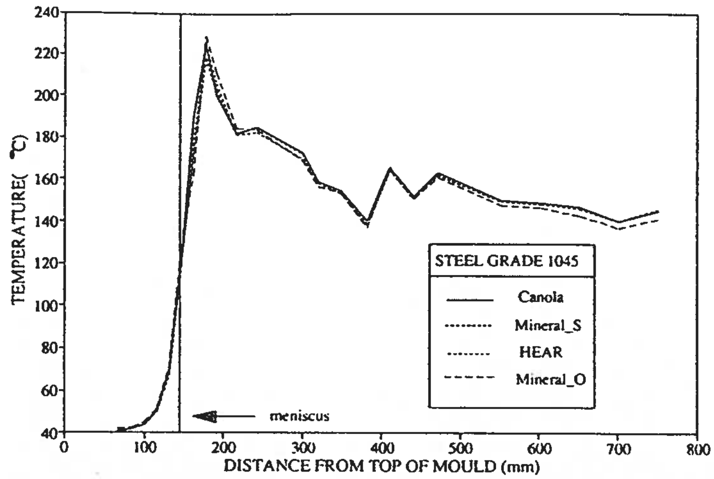

Figure 5.6 Time-averaged axial temperature profile for a 1045 grade of steel billets cast at 25 ml/min of Canola, Mineral_S, HEAR and Mineral_O lubricating oils at Company C. (Note that the temperatures are those recorded by thermocouples located approximately midway between the cold and hot faces of the mould).

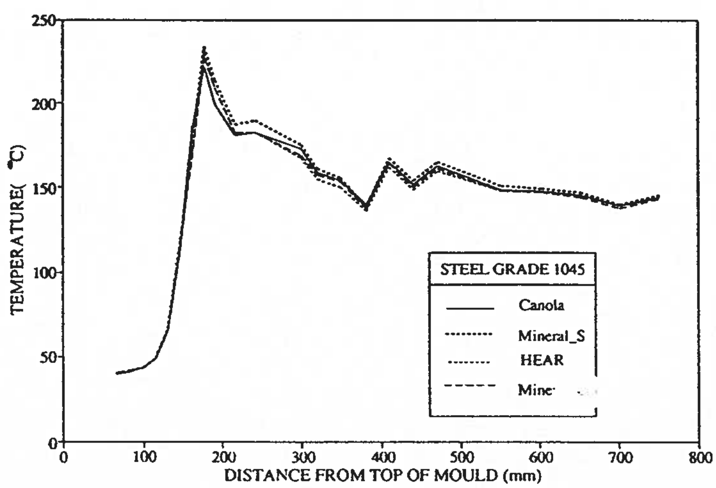

Figure 5.7 Time-averaged axial temperature profile for a 1045 grade of steel billets cast at 100 ml/min of Canola, Mineral_S, HEAR and Mineral_O lubricating oils at Company C. (Note that the temperatures are those recorded by thermocouples located approximately midway between the cold and hot faces of the mould).

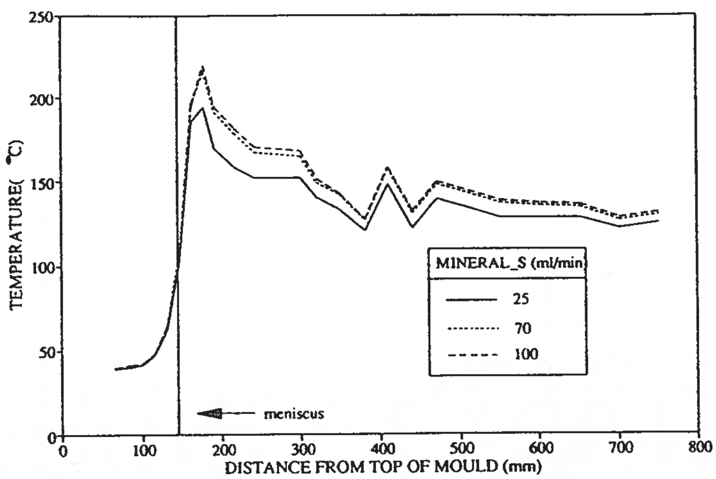

Figure 5.8 Time-averaged axial temperature profile for a 1018 grade steel billets cast at 25, 70 and 100 ml/min of Mineral_S oil at Company C. (Note that the temperatures are those recorded by thermocouples located approximately midway between the cold and hot faces of the mould).

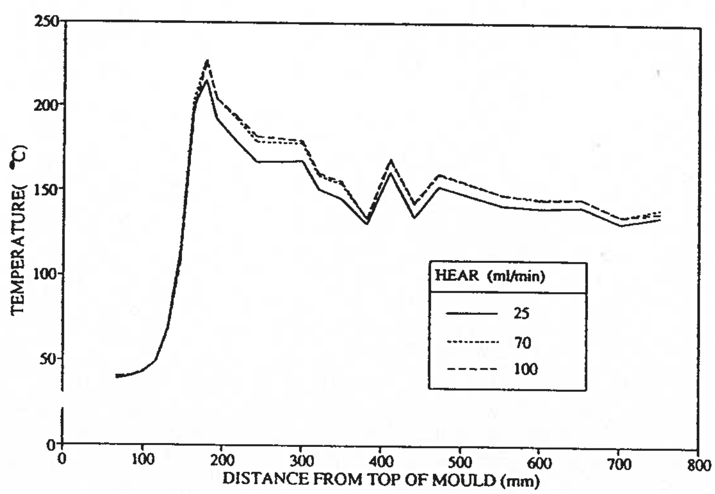

Figure 5.9 Time-averaged axial temperature profile for a 1018 grade steel billets cast at 25, 70 and 100 ml/min of HEAR oil at Company C. (Note that the temperatures are those recorded by thermocouples located approximately midway between the cold and hot faces of the mould).

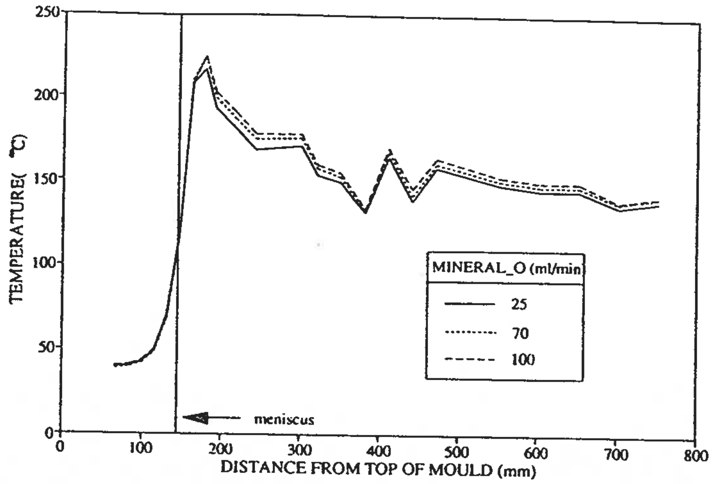

Figure 5.10 Time-averaged axial temperature profile for a 1018 grade steel billets cast at 25, 70 and 100 ml/min of Mineral_O oil at Company C. (Note that the temperatures are those recorded by thermocouples located approximately midway between the cold and hot faces of the mould).

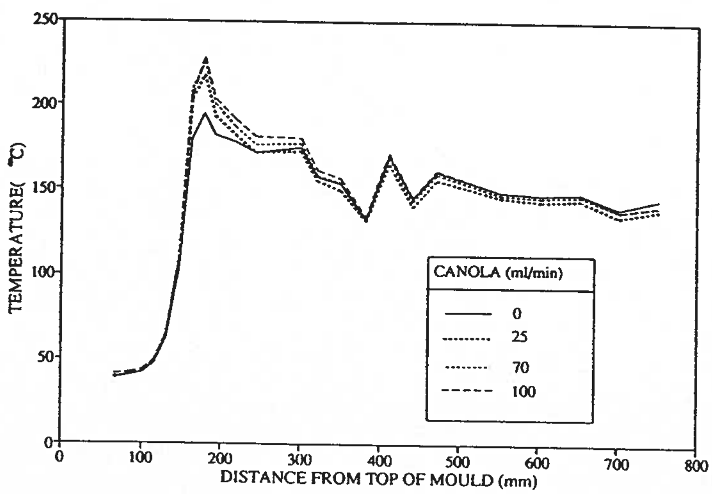

Figure 5.11 Time-averaged axial temperature profile for a 1018 grade steel billets cast at 0, 25, 70 and 100 ml/min of Canola oil at Company C. (Note that the temperatures are those recorded by thermocouples located approximately midway between the cold and hot faces of the mould).

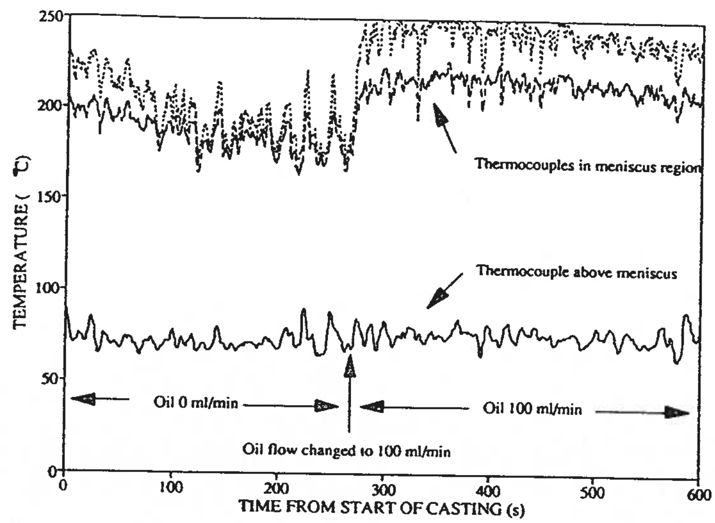

Figure 5.12 Response of selected thermocouples at Company C with change in oil flow rate from 0 ml/min (no oil) to 100 ml/min of Canola oil for 1018 grade steel billet at Company C. (Note that the temperatures are those recorded by thermocouples located approximately midway between the cold and hot faces of the mould).

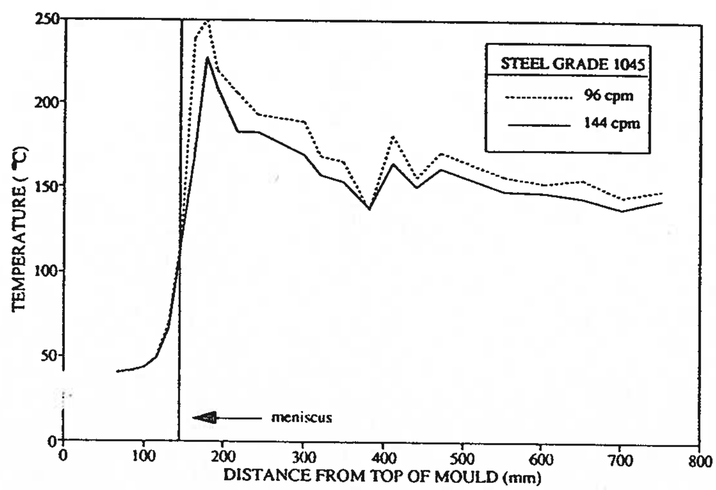

Figure 5.13 Time-averaged axial temperature profile for a 1045 grade of steel cast at 144 and 96 cpm of mould oscillation at Company C. (Note that the temperatures are those recorded by thermocouples located approximately midway between the cold and hot faces of the mould).

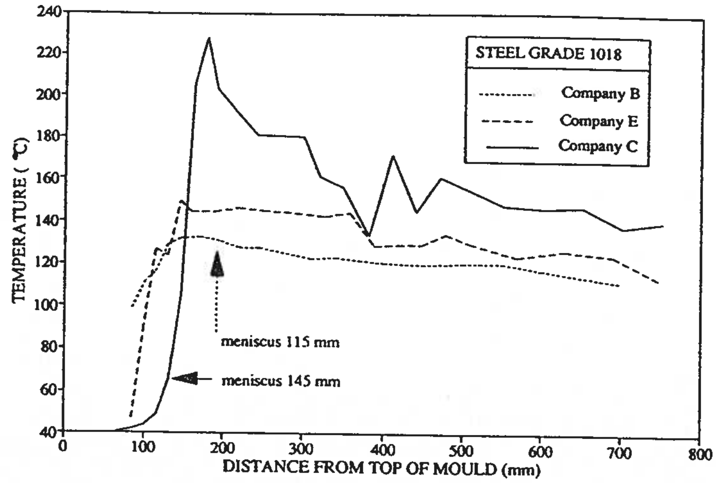

Figure 5.14 Time-averaged axial temperature profile obtained at Company B, E and C while casting a 1018 grade steel billet. (Note that the temperatures are those recorded by thermocouples located approximately midway between the cold and hot faces of the mould).

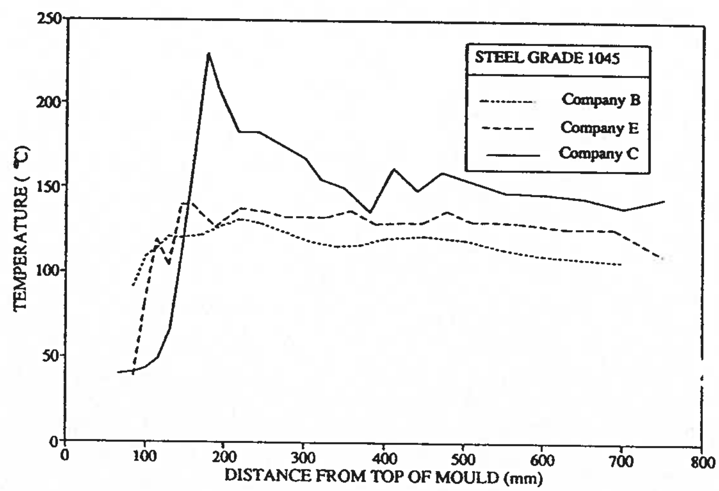

Figure 5.15 Time-averaged axial temperature profile obtained at Company B, E and C while casting a 1045 grade steel billet. (Note that the temperatures are those recorded by thermocouples located approximately midway between the cold and hot faces of the mould).

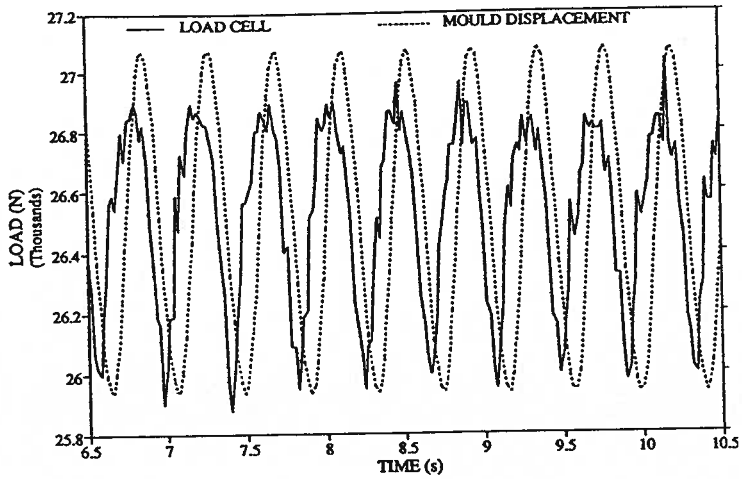

Figure 5.16 Load cell response for a 1045 grade billet cast with Canola oil at 25 ml/min at Company C.

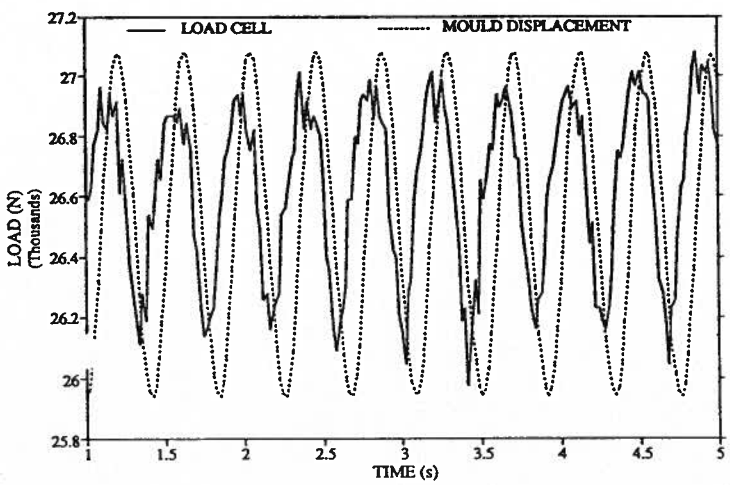

Figure 5.17 Load cell response for a 1045 grade billet cast with Canola oil at 100 ml/min at Company C.

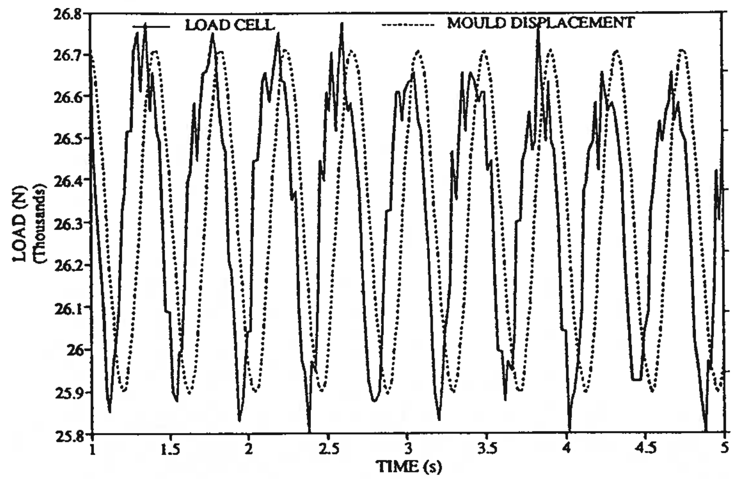

Figure 5.18 Load cell response for a 1045 grade billet cast with Mineral_S oil at 25 ml/min at Company C.

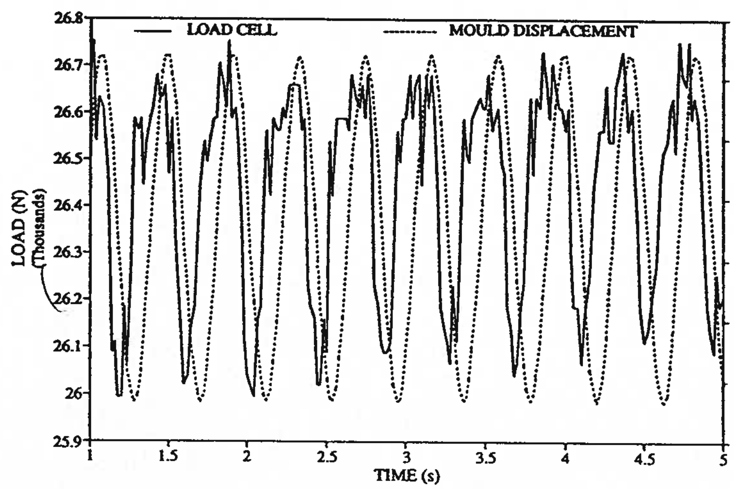

Figure 5.19 Load cell response for a 1045 grade billet cast with Mineral_S oil at 100 ml/min at Company C.

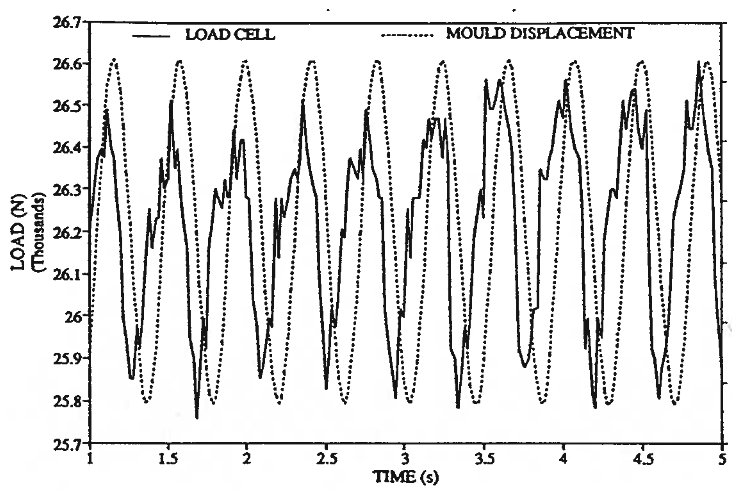

Figure 5.20 Load cell response for a 1045 grade billet cast with HEAR oil at 25 ml/min at Company C.

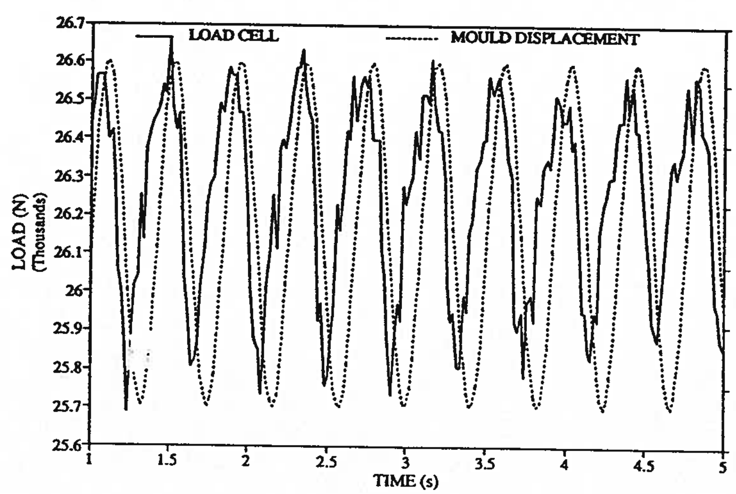

Figure 5.21 Load cell response for a 1045 grade billet cast with HEAR oil at 100 ml/min at Company C.

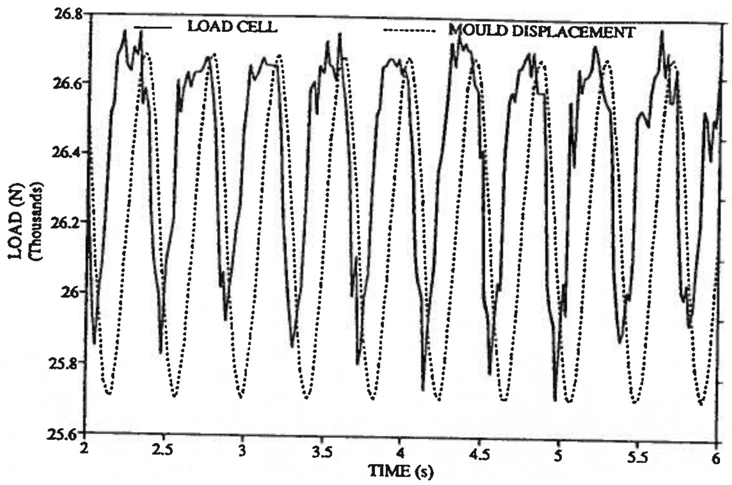

Figure 5.22 Load cell response for a 1045 grade billet cast with Mineral_O oil at 25 ml/min at Company C.

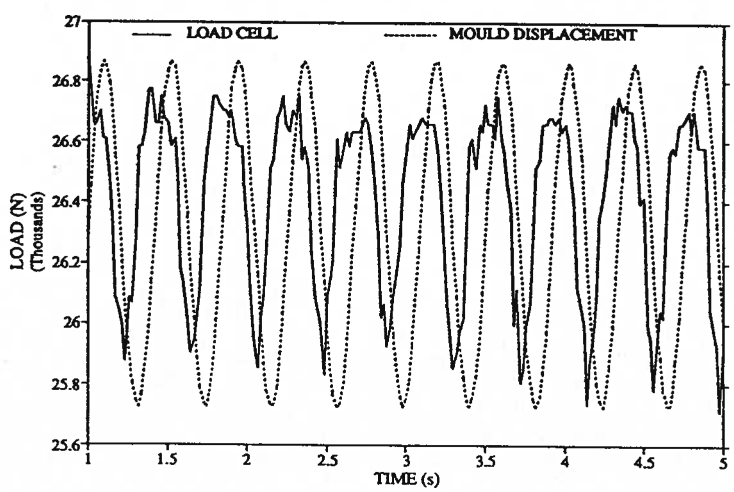

Figure 5.23 Load cell response for a 1045 grade billet cast with Mineral_O oil at 100 ml/min at Company C.

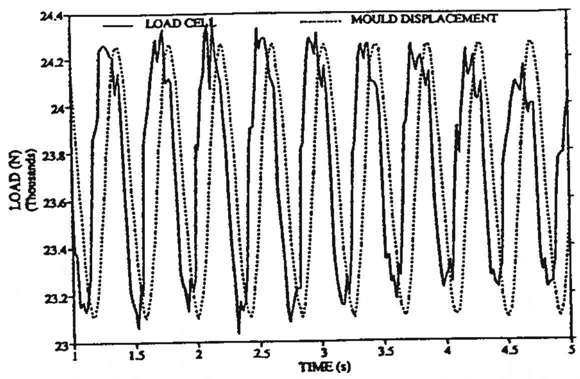

Figure 5.24 Load cell response for a 1018 grade billet cast with Canola oil at 25 ml/min at Company C.

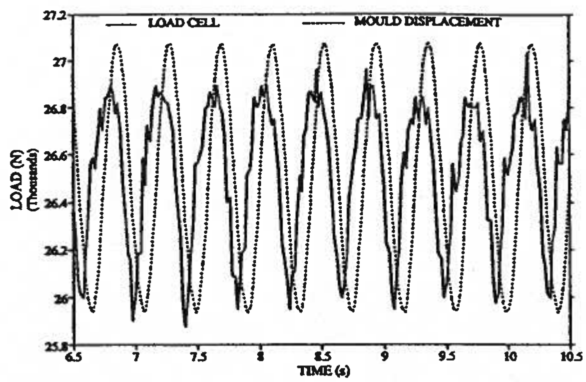

Figure 5.25 Load cell response for a 1045 grade billet cast with Canola oil at 25 ml/min at Company C.

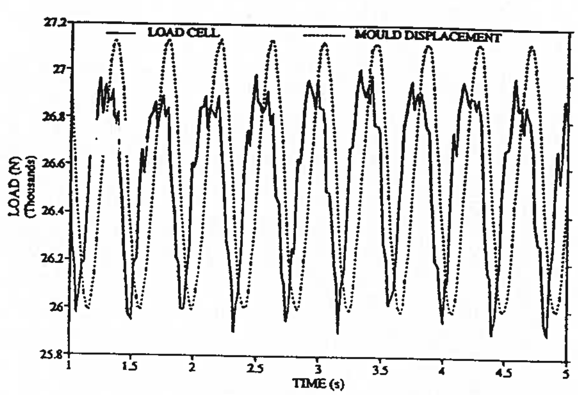

Figure 5.26 Load cell response for a 5160 grade billet cast with Canola oil at 25 ml/min at Company C.

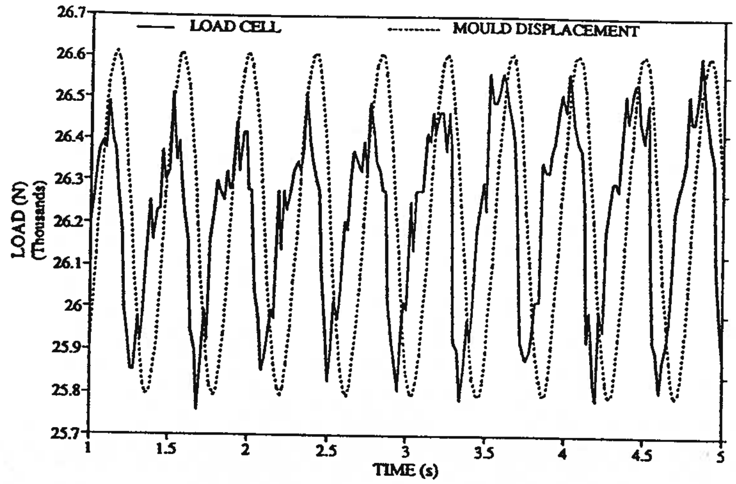

Figure 5.27 Load cell response for a 1045 grade billet cast with HEAR oil at 25 ml/min and at 144 cpm of mould oscillation at Company C.

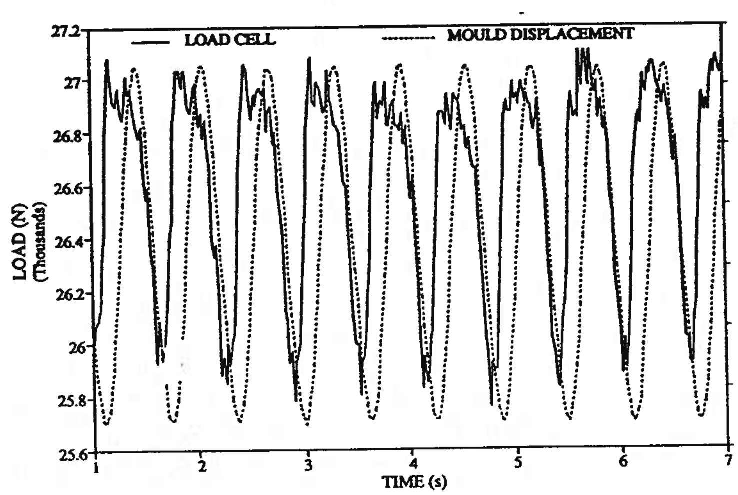

Figure 5.28 Load cell response for a 1045 grade billet cast with HEAR oil at 25 ml/min and at 96 cpm of mould oscillation at Company C.

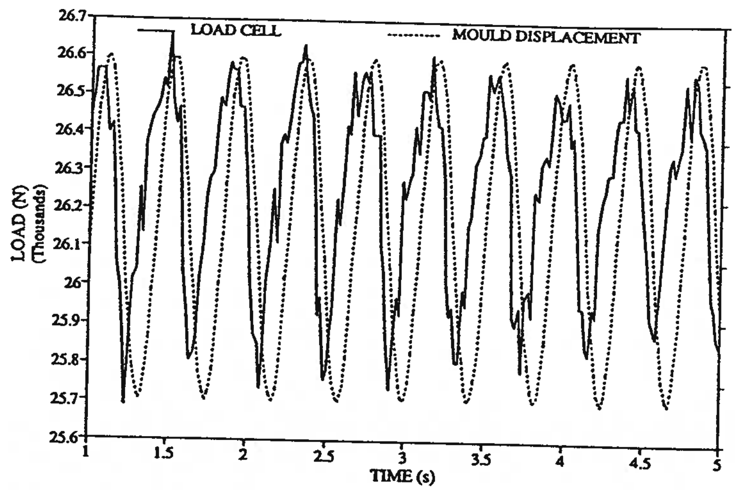

Figure 5.29 Load cell response for a 1045 grade billet cast with HEAR oil at 100 ml/min and at 144 cpm of mould oscillation at Company C.

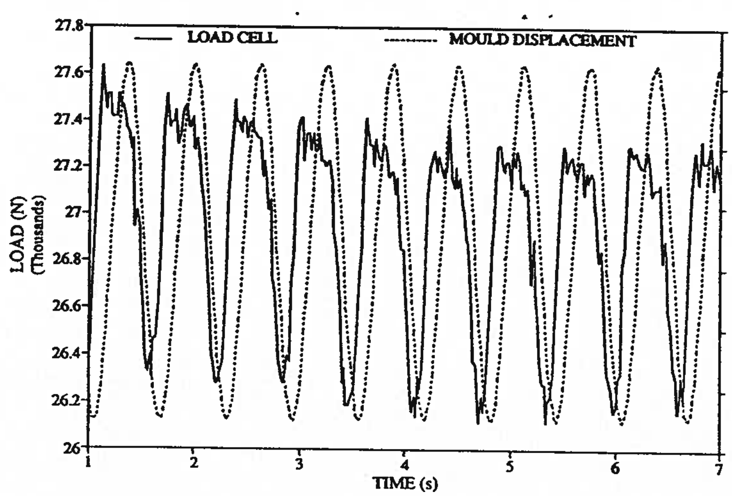

Figure 5.30 Load cell response for a 1045 grade billet cast with HEAR oil at 100 ml/min and at 96 cpm of mould oscillation at Company C.

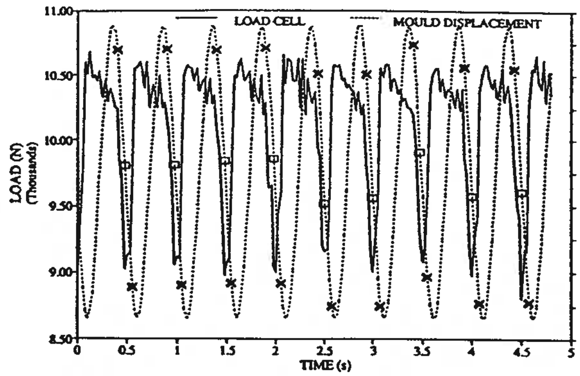

Figure 5.31 A typical load cell response for Company B. (Note: Cross marks indicate start and end of negative strip time; open markers correspond to end of load cell decompression).

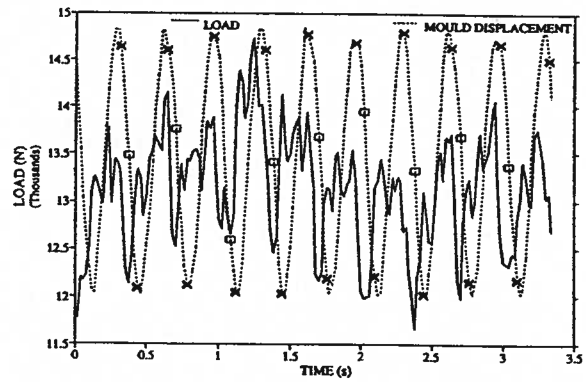

Figure 5.32 A typical load cell response for Company E. (Note: Cross marks indicate start and end of negative strip time; open markers correspond to end of load cell decompression).

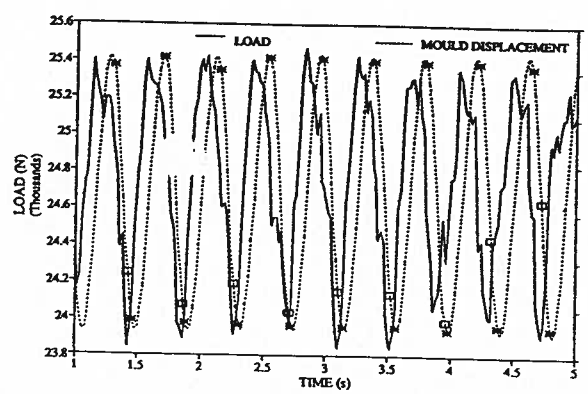

Figure 5.33 A typical load cell response for Company C. (Note: Cross marks indicate start and end of negative strip time; open markers correspond to end of load cell decompression).

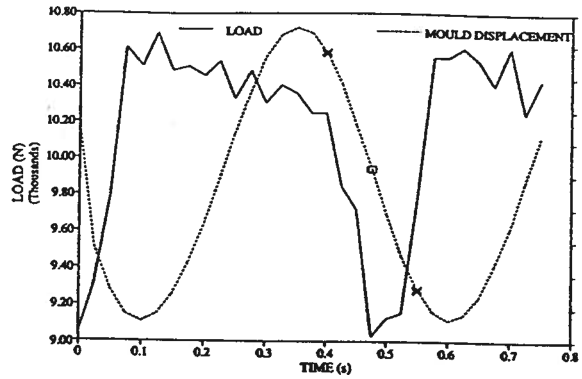

Figure 5.34 A typical load cell response for Company B (enlarged). (Note: Cross marks indicate start and end of negative strip time; square marker corresponds to end of load cell decompression).

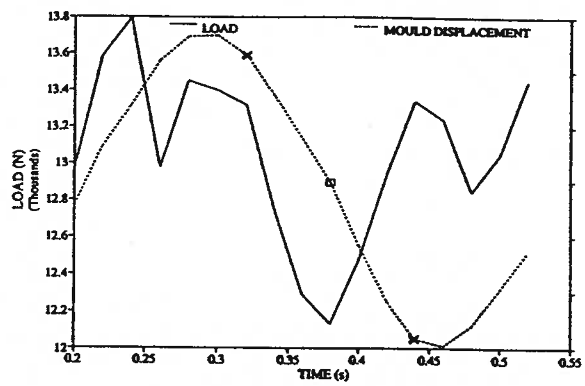

Figure 5.35 A typical load cell response for Company E (enlarged). (Note: Cross marks indicate start and end of negative strip time; square marker corresponds to end of load cell decompression).

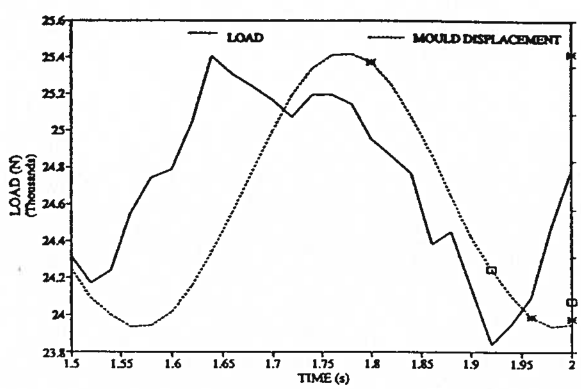

Figure 5.36 A typical load cell response for Company C (enlarged). (Note: Cross marks indicate start and end of negative strip time; square marker corresponds to end of load cell decompression).

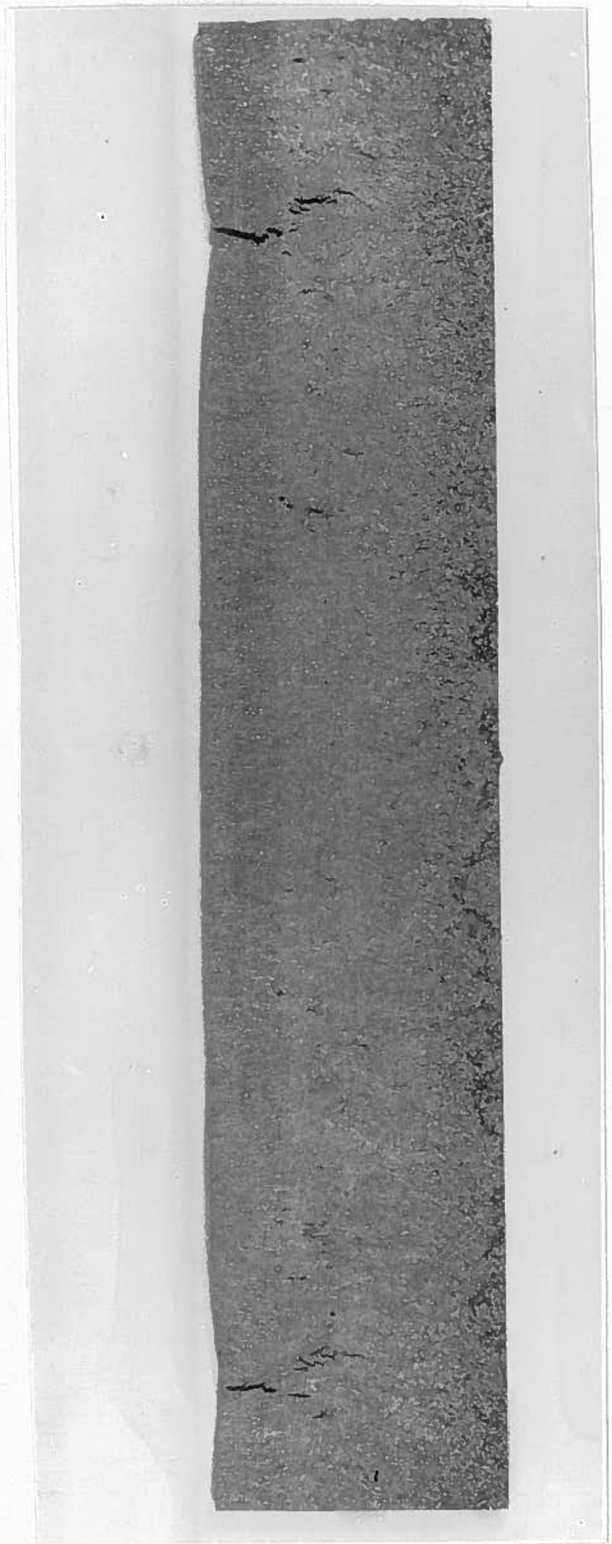

Figure 5.37 Macro-etch of a longitudinal section of a 1008 grade billet from Company B showing transverse depressions and cracks at the base of these depressions (Mag. 0.8 X).

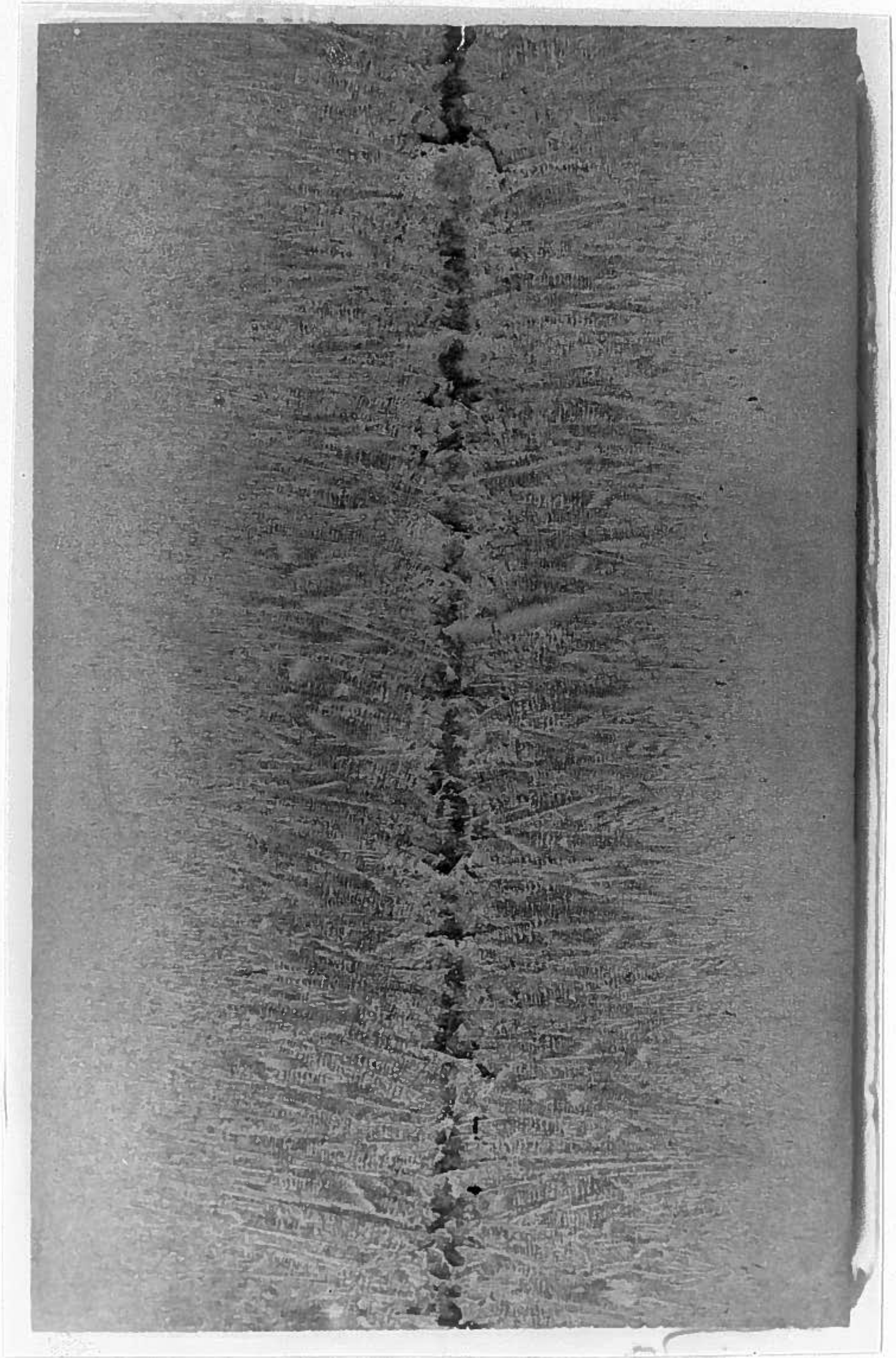

Figure 5.38 Macro-etch of a longitudinal section of a 1039 grade bilet from Company B showing a 'smooth' surface (Mag. 1.0 X).

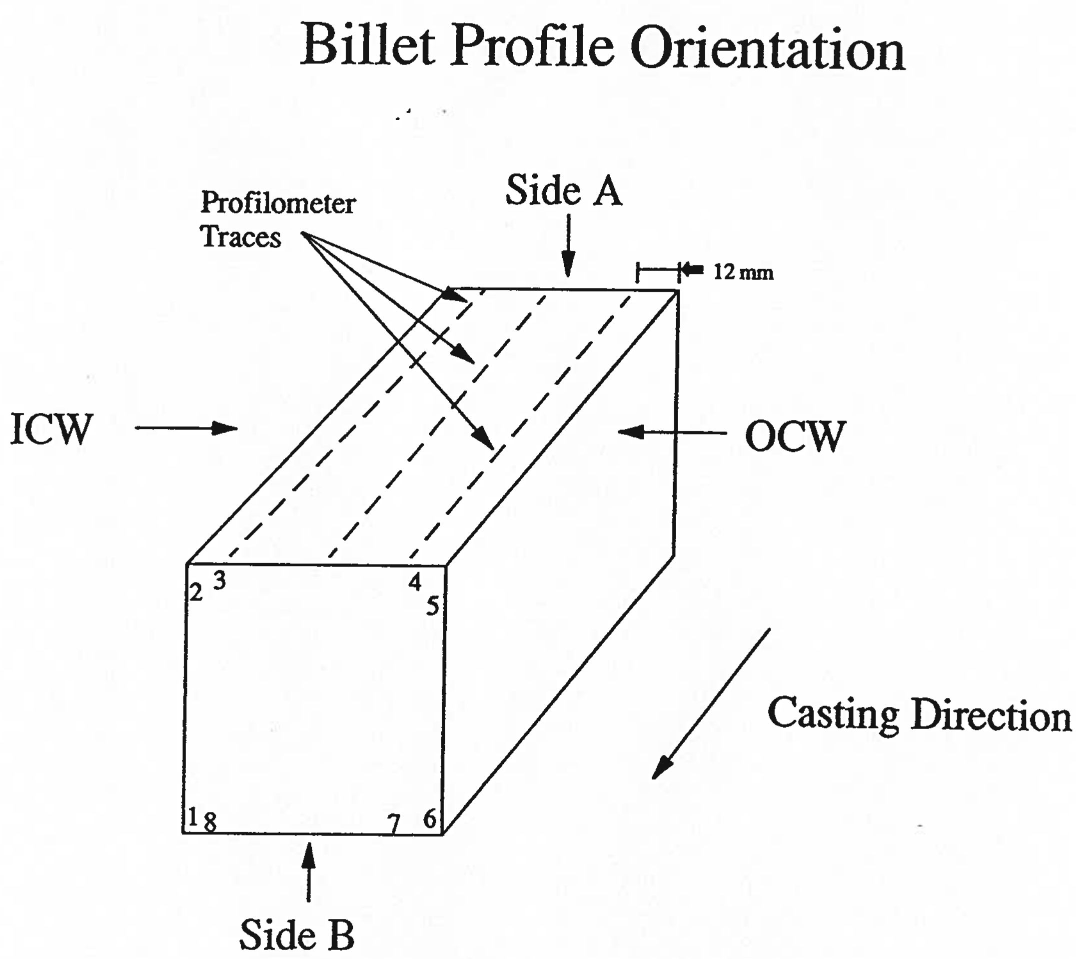

Figure 5.39 Schematic diagram showing the eight off-corner sites of a billet.

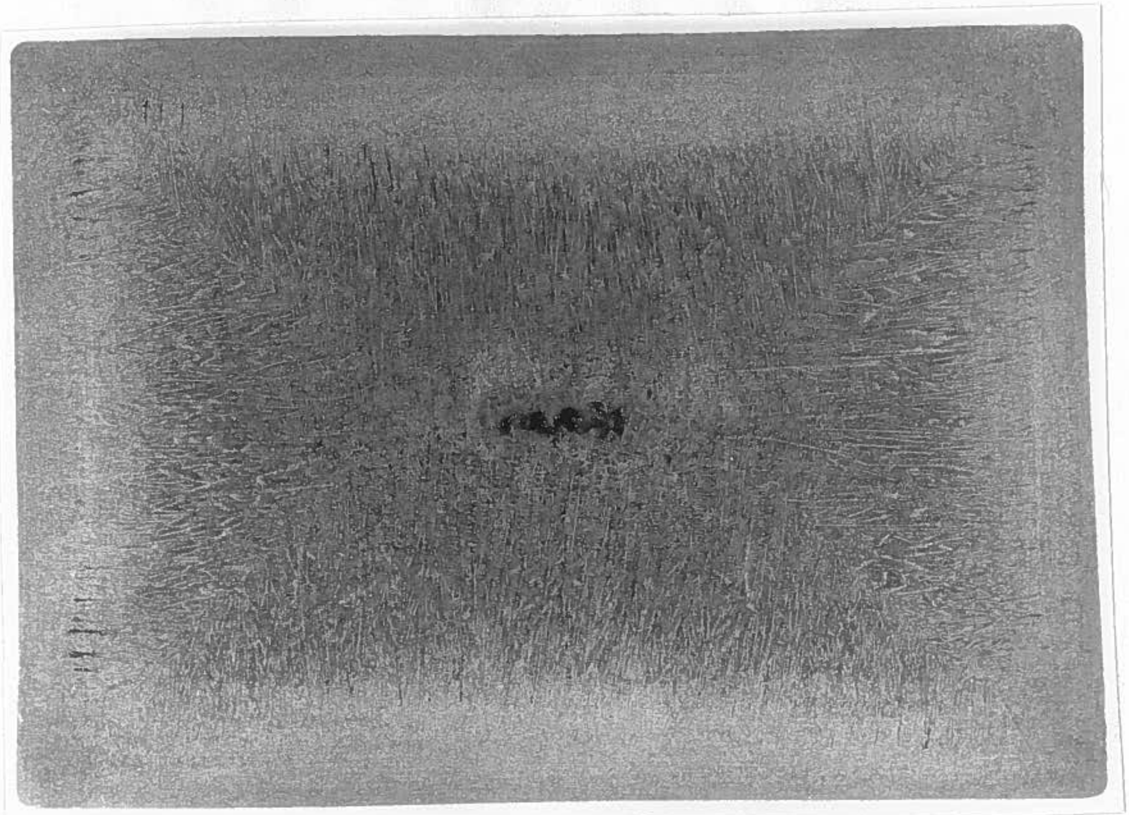

Figure 5.40 Macro-etch of a transverse section of a 1090 grade billet from Company E showing typical off-corner, internal cracks (Mag. 0.8 X).

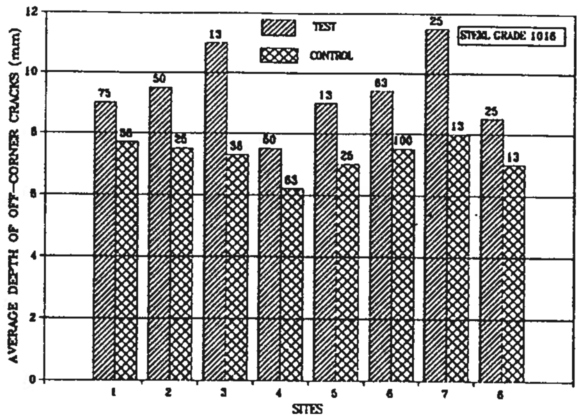

Figure 5.41 Bar graph showing average depth of off-corner, internal cracks at the eight off-corner sites on the test and control strand for a 1018 grade billet from Company E. (Note: Numbers on the top of the bars represent percentage of billets with cracks

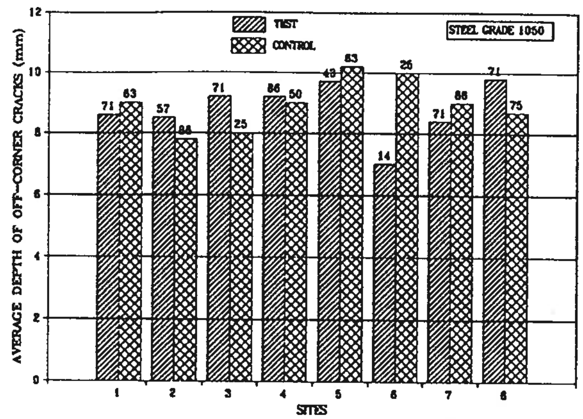

Figure 5.42 Bar graph showing average depth of off-corner, internal cracks at the eight off-corner sites on the test and control strand for a 1050 grade billet from Company E. (Note: Numbers on the top of the bars represent percentage of billets with cracks

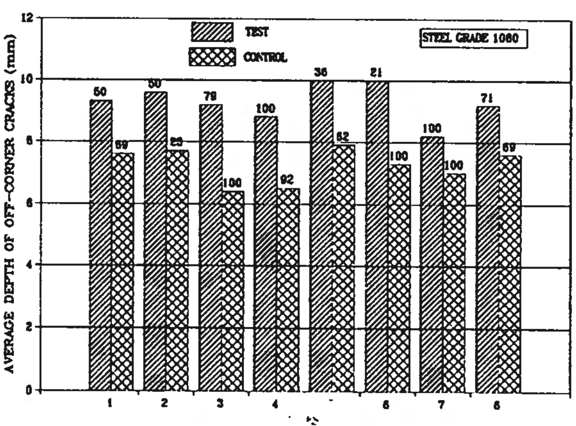

Figure 5.43 Bar graph showing average depth of off-corner, internal cracks at the eight off-corner sites on the test and control strand for a 1080 grade billet from Company E. (Note: Numbers on the top of the bars represent percentage of billets with cracks

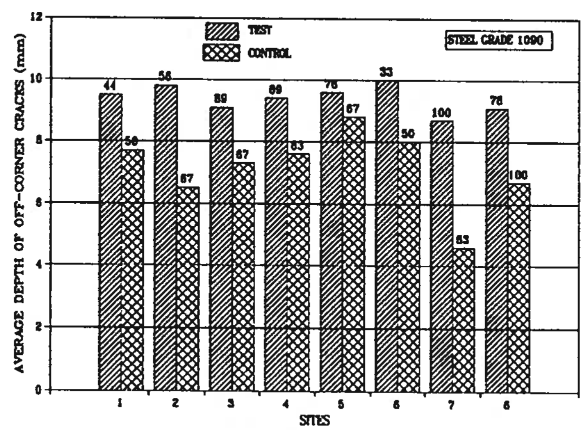

Figure 5.44 Bar graph showing average depth of off-corner, internal cracks at the eight off-corner sites on the test and control strand for a 1090 grade billet from Company E. (Note: Numbers on the top of the bars represent percentage of billets with cracks

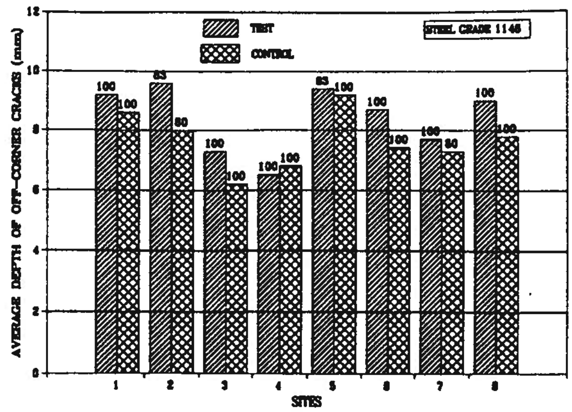

Figure 5.45 Bar graph showing average depth of off-corner, internal cracks at eight off-corner sites on the test and control strand for a 1146 grade billet from Company E. (Note: Numbers on the top of the bars represent percentage of billets with cracks).

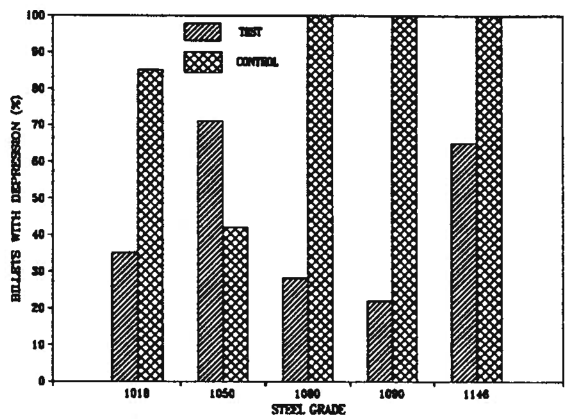

Figure 5.46 Bar graph showing longitudinal off-corner depressions on the test and control strand for 1018, 1050, 1080, 1090 and 1146 grade of billets from Company E.

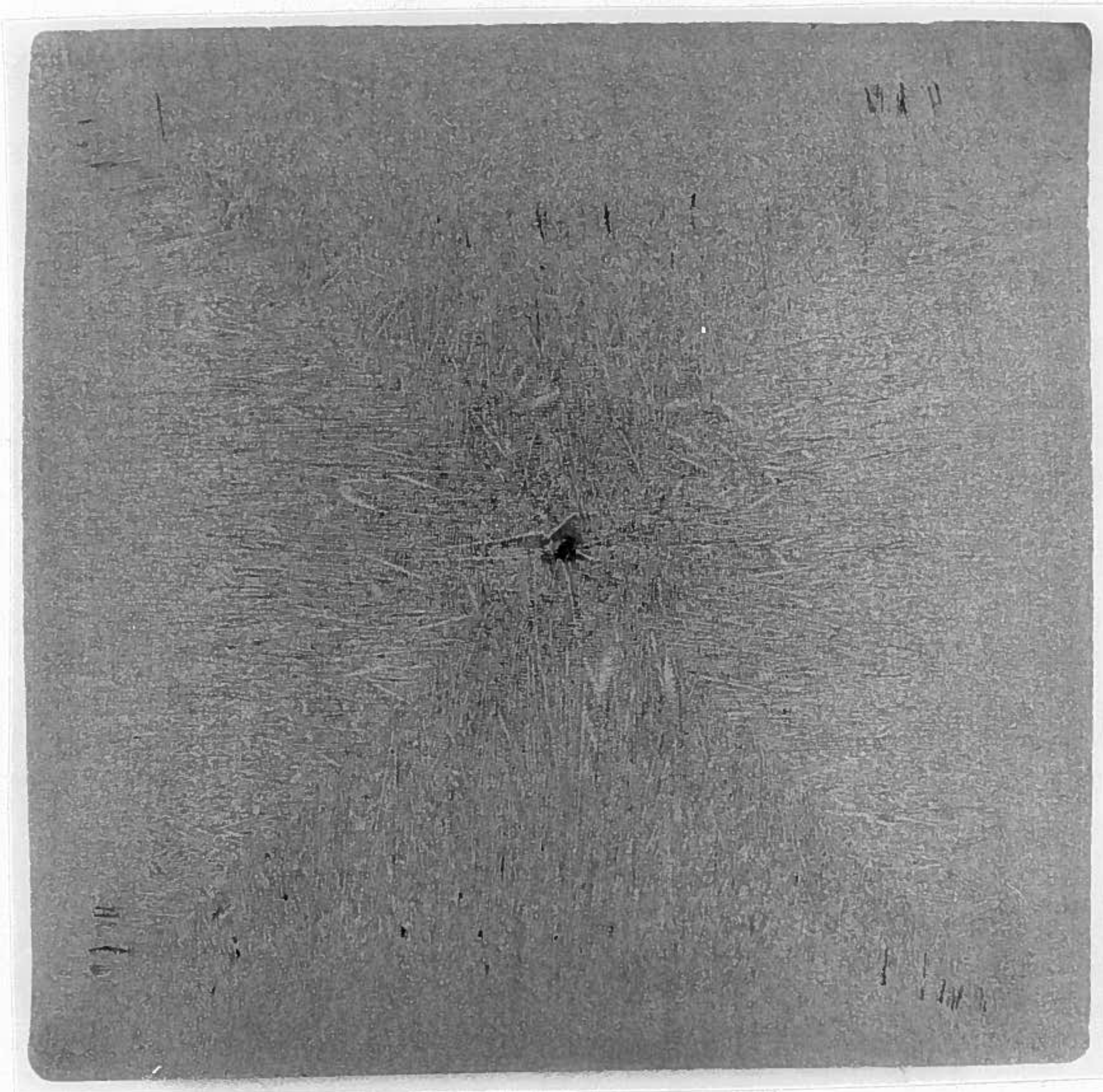

Figure 5.47 Macro-etch of a transverse section of a 1045 grade billet from Company C showing typical off-corner, internal cracks (Mag. 1.0 X).

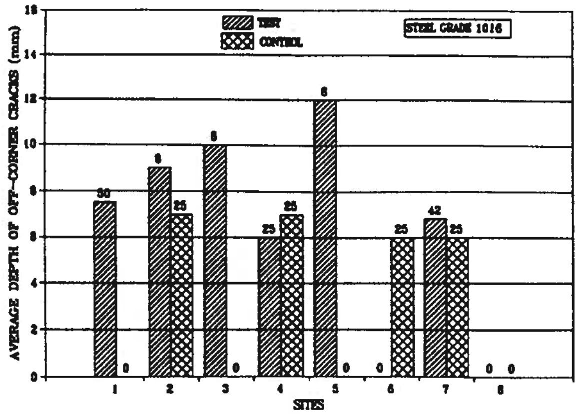

Figure 5.48 Bar graph showing average depth of off-corner, internal cracks at the eight off-corner sites on the test and control strand for a 1018 grade billet from Company C. (Note: Numbers on the top of bars represent percentage of billets with cracks).

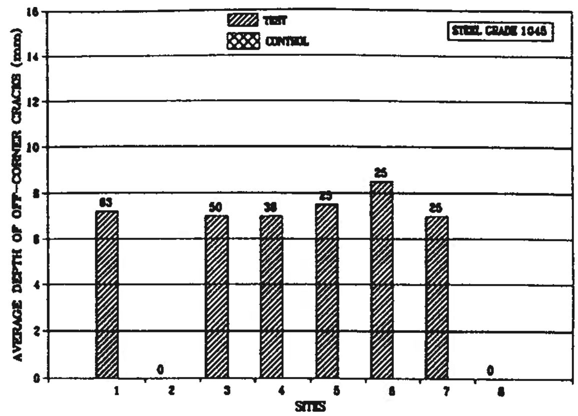

Figure 5.49 Bar graph showing average depth of off-corner, internal cracks at the eight off-corner sites on the test and control strand for a 1045 grade billet from Company C. (Note: Numbers on the top of bars represent percentage of billets with cracks).

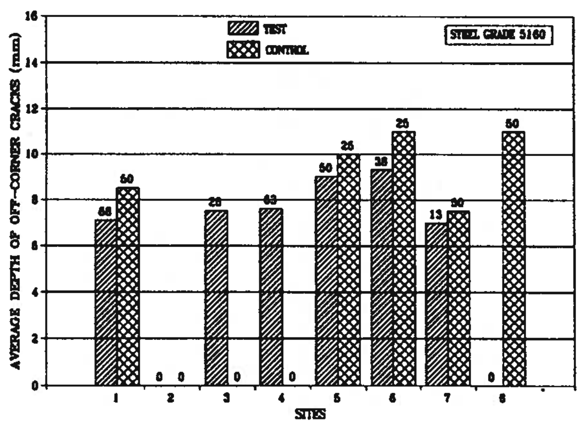

Figure 5.50 Bar graph showing average depth of off-corner, internal cracks at the eight off-corner sites on the test and control strand for a 5160 grade billet from Company C. (Note: Numbers on the top of bars represent percentage of billets with cracks).

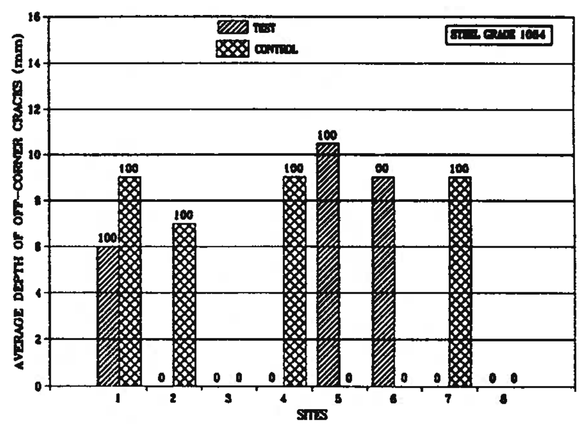

Figure 5.51 Bar graph showing average depth of off-corner, internal cracks at the eight off-corner sites on the test and control strand for a 1084 grade billet from Company C. (Note: Numbers on the top of bars represent percentage of billets with cracks).

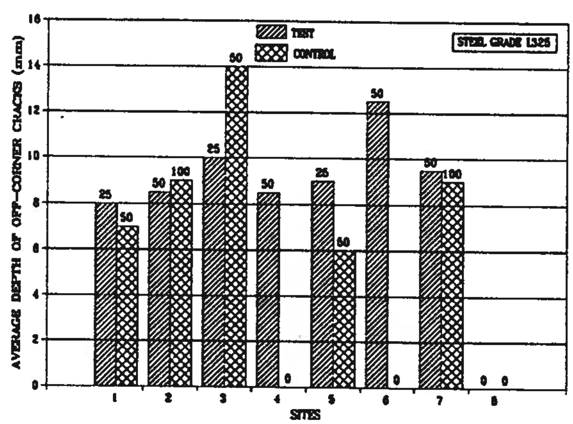

Figure 5.52 Bar graph showing average depth of off-corner, internal cracks at eight off-corner sites on the test and control strand for a L-325 grade billet from Company C. (Note: Numbers on the top of bars represent percentage of billets with cracks).

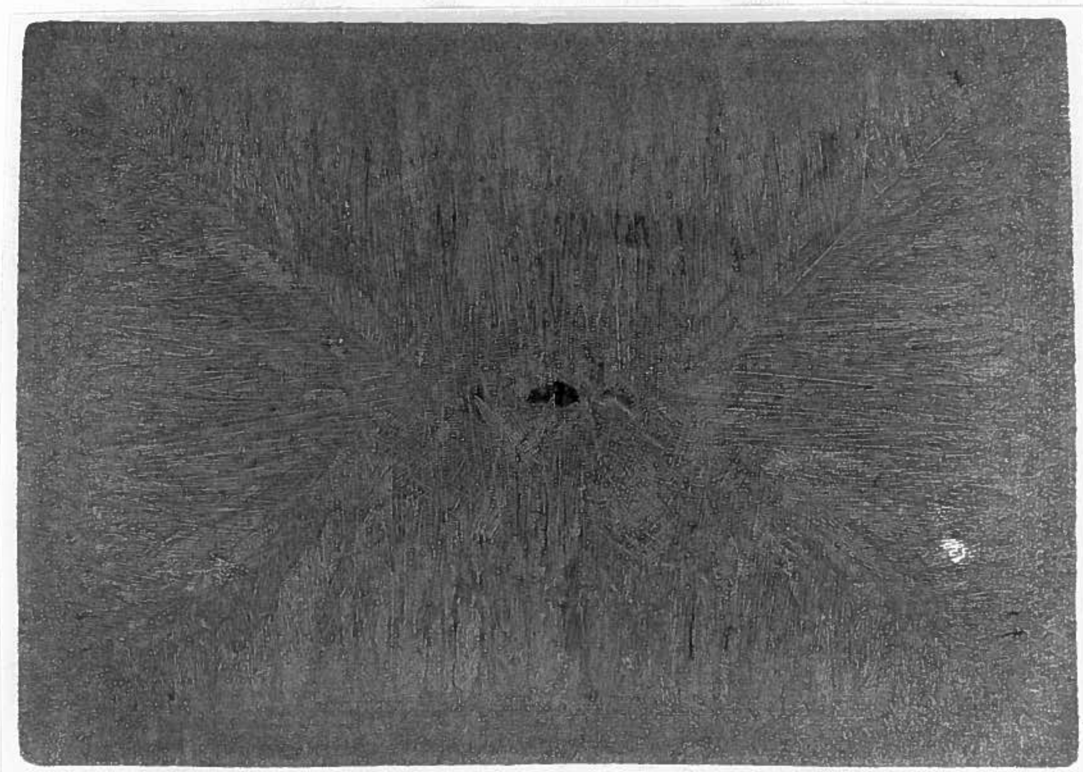

Figure 5.53 Macro-etch of a transverse section of a 1018 grade billet from Company E showing typical mid-way cracks (Mag. 0.8 X).

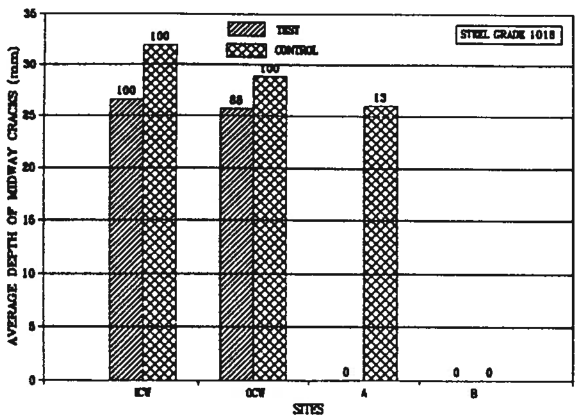

Figure 5.54 Bar graph showing average depth of mid-way cracks at four locations on the test and control strand for a 1018 grade billet from Company E. (Note: Numbers on top of bars represent percentage of billets with cracks).

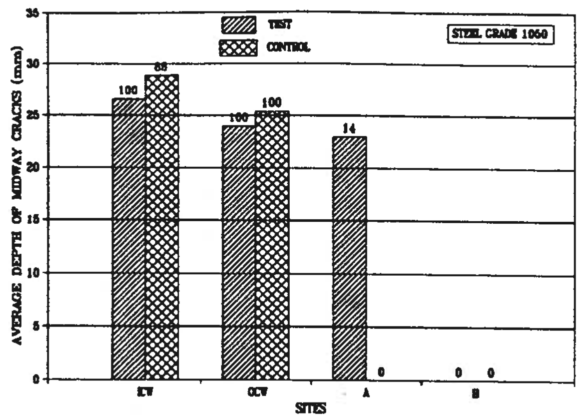

Figure 5.55 Bar graph showing average depth of mid-way cracks at four locations on the test and control strand for a 1050 grade billet from Company E. (Note: Numbers on top of bars represent percentage of billets with cracks).

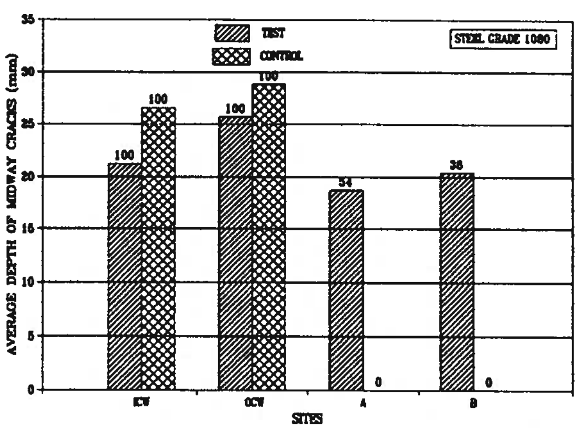

Figure 5.56 Bar graph showing average depth of mid-way cracks at four locations on the test and control strand for a 1080 grade billet from Company E. (Note: Numbers on top of bars represent percentage of billets with cracks).

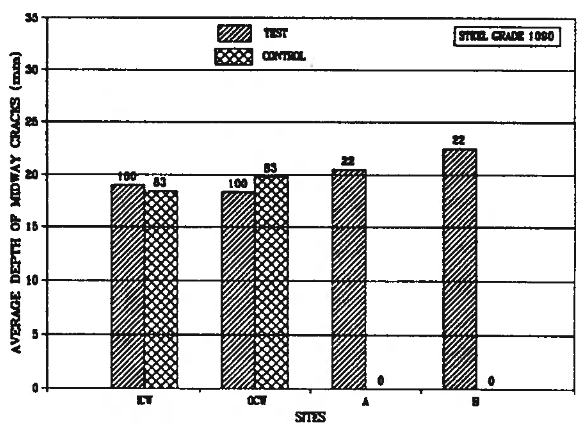

Figure 5.57 Bar graph showing average depth of mid-way cracks at four locations on the test and control strand for a 1090 grade billet from Company E. (Note: Numbers on top of bars represent percentage of billets with cracks).

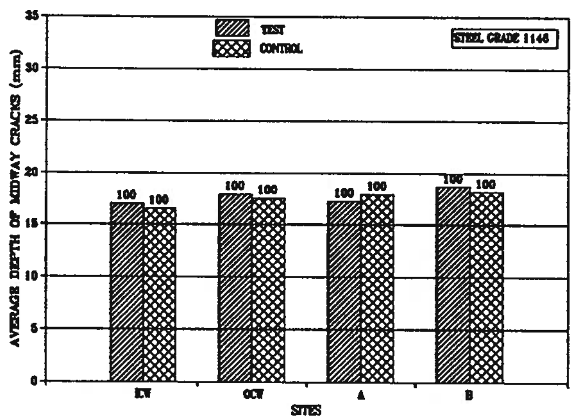

Figure 5.58 Bar graph showing average depth of mid-way cracks at four locations on the test and control strand for a 1146 grade billet from Company E. (Note: Numbers on top of bars represent percentage of billets with cracks).

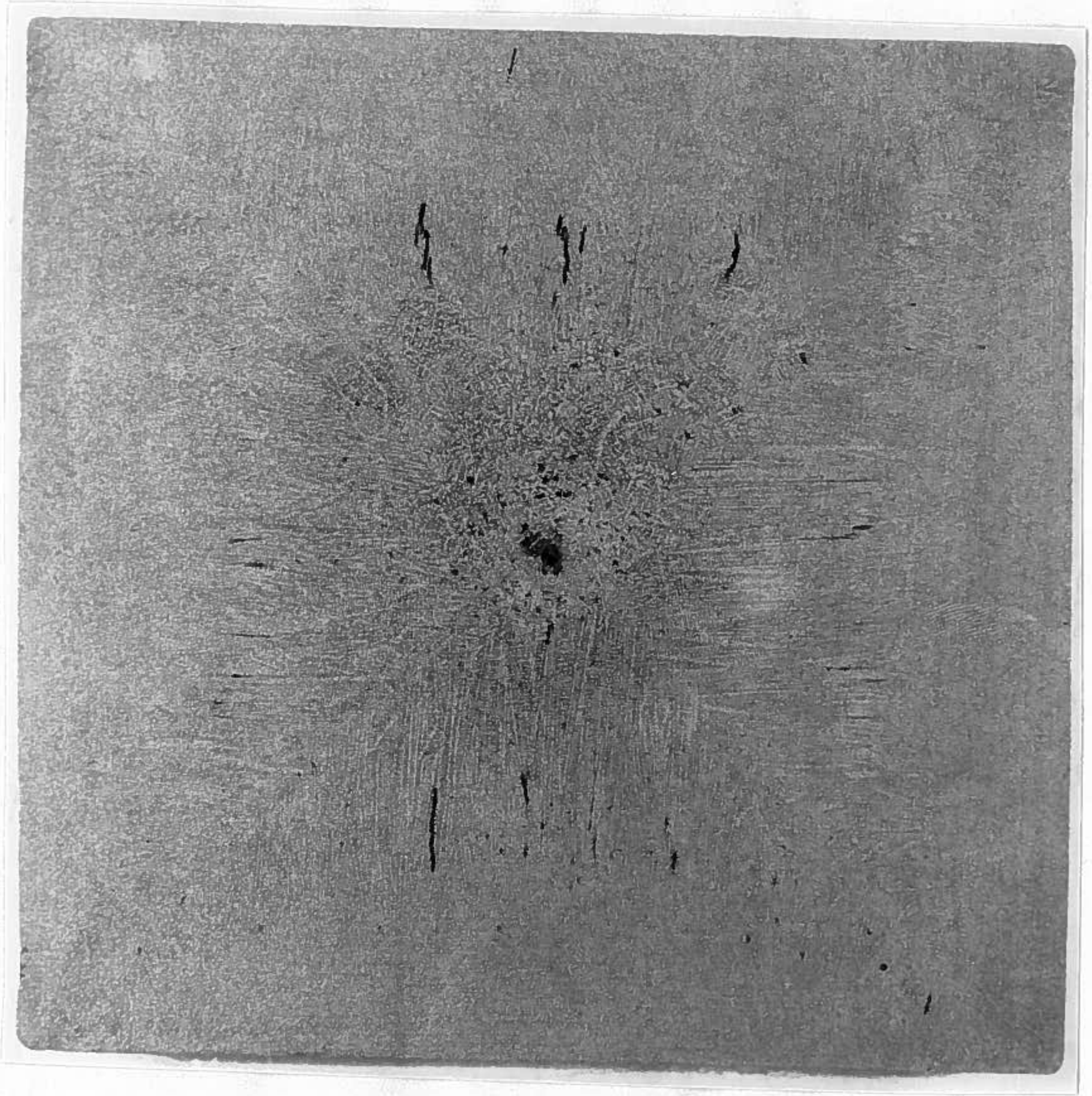

Figure 5.59 Macro-etch of a transverse section of a 1018 grade billet from Company C showing typical mid-way cracks (Mag. 1.0 X).

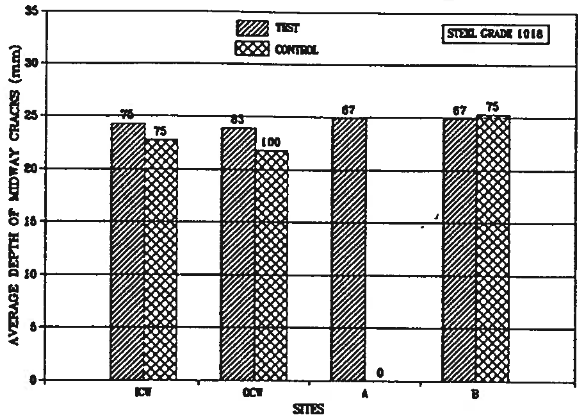

Figure 5.60 Bar graph showing average depth of midway cracks at four locations on the test and control strand for a 1018 grade billet from Company C. (Note : Numbers on the top of the bars represent percentage of billets with cracks).

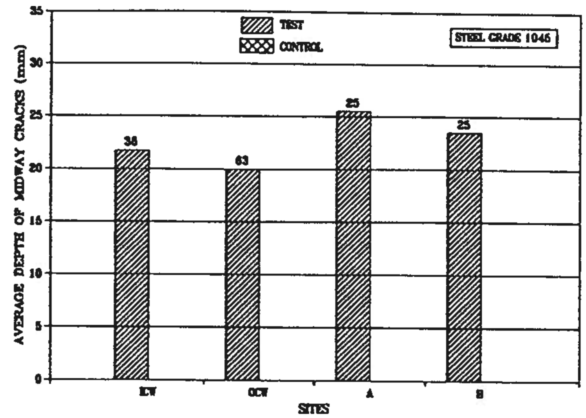

Figure 5.61 Bar graph showing average depth of midway cracks at four locations on the test and control strand for a 1045 grade billet from Company C. (Note : Numbers on the top of the bars represent percentage of billets with cracks).

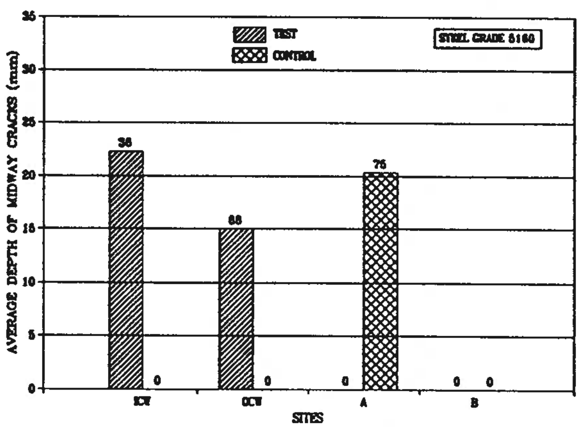

Figure 5.62 Bar graph showing average depth of midway cracks at four locations on the test and control strand for a 5160 grade billet from Company C. (Note : Numbers on the top of the bars represent percentage of billets with cracks).

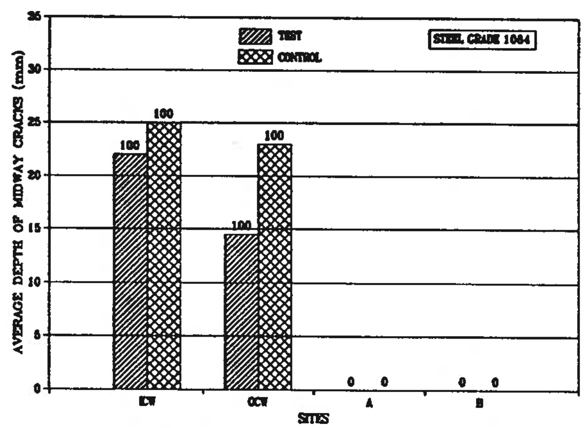

Figure 5.63 Bar graph showing average depth of midway cracks at four locations on the test and control strand for a 1084 grade billet from Company C. (Note : Numbers on the top of the bars represent percentage of billets with cracks).

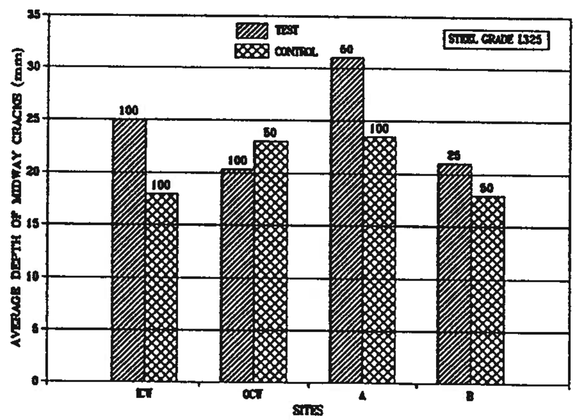

Figure 5.64 Bar graph showing average depth of mid-way cracks at four locations on the test and control strand for a L-325 grade billet from Company C. (Note: Numbers on top of bars represent percentage of billets with cracks).

Figure 5.65 Photograph of the surface of a 1008 grade billet from Company B (Mag. 1.0 X).

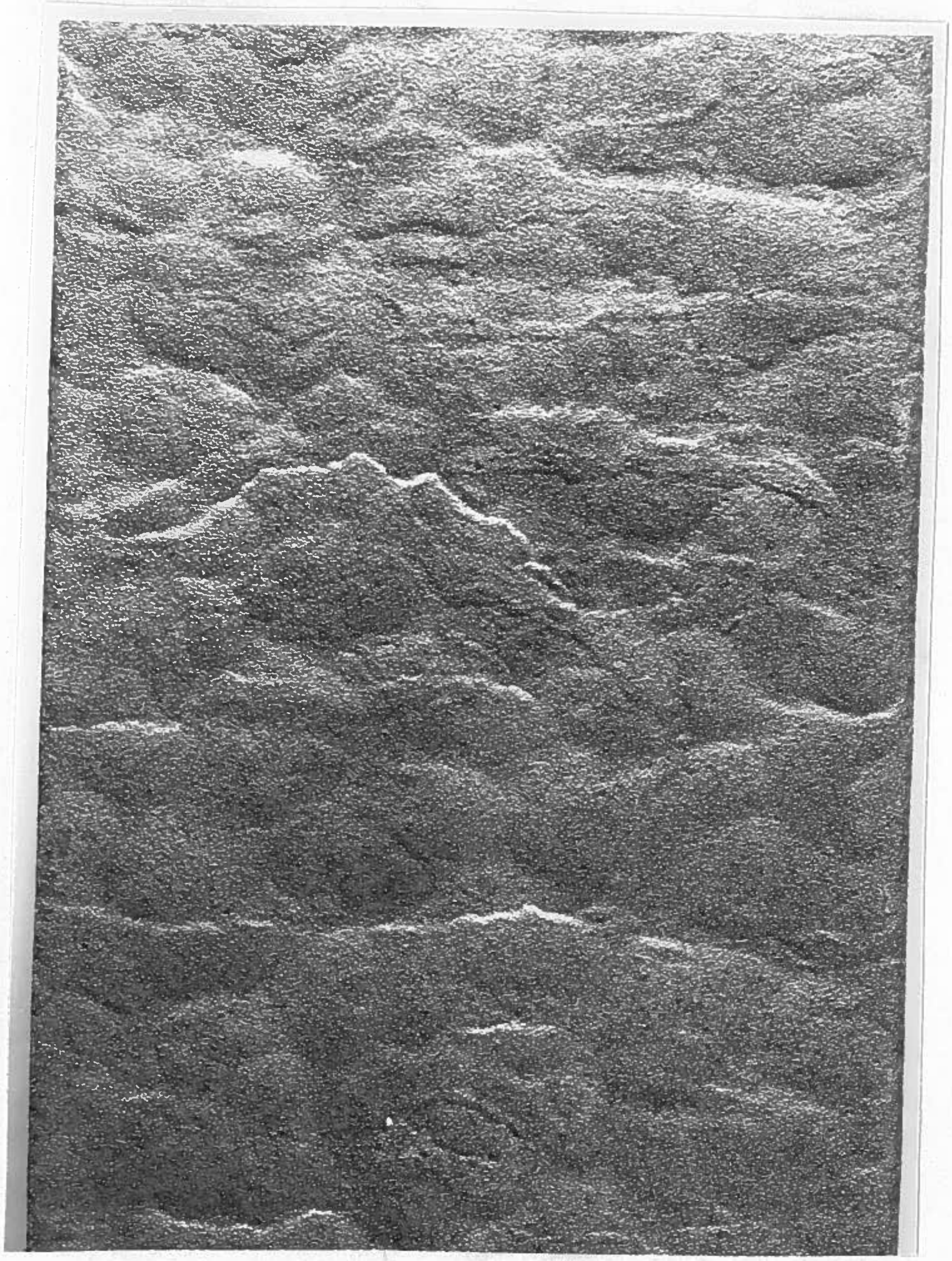

Figure 5.66 Photograph of the surface of a 1012 grade billet from Company B (Mag. 1.0 X).

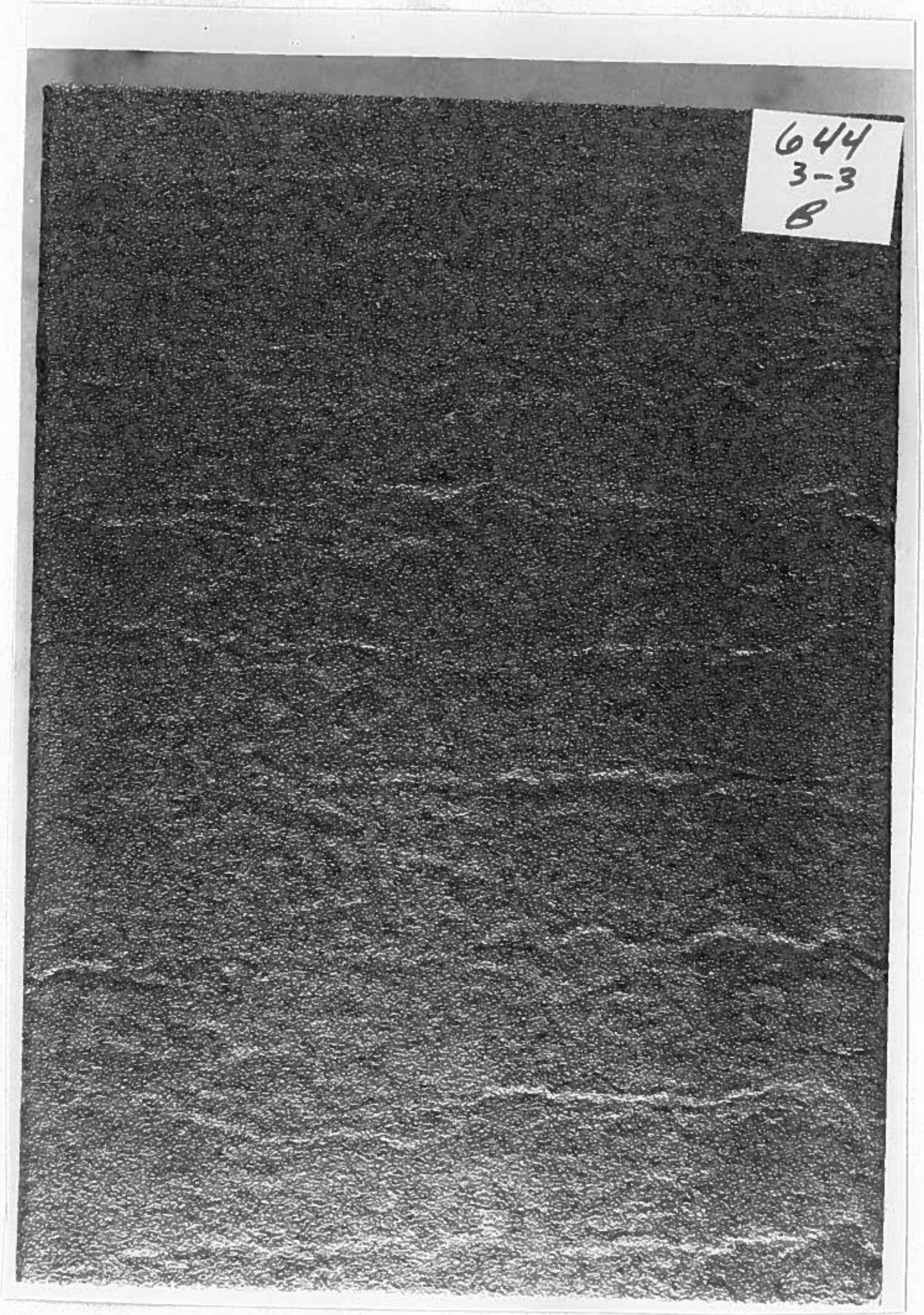

Figure 5.67 Photograph of the surface of a 1039 grade billet from Company B (Mag. 1.0 X).

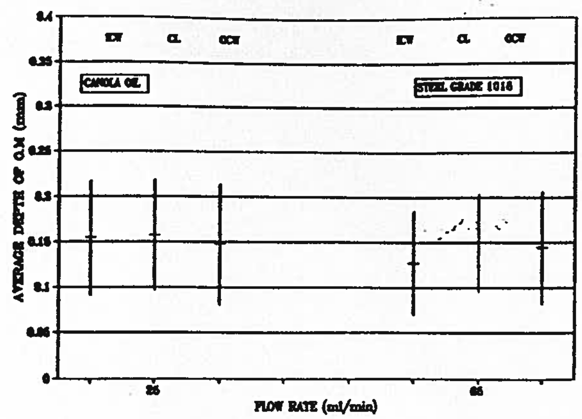

Figure 5.68 Graph showing the influence of oil flow rate on oscillation mark depth of a 1018 grade test strand billet cast with Canola oil at Company E.

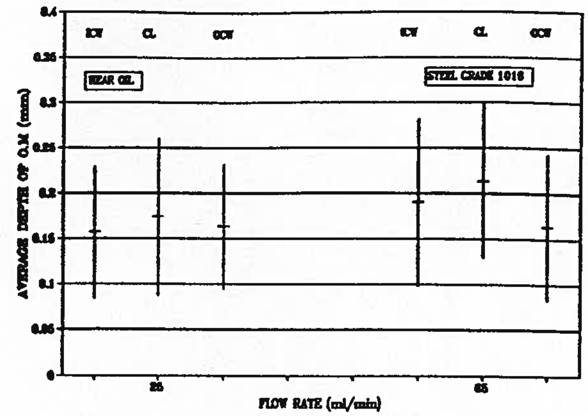

Figure 5.69 Graph showing the influence of oil flow rate on oscillation mark depth of a 1018 grade test strand billet cast with HEAR oil at Company E.

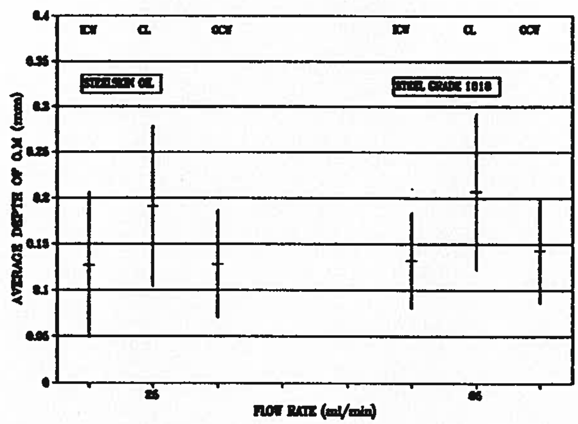

Figure 5.70 Graph showing the influence of oil flow rate on oscillation mark depth of a 1018 grade test strand billet cast with Mineral_S oil at Company E.

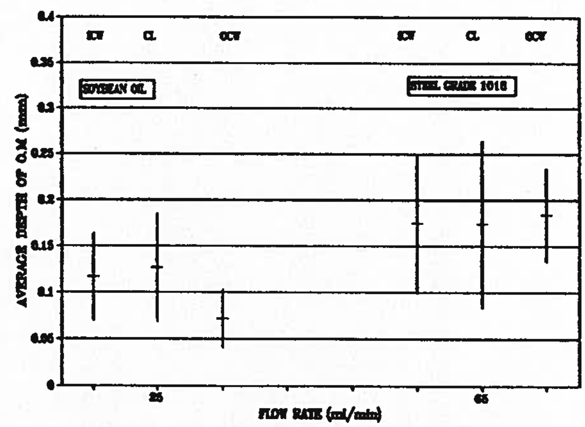

Figure 5.71 Graph showing the influence of oil flow rate on oscillation mark depth of a 1018 grade test strand billet cast with Soybean oil at Company E.

Figure 5.72 Photograph of the surface of a 1018 grade billet cast on the test strand with Canola oil at 65 ml/min at Company E (Mag. 1.0 X).

Figure 5.73 Photograph of the surface of a 1018 grade billet cast on the test strand with HEAR oil at 65 ml/min at Company E (Mag. 1.0 X).

Figure 5.74 Photograph of the surface of a 1018 grade billet cast on the test strand with Mineral_S oil at 65 ml/min at Company E (Mag. 1.0 X).

Figure 5.75 Photograph of the surface of a 1018 grade billet cast on the test strand with Soybean oil at 65 ml/min at Company E (Mag. 1.0 X).

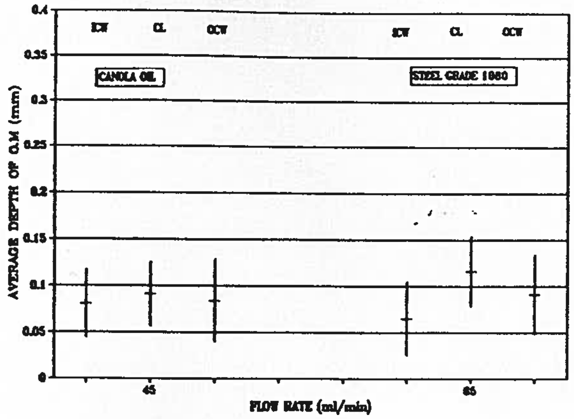

Figure 5.76 Graph showing the influence of oil flow rate on oscillation mark depth of a 1080 grade test strand billet cast with Canola oil at Company E.

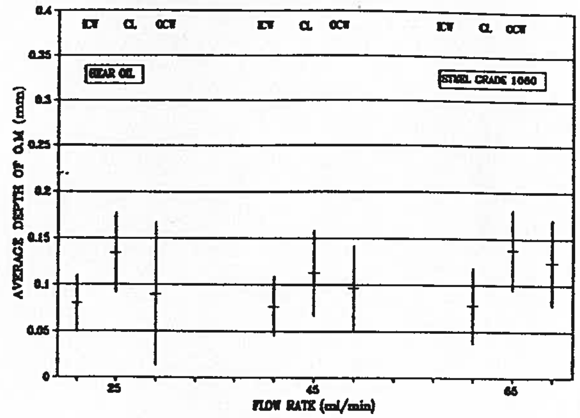

Figure 5.77 Graph showing the influence of oil flow rate on oscillation mark depth of a 1080 grade test strand billet cast with HEAR oil at Company E.

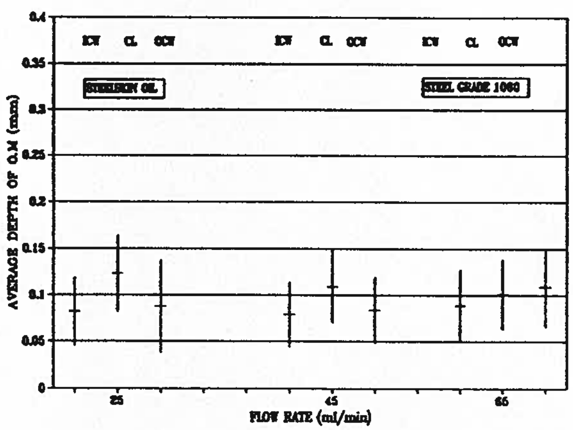

Figure 5.78 Graph showing the influence of oil flow rate on oscillation mark depth of a 1080 grade test strand billet cast with Mineral_S oil at Company E.

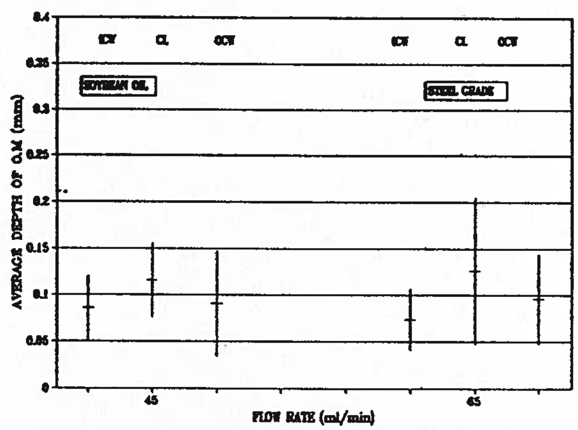

Figure 5.79 Graph showing the influence of oil flow rate on oscillation mark depth of a 1080 grade test strand billet cast with Soybean oil at Company E.

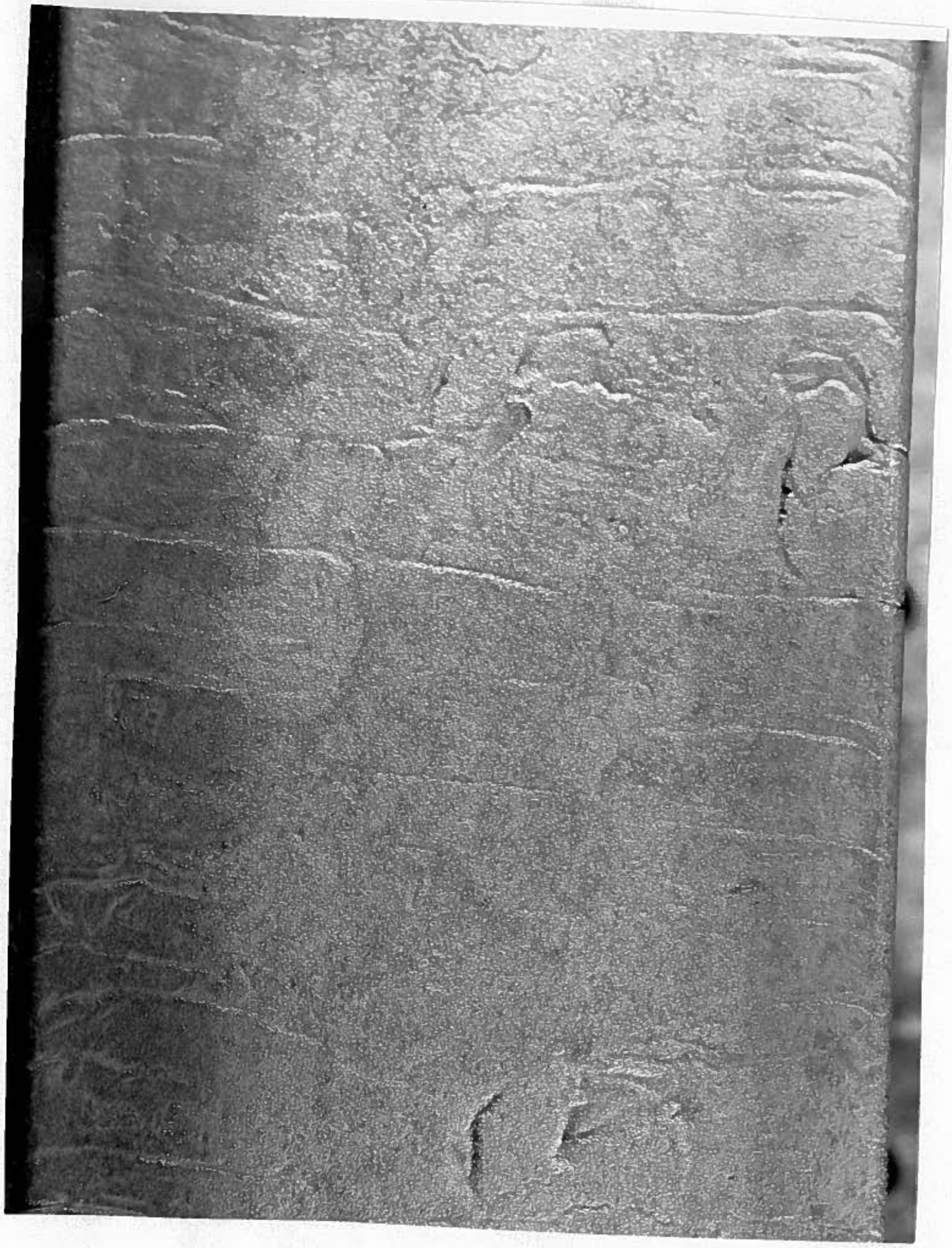

Figure 5.80 Photograph of the surface of a 1080 grade billet cast on the test strand with Canola oil at 45 ml/min at Company E (Mag. 1.0 X).

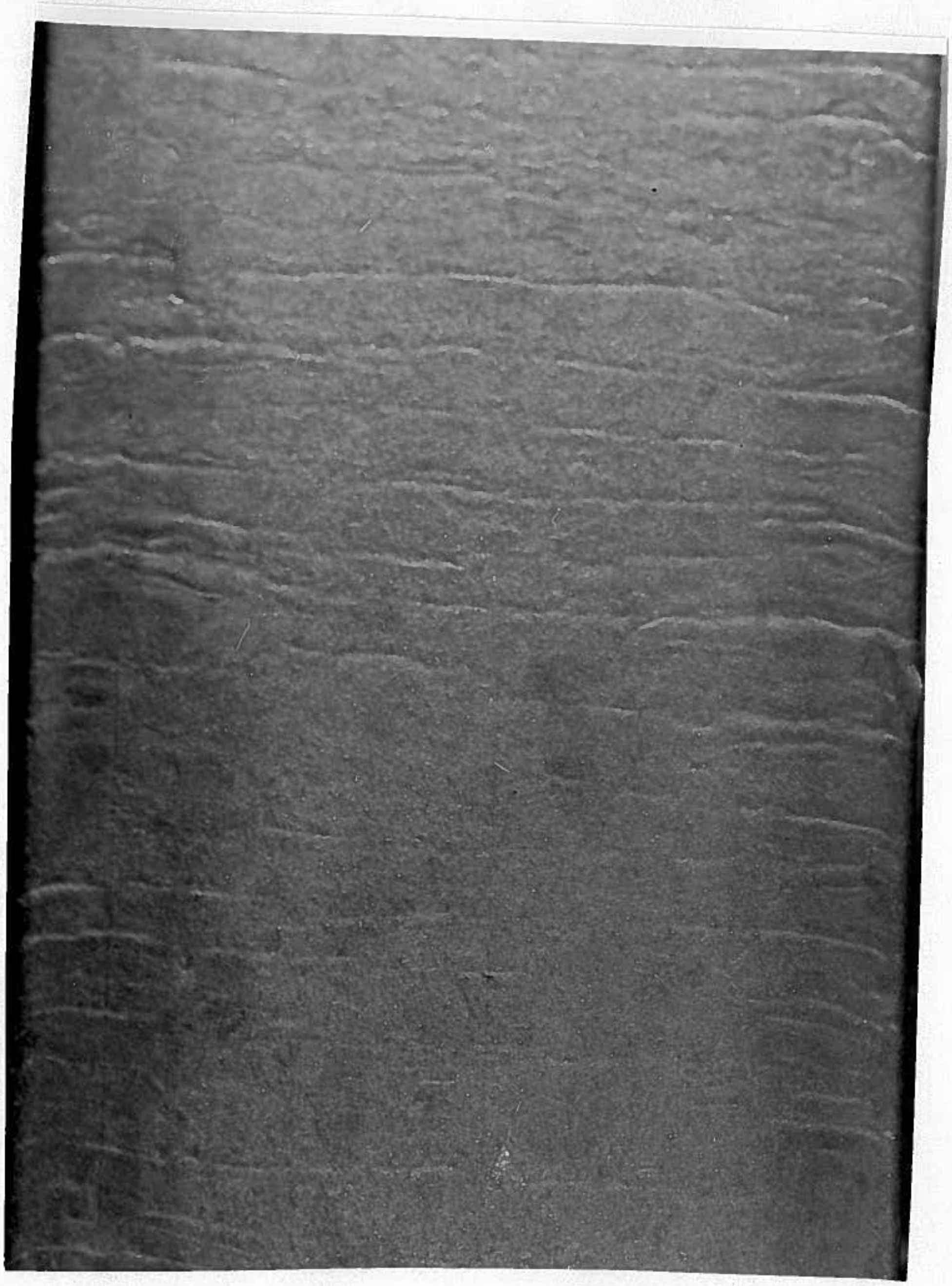

Figure 5.81 Photograph of the surface of a 1080 grade billet cast on the test strand with HEAR oil at 45 ml/min at Company E (Mag. 1.0 X).

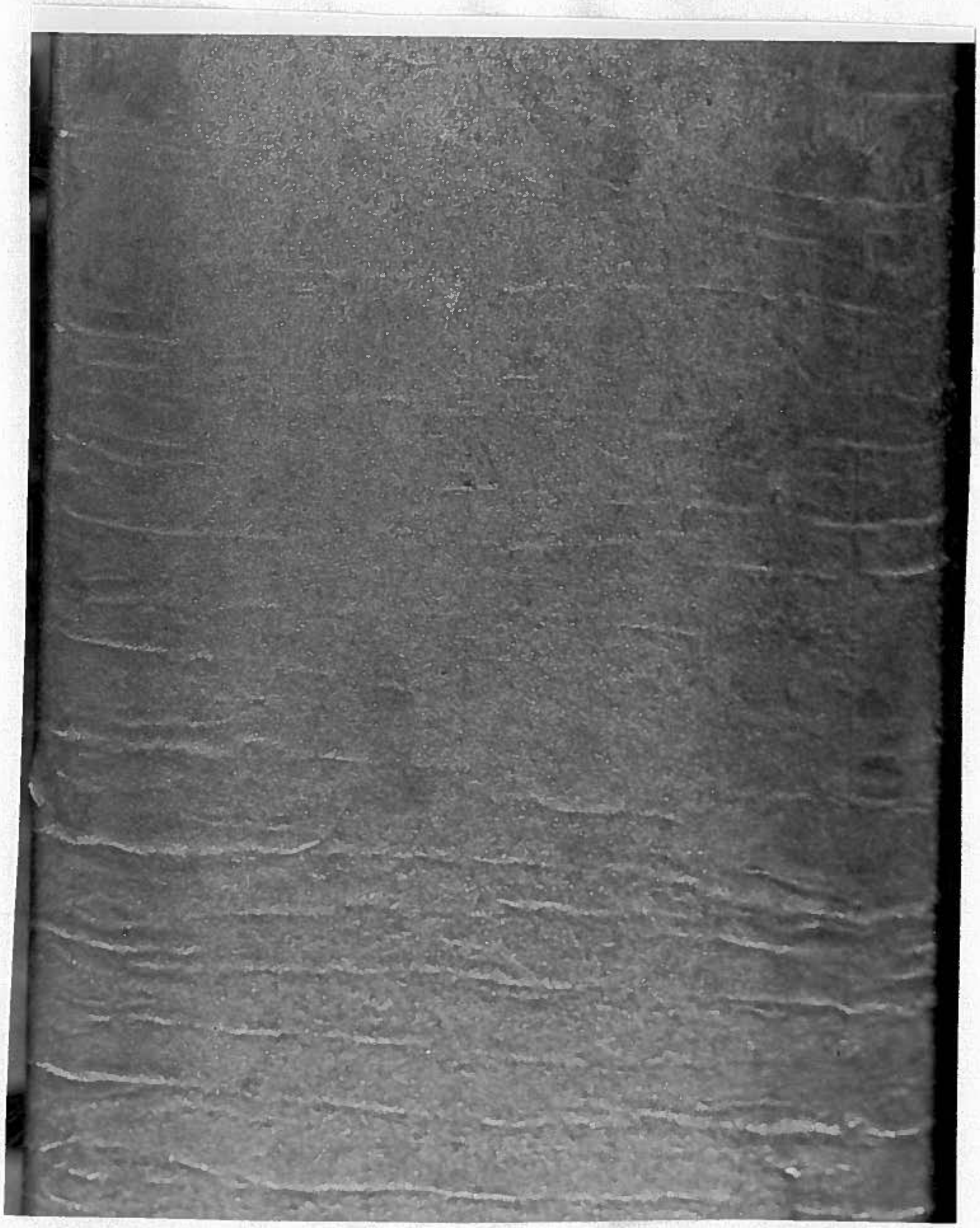

Figure 5.82 Photograph of the surface of a 1080 grade billet cast on the test strand with Mineral_S oil at 45 ml/min at Company E (Mag. 1.0 X).

Figure 5.83 Photograph of the surface of a 1080 grade billet cast on the test strand with Soybean oil at 45 ml/min at Company E (Mag. 1.0 X).

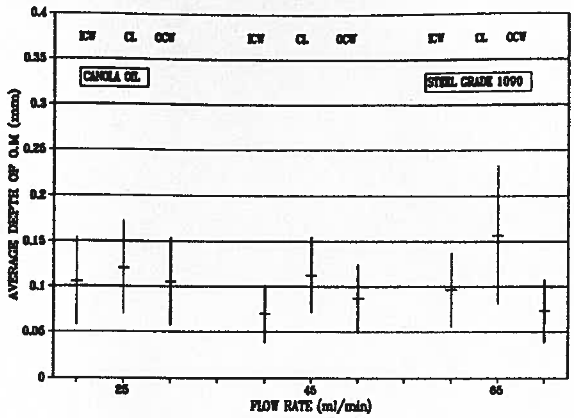

Figure 5.84 Graph showing the influence of oil flow rate on oscillation mark depth of a 1090 grade test strand billet cast with Canola oil at Company E.

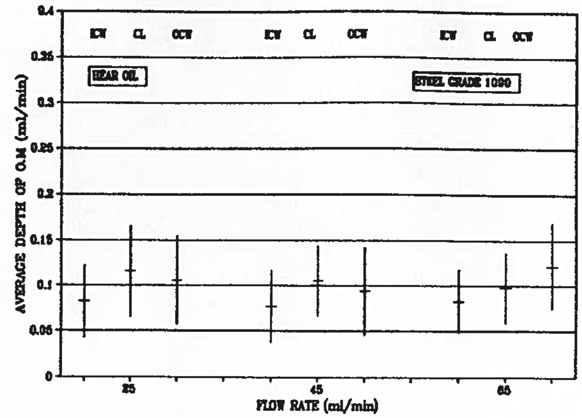

Figure 5.85 Graph showing the influence of oil flow rate on oscillation mark depth of a 1090 grade test strand billet cast with HEAR oil at Company E.

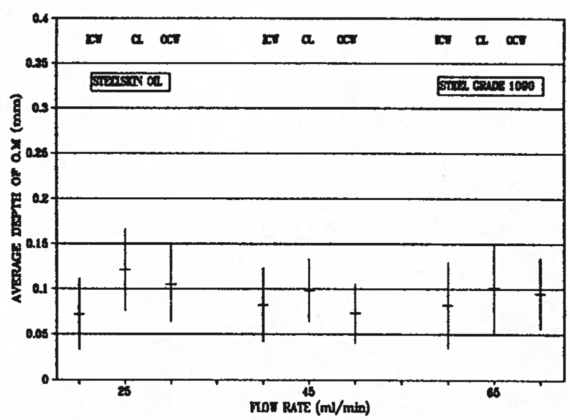

Figure 5.86 Graph showing the influence of oil flow rate on oscillation mark depth of a 1090 grade test strand billet cast with Mineral_S oil at Company E.

Figure 5.87 Photograph of the surface of a 1090 grade billet cast on the test strand with Canola oil at 45 ml/min at Company E (Mag. 1.0 X).

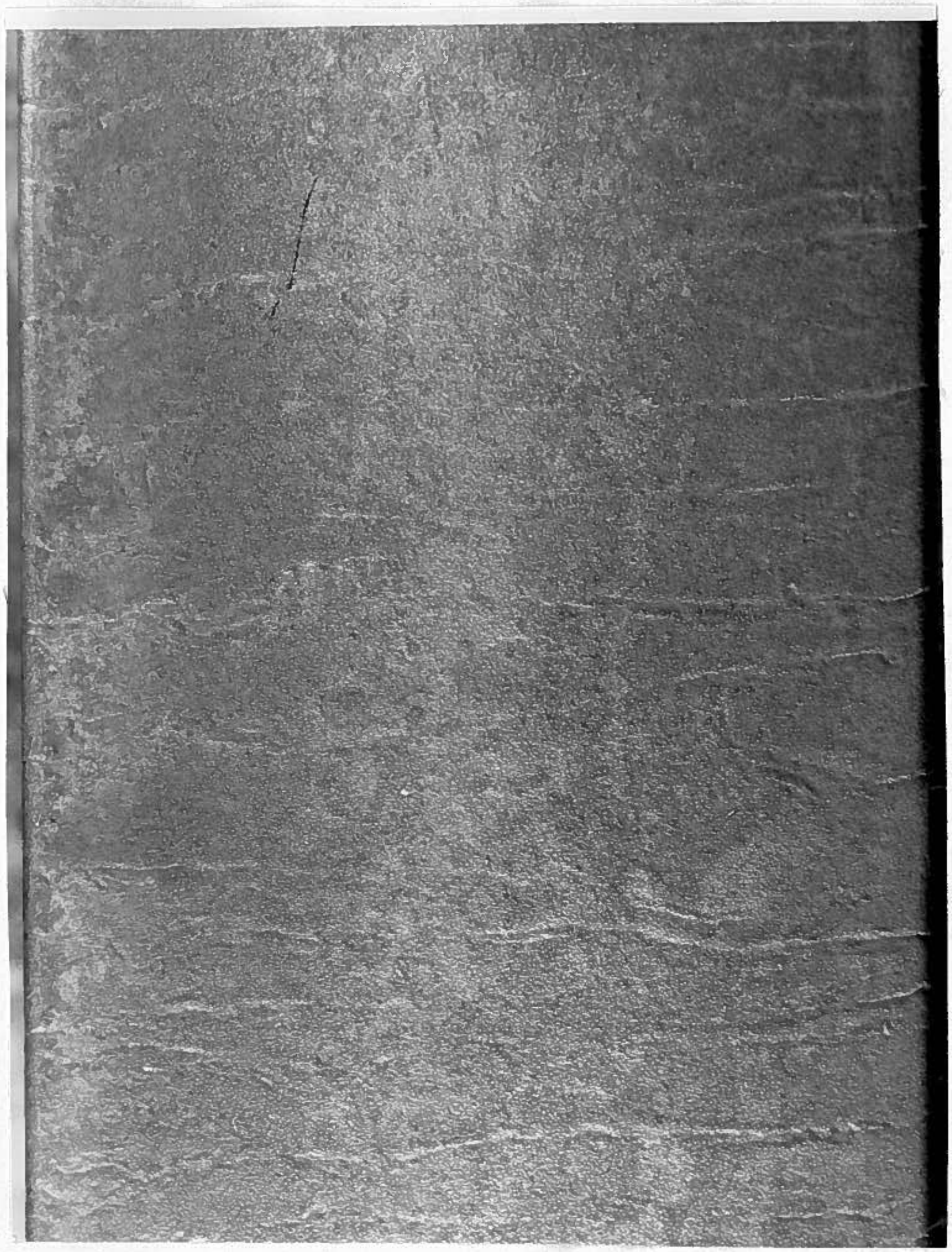

Figure 5.88 Photograph of the surface of a 1090 grade billet cast on the test strand with HEAR oil at 45 ml/min at Company E (Mag. 1.0 X).

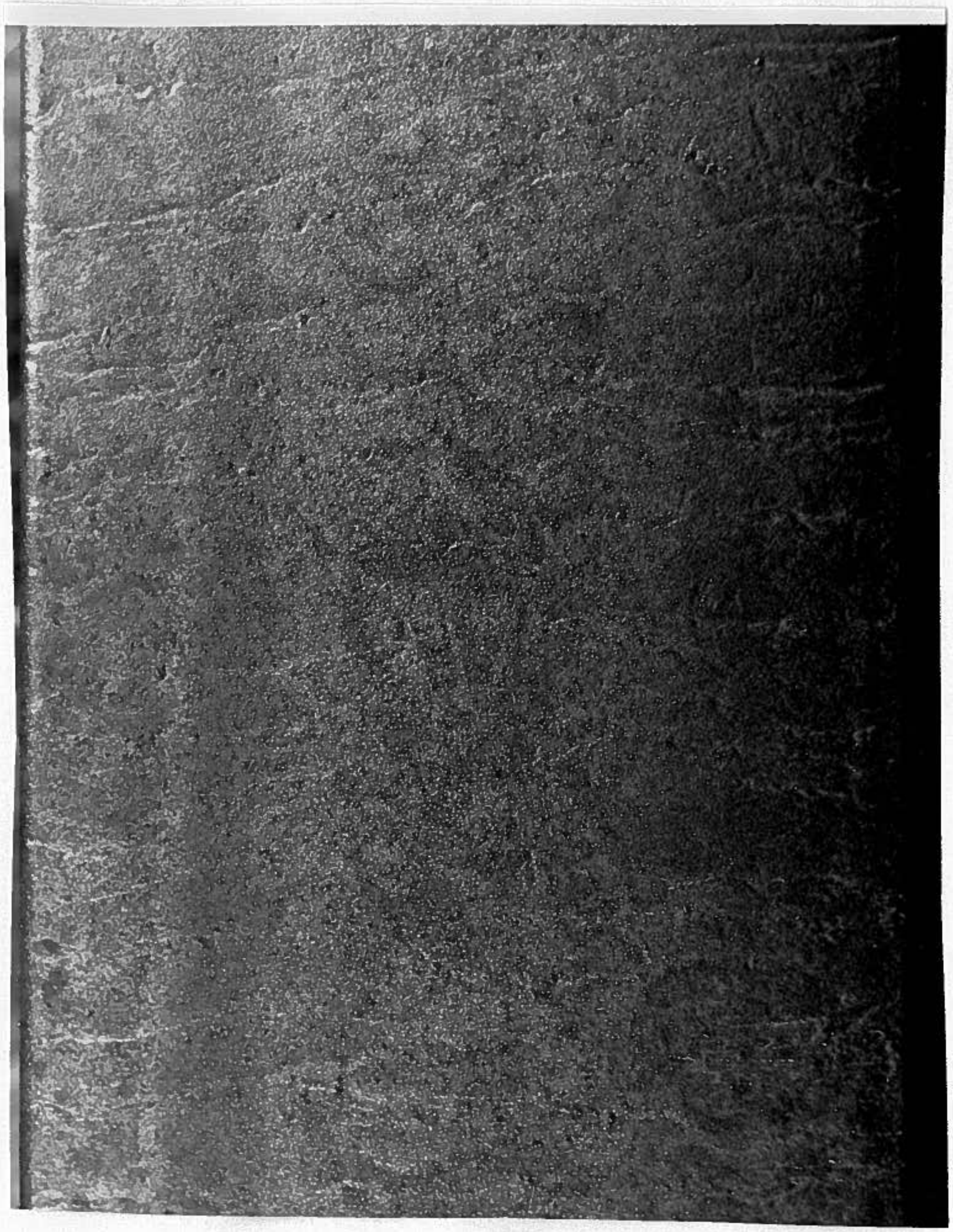

Figure 5.89 Photograph of the surface of a 1090 grade billet cast on the test strand with Mineral_S oil at 45 ml/min at Company E (Mag. 1.0 X).

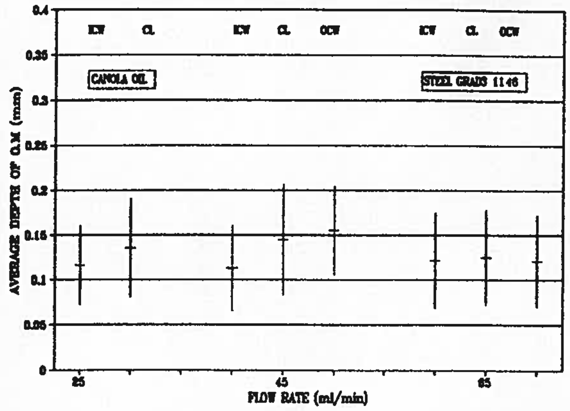

Figure 5.90 Graph showing the influence of oil flow rate on oscillation mark depth of a 1146 grade billet cast with Canola oil at Company E.

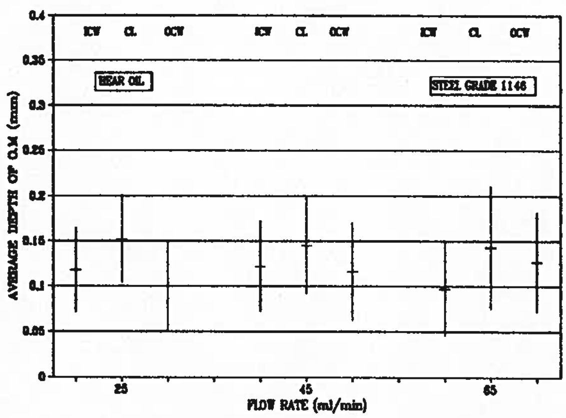

Figure 5.91 Graph showing the influence of oil flow rate on oscillation mark depth of a 1146 grade billet cast with HEAR oil at Company E.

Figure 5.92 Photograph of the surface of a 1146 grade test strand billet cast with Canola oil at 65 ml/min at Company E (Mag. 1.0 X).

Figure 5.93 Photograph of the surface of a 1146 grade test strand billet cast with HEAR oil at 65 ml/min at Company E (Mag. 1.0 X).

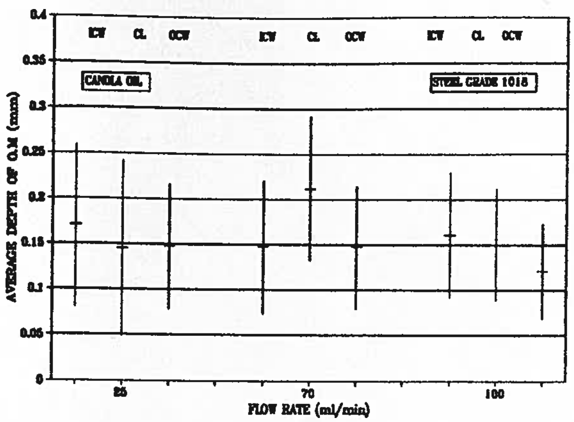

Figure 5.94 Graph showing the influence of oil flow rate on oscillation mark depth of a 1018 grade billet cast with Canola oil at Company C.

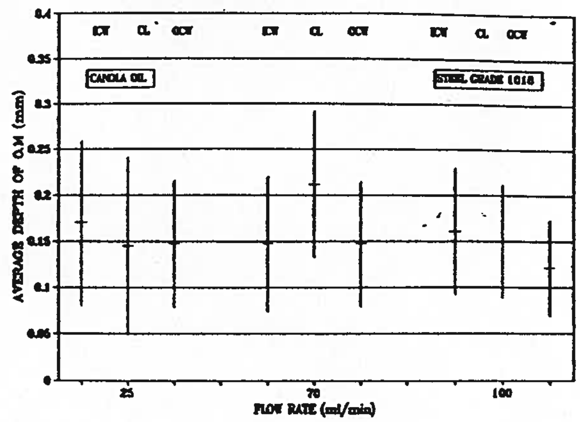

Figure 5.95 Graph showing the influence of oil flow rate on oscillation mark depth of a 1018 grade billet cast with HEAR oil at Company C.

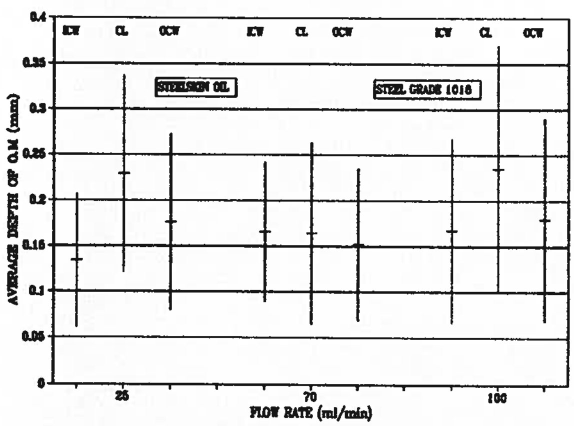

Figure 5.96 Graph showing the influence of oil flow rate on oscillation mark depth of a 1018 grade billet cast with Mineral_S oil at Company C.

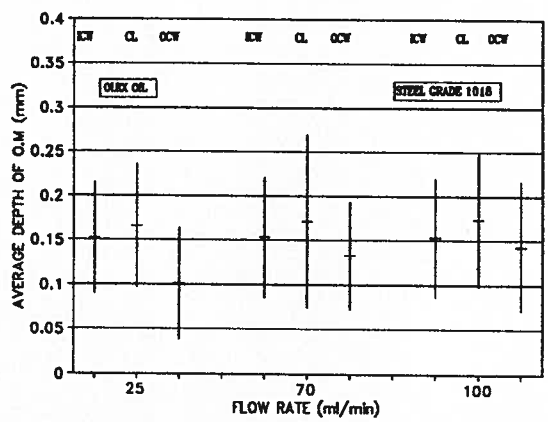

Figure 5.97 Graph showing the influence of oil flow rate on oscillation mark depth of a 1018 grade billet cast with Mineral_O oil at Company C.

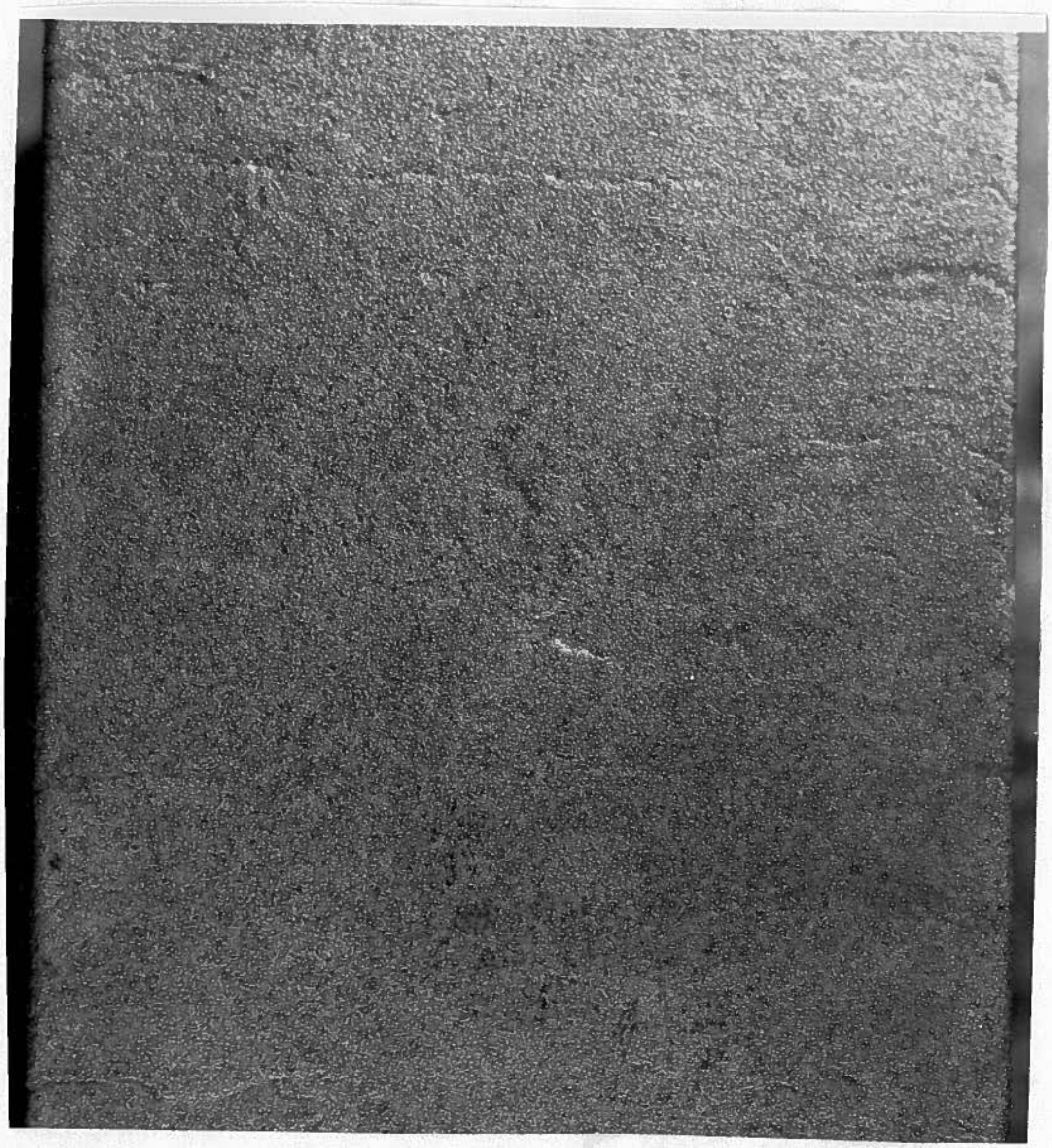

Figure 5.98 Photograph of the surface of a 1018 grade billet cast with Canola oil at 25 ml/min at Company C (Mag. 1.0 X).

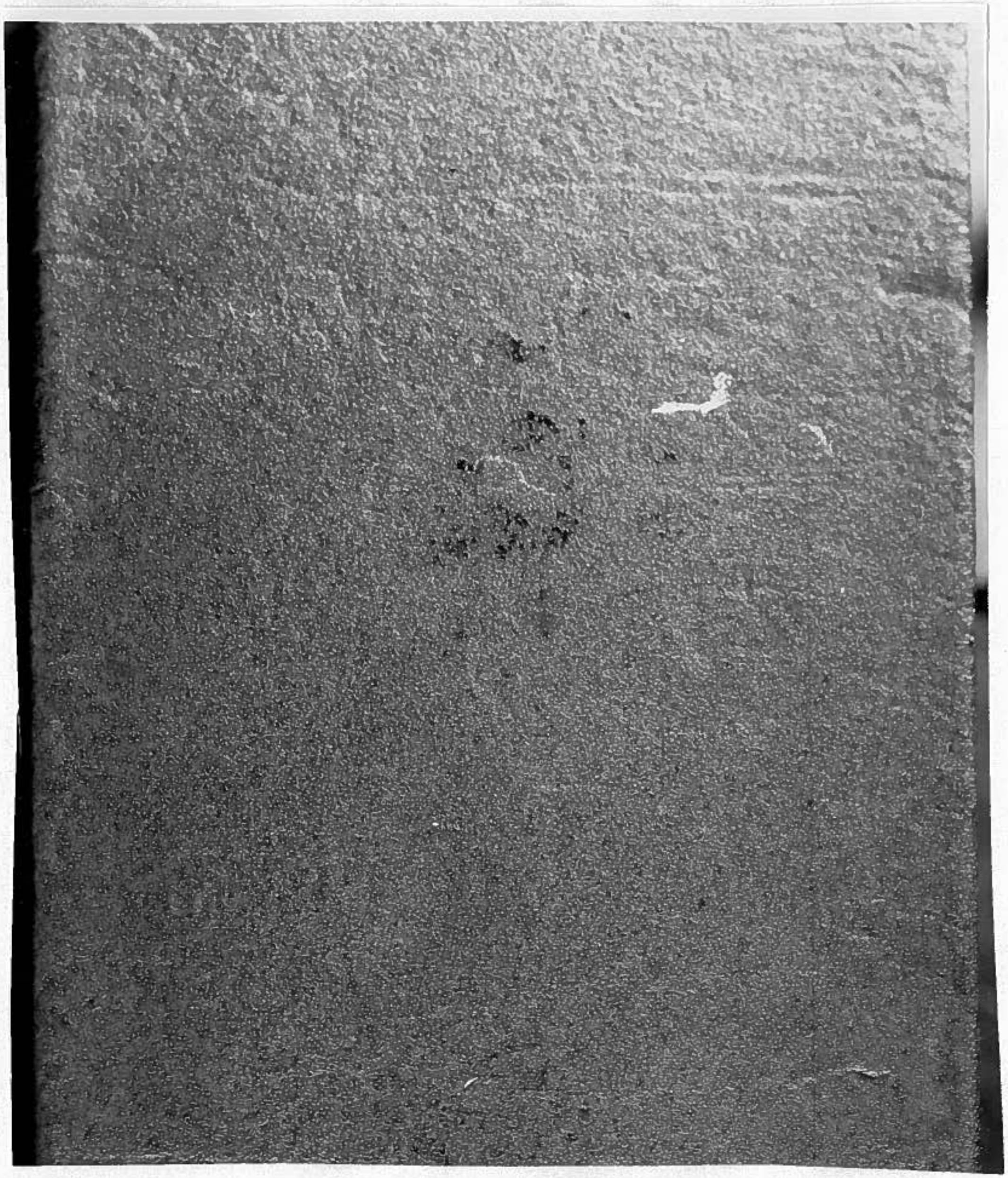

Figure 5.99 Photograph of the surface of a 1018 grade billet cast with HEAR oil at 25 ml/min at Company C (Mag. 1.0 X).

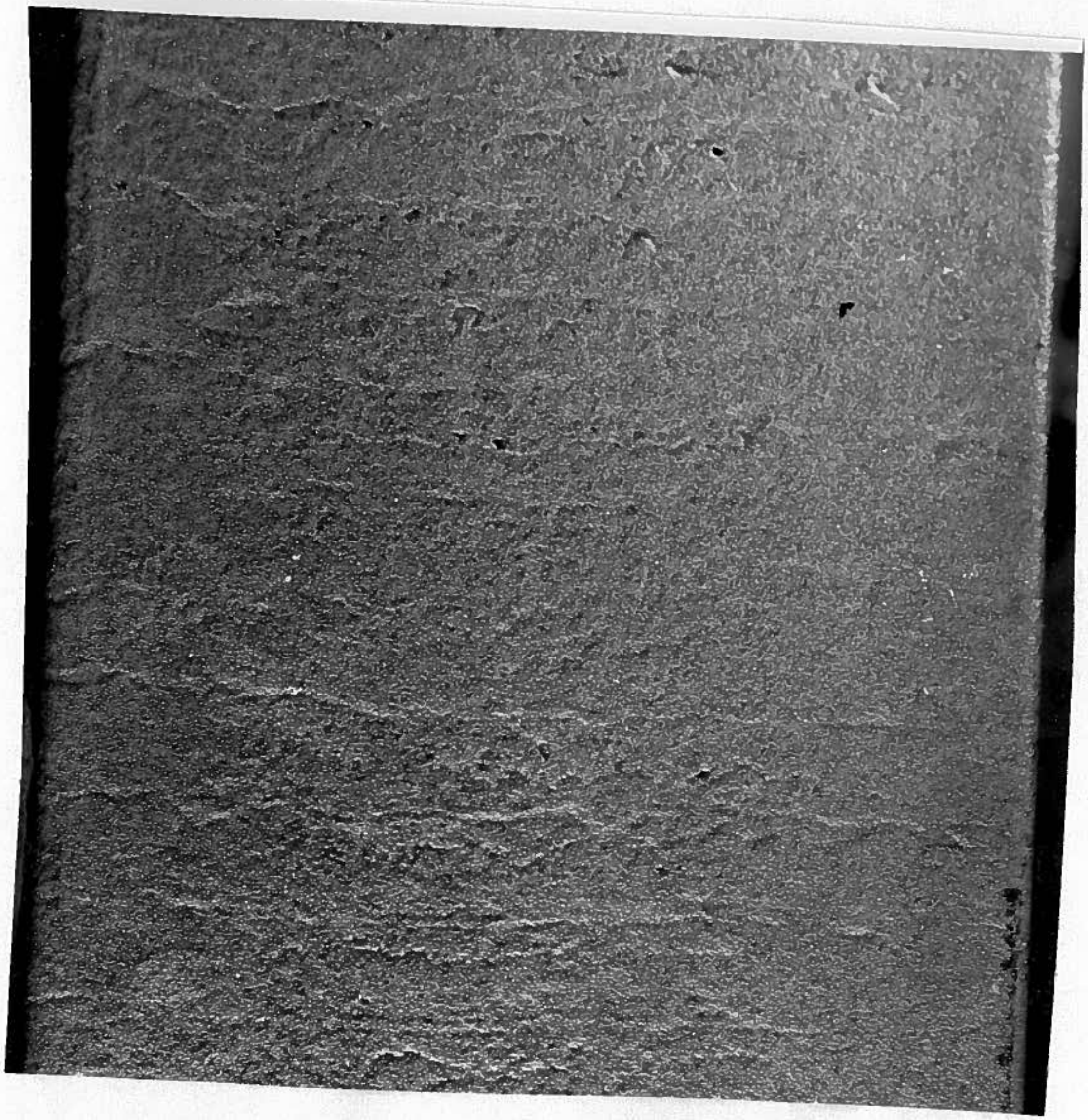

Figure 5.100 Photograph of the surface of a 1018 grade billet cast with Mineral_S oil at 25 ml/min at Company C (Mag. 1.0 X).

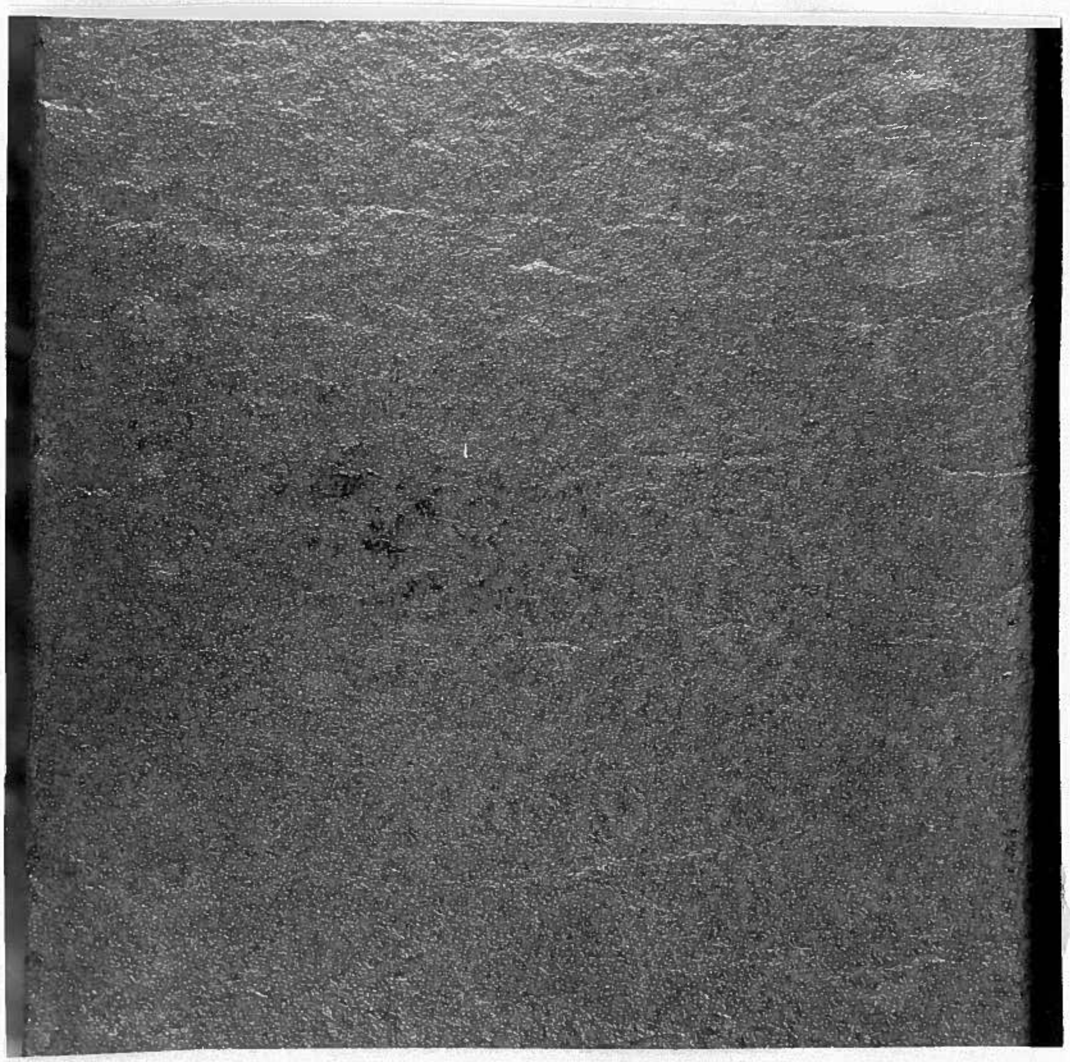

Figure 5.101 Photograph of the surface of a 1018 grade billet cast with Mineral_O oil at 25 ml/min at Company C (Mag. 1.0 X).

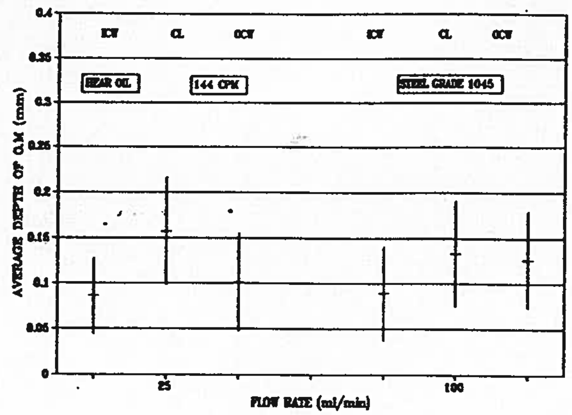

Figure 5.102 Graph showing the influence of oil flow rate on oscillation mark depth of a 1045 grade billet cast with HEAR oil at Company C.

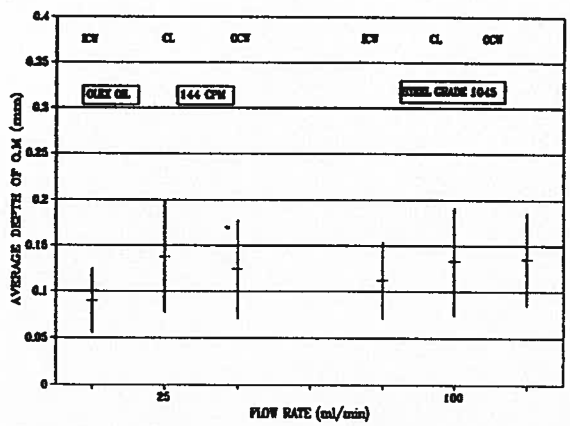

Figure 5.103 Graph showing the influence of oil flow rate on oscillation mark depth of a 1045 grade billet cast with Mineral_O oil at Company C.

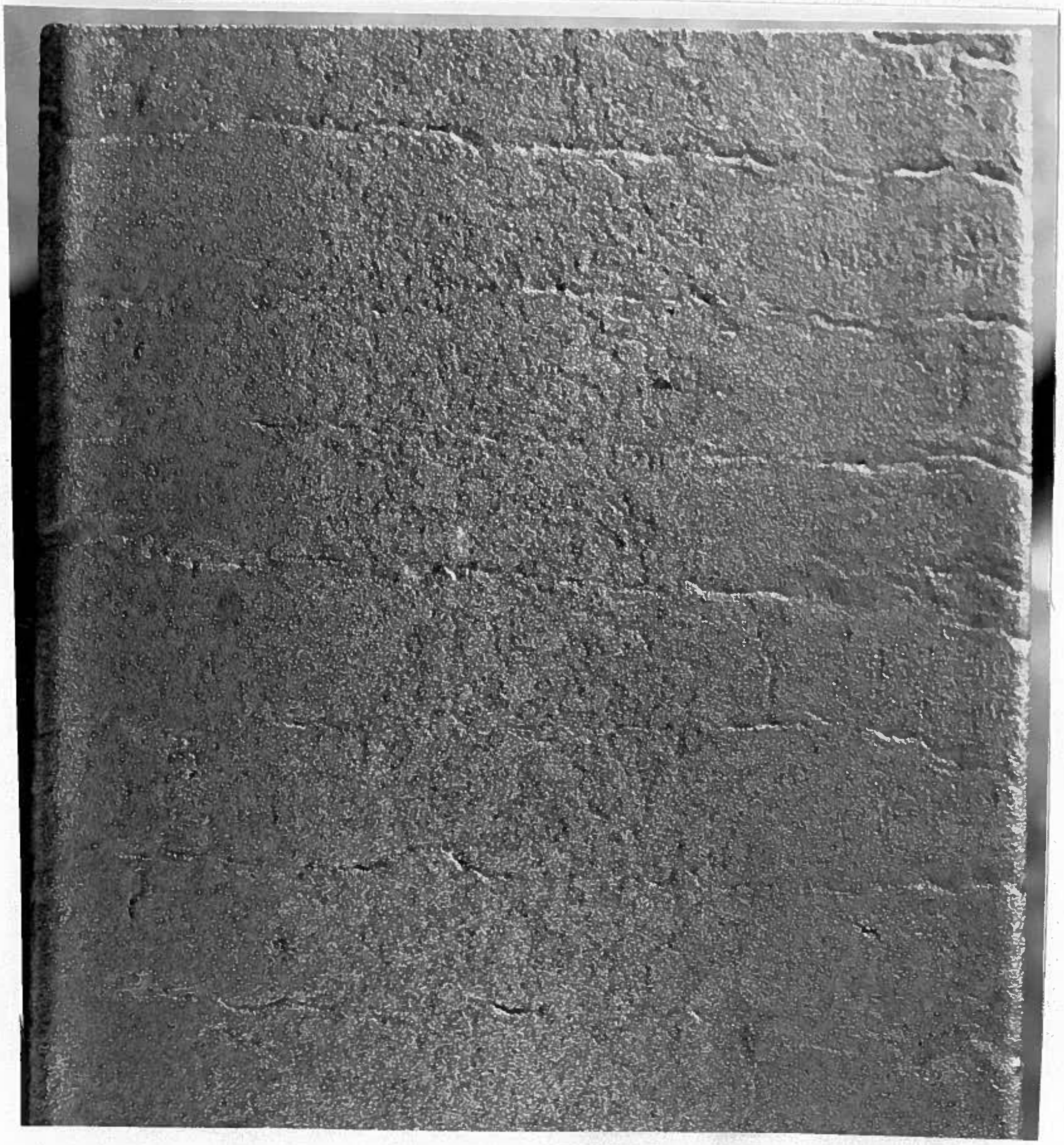

Figure 5.104 Photograph of the surface of a 1045 grade billet cast with HEAR oil at 100 ml/min at Company C (Mag. 1.0 X).

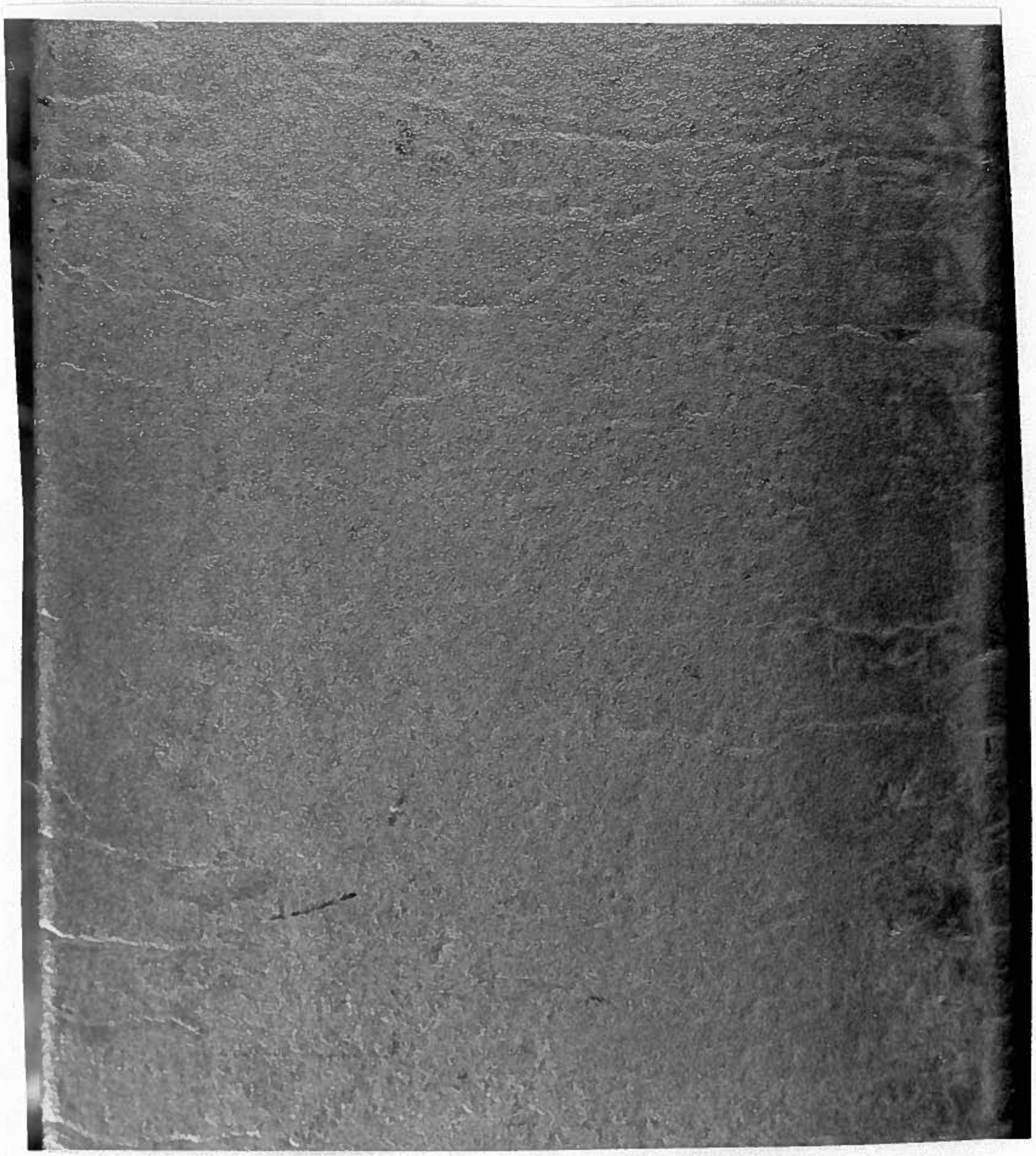

Figure 5.105 Photograph of the surface of a 1045 grade billet cast with Mineral_O oil at Company C (Mag. 1.0 X).

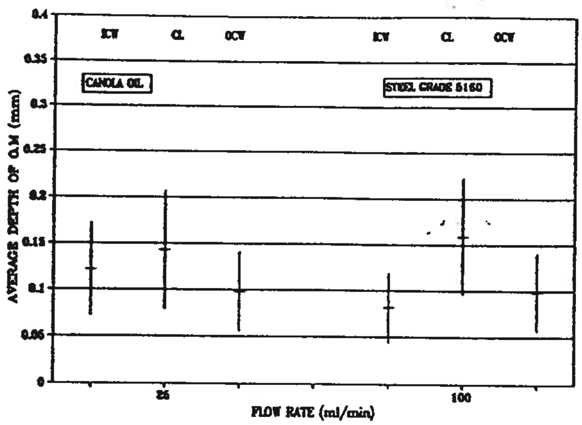

Figure 5.106 Graph showing the influence of oil flow rate on oscillation mark depth of a 5160 grade billet cast with Canola oil at Company C.

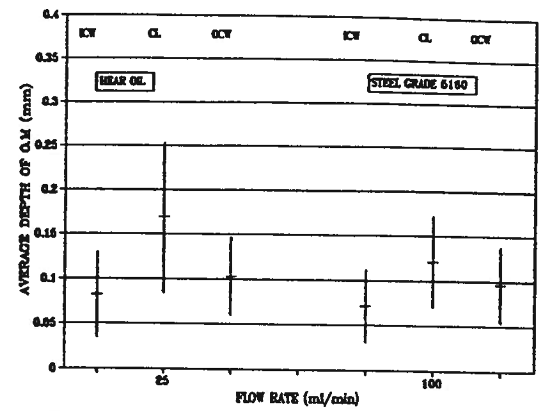

Figure 5.107 Graph showing the influence of oil flow rate on oscillation mark depth of a 5160 grade billet cast with HEAR oil at Company C.

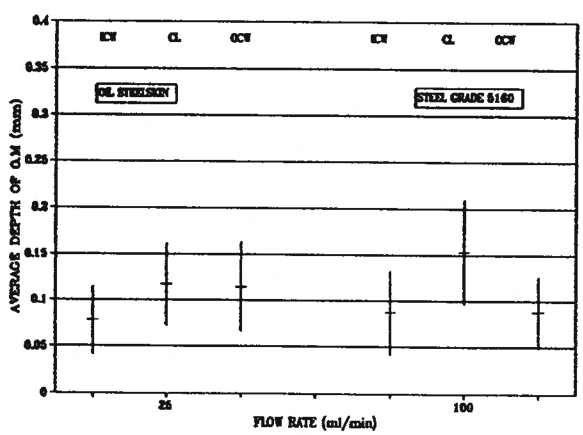

Figure 5.108 Graph showing the influence of oil flow rate on oscillation mark depth of a 5160 grade billet cast with Mineral_S oil at Company C.

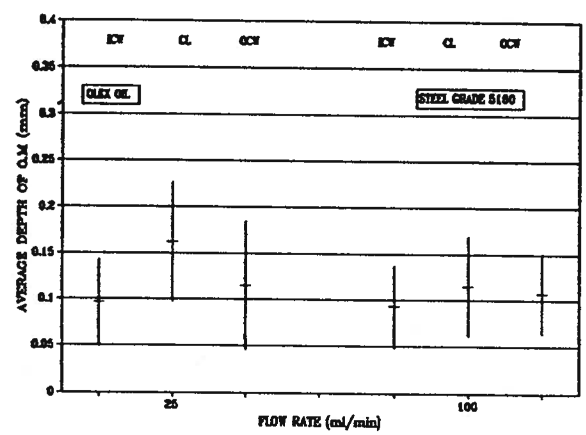

Figure 5.109 Graph showing the influence of oil flow rate on oscillation mark depth of a 5160 grade billet cast with Mineral_O oil at Company C.

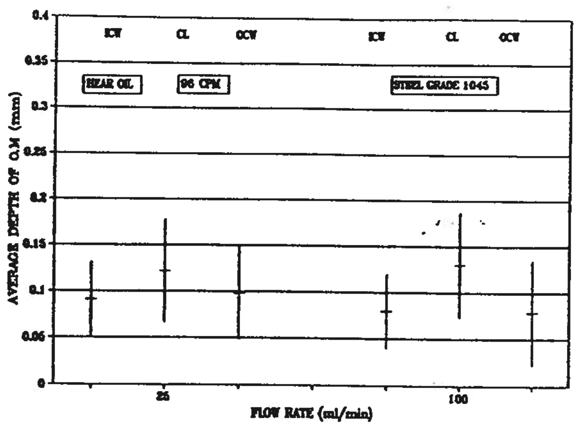

Figure 5.110 Graph showing the oscillation mark depth for a 1045 grade billet cast with HEAR oil and with a mould oscillation of 96 cpm at Company C.

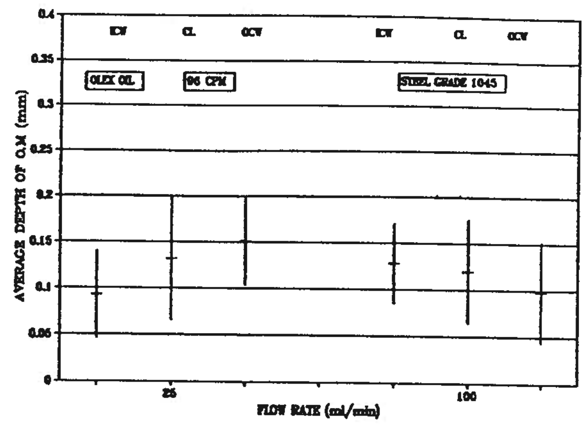

Figure 5.111 Graph showing the oscillation mark depth for a 1045 grade billet cast with Mineral_O oil and with a mould oscillation of 96 cpm at Company C.

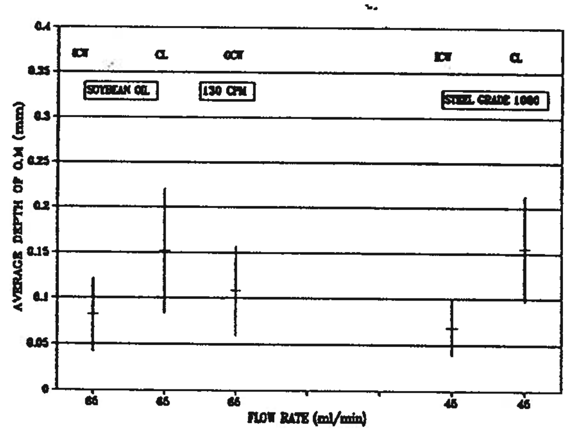

Figure 5.112 Graph showing the oscillation mark depth on a 1080 grade billet cast with Soybean oil and with a mould oscillation of 130 cpm at Company E.

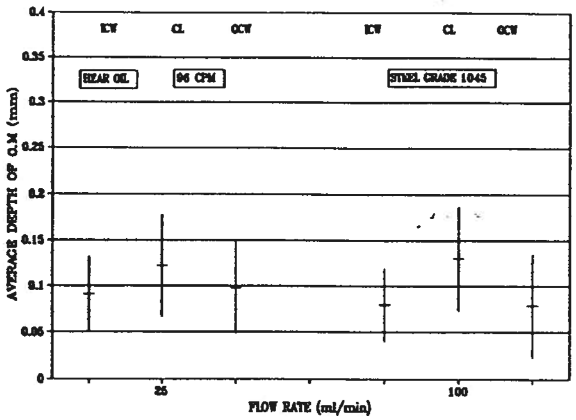

Figure 5.110 Graph showing the oscillation mark depth for a 1045 grade billet cast with HEAR oil and with a mould oscillation of 96 cpm at Company C.

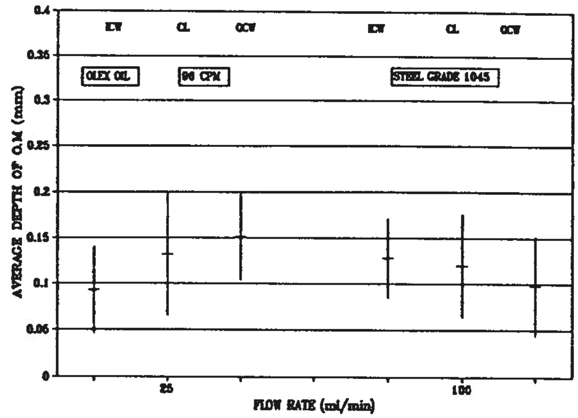

Figure 5.111 Graph showing the oscillation mark depth for a 1045 grade billet cast with Olex oil and with a mould oscillation of 96 cpm at Company C.

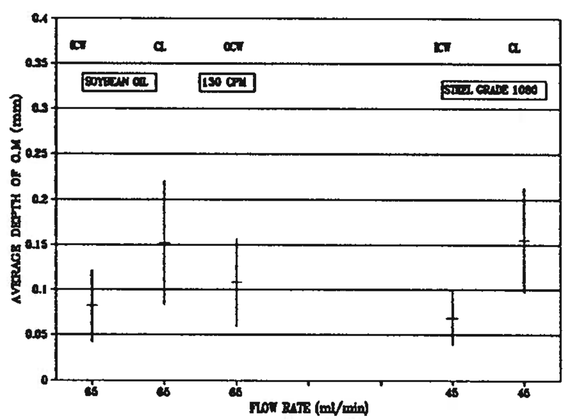

Figure 5.112 Graph showing the oscillation mark depth for a 1080 grade billet cast with Soybean oil and with a mould oscillation of 130 cpm at Company E.

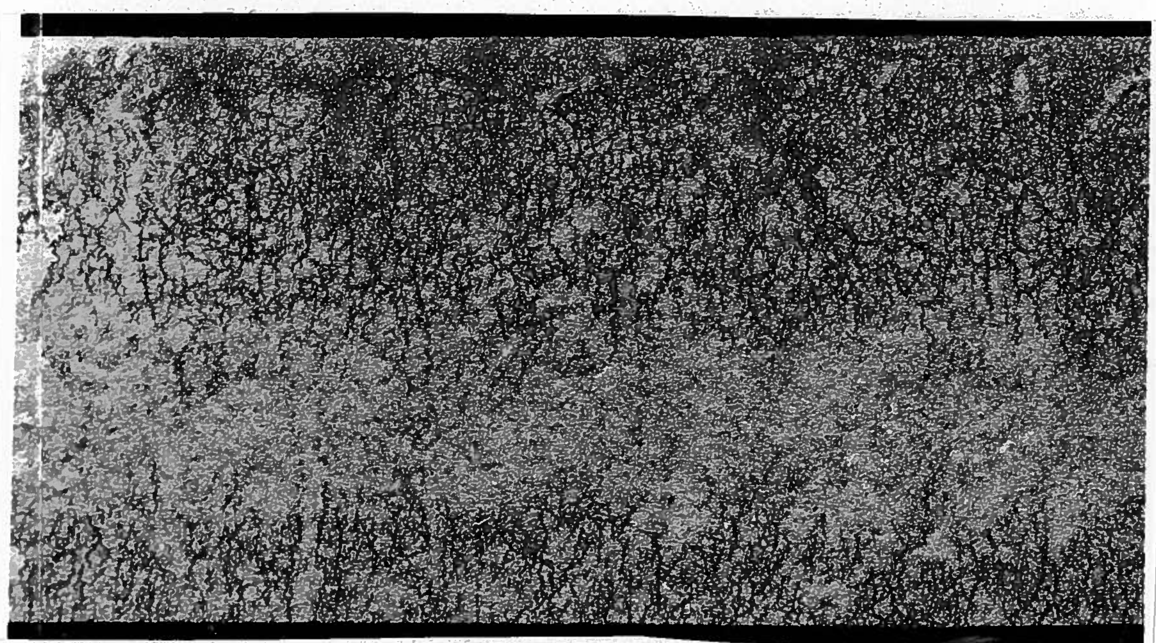

Figure 5.114 Macro-etched longitudinal section of a 1018 grade billet showing a typical example of craze cracking on the inside radius at Company B (Mag. 1.0 X).

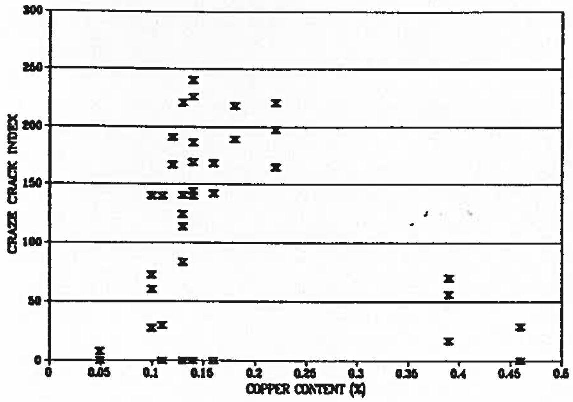

Figure 5.115 Plot of craze crack index versus copper content of billets collected at Company C.

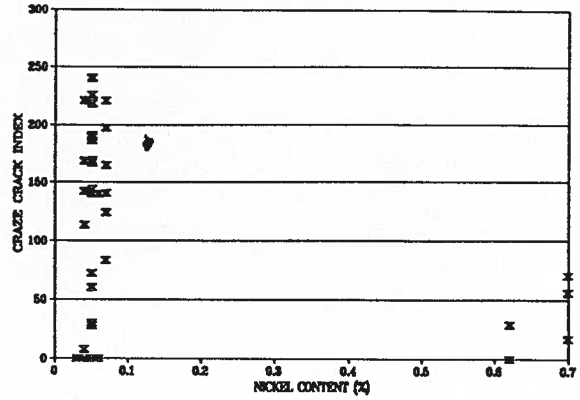

Figure 5.116 Plot of craze crack index versus nickel content of billets collected at Company C.

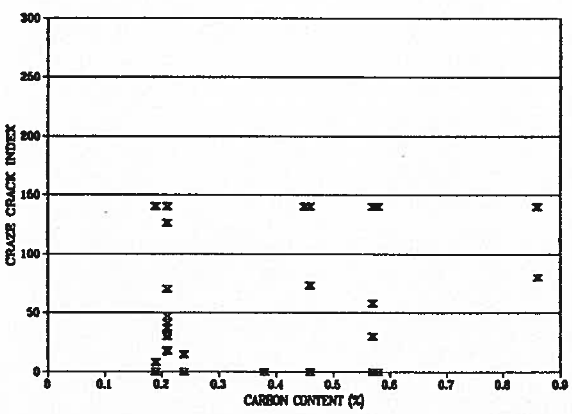

Figure 5.117 Plot of craze crack index versus carbon content of billets collected at Company C.

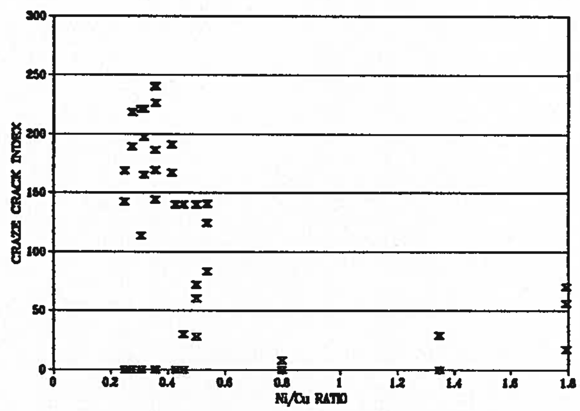

Figure 5.118 Plot of craze crack index versus Ni/Cu ratio of billets collected at Company C.

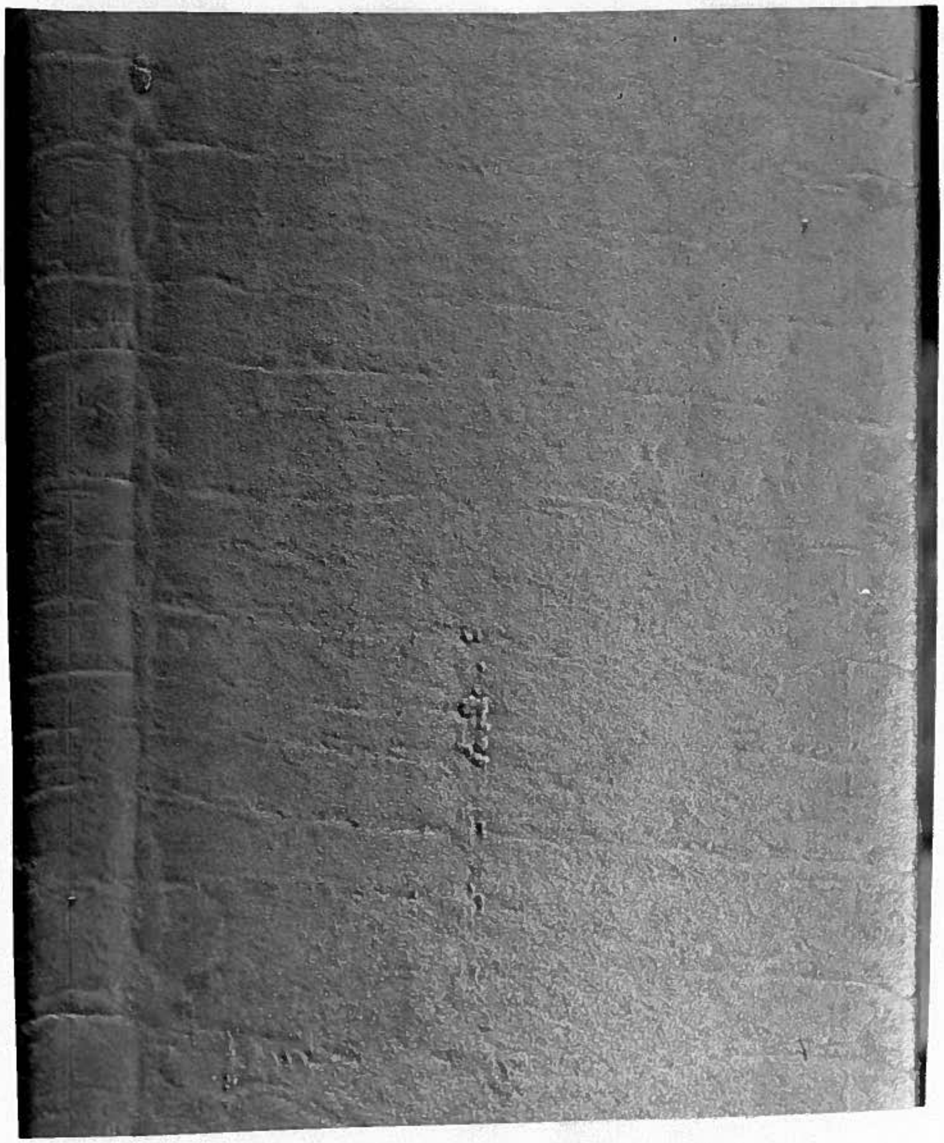

Figure 5.119 Surface of a 1080 grade control strand billet cast with Soybean oil at 65 ml/min at Company E showing evidence of beads (Mag. 1.0 X).

Figure 5.120 Surface of a 1080 grade test strand billet cast with Canola oil at 65 ml/min showing severe "zipper marks" at Company E (Mag. 0.8 X).

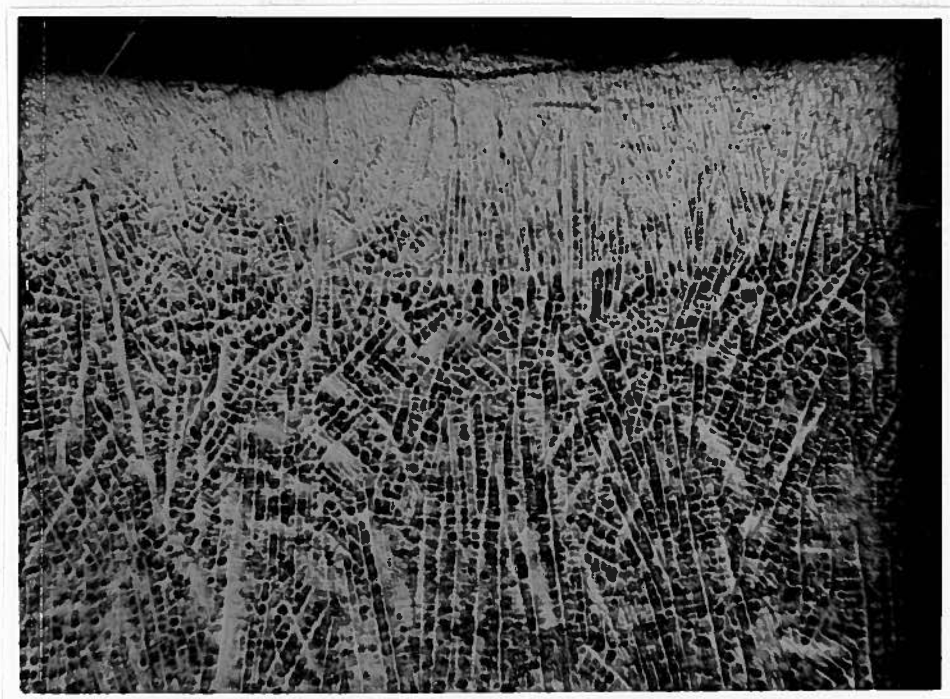

Figure 5.121 Transverse macroetch through a bead on a 1080 grade billet at Company E (Mag. 14 X).

Chapter 6 : MATHEMATICAL MODELLING OF MOULD BEHAVIOUR

The three main mathematical models used in the study are discussed in this and the following chapter. This chapter discusses the two mathematical models of the mould - the first to obtain the heat flux from the billet to the mould wall and the second to obtain the distortion of the mould during service. A detail presentation of the results of the models is deferred till Chapter 8.

6.1 Mathematical Model of Heat-Flow in the Mould

The mathematical model of heat flow in the mould is used to obtain the heat flux profile down the mould length. A pre-existing mathematical model of the mould [18] that simulates the heat flow down the length of the mould was used. The program models a longitudinal section through the mid-face of the mould wall. The input to the model is an assumed heat flux profile which is altered iteratively so as to match the predicted mould temperatures with those recorded by the thermocouples. Owing to the iterative nature of the calculations, the mathematical model was considerably modified to facilitate it use.

A schematic diagram of a longitudinal mid-plane through the mould wall is shown in Figure 6.1. The simplifying assumptions of the unsteady-state, two-dimensional, finite-difference, mathematical model are as follows.

[1] Transverse heat flow in a direction perpendicular to the plane of interest are negligibly small. This follows from symmetry.

[2] Temperature variations due to mould oscillation and metal level fluctuations are ignored. This is permissible as an average value of the temperature distribution in the mould is used.

[3] Temperature dependence of the thermal diffusivity has not been considered as its effect on mould temperature is negligible.

[4] The top and bottom surfaces of the mould are treated as adiabatic surfaces as they have temperatures that are close to the ambient temperature.

[5] The cooling water channel extends to the top and bottom ends of the mould and the cooling water is in plug flow. The latter assumption is supported by the fact that the water flow is turbulent (Re ~ 70,000) and the channel gap is less than 5 mm. There is no heat transfer between the cooling water and water jacket.

The governing equation for heat conduction in the mould wall in two dimensions is

$$\frac{\partial}{\partial x}\left(K_m \frac{\partial T}{\partial x}\right)+\frac{\partial}{\partial z}\left(K_m \frac{\partial T}{\partial z}\right)=\rho_m C_{p_m} \frac{\partial T}{\partial t} \quad (6.1)$$

while a sectional heat balance for the cooling water yields

$$\rho_w V_w d_w C_{p_w} \frac{\partial T_w}{\partial z}-h_w(z,t)\,(T(0,z,t)-T_w(z,t))=0 \quad (6.2)$$

The boundary conditions and the details of the model have been discussed in the original work [18]. The mould continuum was discretized (Figure 6.1) and the finite difference equations for the system of nodes obtained by transforming the heat flow equations and relevant boundary conditions for each node into a finite difference form was solved by the alternating direction implicit method [68].

6.1.1 Characterisation of heat transfer in the water channel

In a procedure described by Rohsenow [69] and discussed in detail by Samarasekera and Brimacombe [18], forced convection boiling curve for water was constructed (Figure 6.2). There are three distinct regions of the forced convection boiling curve : Forced Convection (FC), the Transitions region (TR) and the Fully Developed Boiling region (FDB). In the forced convection regime of the above mentioned curve the heat flux can be calculated by the following expression [18].

$$Q_{FC} = h_{fc}(T_w - T_{sat}) \tag{6.3}$$

$$\text{where} \quad \frac{h_{fc} D_H}{K_f} = 0.023 \left(\frac{\rho_f V_f D_H}{\mu_f} \right)^{0.8} \left(\frac{C_{pf} \mu_f}{K_f} \right)^{0.4} \tag{6.4}$$

and all values are evaluated at the average temperature of water.

The heat flux in the fully developed nucleate boiling region is given by

$$Q_{FD} = \left(\frac{(T_w - T_{sat})}{H_{fg}} \times \frac{1}{C_{sf}} \times \frac{K}{\mu} \right)^3 \times \left(\frac{(\rho_l - \rho_v)}{\sigma} \times \frac{g}{g_0} \right)^{0.5} \tag{6.5}$$

The heat flux in the transition region is given by

$$Q_{TR} = Q_{FC} \left(1 + \frac{Q_{FD}}{Q_{FC}} \left(1 - \frac{Q_\Phi}{Q_{FD}} \right)^2 \right)^{0.5} \tag{6.6}$$

The heat flux at the inception of boiling is given by the expression

$$Q_{FN} = 5.281 \times 10^{-3} P^{1.156} (1.8(T_w - T_{sat}))^{\frac{2.40}{P^{0.0234}}} \tag{6.7}$$

With a decrease in the number of active nuclei for bubble formation due to degassing of a surface over a long period of time, larger superheats than predicted by Equation 6.7 are required to initiate and sustain boiling. The boiling of the water in the water channel can thus cause a hysteresis in the boiling curve leading to thermal cycling - a point explained in detail in the original work [18]. A transient heat flow model was developed to simulate the time-dependent effects of boiling on the thermal field in the mould.

The changes made in the programme were done mostly to make the code easier to use.

6.2 Mathematical Model of Mould Distortion

A three-dimensional, elastic-plastic, finite-element model of the mould wall, described in detail in an earlier publication [62], was used to compute the thermal expansion of the mould during service. This model was used as a "black box" and a programme was written to generate data for input to the finite-element model. This programme generates the appropriate mesh and uses the temperature distribution in the mould, available from the previous programme, to associate a temperature with each element in the mould wall. The mesh generated by this programme and used in the finite-element model is shown in Figure 6.3. It may be mentioned in the passing that the mesh-generating programme is semi-general purpose programme in that it can generate the mesh given the mould dimension and the number of nodes in each direction.

The use of a three-dimensional model has been rationalised [62] on the basis of the mould shape : since the mould is a square or rectangular tube with an inherent rigidity, the corners can be expected to exert a restraining effect on the movement of the mid-face and thus a three-dimensional analysis becomes a necessity.

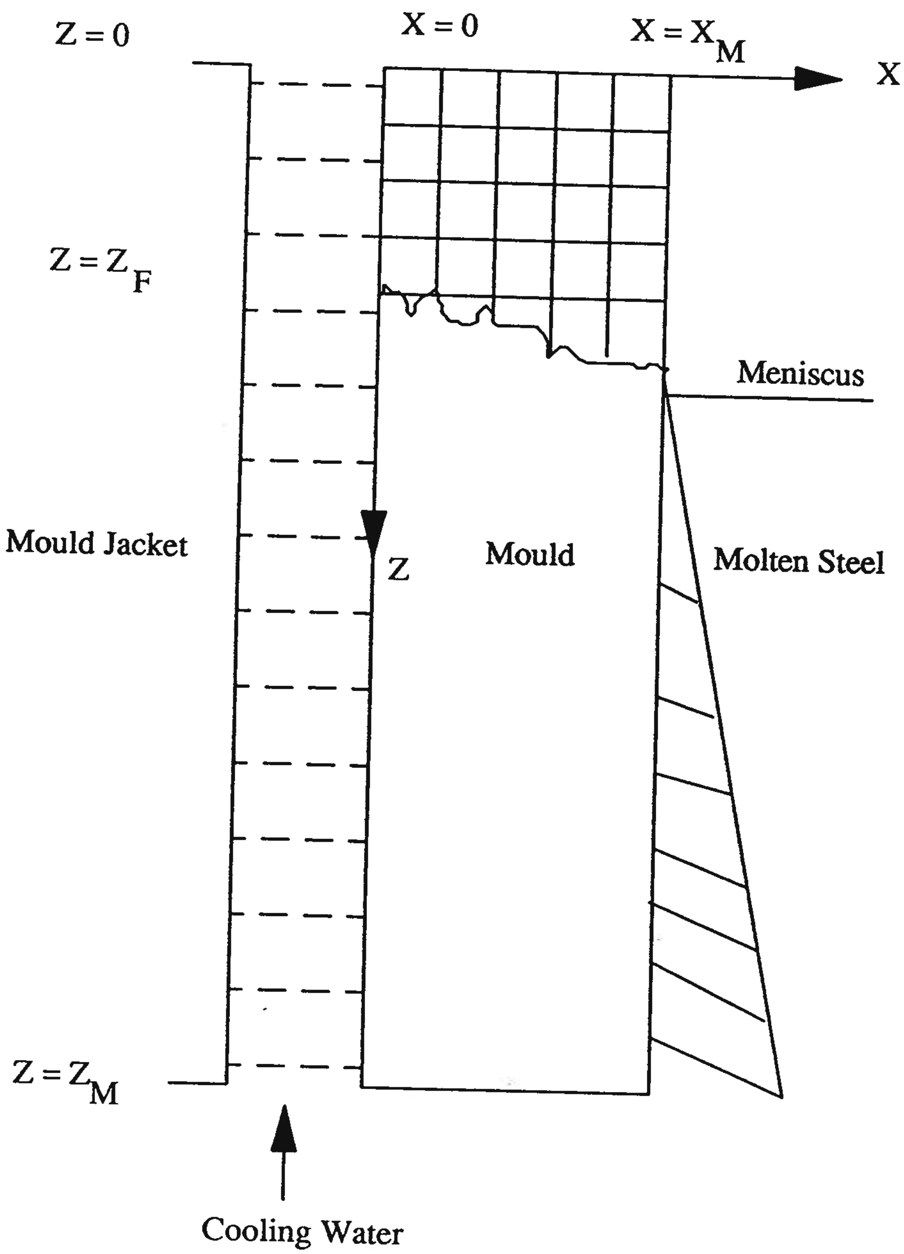

Figure 6.1 Mesh used for modelling a longitudinal section of the mould wall [18].

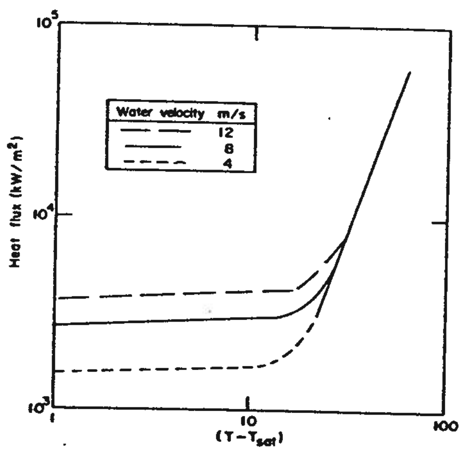

Figure 6.2 Forced convection - heat transfer curve [18].

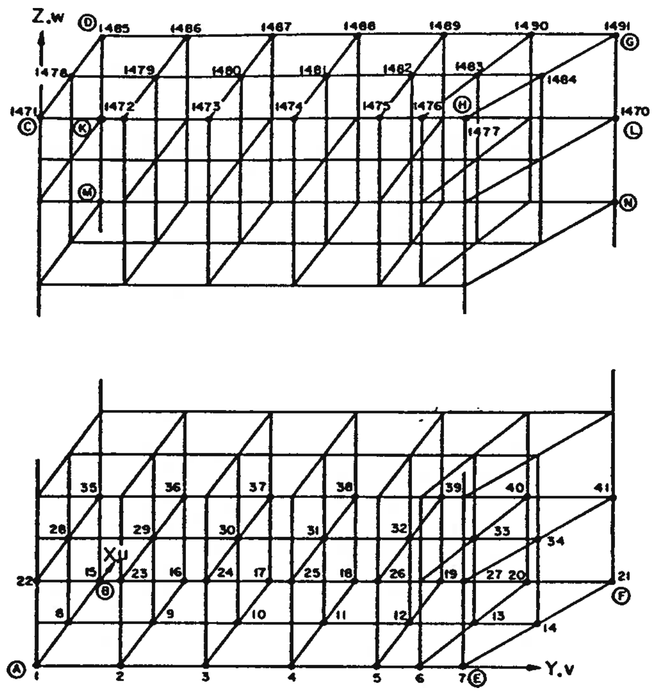

Figure 6.3 Mesh used to model mould distortion [62].

Chapter 7 : MATHEMATICAL MODELLING OF BILLET SOLIDIFICATION AND SHRINKAGE

This chapter describes the development of a mathematical model that predicts the progress of solidification and estimates the shrinkage profile of a billet during its passage through the mould.

7.1 Mathematical Model of Billet Contraction

A mathematical model to describe the heat flow in a continuously cast strand and to compute the shrinkage of the billet as a function of its axial position in the mould was developed. The model is based on the equation for two-dimensional, unsteady-state heat conduction in one quarter of a transverse slice of the strand, as follows:

$$\frac{\partial}{\partial x}\left(k_s\frac{\partial T}{\partial x}\right)+\frac{\partial}{\partial y}\left(k_s\frac{\partial T}{\partial y}\right)=\rho C_p\frac{\partial T}{\partial t} \tag{7.1}$$

The initial and surface boundary conditions (see Figure 7.1 for the mesh used), expressed mathematically, are as follows

$$t=0,\quad 0<x<\frac{X}{2},\quad 0<y<\frac{Y}{2},\quad T(x,y)=T_p \tag{7.2}$$

$$t>0,\quad x=0,\quad 0\le y\le\frac{Y}{2},\quad -k_s\frac{\partial T_s}{\partial x}=q_0 \tag{7.3}$$

$$t>0,\quad y=0,\quad 0\le x\le\frac{X}{2},\quad -k_s\frac{\partial T_s}{\partial y}=q_0 \tag{7.4}$$

Symmetrical heat flow about the center planes is assumed and formulated as follows:

$$t\ge 0,\quad x=\frac{X}{2},\quad 0\le y\le\frac{Y}{2},\quad -k_s\frac{\partial T_l}{\partial x}=0 \tag{7.5}$$

$$t\ge 0,\quad y=\frac{Y}{2},\quad 0\le x\le\frac{X}{2},\quad -k_s\frac{\partial T_l}{\partial y}=0 \tag{7.6}$$

Equation 7.1 was solved, subject to the above initial and boundary conditions, using an alternating direction implicit, finite-difference method as developed by Peaceman and Rachford [68].

Convective heat transfer in the pool was neglected, an assumption justified by Mizikar [70] and Szekely et al. [71], and the latent heat of solidification was taken into account by considering equilibrium freezing. The specific heat of the steel was increased in the temperature range between the liquidus and the solidus temperature of the steel to account for the release of latent heat. A linear release of specific heat in the mushy zone has been found to be adequate in an earlier work [72]. The temperature dependance of the specific heat and thermal conductivity of steel was obtained from the work of Thomas, Samarasekera and Brimacombe [73] and is shown in Table 7.1 and 7.2. To safeguard against nodes that "jump" over the mushy region in a single time step and thus miss their latent heat evolution, a post-iterative correction technique was used to readjust the temperature of these nodes. Calculations were performed with different node sizes and time steps to determine the optimum magnitude of these variables.

7.2 Shrinkage Calculation

The following assumptions were made in the calculation of billet contraction.

(i) The different phases present in the billet at any temperature are those given by the Fe-C phase diagram. This is in contrast to an earlier work [1] where austenite was taken to be the only phase present.

(ii) The shrinkage of a billet is computed by incorporating the contraction associated with phase change (wherever applicable) with the normal thermal contraction associated with cooling.

(iii) The effect of ferro-static pressure is neglected.

(iv) The mechanical behavior of the solidified shell is neglected. Neither the strains imposed by the stress field nor creep of the solidified shell is included in the model.

The initial dimensions of the steel billet were taken as those of the distorted copper mould at the meniscus. The differential coefficient of linear thermal expansion of steel was calculated by computing the fraction of different phases present from the phase diagram by the lever rule and calculating the shrinkage associated with these phases. This represented a major effort in the present work and is examined in some detail in a subsequent section.

The calculation of billet contraction was carried out by the following procedure

(i) A transverse slice of unit thickness of the billet was allowed to move down the mould in discrete time steps. At each time step, the temperature distribution in the slice was calculated.

(ii) The calculation of billet contraction was initiated at the instant the first row of nodes solidified. Prior to the initiation of solidification the billet dimensions were taken to be the dimensions of the distorted mould.

(iii) For the shrinkage calculation, at a given time step, the temperature change of each node relative to the previous time step was determined.

(iv) The length change of each node in the row of solidified nodes, due to the temperature change, was calculated relative to the previous time step.

(v) The change in the length of the first solidified row was obtained by summing the linear expansion/contraction of all nodes in that row.

(vi) The calculation of the linear expansion/contraction of the second row was started as soon as all nodes in that row had solidified and so on.

(vii) As soon as a row solidified, its starting length at that instant was taken as the average length of the rows adjacent to it that had already solidified.

(viii) The average length of all the solidified rows at any given time step was taken as the billet dimension at that time step.

(ix) This procedure was repeated until the bottom of the mould was reached.

The procedure outlined above could be done for rows or columns but the interaction between rows and column was not considered. The model does not account for the bulging of the steel shell on account of ferro-static pressure but this approach enables quantification of mould taper necessary to prevent the outward bulging of the shell.

7.3 Transverse Variation of Heat Flux

The drop in heat flux from the mid-face to the corner of the billet is well documented [6,17,32,74]. The drop in heat flux arises from a wider air gap in the corner region compared to the width of the gap between the mould wall and the mid-face of the billet. In order to characterize this transverse heat-flux variation, a trial-and-error approach had been adopted in the past [1] where the calculated contour of the solid-liquid interface was made to match metallographically observed dark bands in macro-etched transverse billet sections, by varying the heat flux in the transverse direction (Bommaraju et al. [17,58,75], have shown that the dark solidification bands formed near the exit of the mould). Additionally, the transverse variation in the heat flux had been allowed to commence only after an initial solidification time of one second elapsed.

Unfortunately the dark solidification bands are extremely difficult to observe in low-carbon billets and thus a different method was adopted as follows. The heat-transfer coefficient was calculated from the measured heat flux at the mid-face of the billet and the temperature difference between the billet surface (calculated) and the cooling water, then was held constant across the billet face. Subsequently the heat flux at any transverse position on the billet face was obtained by the product of the heat-transfer coefficient and the difference between the local billet surface temperature and the mould cooling water temperature. Toward the corners of the billet, the surface cools more rapidly due to two-dimensional effects and thus the temperature difference, and heat flux decline. This approach to account for the lower heat flux in the corner region of the billet is, at the best, an approximation but appears to give reasonable results.

7.4 Calculation of (Carbon- and Temperature-Dependent) Coefficient of Thermal Linear Expansion of Steel.

In computing billet shrinkage in the past [1] the coefficient of linear thermal expansion for steel has been assumed to be a constant, independent of temperature and steel grade. While this approach may have been adequate as a first approximation, it is imperative to obtain a more representative value of this coefficient to incorporate the effect of the delta ferrite-gamma phase transformation during cooling.

One of the greatest stumbling blocks in the present work has been the paucity of data on the coefficient of linear thermal expansion of delta and gamma iron in the temperature range of interest (> 1200 °C). A search of published literature failed to reveal any direct data on the coefficient of expansion of gamma and delta phases. The only relevant publication that could be used, to a limited extent, is the work of Wray [76] in which there is a compilation of the measurements of the mechanical, physical and thermal properties of iron and plain carbon steels. However, when examined in detail, there is difficulty in using some of the relationships given in the publication. For instance, the equation suggested by Wray for the volume increase of austenite with carbon does not appear to show any effect of temperature on the dilation of the gamma iron lattice caused by a given amount of carbon. This is in contradiction to the work of Ridley and Stuart [77], *on which Wray's equation is based*, where the authors clearly show that with increasing temperature the amount of dilation caused by a given amount of carbon, decreases. Furthermore, no source is referred to in Wray's paper for the equation governing the dilation of delta iron by carbon. However, the approach suggested in his work was followed in this study to calculate the desired equations independently.

To be able to predict the thermal expansion-contraction in a two-phase region of the steel, it is necessary to know the temperature and composition dependence (if any) of the density of the two phases. Once these are obtained, the phase diagram and the lever rule can be applied to predict the density and contraction of steel in the two-phase region as indicated earlier. Unfortunately the densities of the delta and gamma phases, as a function of carbon content and temperature, are not available in the temperature range of interest (> 1200 °C). These values, therefore, have to be computed first from the dimensions of the corresponding unit cell for the pure delta and gamma iron and then modified by superimposing the effect of dilation due to the carbon atoms. Thus the lattice parameters of the unit cell are functions of temperature and the carbon content (which dilates the cell). Furthermore, the degree of dilation for a given carbon content may, by itself, be temperature dependent.

7.4.1 Variation of lattice parameter of delta phase with carbon content and temperature

For the temperature dependence of the specific volume of pure delta iron, Wray's [76] modification of Lucas' [78] data was adopted.

$$V_\delta = 0.1242 + 8.70\,(10^{-6})\,(T - 20) \qquad (Lucas) \qquad (7.7)$$

$$V_\delta = 0.1234 + 9.38\,(10^{-6})\,(T - 20) \qquad (Wray) \qquad (7.8)$$

where T is the temperature in °C and V_δ is the specific volume in cm^3/g of δ iron.

Fasiska and Wagenblast, in an earlier work [79], have tabulated the lattice parameter of the alpha phase for different carbon contents at room temperature. Regression analysis on their carefully obtained experimental data leads to the following equation :

$$a^T_{\delta_c} = a^T_{\delta_{c=0}} + 8.40\,(10^{-3})\,(X_c) \qquad (7.9)$$

where a is the lattice parameter of the δ phase in Å and X_c is the carbon content of the phase in atomic percentage.

The researchers have also noted that the expansion in the lattice of alpha iron (henceforth referred to as 'lattice dilation coefficient'), on account of carbon, was not temperature dependent. Based on the last observation this 'lattice dilation coefficient' was taken to be representative for the high-temperature delta iron having a BCC structure as well.

7.4.2 Variation of lattice parameter of pure gamma iron with temperature

As in the case of pure delta iron, the temperature dependance of the specific volume of pure gamma iron was also taken from Wray's [76] modification of Lucas' data [78].

$$V_\gamma = 0.1221 + 9.70\,(10^{-6})\,(T-20) \qquad (Lucas) \qquad (7.10)$$

$$V_\gamma = 0.1225 + 9.45\,(10^{-6})\,(T-20) \qquad (Wray) \qquad (7.11)$$

where T is the temperature in °C and V_γ is the specific volume in cm^3/g of γ iron.

7.4.3 Variation of lattice parameter of gamma phase with carbon content

Ridley and Stuart, in their work on partial molar volumes of iron-carbon austenite [77], have graphed the variation with carbon content of the lattice parameters of austenite for a wide range of temperatures (25 - 1200 °C) and given equations for some of the plots. Furthermore, they observed that the slope of the lines gradually decreased with increasing temperature indicating that the dilation effect of a specific amount of carbon decreased.

As a first step toward obtaining the effect of carbon content and temperature on the dilation coefficient, the method of least squares was used to fit curves to their raw data. The results are summarized in Table 7.3 and Figure 7.2. It was then possible to derive, for a given temperature, the effect of carbon content on the dilation coefficient. A separate curve fitting exercise had to be conducted to determine the effect of temperature on the dilation coefficient, the results of which are shown in Figure 7.3. The parabolic nature of the curve is consistent with the observation of Ridley and Stuart that the slope of the plot of lattice parameter versus carbon content gradually decreases with temperature.

As a result of the curve fitting exercise it was possible to predict the lattice parameters (and therefore density or specific volume) of the gamma phase for any given carbon content and temperature combination as follows.

$$a^T_{\gamma_c} = a^T_{\gamma_{c=0}} + (0.0317 - 11.65\,(10^{-7})\,T - 0.05\,(10^{-7})\,T^2)\,(W_c) \tag{7.12}$$

where T is the temperature in °C, a_γ is the lattice parameter of γ phase in Å and W_c is the carbon content of the phase in weight percent.

The variation of the coefficient of linear expansion of steel is shown in Figure 7.4 for three different carbon contents. It should be noted that the plots are of the *mean* (and not *differential*) coefficient of linear expansion of steel which is based on a reference length at the solidus temperature of steel and can only be used to compute *contractions in length from the dimensions at the solidus temperature.*

The value of the linear expansion coefficient for those grades that do not undergo phase transformation (C > 0.18%) over the temperature range of interest, is nearly constant with temperature. The plot for steel with a carbon content of 0.15% represents grades (0.10% < C < 0.18%) where cooling below the solidus temperature causes shrinkage on account of both thermal contraction and phase transformation, the latter being much greater in magnitude. In such cases the total contraction in the early stages of cooling, is dominated by the effect of phase change in which the expansion coefficient has a high initial value reflecting the transformation. With further cooling below the transformation-end temperature, the contribution of thermal contraction to the *total contraction from the solidus* becomes progressively higher than the contribution from the phase change as can be seen in Figure 7.4. The third plot for steel with a carbon content of 0.05% represents grades (C < 0.10%) that undergo phase change only after the temperature is well below the solidus. The almost constant value of mean expansion coefficient around 1500 °C is indicative of contraction on account of thermal cooling of delta phase only. With the onset of phase transformation the expansion coefficient increases to a relatively large number as explained above and then gradually decreases with temperature. Because a *mean* coefficient of linear expansion is being considered, its highest value in the latter case (C = 0.05%) is lower than that attained with the 0.15% carbon steel.

7.5 Model Verification

While a detailed discussion on the results from the model is deferred to the next chapter, a tabulation of the model predicted shell thickness is given in Table 7.4 along with the measured shell thickness of the billet. As can be seen from the table the predicted shell thickness at the bottom of the mould adequately matches those measured from solidification bands in macro-etches of billet samples.

Table 7.1 Enthalpy and specific heat functions used in the heat-flow model [73].

Temperature (°C)	**Enthalpy (kJ/kg)**	**Specific heat (kJ/kg°C)**
0.0 to 114.3	-	.499
114.3 to 491.4	$-23.3+0.456T+1.88\times10^{-4}T^2$	$0.456+2\times1.88\times10^{-4}T$
491.4 to 697.1	$-13.4+0.268T+4.18\times10^{-4}T^2$	$0.268+2\times4.18\times10^{-4}T$
697.1 to 742.9	$-595+1.431T$	1.431
742.9 to 868.6	$-1348.9+3.849T-1.883\times10^{-3}T^2$	$3.849-2\times1.883\times10^{-3}T$
868.6 to 1142.9	$11.7+0.648T$	0.648
1142.9 to T_{sol}	$228.3+0.268T+1.67\times10^{-4}T^2$	$0.268+2\times1.67\times10^{-4}T$
T_{sol} to T_{liq}	$H_S+272\frac{(T-T_{sol})}{T_{liq}-T_{sol}}$	$C_{psol}+\frac{272}{T_{liq}-T_{sol}}$
$> T_{liq}$	$97.5+0.787T$	0.787

Table 7.2 Thermal conductivity function for low carbon steel used in the heat flow model [73].

Temperature (°C)	**(kW/mK)**
0 - 800	$59.4-0.418T$
800 - T_{sol}	$18.4+0.0094T$
T_{sol} - T_{liq}	$K_{sol}+(43-K_{sol})\frac{T-T_{sol}}{T_{liq}-T_{sol}}$
$> T_{liq}$	43

Table 7.3 Results of regression analysis on the experimental data of Ridley and Stuart [77].

Temperature (°C)	Lattice Parameter of gamma iron (Å)	r^2
$25°C$	$3.5737 + 0.0316\ (wt\ \%\ C)$	0.986
$200°C$	$3.5878 + 0.0314\ (wt\ \%\ C)$	0.989
$400°C$	$3.6035 + 0.0311\ (wt\ \%\ C)$	0.993
$600°C$	$3.6193 + 0.0304\ (wt\ \%\ C)$	0.991
$800°C$	$3.6356 + 0.0296\ (wt\ \%\ C)$	0.994
$1000°C$	$3.6521 + 0.0291\ (wt\ \%\ C)$	0.986
$1200°C$	$3.6684 + 0.0282\ (wt\ \%\ C)$	0.982

Table 7.4 Mid-face shell thickness at the bottom of mould for billets of different grades at Company B.

Carbon (%)	Measured Shell Thickness (mm)	Computed Shell Thickness (mm)
0.05	8.5	8.0
0.09	7.0	7.1
0.12	(not observable)	6.0
0.15	9.5	9.4
0.42	9.5	9.4

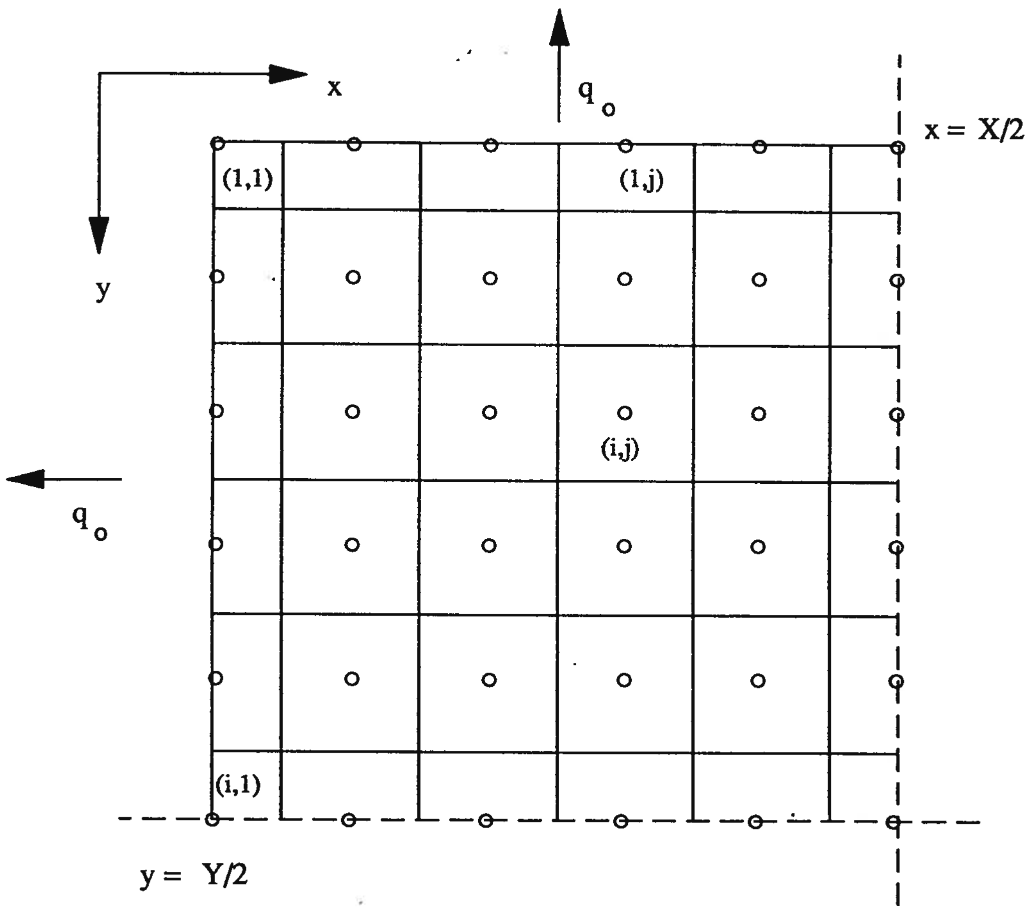

Figure 7.1 Mesh used for modelling one quarter of a transverse section of a billet.

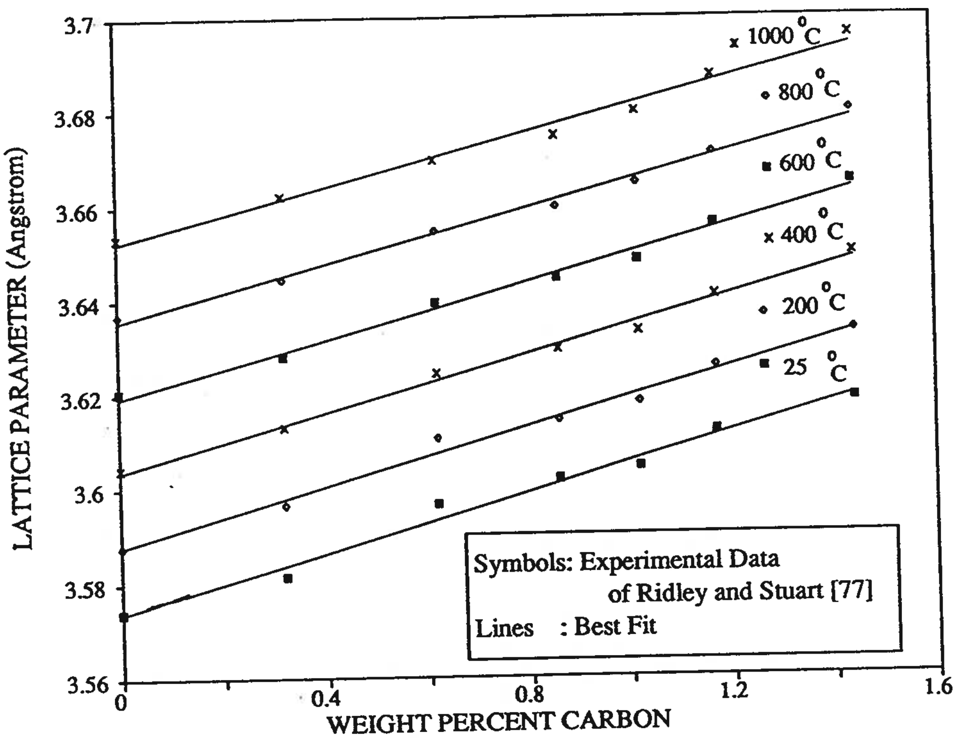

Figure 7.2 Lattice parameter of austenite as a function of carbon content at various temperatures [77].

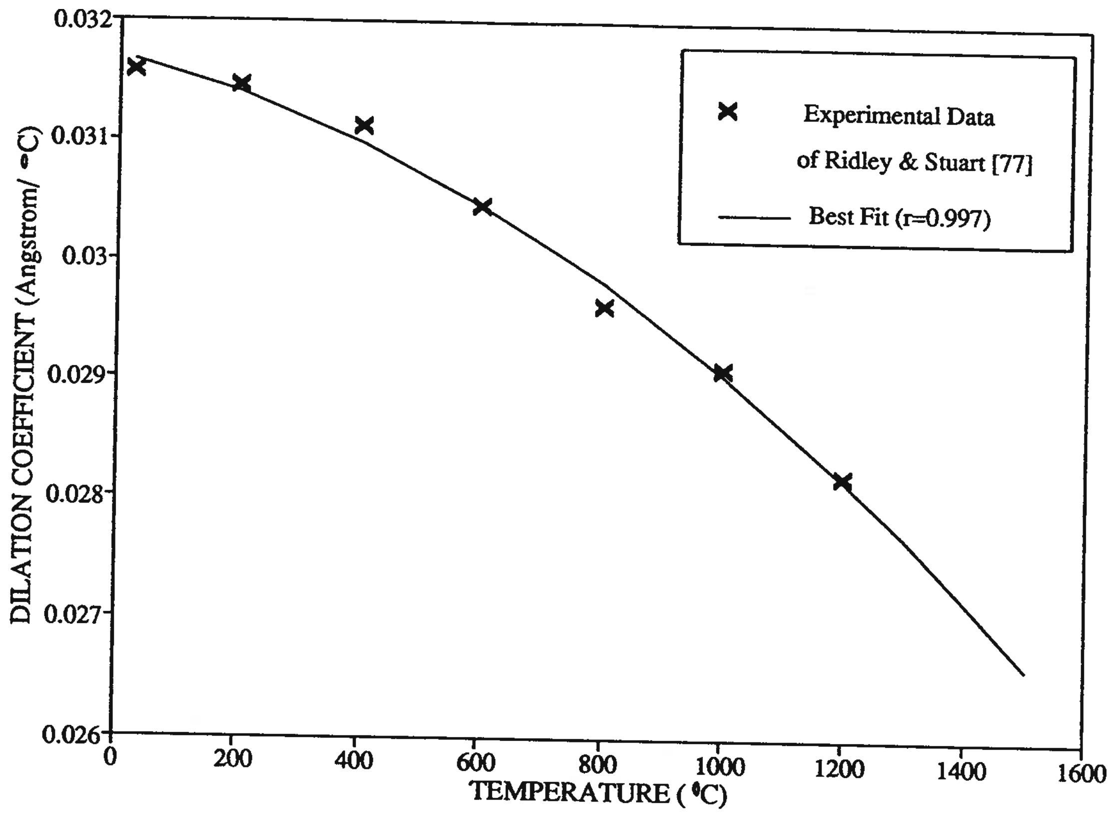

Figure 7.3 Effect of temperature on the dilation coefficient for austenite.

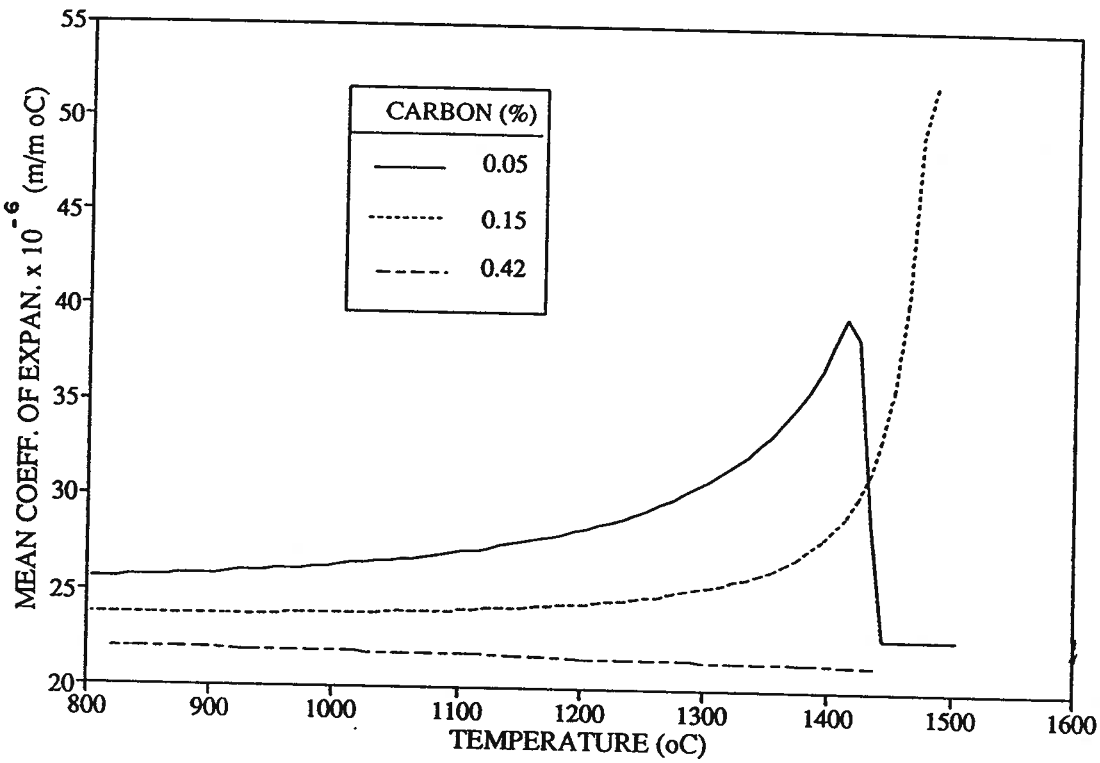

Figure 7.4 Variation of mean-linear coefficient of thermal expansion of steel with temperature.

Chapter 8 : MODEL PREDICTIONS

This chapter describes the results of the various mathematical models utilized to analyse mould thermocouple data. The details of the three models used have been described in the preceding two chapters. Most of the model predictions are analysed in this chapter itself while a discussion on the mechanism of mould heat transfer is deferred until the next chapter.

8.1 Heat-Flux Profile and Mould Wall Temperatures

Axial heat-flux profiles were obtained by applying the mathematical model of heat flow in the mould. As explained earlier, the input to the model is an assumed heat-flux profile that is changed iteratively until the predicted mould temperature profile matches that measured by mould thermocouples. The results from the model runs are presented below.

8.1.1 Typical heat-flux profile

Figure 8.1 is a plot of heat-flux profiles as a function of position below the meniscus as obtained while casting different steel grades (C = 0.05% 0.42%), at Company B

A typical feature of the heat-flux profile is that it starts with a high value at the meniscus and then drops to a lower value after which it remains more or less constant. The shape of the curve is explained in three parts as follows.

[A] The first contact of liquid steel with the copper mould leads to a high value of heat transfer. This corresponds to the peak heat flux.

[B] The formation of a solid shell, that pulls away from the mould wall, gives rise to the formation of an air gap, thereby lowering the heat transfer to the mould.

[C] The almost constant nature of the heat flux in the lower part of the mould is indicative of how well the parabolic taper of the mould wall, at Company B, follows the shrinking billet profile. (It will be shown in a subsequent section that this taper is excessive for casting low carbon steels).

8.1.2 Effect of carbon content of steel

The effect of carbon content of steel billets on the heat transfer to the mould can be seen in Figure 8.1 for steels with carbon contents between 0.05% and 0.42%.

It can also be seen from Figure 8.1 that the lowest heat flux is obtained with a 0.12% C steel and the highest with a 0.42% C steel in the carbon range for which data was collected at this plant. Both these observations are consistent with those reported in literature [17,34]. The low heat flux in the case of 0.12% C has been attributed to the shrinkage accompanying the $\delta-\gamma$ transformation, which occurs in the solid state closest to the meniscus at this carbon level. Differential shrinkage causes the surface to become rippled thereby increasing the local billet-mould gap which leads to a drop in heat transfer.

It was shown in Table 7.4 that the mathematical model of billet solidification employing these heat-flux profiles predicts a solid shell thickness at the bottom of the mould in agreement with the experimentally measured values of the shell thickness (obtained from dark solidification bands).

The heat-flux profiles for higher carbon billets cast at Company C are shown in Figure 8.2 (C = 0.18% - C = 0.56%). The plot clearly shows there is little dependence of the heat flux on the carbon content provided the carbon content of the billet is not in the range that undergoes peritectic reaction (C = 0.10% - C = 0.18%).

8.1.3 Effect of oil flow rate

As was mentioned in the previous chapter, the flow rates of all four oils tested, could be changed in a systematic manner at Plant C. Figure 8.3 shows the axial heat-flux profiles for a 1018 grade heat cast with Canola oil at 0, 25, 70 and 100 ml/min. (Note : The axial heat-flux profile with 70 ml/min of Canola oil lies between those obtained with a flow rate of 25 and 100 ml/min and has been omitted from the graph for clarity). Thus the main effect of the oil flow rate on the heat flux profile is seen near the meniscus; to observe the oil effect more clearly an enlarged graph of the heat-flux profile in the meniscus region is shown in Figure 8.4. In addition Figure 8.5 shows, in the form of a bar chart, the amount of heat extracted in the meniscus region of the mould for the four oil flow rates while Figure 8.6 shows the hot face temperature of the mould in the above cases.

It is clear from Figures 8.3 and 8.4 that an increase in the oil flow rate leads to an enhancement in heat transfer at the meniscus. This can be explained by the fact that the temperature of the hot face of the mould at Company C (~280°C) is well above the boiling points of all the oils (Mineral_S oil starts boiling at 170°C while Canola oil begins boiling at 205°C). Consequently any oil that is pushed past the meniscus, during the down stroke of the mould, will boil and the gaseous hydrocarbons thus produced will "crack" against the hot steel shell leading to their decomposition predominantly into carbon and hydrogen. Because the thermal conductivity of hydrogen (k = 0.475 $W/m^{2o}C$) is about 7 times that of nitrogen (k = 0.0675 $w/m^{2o}C$), the thermal resistance of the air gap (80% Nitrogen) is considerably decreased with the presence of Hydrogen gas, leading to a significant enhancement in heat transfer. *(While a detailed discussion on this subject will be presented in the next chapter, it needs to pointed out that such enhancements in heat transfer at the meniscus seem to depend on the temperature of the hotface of the mould being above the boiling point of the lubricating oil).* An increase in the flow rate of oil would clearly increase the amount of hydrogen in the gap leading to a further increase in the heat transfer to the mould as shown in Figures 8.3 and 8.4.

Figure 8.5 reveals an extremely important feature : *an increase in the flow rate of the oil has a significant effect on the heat transfer at the meniscus only at lower flow rates.* With an increase in oil flow rate from 0 to 25 ml/min the enhancement in heat transfer is ~ 13% while from 25 to 70 ml/min it is ~ 2% and from 70 - 100 ml/min it is ~ 1%. An understanding of the largest effect at low oil flow rates was obtained from the video tapes of the meniscus region taken during the industrial trials. Thus it was seen that an increase in the flow rate of oil beyond 25 ml/min created a discontinuous layer of oil on the liquid steel surface as excess oil was squirted out of the meniscus area during the negative strip period. This "excess" oil does not flow past the meniscus but progressively boils on the steel surface itself. Other evidence in support of this is the observation made in an earlier chapter that the flow rate of oil had no influence on mould-billet friction forces as determined by the load cell response.

An obvious inference from the above discussion is that, provided uniform oil distribution around the mould periphery is maintained, there is little to be gained, both form the viewpoint of heat transfer and mould lubrication, in increasing the oil flow rate beyond 25 ml/min (which is approximately 0.05 ml/min per mm of mould perimeter). It will not be out of place to mention that at the three companies at which trials were carried out the standard oil flow rate was 2.5 - 3.5 times the above value.

8.1.4 Effect of oil type

Having established the mechanism by which oil enhances heat transfer, it is now possible to compare the relative effects of different oils. The axial heat-flux profile for a 1018 grade steel cast with four different oils at Company C is presented in Figure 8.7. To maintain clarity in the figures only the two extreme cases are shown viz., a vegetable based oil (Canola) and a mineral oil (Mineral_S). It can be clearly seen that the heat flux for the vegetable based oil is higher than that for the mineral based oil.

Table 4.3, giving the properties of the oils, indicates that the boiling point of Mineral_S oil is much lower than that of Canola oil (20% of Mineral_S boils off at 230 °C compared to around

5% of Canola oil at the same temperature) . Consequently for a given flow rate of lubricant and a mould hot face temperature that is sufficient to cause the oils to boil, more of the Canola than Mineral_S oil would make its way below the meniscus leading to a higher heat transfer as explained in the previous section. This theory is further confirmed by the fact that the heat flux in the meniscus region is almost the same for the case of Mineral_S oil at 25 ml/min and the "no oil" situation.

The enhancement of heat transfer with the Canola oil in the lower part of the mould is also explained on the basis of an increase in the thermal conductivity of the mould-billet gap arising from the presence of hydrogen. The increase, however, is less than that in the upper part of the mould, as expected, because in the lower part of the mould the thermal resistance of the solid shell and the mould-billet gap are comparable. This issue is revisited in the next chapter.

8.1.5 Effect of mould-oscillation frequency

The effect of a change in mould-oscillation frequency is depicted in Figure 8.8 which is a plot from data collected at Company C. As shown in the figure the axial heat-flux profile for the (normal) high frequency of 144 cpm is lower both at the meniscus and toward the bottom of the mould. Table 5.1 summarizes the change in oscillation related parameters corresponding to a change in the oscillation frequency of the mould.

The explanation for the lower rate of heat extraction at the meniscus is deferred until the next chapter. The difference in the heat extraction rate in the lower part of the mould can be explained as follows. An increase in the oscillation frequency of the mould increases the number of oscillation marks per unit length of the billet which widens the local billet-mould gap thereby lowering the heat transfer to the mould. (It should noted that the depth of the oscillation marks (0.18 mm) is the same in the two cases). The pitch of the oscillation marks is given by $\frac{V_c}{f}$ (where V_c is the casting speed and f is the oscillation frequency of the mould) so that the number of oscillation marks per meter of billet is 47 and 71 for an oscillation frequency of 96 and 144 cpm respectively. Thus at the high oscillation frequency, the mould leaves 1.5 times as many oscillation marks on the billet as at the low frequency oscillation; thus, on average the local air gap is 1.5 times wider in the 144 cpm case. That these differences in the pitch of the oscillation marks can indeed cause the observed enhancement in heat transfer is verified quantitatively in the next chapter.

It is not very clear why there is a shift of 20 mm in the position of the heat flux with a change in the oscillation frequency but it may be due to an unintended change in the meniscus level.

8.1.6 Difference in the mould heat extraction rate at the three plants

The axial heat-flux profiles for 1045 grade steel at Companies B, E and C are compared in Figure 8.9 and show that considerably more heat is extracted by the mould at Company C compared to that at the other two Plants. Figure 8.10 shows a plot of the average heat extracted in the mould (as obtained from the mathematical model) against the heat extracted by the mould cooling water (calculated using the water flow rate and the change in the inlet and outlet water temperature). The agreement is excellent with two exceptions which corresponded to 1012 and 1010 grades of steels where, on account of the low heat flux the increase in the cooling water temperature was around 1.5 C°. Since each water thermocouple (measuring inlet and outlet water temperature) has an accuracy of +/- 1C°, it is suspected that temperature rise of just 1 or 2 C° cannot be very accurately measured. The agreement seen in Figure 8.10 reinforces the validity of the values of heat transfer obtained through the use of the mathematical model, and especially the high heat extraction rate at Company C.

The high heat extraction rates at Plant C are also indirectly corroborated by the following.

(a) Among the three Plants studied, the tendency for the formation of rhomboid billets was the highest at Plant C. As explained in an earlier chapter, billet rhomboidity may arise when the mould cooling water boils in the cooling channel [18]. A combination of a high heat extraction rate in the mould and a low flow rate of mould cooling water leads to this condition. The mathematical model of heat transfer in the mould at Plant C has shown that the cold face temperature of the test mould is 145 °C, very near the boiling point of water at the prevailing pressure. Furthermore, the control mould which had a much lower water flow rate, 9.7 m/s compared to 12 m/s in the test strand, is more likely to produce rhomboid billets. This indeed was the case as was shown in Chapter 4.

(b) Another piece of evidence, though somewhat subjective, is the observation of the operating personnel at Plant C who complain of low mould life on their caster. The mould material at Plant C is DHP copper which has a lower half softening temperature compared to the recommended Cu-Cr-Zr alloy.

Figure 8.11 shows a bar chart of the amount of heat extracted per kilogram of steel cast. This approach eliminates differences in heat extraction at the three plants on account of differences in casting speed and/or section sizes. As can be seen, the moulds at Company C extract around 60% more heat than those at Company B and about 25% more heat than those at Company E. *This effectively means that, barring other bottlenecks, the production rate at Company C can be increased substantially by increasing casting speed while the production rate at Company B can be increased significantly through mould design.* The latter will be evident in the subsequent chapter.

8.2 Variables Affecting Distorted Mould Shape

During service the billet mould is expected to distort and assume a bulged shape [62]. The following section examines the influence of the steel composition as well as the pre-existing mould taper on the shape the mould assumes when in operation. It needs to be noted that the distorted mould shape is obtained by adding the distortion predicted by the finite-element mathematical model to the mould dimensions prior to it being put in service.

8.2.1 Steel composition

Steel composition affects mould distortion by virtue of its affect on heat transfer in the mould (shown in the previous section). The dimension of a new mould and its shape when in service are shown in Figure 8.12 for Company B. In the figure the distorted shape is plotted for a low carbon (C = 0.05%) and a high carbon (C = 0.42%) heat. No significant difference in the distortion of the mould is seen for the two cases and either of the two profiles can be used for computation of mould taper.

8.2.2 Pre-existing mould taper

The following discussion shows that the shape (taper) of the mould prior to being put in service is a factor that has a profound effect on the shape the mould acquires during service. This is only to be expected as, mathematically speaking, the distorted mould profile is obtained by adding the distortion of the mould to the dimensions of a new mould. *This finding, however, has considerable significance for it explains most clearly the differences in the thermocouple and load cells signals obtained at the three plants as will be shown in the next Chapter.*

Figures 8.13 and 8.14 show the new and distorted mould profile for Companies E and C. Thus during service the moulds at Company B (figure 8.12) and E do not assume a bulged shape near the meniscus while the mould at Company C, in contrast, has a substantial "negative taper". *The reason for this lies in the measured mould wall profiles of the new moulds from these companies. The steep inward taper of the upper region of the moulds at Company B (4.9%/m) and at Company E (2.7%/m) almost negates the outward bulging of the mould wall.* The distorted mould wall in these two cases thus has an almost neutral taper. However, in the case of Company C, the measured upper taper of the mould is very shallow (0.4%/m) even though the design specification was 1.8%/m; indeed the as-delivered mould actually had several tapers (0 %/m to 0.4 %/m) as can be inferred from Figure 8.14. Such a mould during service would acquire a steep "negative taper" in the meniscus which during the negative strip period of the mould oscillation cycle would interact most strongly with the billet.

8.3 Billet Solidification and Quality

The billet mid-face temperature, shell thickness and shrinkage profile were all obtained from the mathematical model of billet solidification and shrinkage.

8.3.1 Billet mid-face temperature

The predicted mid-face temperature of a billet passing through the mould of Company B for different steel grades is shown in Figure 8.15. The temperature profiles, as expected, follow the heat-flux profiles shown in Figure 8.1, with the 0.42% carbon steel cooling the most and 0.12% carbon steel cooling the least.

8.3.2 Billet shell thickness

The computed shell thickness for different steel grades at Company B has been tabulated in the previous chapter (Table 7.4) where it was shown that the predicted shell thicknesses at the bottom of the mould adequately match those measured from the solidification bands in macro-etches of billet samples. Figures 8.16 - 8.18 show the shell growth profile for different steel grades at Companies B, E and C respectively.

The solid shell profile for a 1080 grade steel, shown in Figure 8.17, clearly indicates that for high carbon billets the start of solidification, as determined by achievement of the solidus temperature, is delayed significantly compared to the lower carbon grades. This can be explained in terms of the size of the mushy zone. The release of latent heat is simulated in the mathematical model by an increase in the specific heat capacity of the steel while in the mushy zone. Thus under the same cooling conditions, steels that have a smaller difference between their liquidus and solidus temperature, and therefore a narrower mushy zone, will solidify at a faster rate than steels with a broader mushy zone. The initial slow growth of the solid shell in the case of high carbon steel billets could potentially have an adverse impact on their surface quality as is explained in a subsequent chapter.

8.3.3 Billet shrinkage profile

Computed billet shrinkage profiles for medium and low carbon grades are shown together with the distorted mould profile for Company B in Figures 8.19 and 8.20 respectively. Thus the "medium" carbon billets (C > 0.15%) shrink sufficiently to clear the distorted mould while the "low" carbon billet (C < 0.15%) shrinks less to cause binding in the mould.

The greater shrinkage associated with the "medium carbon" grade is due to the high heat flux (and contraction on account of phase change for 0.15% carbon steel) for these grades. Interestingly, despite the lower heat flux of 0.15% carbon steel (compared to 0.42% carbon steel) the former shrinks at a faster rate initially on account of the large contraction associated with the delta-gamma phase change. As discussed in an earlier paragraph, the release of latent heat is simulated in the mathematical model by an increase in the specific heat of the steel while in the mushy zone. Thus steels with a narrower mushy zone shrink at a faster rate than steels with a broader mushy zone. Thus, the initiation and subsequent progress of solidification is delayed in the 0.42% carbon steel on account of the large mushy zone (difference between liquidus and solidus temperatures for 0.15% carbon = 25 C° and 45 C° for 0.42% carbon steel). After some distance from the meniscus, however, the effect of the higher heat flux of 0.42% carbon steel dominates and the higher rate of shrinkage for this grade, compared to the 0.05% carbon, can be inferred from the slopes of their shrinkage profiles.

The binding of the billets in the low carbon group in one case (1010 and 1012 grades) stems from the comparatively low heat transfer such that even the high contraction associated with the phase change in these grades is insufficient to cause the billet to shrink enough to clear the mould.

The billet dimensions then are larger than those of the mould and this results in binding. In the other case (1008 grade), though the heat flux is relatively higher compared with the 1010 and 1012 grades, the transformation temperature is low so that before the large transformation shrinkage begins, the billet has already interacted with the mould.

Independent evidence of the binding of the 1008,1010 and 1012 billets in the mould was the appearance of transverse depressions on the billet surfaces and the nature of the load cell response curve. The mechanism for the formation of depressions on the surface of billets has been proposed by Samarasekera and Brimacombe in an earlier work [29]. This mechanism has been illustrated in Figure 2.12 which shows a longitudinal section through the shell at an instant when it is sticking to, or binding in, the mould tube. Under these conditions of local mould/shell friction, the shell is subjected to a high tensile stress due to the mechanical pulling of the withdrawal system. Depending on the magnitude of the stress, the shell can begin to flow plastically and form a neck, much as in a laboratory tensile test. The neck is manifested as a depression on the billet surface. Close to the solidification front, within about 50 °C of the solidus temperature, however, the steel has virtually zero ductility so that, under the influence of tensile strains, a transverse crack forms. Thus binding in the mould should manifest itself in the form of depressions on the surface of the billet and transverse cracks either on the surface or in the subsurface.

The results of surface roughness measurements of billets carried out by a profilometer designed by Bakshi et al. [80] are presented in Figures 8.21 and 8.22. The presence of depressions on the billet surface of a low carbon steel (1008) can be seen in the profilometer trace in Figure 8.22 and the photograph of the billet surface Figure 5.37. Furthermore, Brendzy [13] has clearly shown that the pronounced peaks of the load cell signal during the casting of a 1008 grade steel billet is an indicator that the billet is binding in the mould.

As the preceding paragraphs have shown, the model predicted binding of the low carbon billets in the mould has been corroborated by other observations. Clearly then the existing mould taper at Company B for the grades 1008, 1010, 1012 is too steep and needs to be relaxed for improved billet quality.

Figure 8.23 shows the billet shrinkage profile for a 1045 grade billet at Company C. Note that the shrinkage profile of the billet is well in excess of the narrowing dimensions of the tapered mould such that a gap of about 0.7 mm opens up by the bottom of the mould. Such a gap is expected to allow the solid shell to bulge under the influence of ferrostatic pressure and to cause a hinging action at the off-corner sites leading to the generation of internal cracks near the solidification front. This mechanism has been explained in detail in an earlier chapter. The depth of off-corner cracks in billets from this company is between 8 and 12 mm (Chapter 5) indicating that off-corner cracks are forming below 400 mm from the top of the mould, in the zone of second taper. This matches well with the billet shrinkage profile (Figure 8.23) which shows a major increase in billet-mould gap in this zone.

The absence of off-corner cracks on billets from Company C where the mould dimensions, particularly in the lower part of the mould, matched the shrinking billet profile reinforces the mechanism for the formation of off-corner cracks.

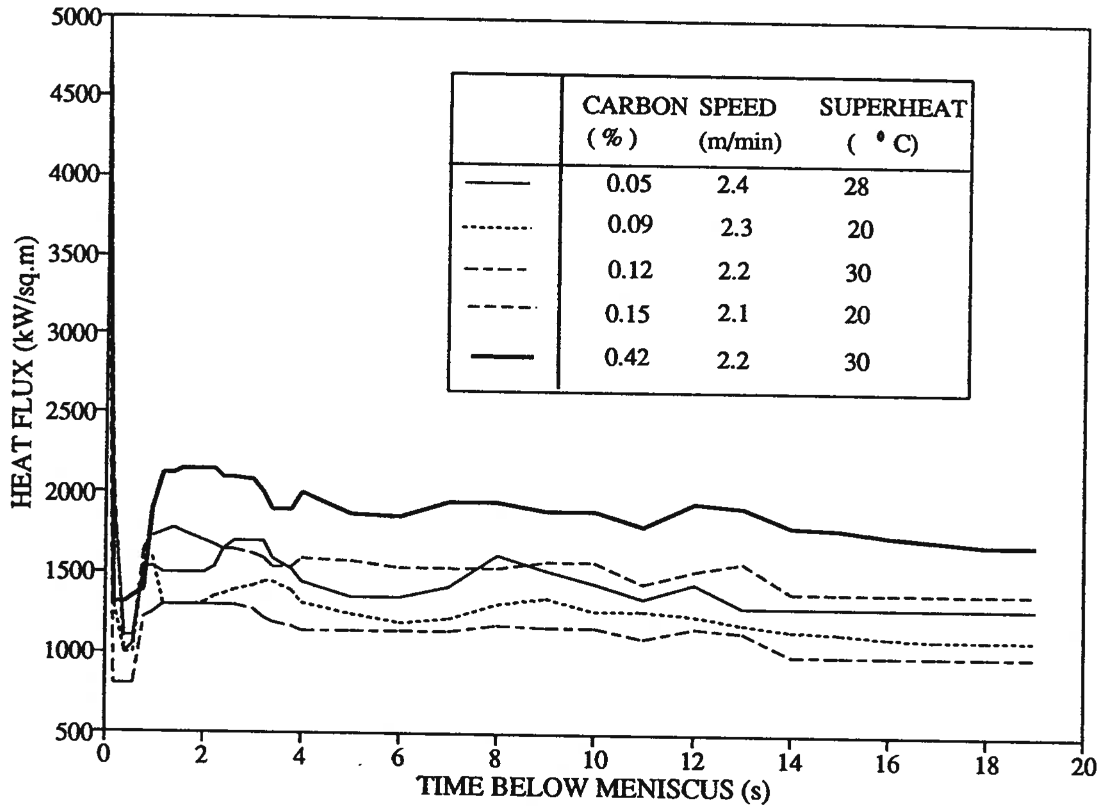

Figure 8.1 Heat-Flux profiles at Company B for billets with different carbon contents.

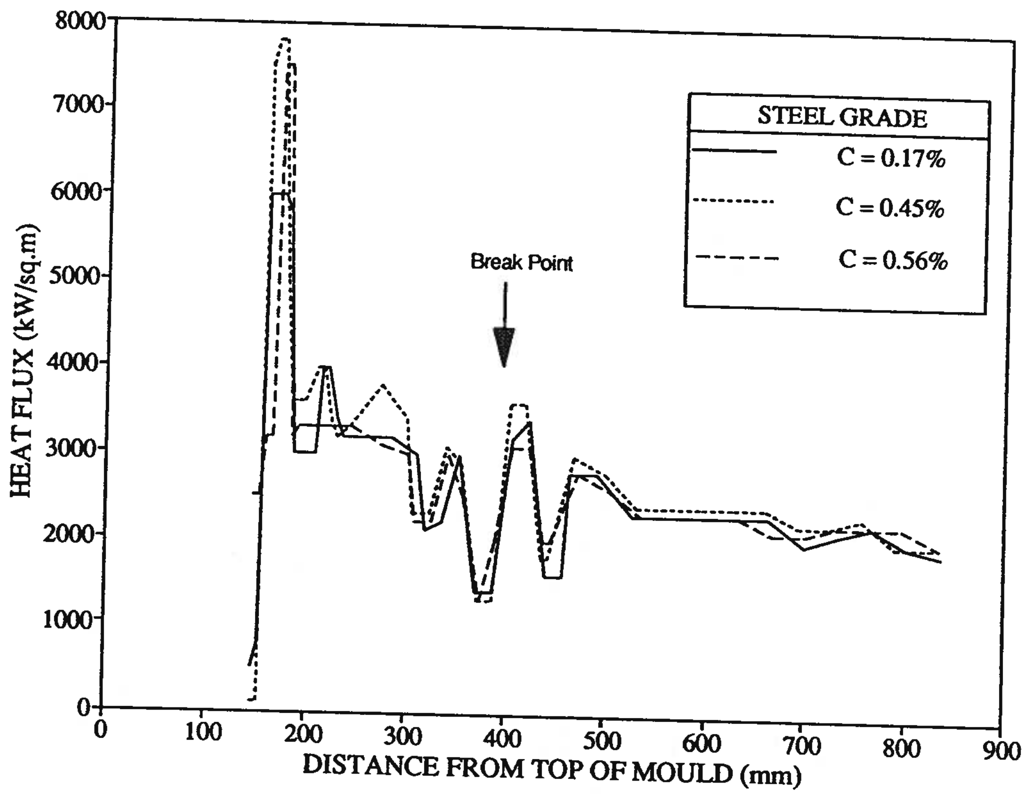

Figure 8.2 Heat-Flux profiles at Company C for billets with different carbon contents.

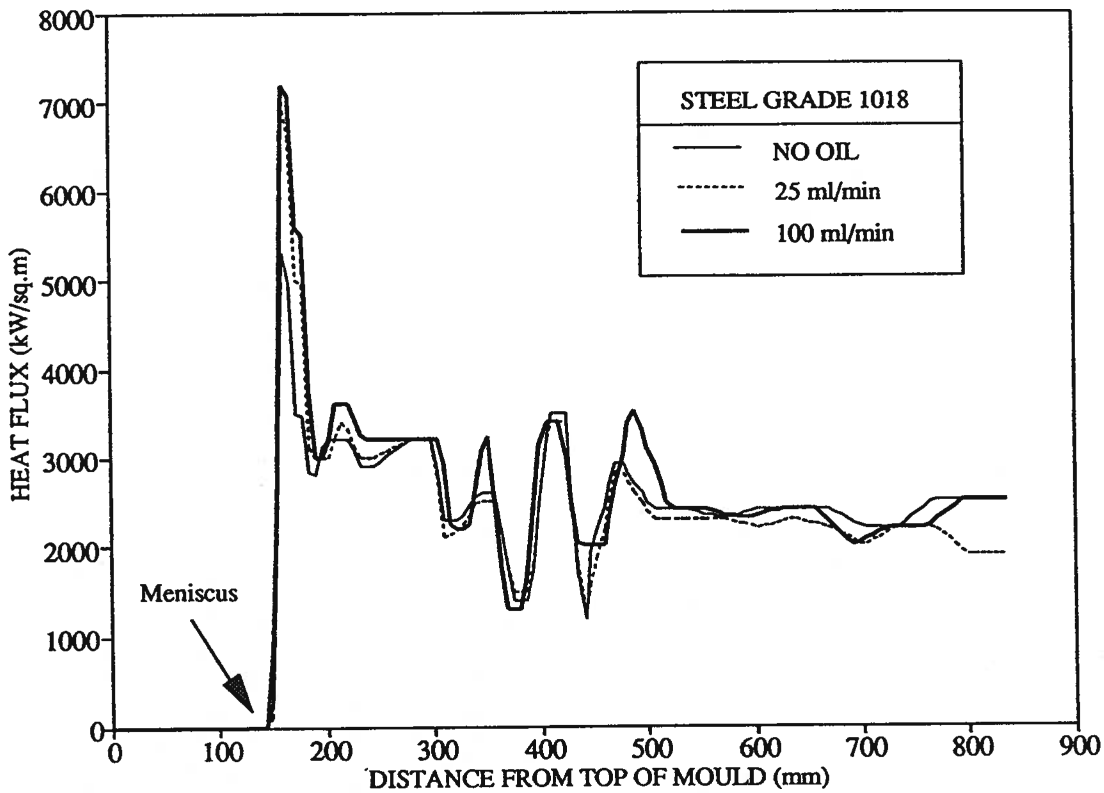

Figure 8.3 Heat-Flux profiles for 1018 grade steel billets cast with Canola oil at 0, 25, 70 and 100 ml/min at Company C. (Note: plot for 70 ml/min of oil lies in between those for 25 and 100 ml/min, but has not been shown for clarity).

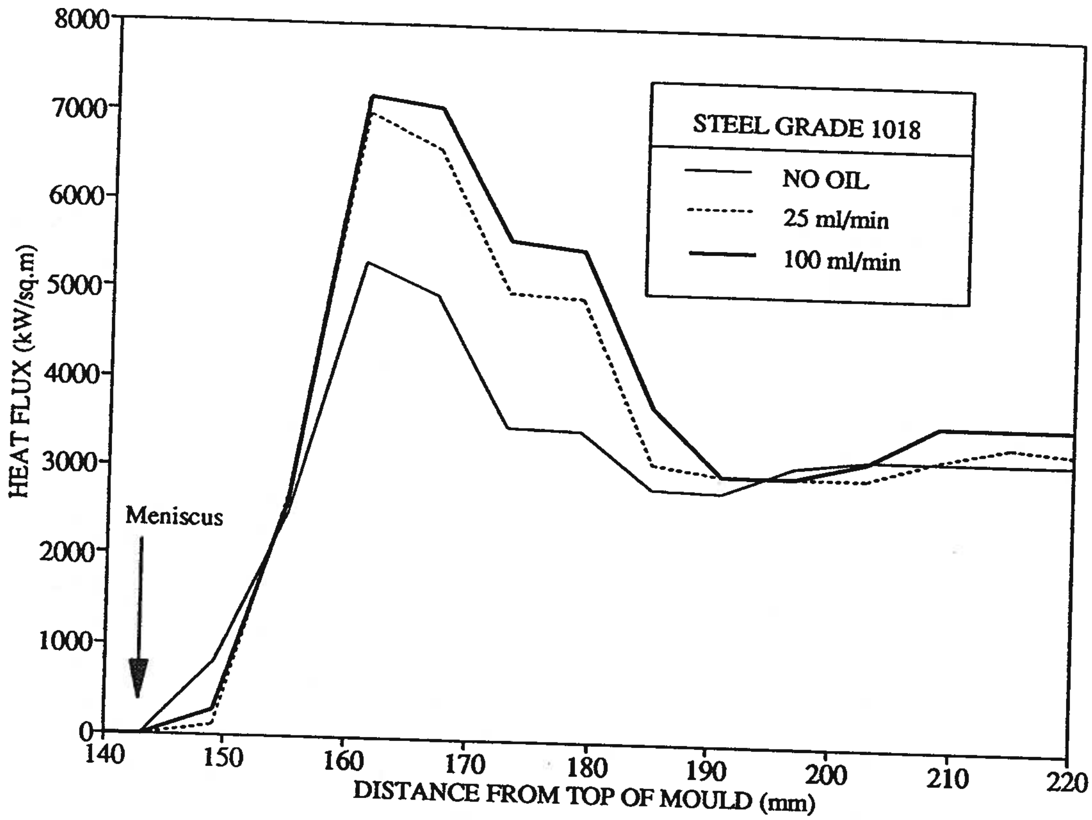

Figure 8.4 Heat-Flux profiles for 1018 grade steel billets cast with Canola oil at 0, 25, 70 and 100 ml/min at Company C (enlarged in the meniscus region). (Note: plot for 70 ml/min of oil lies in between those for 25 and 100, but has not been shown for clarity).

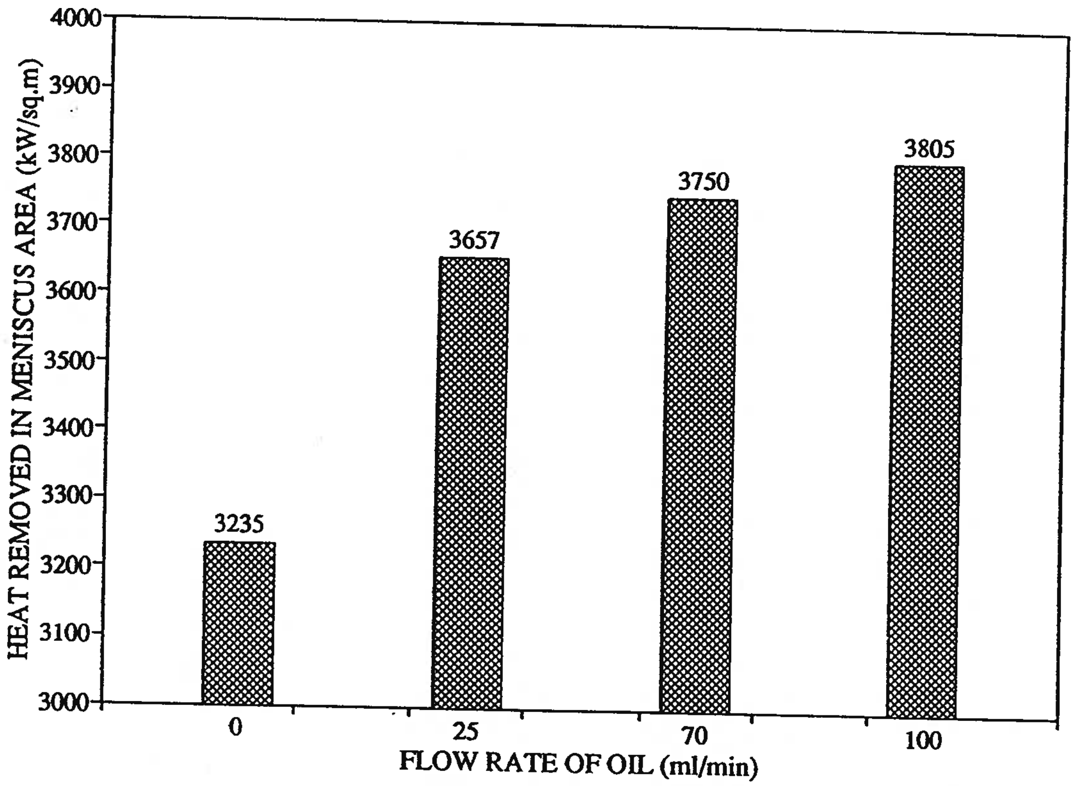

Figure 8.5 Heat extracted in the meniscus area of the mould for 1018 grade steel billets cast with Canola oil at 0, 25, 70 and 100 ml/min at Company C.

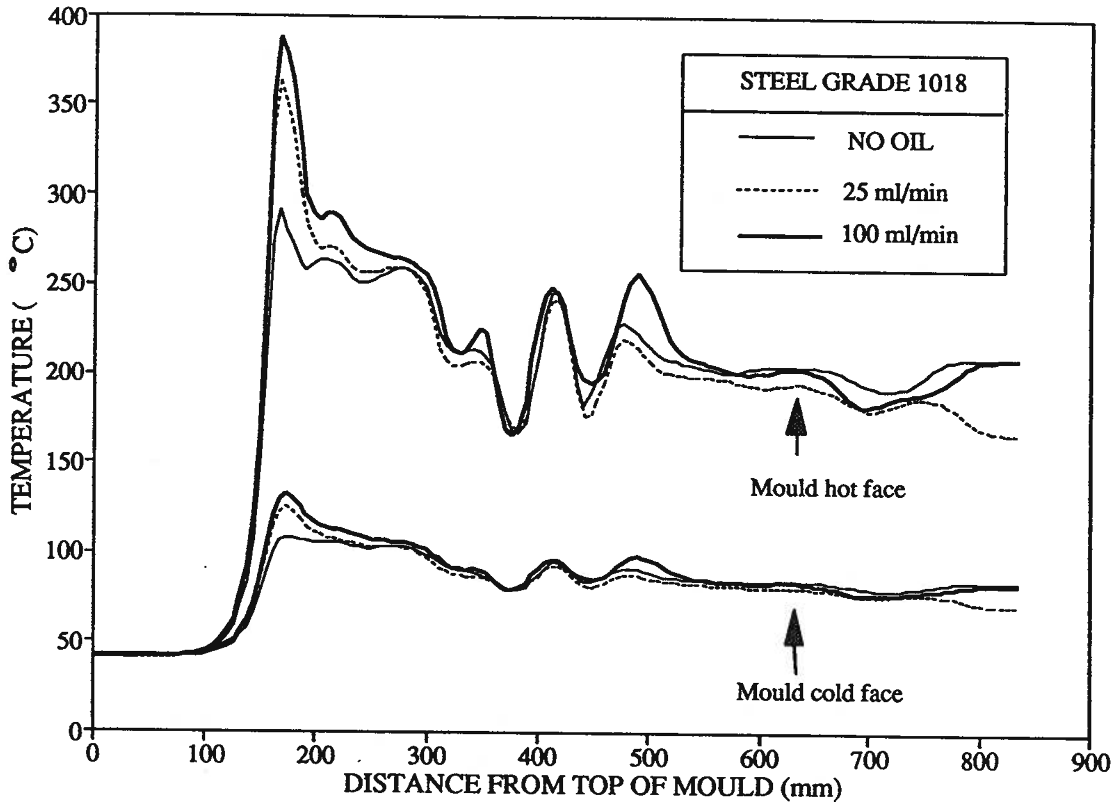

Figure 8.6 Mould hot face temperature during casting of 1018 grade steel billets with Canola oil at 0, 25 and 100 ml/min at Company C.

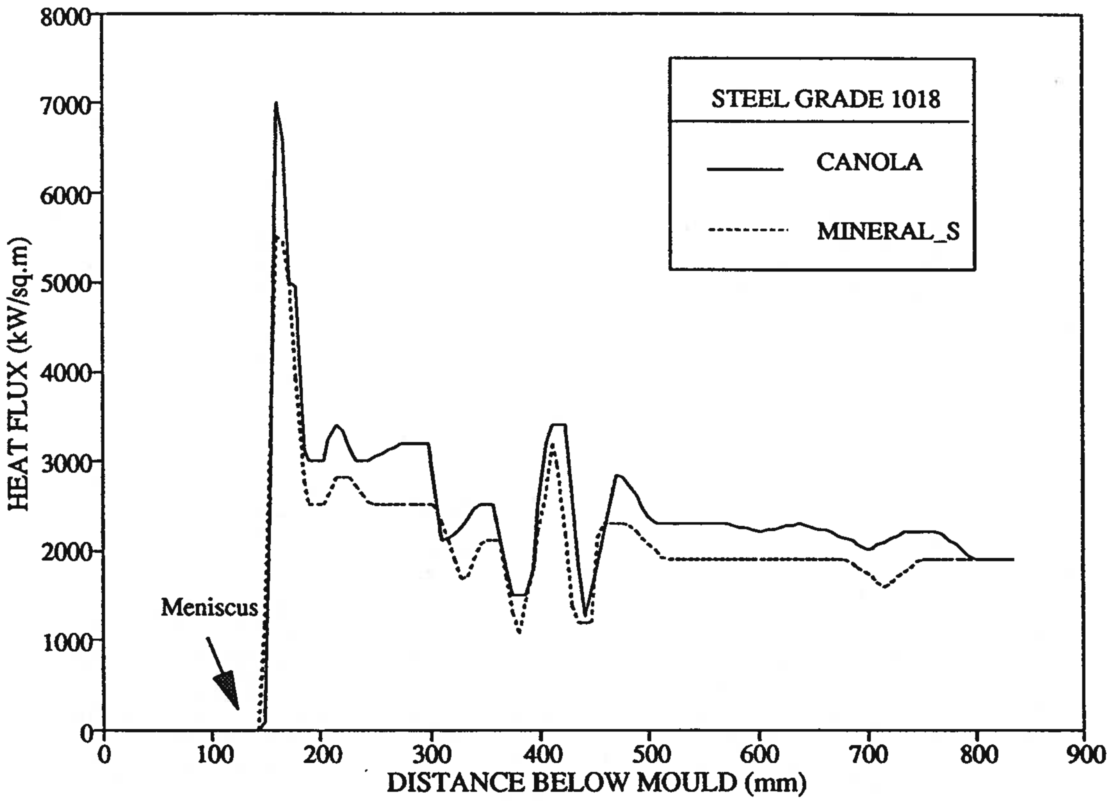

Figure 8.7 Heat-Flux profiles for 1018 grade steel billet cast with Canola, HEAR, Mineral_O and Mineral_S lubricating oil at 25 ml/min. (Note : the plots for Mineral_O and HEAR oils lie between those for Canola and Mineral_S oils but have been omitted for clarity).

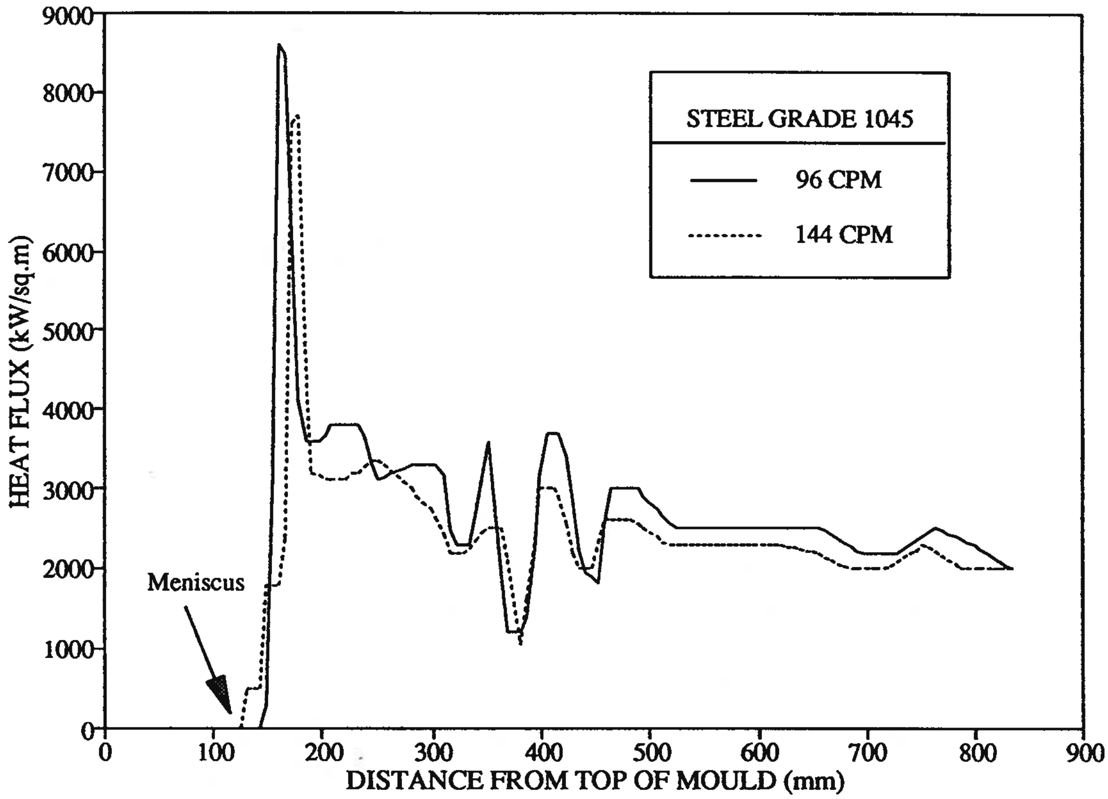

Figure 8.8 Heat-Flux profiles for 1045 grade steel billets cast at mould oscillation frequencies of 96 and 144 cpm at Company C.

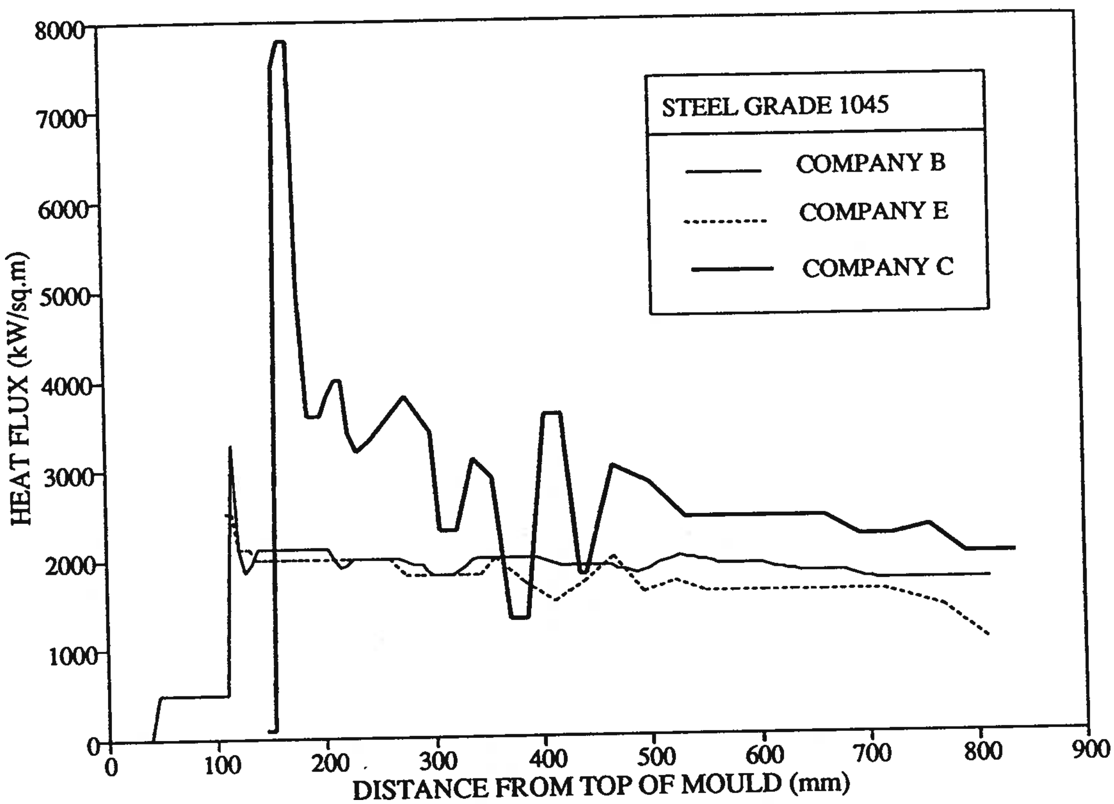

Figure 8.9 Heat-Flux profiles for 1045 grade steel billets cast at Companies B, E and C.

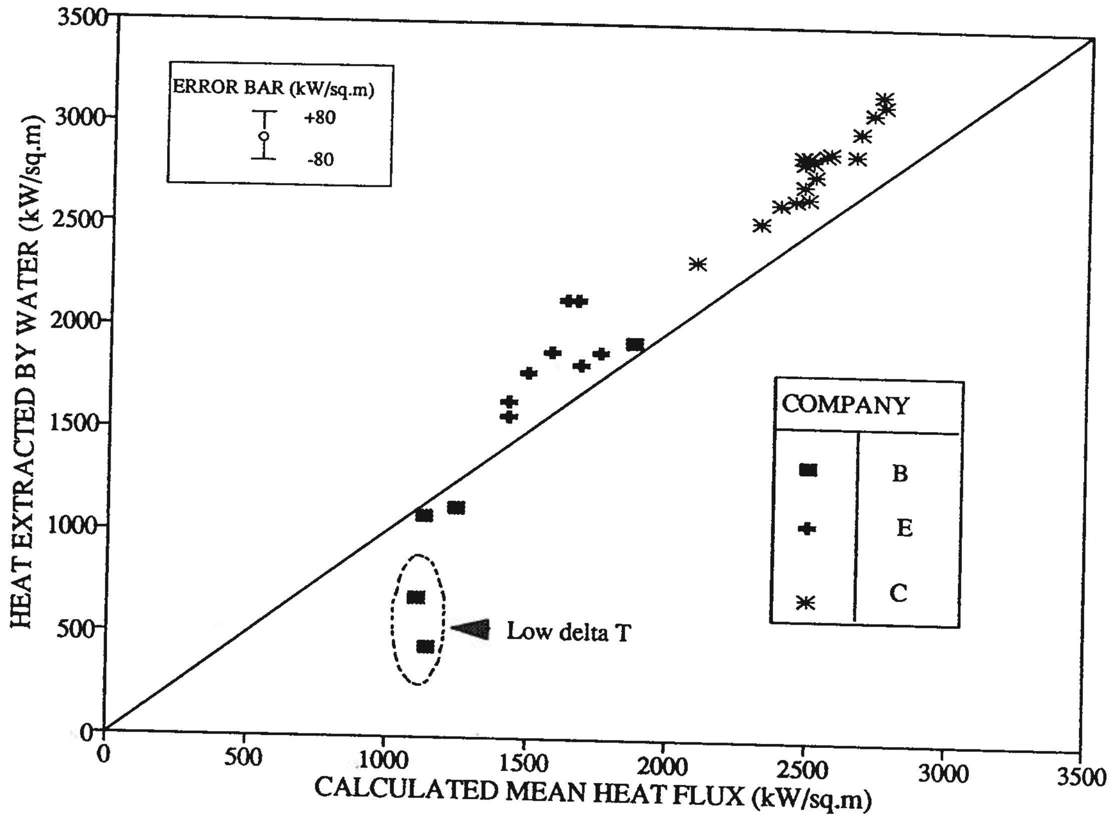

Figure 8.10 Graph showing the match between predicted heat extraction rate in the mould and the heat extracted by the mould cooling water.

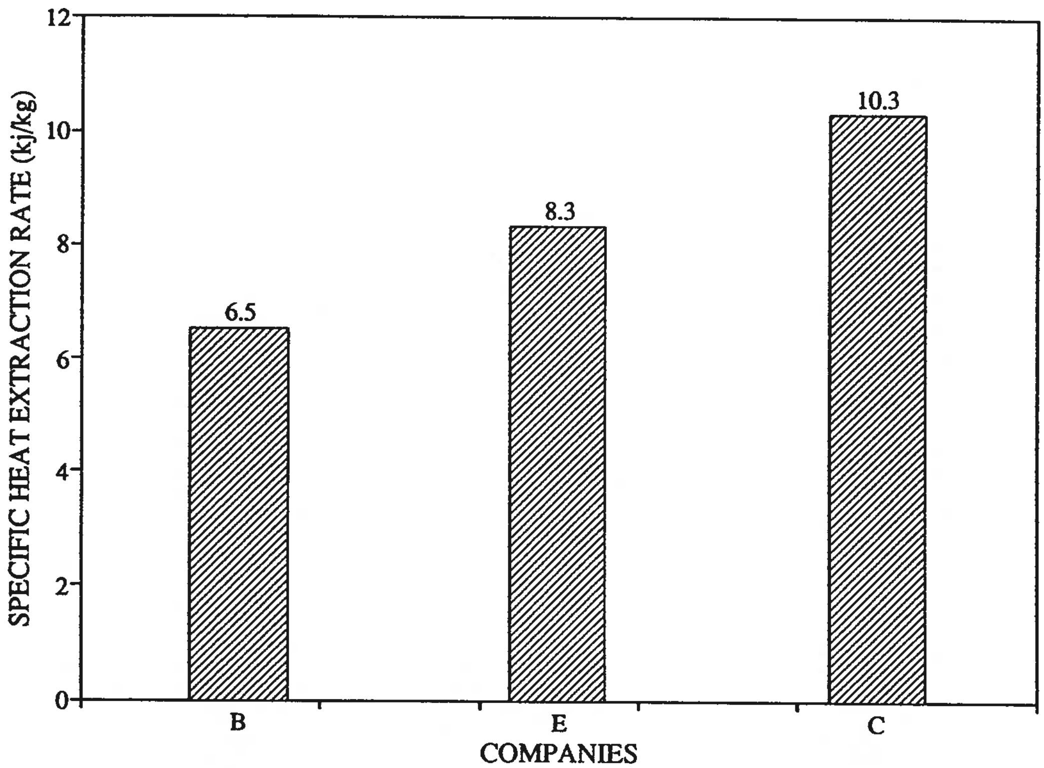

Figure 8.11 Specific heat extraction rate (kj/kg), for the moulds at Companies B, E and C.

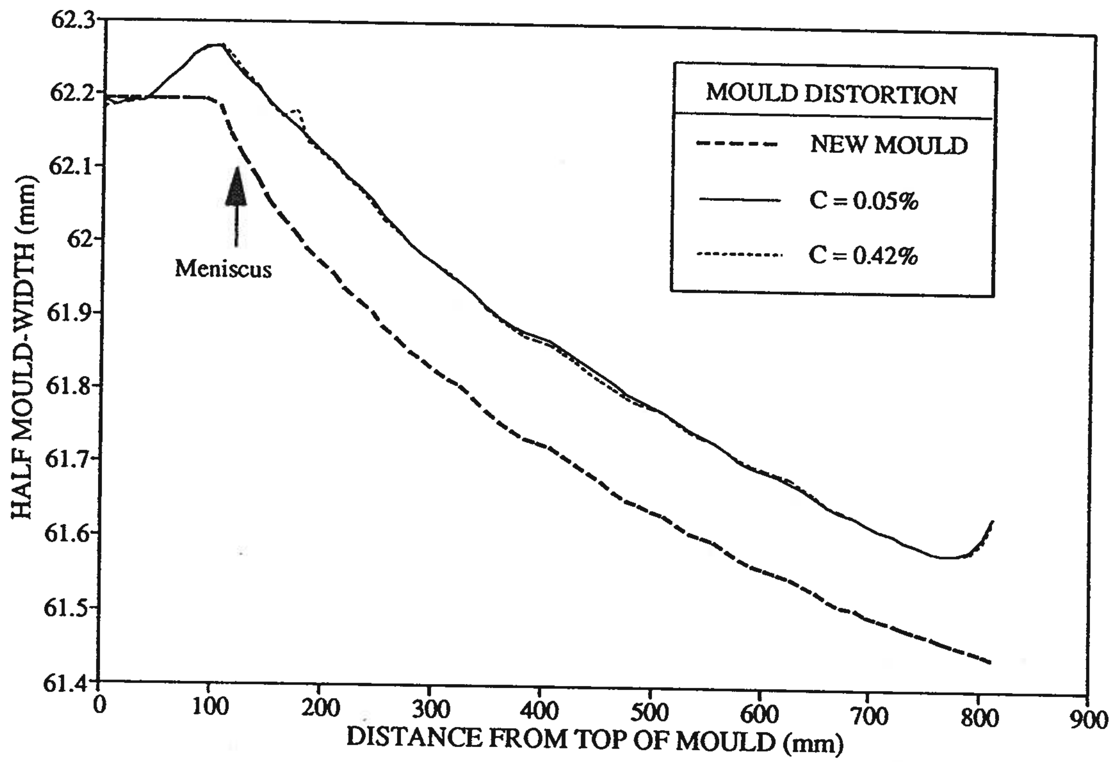

Figure 8.12 Calculated distortion of the mould during the casting of low and high carbon heats at Company B.

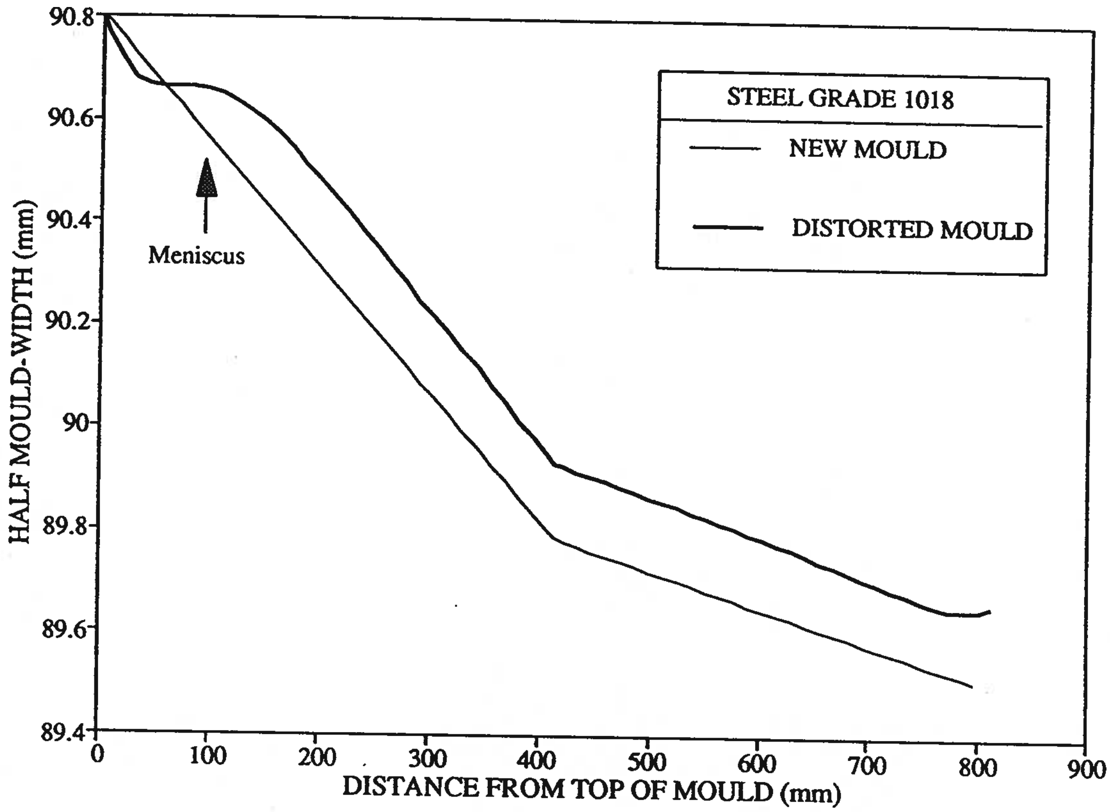

Figure 8.13 Computed distortion of the mould during service at Company E.

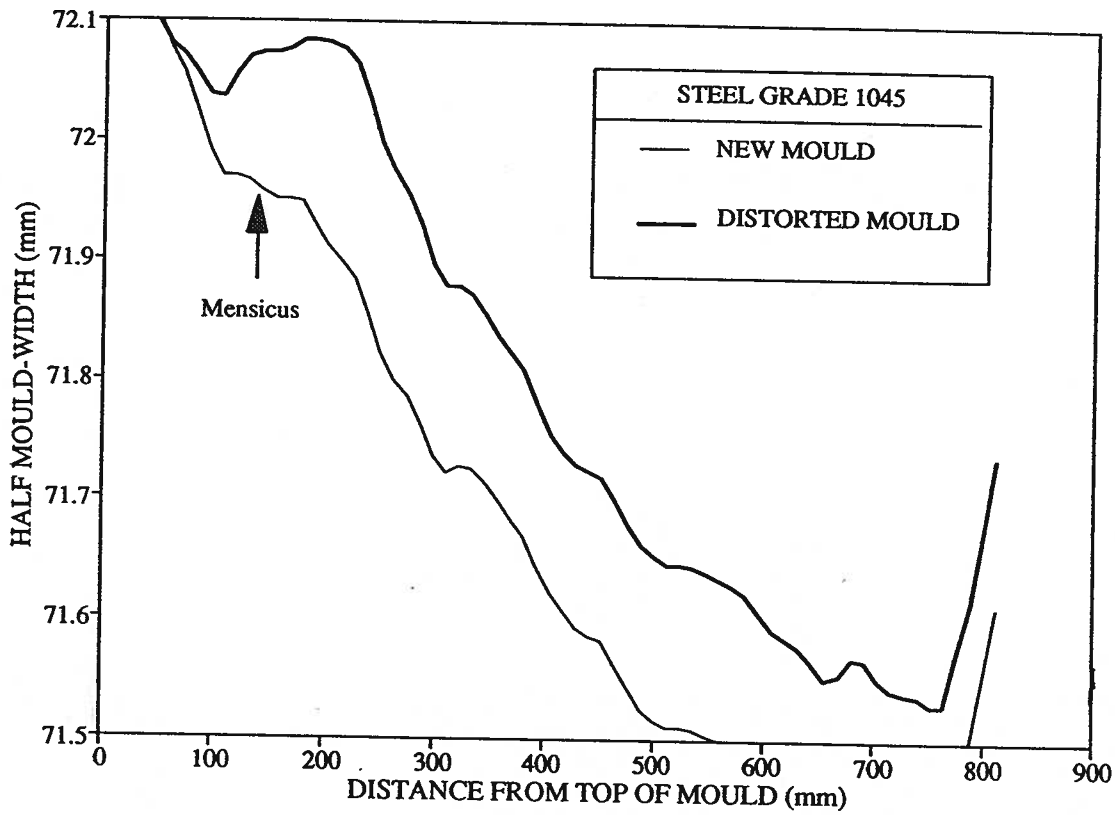

Figure 8.14 Computed distortion of the mould during service at Company C.

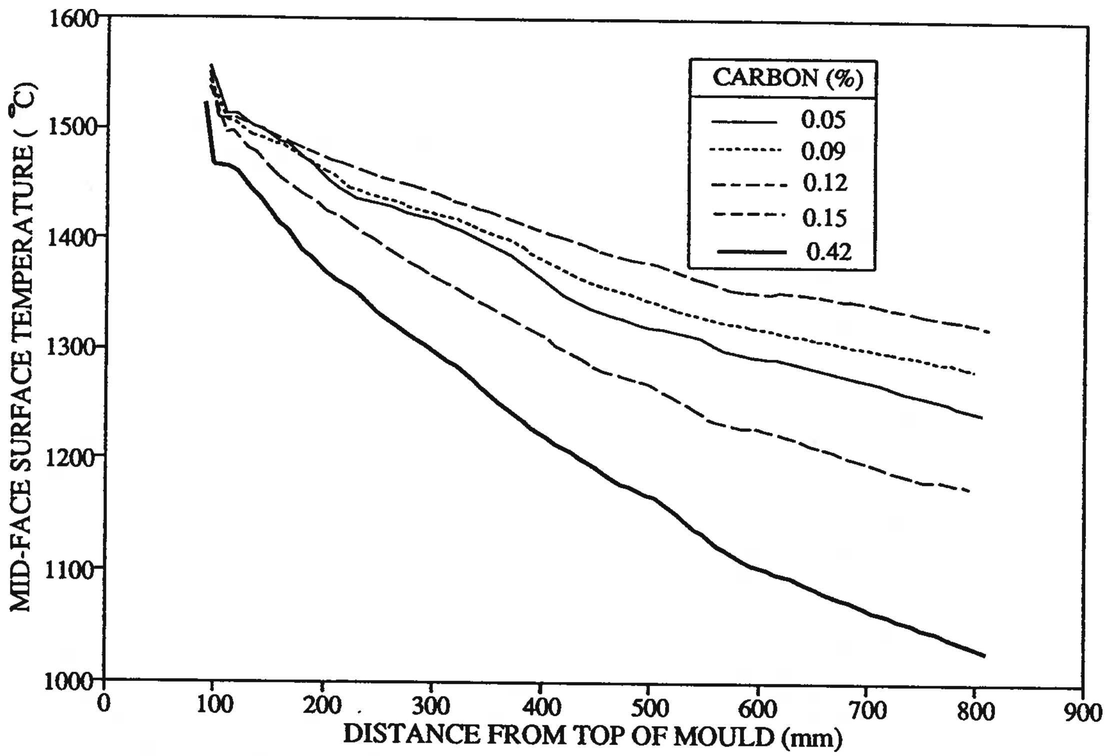

Figure 8.15 Surface temperature at the mid-face of the billet for different grades at Company B.

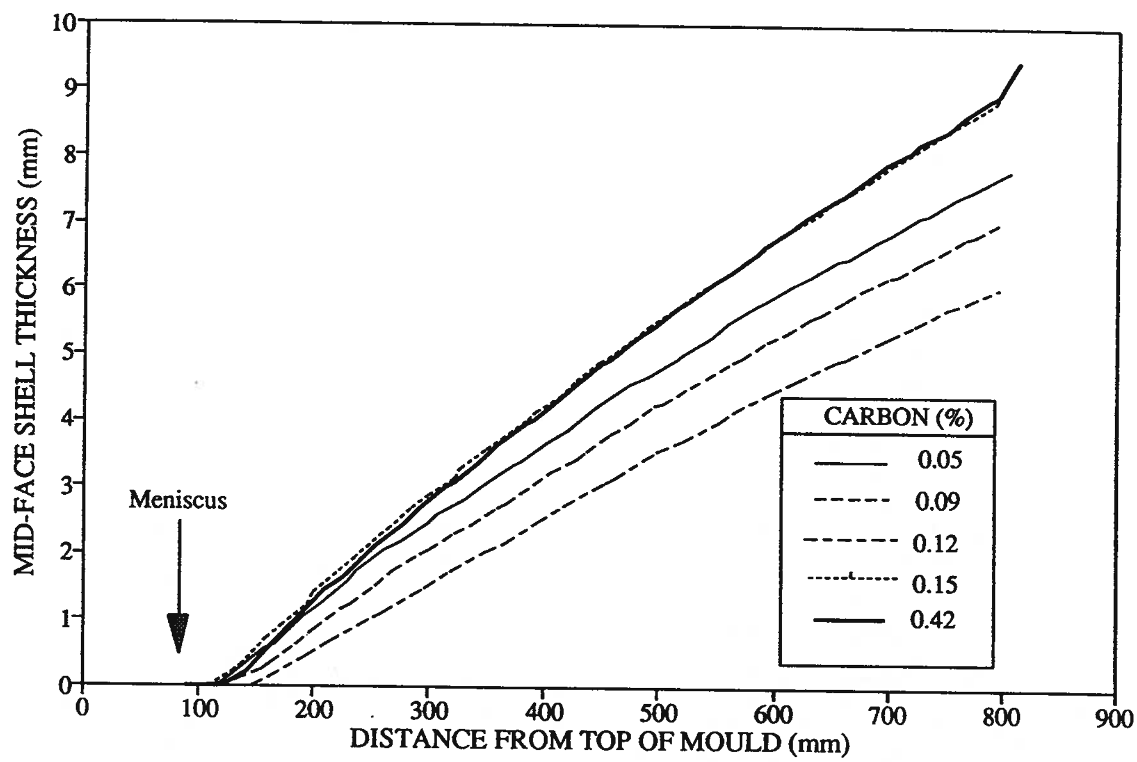

Figure 8.16 Shell thickness at the mid-face of the billets for different steel grades at Company B.

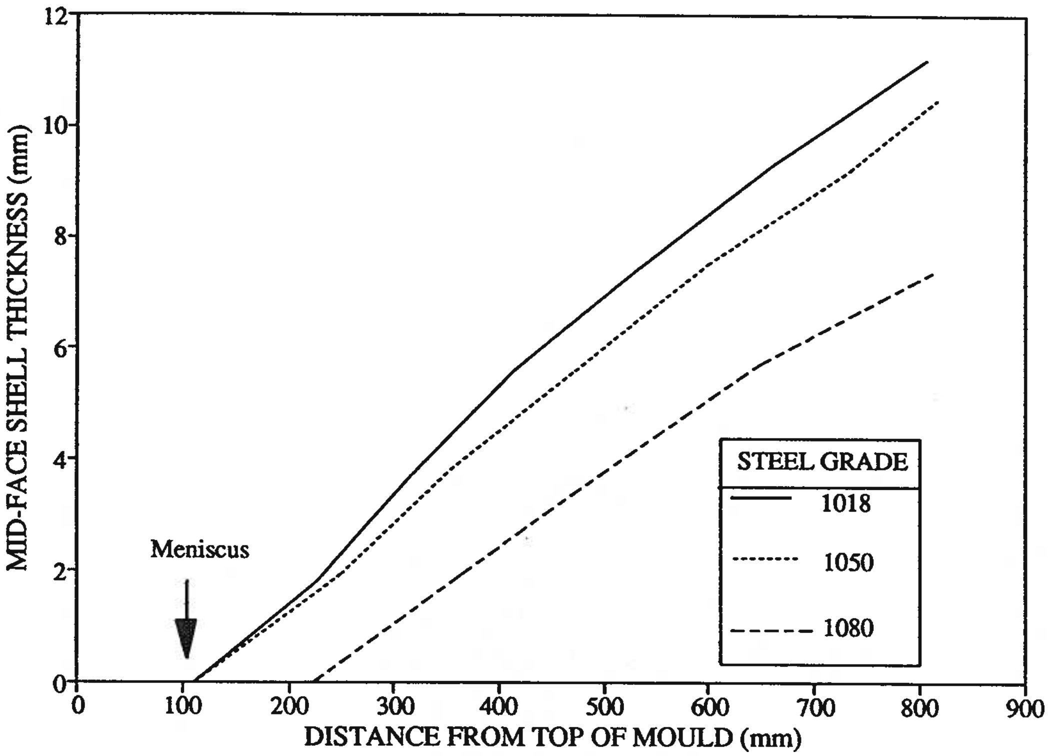

Figure 8.17 Shell thickness at the mid-face of the billets for different steel grades at Company E.

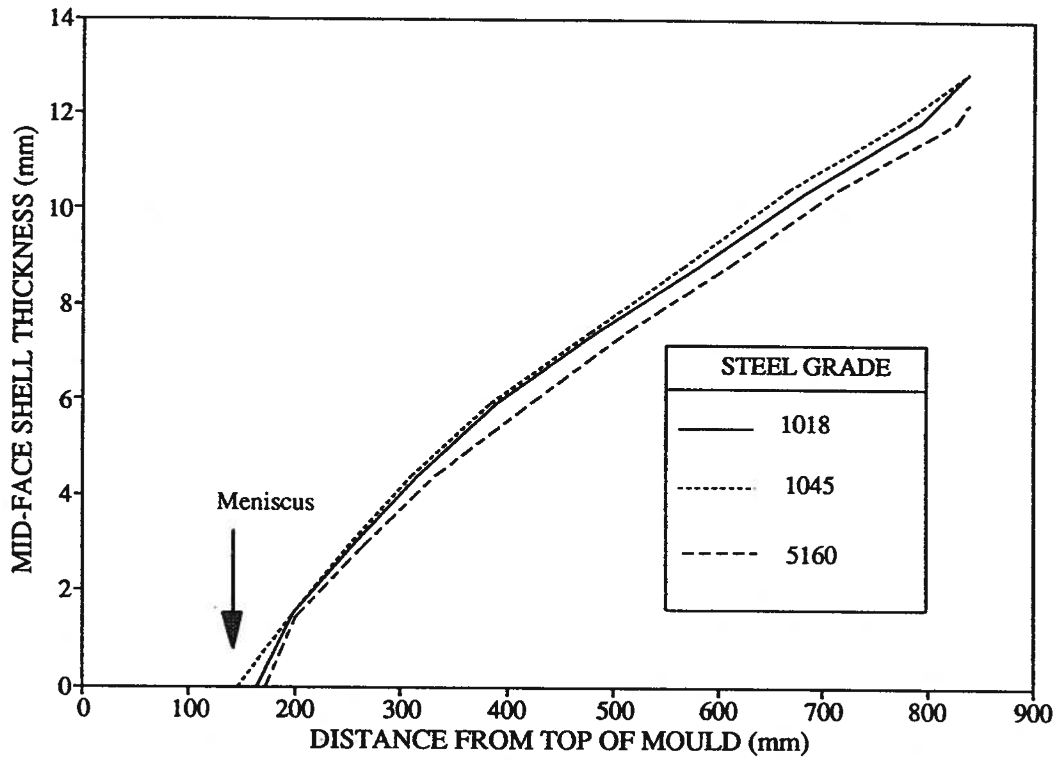

Figure 8.18 Shell thickness at the mid-face of the billets for different steel grades at Company C.

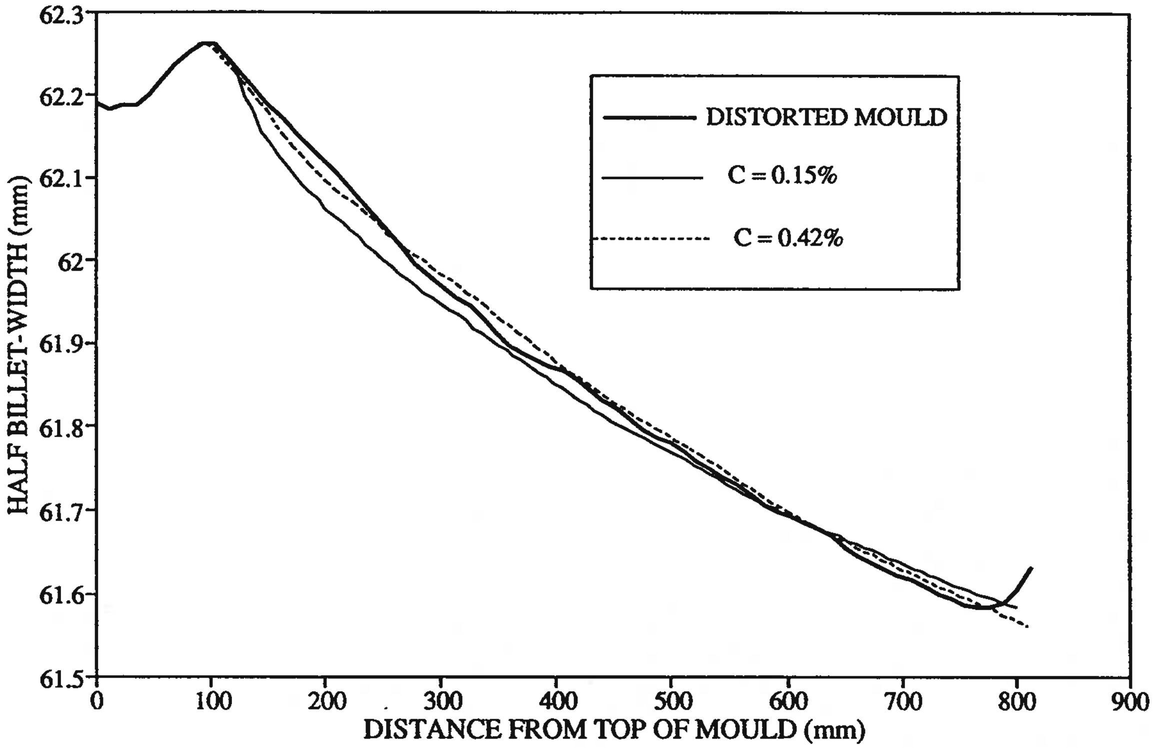

Figure 8.19 Billet shrinkage profile, at Company B, for "medium" and "high" carbon steels.

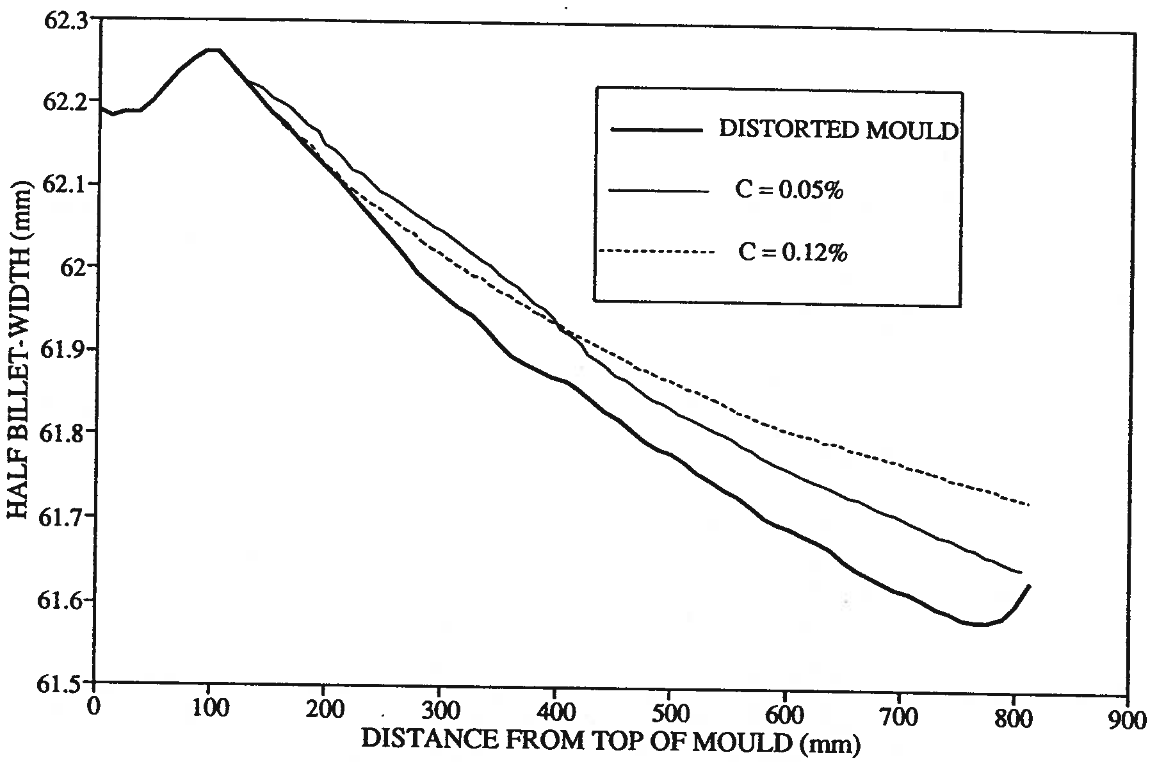

Figure 8.20 Billet shrinkage profile, at Company B, for low carbon steels.

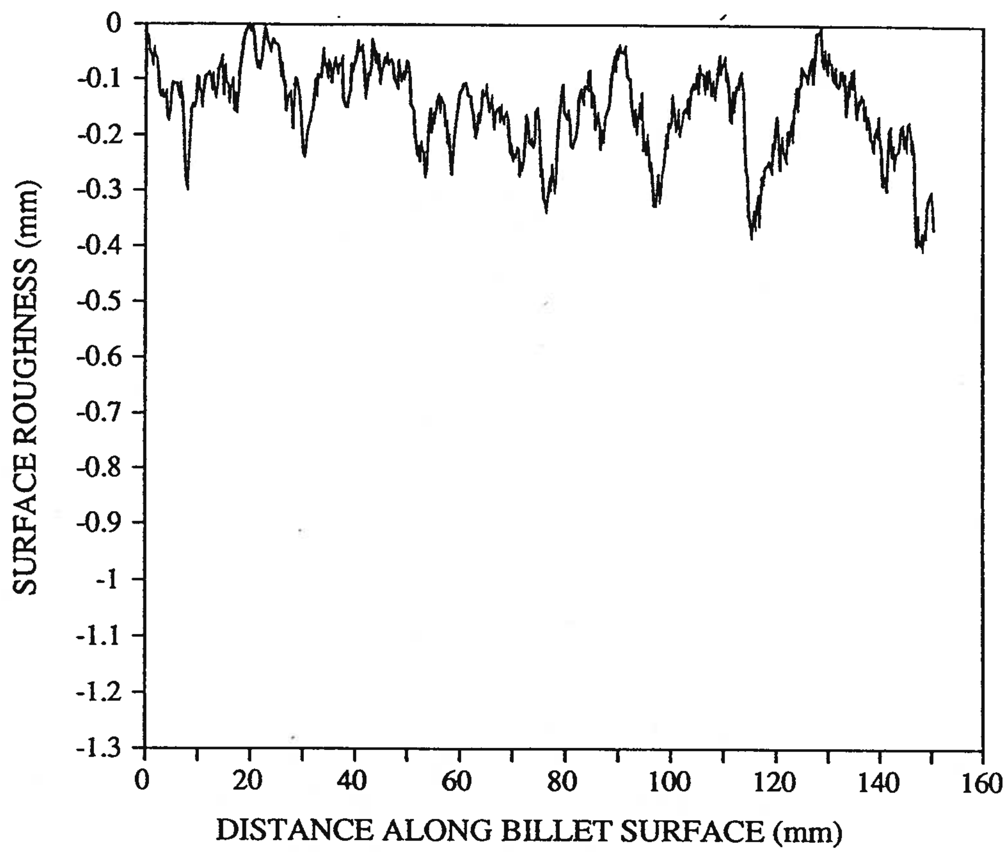

Figure 8.21 Surface roughness of a "high" carbon steel billet cast at Company B.

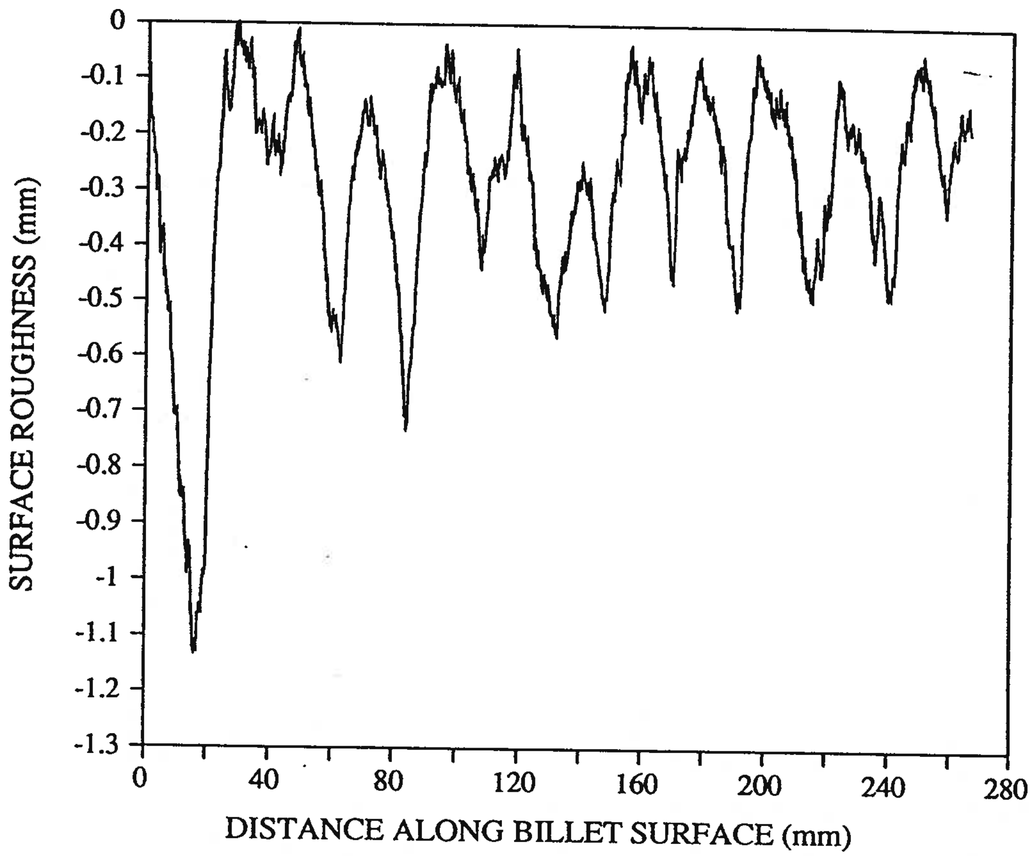

Figure 8.22 Surface roughness of a low carbon steel billet cast at Company B.

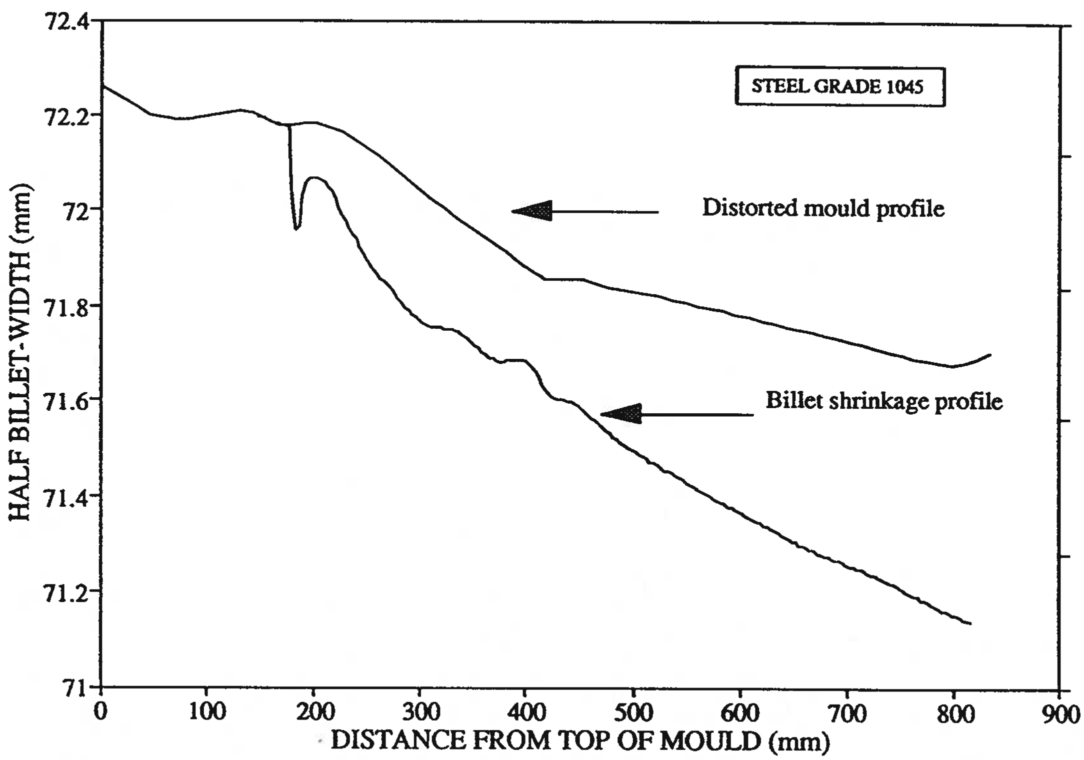

Figure 8.23 Billet shrinkage profile for 1045 grade steel cast at Company C.

Chapter 9 : MECHANISM OF MOULD HEAT TRANSFER

A mechanism for heat transfer in the mould is developed in this chapter by linking the results obtained from various mathematical models. It will be shown in this chapter that, from the stand point of heat transfer, the mould can be divided into different zones. As an aid to understanding the various zones in the mould, a classical resistance analysis of mould heat transfer is carried out as discussed in an earlier work by Samarasekera and Brimacombe [29].

Under conditions of steady state, one-dimensional heat flow (which is approximately true in continuous casting), the heat flux from the solidification front at the solidus temperature T_s to the cooling water at temperature T_w can be written as follows:

$$q = \frac{1}{R_T}(T_s - T_w) \tag{9.1}$$

where R_T, the total resistance to heat flow, is given by

$$R_T = \frac{\delta_s}{K_s} + R_g + \frac{\delta_m}{K_m} + \frac{1}{h_w} \tag{9.2}$$

where the terms refer respectively to in order, to the thermal resistances offered by the shell, the gap width, the mould wall and the mould cooling water.

It can be shown that the thermal resistances of the mould wall (~ 0.40 cm^2 °C/W) and the cooling water (~ 0.25 cm^2 °C/W) together do not amount to more than 10% of the total thermal resistance. Clearly then the magnitude of the resistance of the mould-billet gap and the solid shell determine the heat flow in the mould. The relative importance of the resistance of the two items can be seen in Figures 9.1 to 9.3 where the axial profiles of the gap and the shell thermal resistances have been plotted as a percentage of the total resistance. In keeping with the results of an earlier work [29], the gap resistance dominates in the top half of the mould while the shell resistance begins to exert its influence on heat flow towards the bottom of the mould. Heat transfer in the upper half of the mould is, thus, influenced by factors that influence the gap width and conductivity while factors that alter both the width of the gap as well as the thickness of the solid shell determine the heat transfer in the lower part of mould. It will be shown that based on a systematic analysis of the mould temperature data, the mould can be divided into three zones from the view point of heat transfer as shown in Figure 9.4.

Zone I — This zone extends from the meniscus downwards to a distance of approximately 30 - 40 mm. Heat transfer in the zone is predominantly affected by the mechanical interaction between the mould and the billet.

Zone II — This zone immediately follows Zone I and extends for 100 - 150 mm. Heat transfer in this zone is principally affected by the behaviour of the mould lubricating oil.

Zone III — This zone extends from the end of Zone II to the bottom of the mould. Heat transfer in this zone is primarily influenced by the pitch and depth of oscillation marks.

The various pieces of evidence that lead to the division of the mould in the zones described above are presented in the sections that follow.

9.1 Heat Transfer in Zone I

The extent of this zone is obtained by a consideration of the length over which the mechanical interaction between the mould and billet takes place. It is related to the stroke length of the mould oscillation and the normal metal level fluctuations in any casting operation. This would put the length of the zone in the range of 30 - 40 mm. The width of the stain marks on the chrome plating on the mould is of the same order as well.

9.1.1 The role of mould shape in the heat transfer in Zone I

It has been shown in the previous chapter that whether or not an operating mould acquires a negative taper at the meniscus depends primarily on the upper taper (shallow at Plant C or steep at

Plants B and E). This, as explained in the preceding chapter, is because the outward bulging of the mould wall, that brings about the negative taper of the upper part of the mould, can be compensated by a pre-existing (steep) positive taper. As a result, a very steeply (positively) tapered, (2 - 3 %/m), mould may acquire, during service, a "neutral taper" or even retain some of its original positive taper.

It proposed that a mould with a large negative taper at the meniscus, would interact most strongly with the solidifying shell during the period of negative strip. It is further proposed that this enhanced interaction is responsible for improved billet-mould heat transfer leading to a high value of heat flux in the meniscus region. The following paragraphs present evidence for this contention.

Figures 9.5 and 9.6 are schematic diagrams of moulds that during service have acquired a *neutral* and a *steep negative* taper respectively. Thus in the former case, during the negative strip period when the mould descends faster than the billet, Figure 9.5, there will be a friction force acting on the billet dragging it down. An equal and opposite reaction force on the mould will act upwards, thereby *reducing the compressive load sensed by the load cells*. In the case of the steeply negatively tapered mould (Figure 9.6), in addition to the above mentioned friction force, there will be another force arising from the *physical "obstruction"* or resistance from the billet as the negatively tapered portion of the mould tries to squeeze past the billet. A strongly negatively tapered mould would thus squeeze the billet for a greater proportion of the negative strip period than would a mould with a neutral taper. Such a squeezing action is expected to enhance heat transfer. The "squeezing" referred to above arises only on account of the negatively tapered mould wall and is likely to be minimal for a mould with neutral taper.

Figures 5.34 to 5.36 are presented as evidence of increased mould-billet interaction. These figures are the load cell signals (one cycle only) together with the mould displacement curve, obtained at the three plants. The position of cross markers refer to beginning and the end of the negative strip period while the position of the square marker indicates the period for which the load cells are decompressed. Thus the location of the square marker relative to the cross markers is a measure of the percentage of the negative strip time for which the load cell is decompressed - *a large percentage would indicate greater mould-billet interaction.* (As mentioned in Chapter 4, on account of differences in pre-loads of the load cells as well as the distribution of the load between the bolts, O-rings, springs and the load cells, it is not possible to compare the absolute values of loads among the three plants). *It can be seen that the period for which the load cell is decompressed (enhanced mould-billet interaction) is around 50-55% at Plant B and E and in excess of 70% at Plant C.*

Evidence of increased mould-billet interaction can also be seen in the oscillation mark depth of billets cast with a steeply tapered parabolic mould and a shallow double tapered mould. Figure 9.7 shows the oscillation mark depth on the billet cast through parabolic moulds on both the test and the control strands at Company B. Although the test strand operated with a shorter stroke and lower negative strip time (9.5 mm, 0.13 s) than the control strand (12.7 mm, 0.17s) there is little difference in the depth of oscillation marks on the billets from the two strands which is contrary to earlier findings [81]. Following the trial at Company B, the mould tubes on the test and control strands were replaced with double-tapered tubes which the company conventionally employs; the upper taper of the tubes is designed for 2.75%/m taper over the first 333 mm followed by a second taper of 0.5%/m. The billets cast on the test strand with a lower negative-strip time (0.13 s) and on the control strand with higher negative strip time of 0.17 s were also subjected to an evaluation of surface roughness. Figure 9.8 shows the results of the surface topography measurements made on 0.052% carbon billets casts through the conventional double-taper moulds and a remarkable improvement in the formation of oscillation marks can be seen on billets cast with lower negative-strip time. This clearly indicates that in case of the parabolic mould, there is very little interaction of the mould with the billet and hence the oscillation mark depth are insensitive to differences in stroke length and negative strip time. Significant interaction, in the case of the double tapered mould, arising from the negative taper that such a mould acquires during service, causes deeper oscillation marks on billet cast with longer stroke lengths and negative-strip times.

It will now be shown that increased mould-billet interaction leads to a higher rate of heat transfer. The first evidence of the effect can be seen in Figure 9.9 which shows the decompression load (i.e. the amount of decompression the load cell experiences during the negative strip period - a measure of mould-billet interaction) for 1018 grade steels at Plant C against the heat flux in the meniscus region. (Note : Since all data refers to the same plant differences arising out of load partitioning and pre-load of load cells can be ignored and loads can then be analysed as a measure of mould-billet interaction). The figure clearly shows that an increase in the decompression load (more mould-billet interaction) leads to higher rates of heat transfer.

A *second piece of evidence* can be seen in Figure 9.10 which is a plot of the period for which decompression of the load cell (an alternate indicator of mould-billet interaction) takes place versus the heat transfer in the meniscus region for 1045 grade steel cast at Company C. Again the influence of enhanced mould billet interaction on the heat transfer rate in the meniscus region is obvious - enhanced interaction leads to improved heat transfer.

A *third piece of evidence* is apparent in Figure 9.11 which shows the heat flux in the meniscus region plotted as a function of the percentage of the negative strip time for which the decompression of the load cell takes place. The plot corresponds to heat fluxes obtained at two different frequencies of mould oscillation, 144 cpm and 96 cpm. The lower oscillation frequency has a higher negative strip time (0.19 seconds) compared to the negative strip time of 0.16 seconds for 144 cpm of mould oscillation (Table 4.3). As before the higher negative strip time causes a larger heat extraction in the meniscus region on account of the increased period of mould-billet interaction. It is intriguing, however, to note that the increase in the negative strip time (with a decrease in the mould oscillation frequency) leads to an increase in the percentage of the negative strip period, for which the decompression of the load cell takes place, from 70% to over 85% of the negative strip time. *This can only be explained by considering that an increase in the heat transfer, arising from a longer negative strip period, causes the mould to acquire an even greater negative taper. This increased negative taper in turn leads to a further increase in the period of mould-billet interaction causing the decompression time to increase from 70% to about 90% of the negative strip time.*

Indirect evidence of enhanced heat transfer in the meniscus region arising from increased mould-billet interaction was also found, as follows :

[1] Figure 9.12 shows the heat flux profile on two adjacent walls (ICW and RSW) of the mould at Plant C. The differences in heat fluxes in the meniscus region on adjacent mould walls have been observed in earlier plant trials too but have been attributed to the unequal distortion of the adjacent mould wall arising from a two sided mould constraint [29]. As the mould at Company C has a four-sided constraint (Table 4.2), the two heat fluxes are expected to have the same value in the meniscus region. The reason why it is not so can be inferred from Figure 9.13 which shows the (computed) distorted mould profile at the mid-face of the two adjacent walls. The higher negative taper on the inner-curved wall (that should lead to enhanced mould-billet interaction with that face) is clearly visible. This supports the theory that the mould shape affects the heat transfer in the meniscus region.

[2] As mentioned in an earlier chapter, Singh and Blazek [33], had reported peak heat fluxes of 3000 - 3200 kW/m^2, while casting steel billets with 0.40% C through an experimental mould. This range is considerably lower than the value of 7800 kW/m^2 obtained while casting the same grade at Company C. The experiments by Singh and Blazek were carried out on

a mould which was very different from a conventional mould in particular with regard to its distortion characteristics. The authors point out that their experimental mould was so designed as to "prevent" mould distortion. Such an experimental mould would, therefore, not acquire a negative taper and would have a lower heat transfer rate at the meniscus than an industrial mould such as that used in Company C.

[3] In an earlier trial Brimacombe and Samarasekera [29] have reported a meniscus heat flux of 3000 kW/m^2 with a double tapered mould (2.6 %/m upper taper) and around 4200 kW/m^2 with a single tapered mould (0.6%m). The lower heat transfer in the case of double taper mould can be explained by the lack of negative taper (and, therefore, lower mould-billet interaction), relative to a the single tapered mould.

[4] In an industrial trial Samarasekera, Brimacombe and Bommaraju [17], have shown a significant increase in meniscus heat transfer from 4000 kW/m^2 to 5000 kW/m^2 with a decrease in the mould cooling water velocity from 7.0 m/s to 5.0 m/s. Such an increase in the meniscus heat transfer can be explained by considering the impact of cooling water velocity on mould distortion. As the mould becomes hotter with a decrease in mould cooling water velocity, its distortion and thus, its negative taper, increases. Such an increase in negative taper would lead to increased mould-billet interaction and therefore heat transfer at the meniscus.

[5] Evidence of a decrease in heat transfer with increasing mould taper is also apparent from the work of Lorento [82] in which he has shown an improvement in billet rhomboidity with change in mould taper from single to parabolic. The difference in diagonals of billets decreased for a 0.40% C steel from 13 mm (single taper mould), 8 mm (double taper mould), to 3 mm (parabolic taper mould). If this data is reviewed in light of the effect of mould taper on heat fluxes, it clearly points to a decrease in heat transfer as the mould taper changes from a single shallow taper to a steep parabolic taper. The decrease in heat transfer arising

from a progressive increase in the initial positive taper (and a resulting decrease in mould negative taper), probably lowers the cold face temperature of the mould below that necessary to cause boiling of the water in the mould cooling channel. As boiling is suppressed the tendency of the billet to assume a rhomboid shape is also reduced [18].

[6] As another indirect evidence of the role of mould shape on heat transfer, the average depth of off-corner cracks on the billets from the control and test strands of Company E can be examined. On average, the off-corner cracks are deeper on the test strands than on the control strand by 1-2 mm. Since the mechanism of cracking is undoubtedly the same on both strands (viz. bulging in the mould), the above observation suggests that the shell thickness at the bottom of the test strand is 1-2 mm greater than that on the control strand. This implies greater heat transfer in the test strand mould. Table 4.2 summarizes the various features of the test and control strands and an important difference between the two is the 2.7 %/m taper of the test strand versus the 3.6 %/m taper of the control strand. When in use the steeper taper mould would certainly not have any negative taper and therefore lead to a lower heat transfer in the mould.

Finally, Figure 9.14 which is a bar graph of the peak heat flux, as measured in plant trials, in the meniscus region for moulds with different initial tapers clearly shows that the creation of a negative taper in mould with shallow initial positive taper, causes a greater amount of heat to be extracted by the mould in the meniscus region.

9.2 Heat Transfer in Zone II

The extent of this zone is obtained by examining Figure 8.9 which is a plot of the heat flux obtained at the three plants. The figure indicates that the heat transfer at all three companies becomes roughly of the same order at around 350 mm from the top of the mould which is approximately 200 mm from the meniscus. Taking away the length of zone I (~ 40 mm), this leaves about 100-150 mm as the length of zone II.

The role of oil in mould heat transfer

The role of oil in the enhancement of heat transfer has been shown in the previous chapter. Figure 9.15 shows the hot face temperature of the mould for a 1045 grade steel cast at Plants B, E and C. The strikingly higher hot face temperature of the mould at Plant C is immediately obvious. On account of the higher heat transfer, due to a strongly negatively tapered mould, at Company C, the hot face temperature of 270°C (Figure 8.6, no oil case) is well above the boiling point of the lubricating oils and much below it at Companies B and E. *It is thus proposed, that an increase in* mould heat transfer beyond that obtained from t*he mould shape, can be affected by the oil provided the hot face temperature of the mould exceeds the boiling point of the lubricating oil, thereby allowing the oil to boil and contribute to the high heat conductivity of the mould-billet gap*. Furthermore, with the enhancement in heat transfer the hot face temperature of the mould at Company C exceeds 350 °C.

That the presence of hydrogen gas in the gap can significantly enhance heat transfer can be seen from the Figure 9.16 where the heat flux between the billet surface and the mould is computed for different levels of hydrogen contents of the gap. (The thermal conductivity of the mould-billet gap is assumed to be given by the law of mixtures). From Figure 9.19 it is clear that at mould-billet gap width of 0.02 mm, the presence of just 25% of hydrogen gas, in the mould-billet gap, is sufficient to increase the heat flux from ~ 3000 kW/m^2 to ~ 7000 kW/m^2.

The fact that the hot face temperature of the mould needs to be above the boiling point of the oil before any enhancement of heat transfer takes place, is supported, indirectly by the following two findings.

[A] Despite the high flow rate of oil at Companies B and E (54 ml/min and 70 ml/min respectively), the heat transfer in the meniscus region is far lower than that obtained at C with 25 ml/min of oil. This suggests that oil does not contribute significantly to the heat transfer at Companies B and E.

[B] Brendzy [13] has shown a dependence of the mould friction force on the oil flow rate. It was shown in her work that a decrease in the oil flow rate at company B led to an increase in the friction force, as inferred from the continuously increasing profile of the load cell signal during the upstroke of the mould. *Load cell signals from Plant C, however, are unaffected by the oil flow rate (Chapter 5) and, regardless of the flow rate (25 ml/min or 100 ml/min), are of the type categorised as "high friction" response by Brendzy.* This would suggest once again that on account of the high hot face temperature of the mould at company C, almost all oil vapourises in the meniscus region creating adverse conditions for lubrication. This is the downside of the high heat transfer rate in the mould.

Notwithstanding the "high friction" condition suggested by the load cell response at Company C, it remains a fact that the low-carbon billet surfaces themselves did not appear to be affected adversely as can be seen in Figure 5.94. This observation is consistent with that of Brendzy who found that a reduction in the oil flow rate resulted in an adverse lubrication condition but did not lead to any measurable deterioration in the billet quality in the range of carbon steels studied (C < 0.45%).

An implication of the above discussion is that high carbon steel billets (C > 0.60%) which, on account of their long freezing range, form an extremely thin shell in the meniscus region, are the ones most likely to feel the impact of adverse lubrication condition. This, in part, may explain the bleeds and laps associated with casting these high carbon billets at a company with a mould similar to that at Company C [83].

9.3 Heat Transfer in Zone III

Figures 9.1 - 9.3, show that the effect of the resistance of the solid shell, on the total resistance to heat flow, begins to become significant in the lower part of the mould (zone III). This should not be taken to mean, that the resistance of the gap ceases to be important; the first statement only emphasizes the fact that in the lower part of the mould, both the shell resistance as well as the gap resistance have a comparable effect on the heat flow.

The importance of the oscillation frequency on heat transfer in this region of the mould can be seen in the heat flux obtained in Company C at 144 and 96 cpm of mould oscillation (Figure 8.8). As mentioned in the previous chapter, at a lower frequency there are 47 oscillation marks per meter of the billet at 96 cpm compared to 71 in the other case. It should be noted that the average depth of oscillation marks in the two cases was the same, about 0.18 mm. To assess the effect of the difference in the pitch of the oscillation marks on the observed heat flux, the resistance to heat flow was plotted for the two cases (Figures 9.17 and 9.18). Thus, the shell resistance is the same in the two cases, but the average gap resistance, in zone III, for billets cast at 144 cpm of mould oscillation is 2.75 $cm^2\,°C/W$ compared to 1.90 $cm^2\,°C/W$ in the latter case. *These resistance are in the same ratio (~1.5) as the ratio of the pitch of the oscillation marks.* This clearly proves that the enhancement in heat transfer on account of a decrease in mould oscillation frequency arises from a decrease in the pitch of the oscillation mark leading to a relatively lower gap resistance compared to the resistance of the oscillation mark in billets cast at higher mould oscillation frequency.

9.4 Interaction of Zones

It has been shown that the shape of the mould at the meniscus and the interaction of the mould with the solidifying shell during the negative strip time is the predominant factor influencing heat transfer in Zone I. The negative taper of the mould is influenced, among other factors, by the temperature of the mould wall in Zone II. The temperature of the mould wall in Zone II is, in turn, largely influenced by the boiling of oil leading to the presence of Hydrogen gas in the gap. *Thus indirectly, oil plays a role in heat transfer in Zone I as well.*

The presence of oil in the gap between the mould and the billet would also affect the heat transfer in Zone III, by increasing the thermal conductivity of the gap. This effect clearly will be diminished because both the shell resistance and the gap resistance play an equally important role in heat transfer in Zone III. The presence of hydrogen in the gap in the lower part of the mould is probably responsible for the higher heat transfer in Zone III for the mould at Company C as compared to Companies B and E. (Figure 8.9).

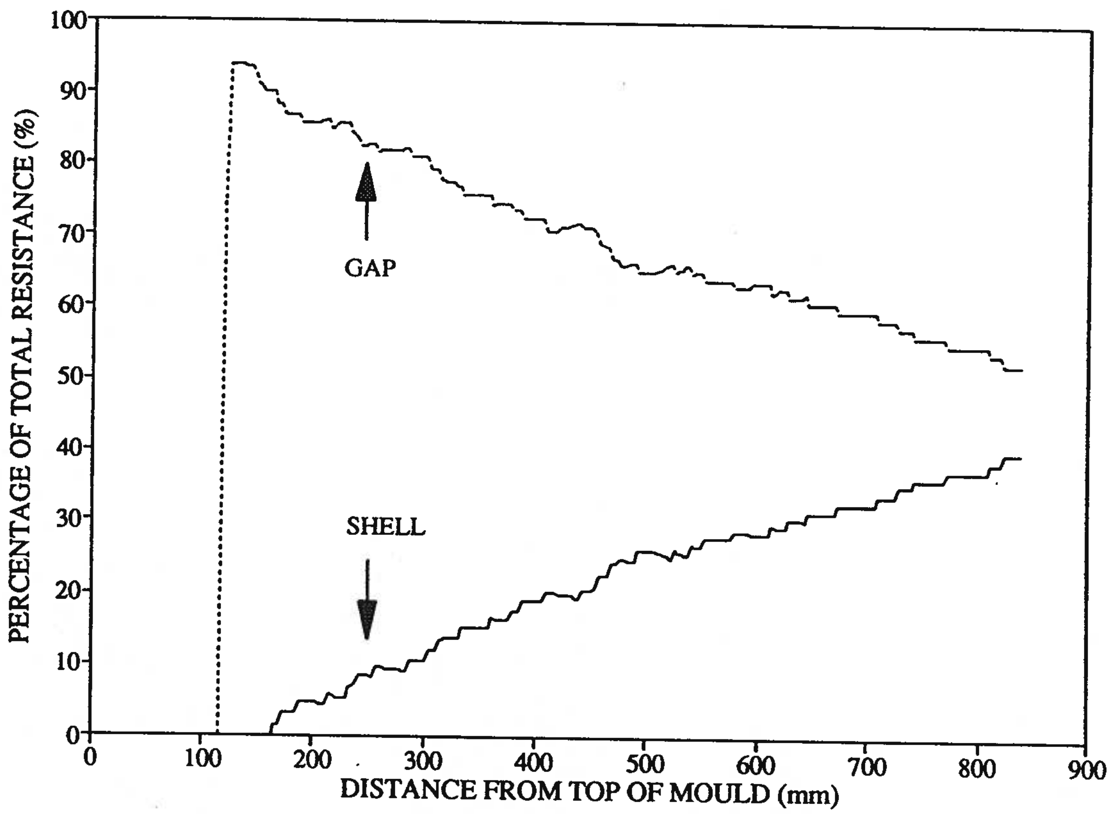

Figure 9.1 Axial profiles of gap and shell thermal resistances at Company B.

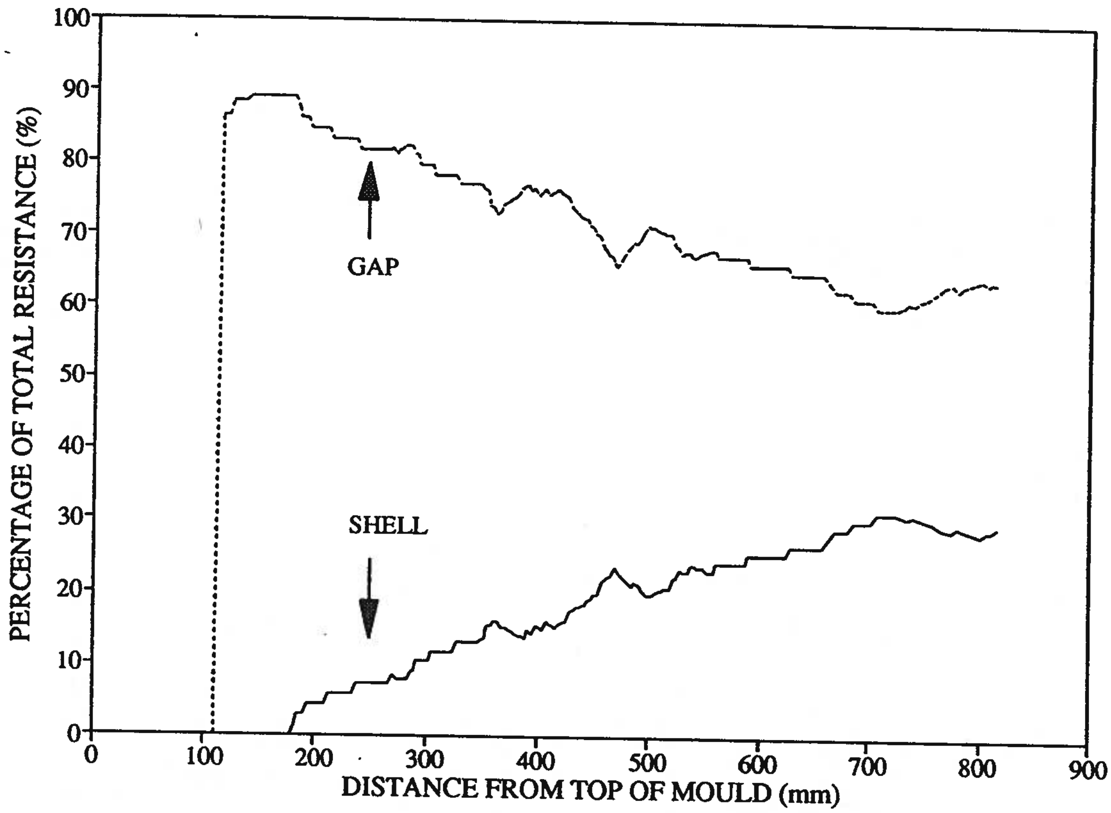

Figure 9.2 Axial profiles of gap and shell thermal resistances at Company E.

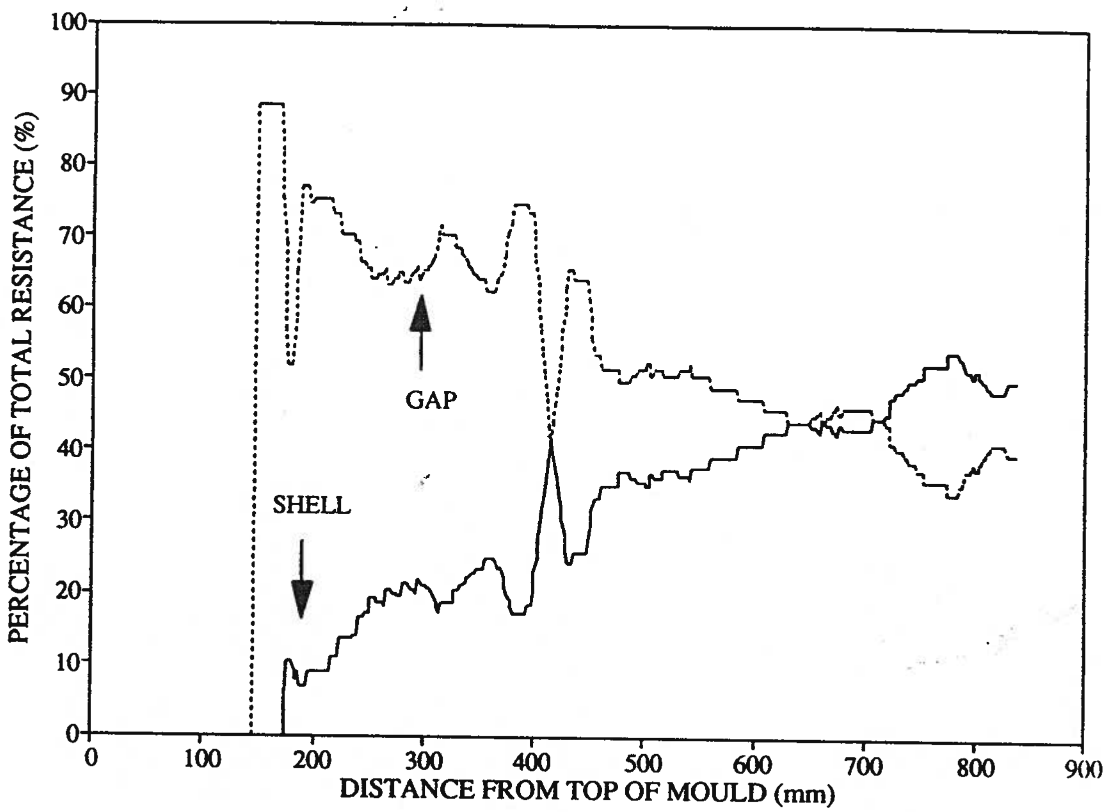

Figure 9.3 Axial profiles of gap and shell thermal resistances at Company C.

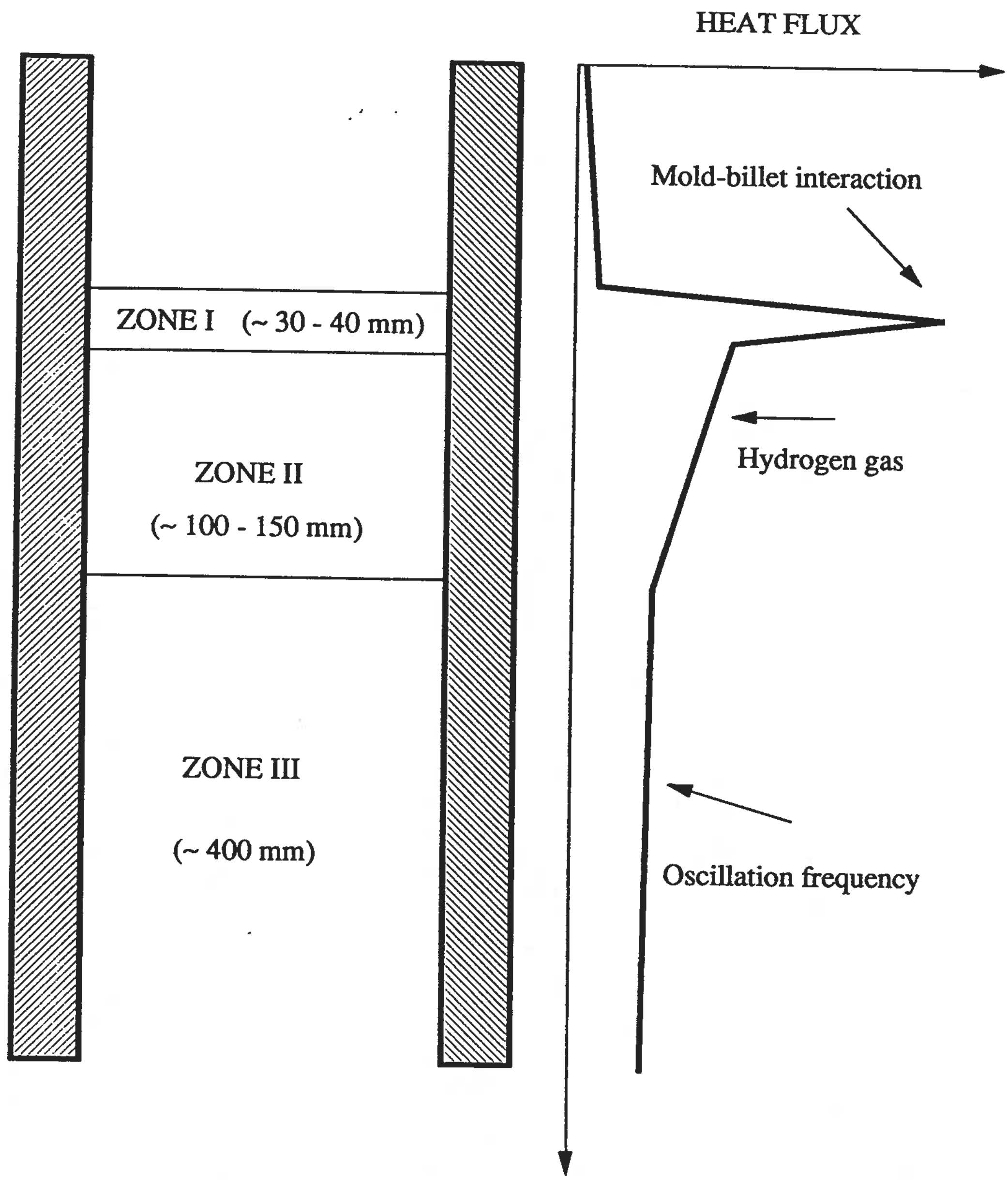

Figure 9.4 The three zones of heat transfer in the continuous casting billet mould.

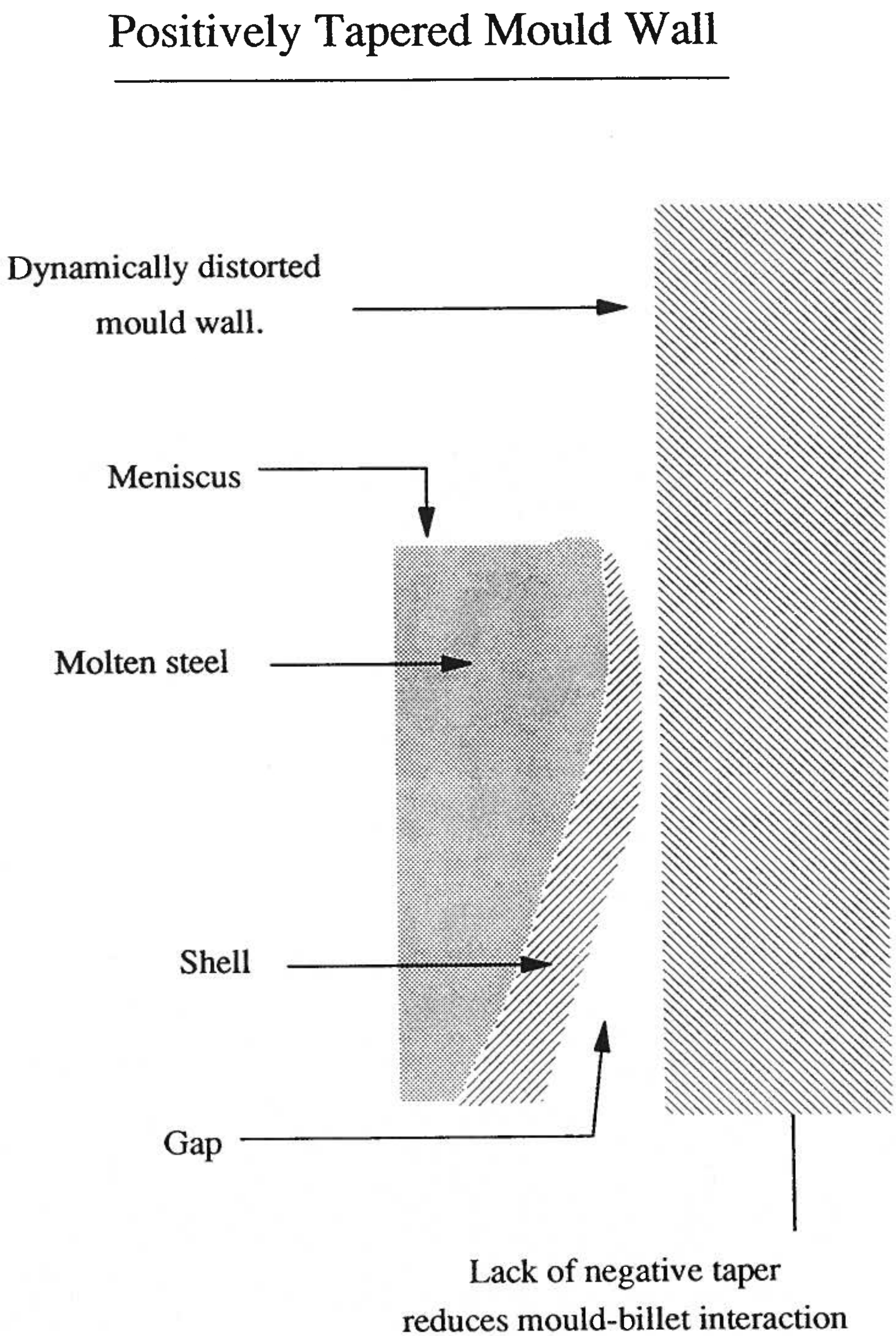

Figure 9.5 Shape acquired during service by a mould with a steep initial taper.

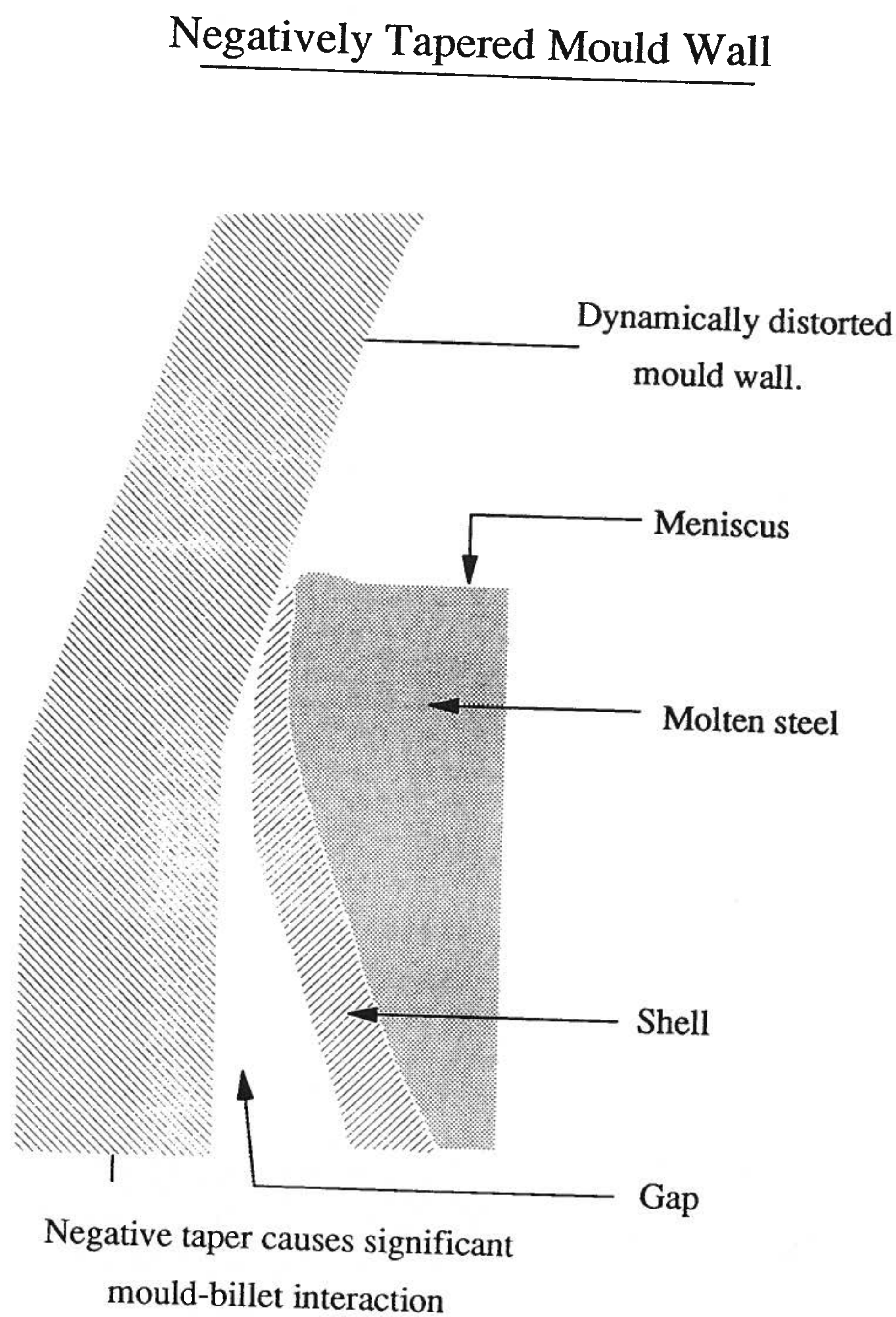

Figure 9.6 Shape acquired during service by a mould with a shallow initial taper.

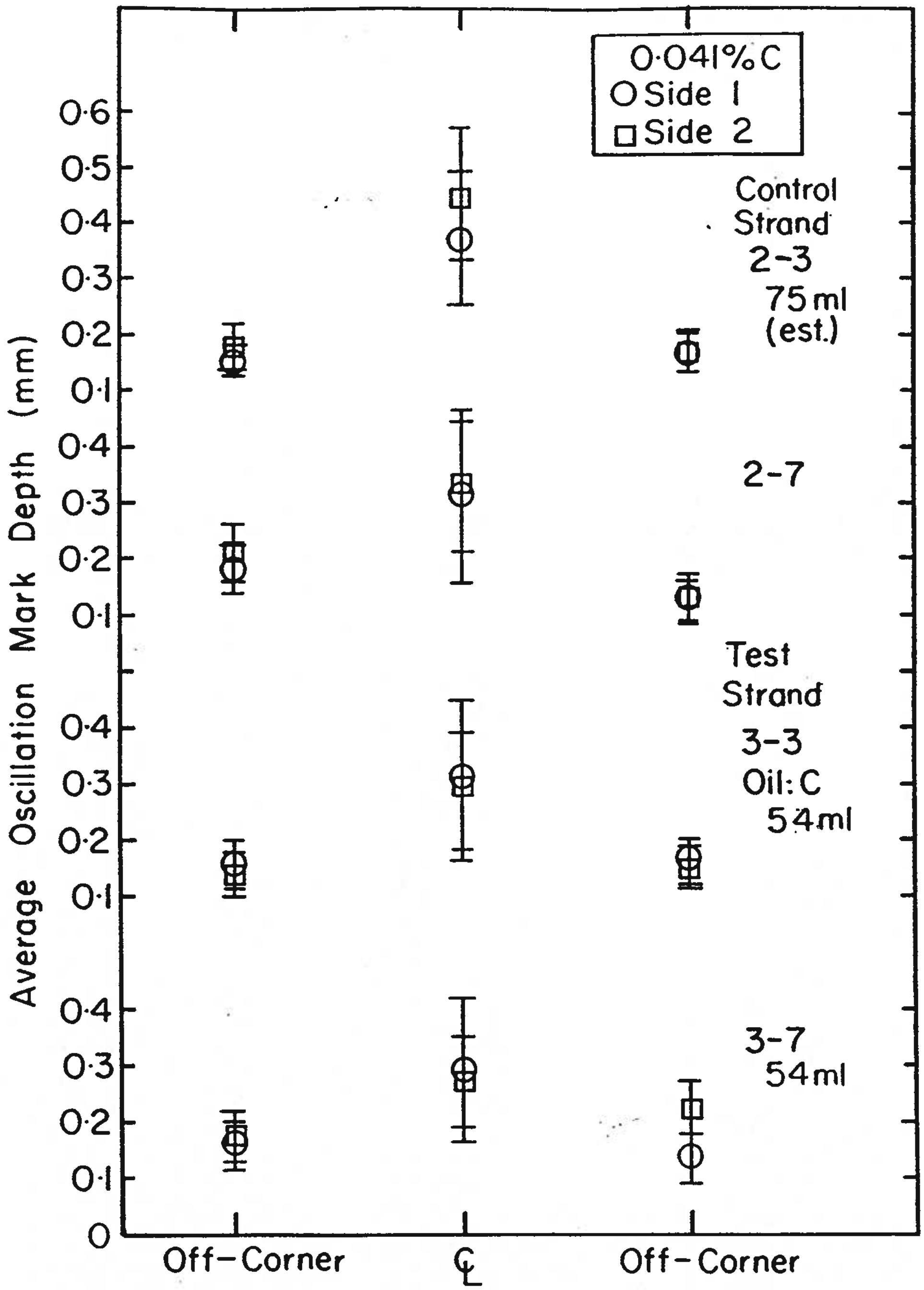

Figure 9.7 Graph showing the effect of negative strip time and stoke length on the oscillation mark depth on 1008 grade billets cast through parabolic taper moulds. (Negative strip time and stroke lengths of the mould at Strand 3 and Strand 4 are 0.13s, 9.5 mm and 0.19 s, 12.7 mm respectively).

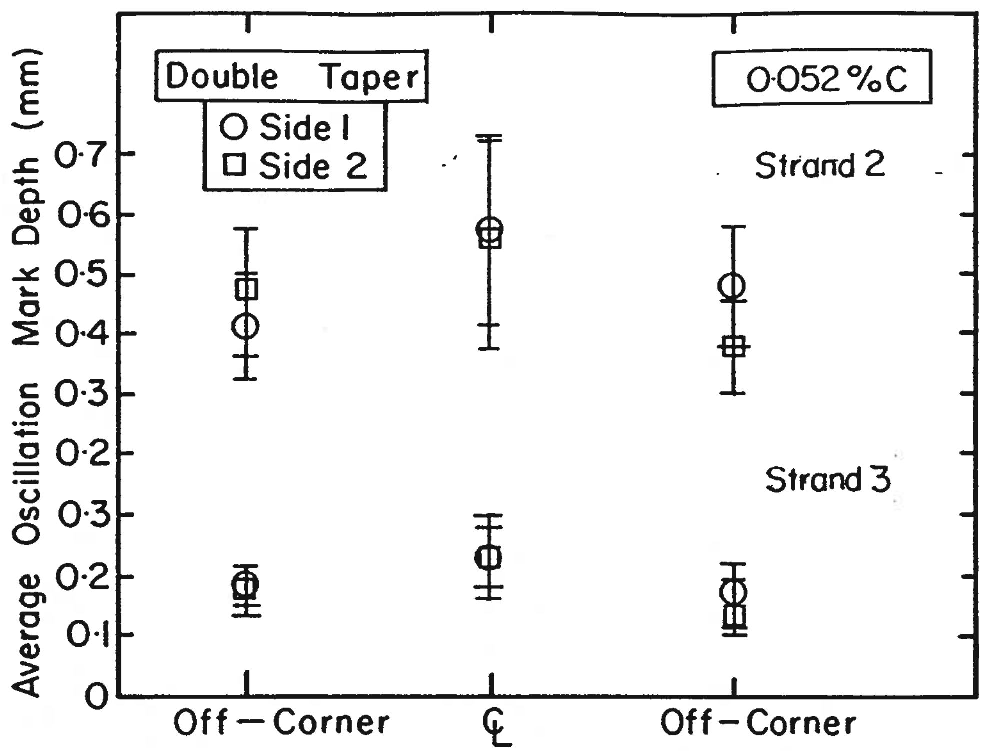

Figure 9.8 Graph showing the effect of negative strip time on the oscillation mark depth on 1008 grade billets cast through double taper mould. (Negative strip time and stroke lengths of the mould at Strand 3 and Strand 4 are 0.13s, 9.5 mm and 0.19 s, 12.7 mm respectively).

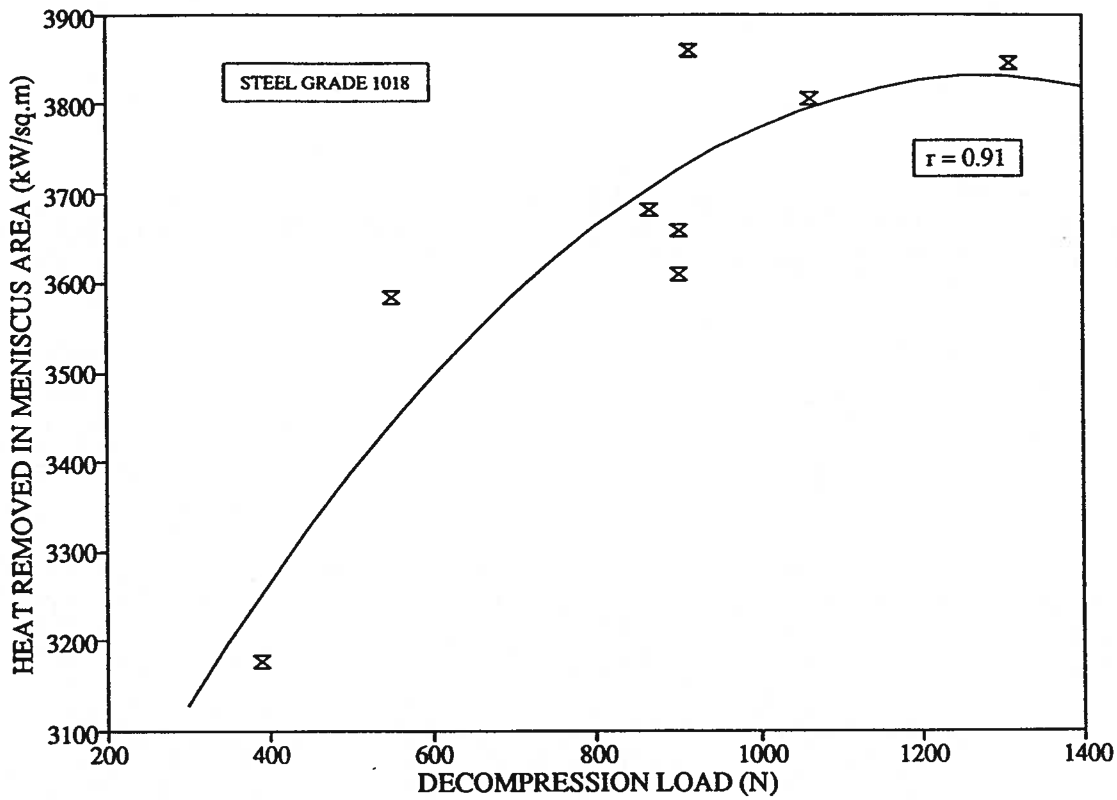

Figure 9.9 Effect of "decompression" load on the mould heat transfer during the casting of 1018 grade billets at Company C.

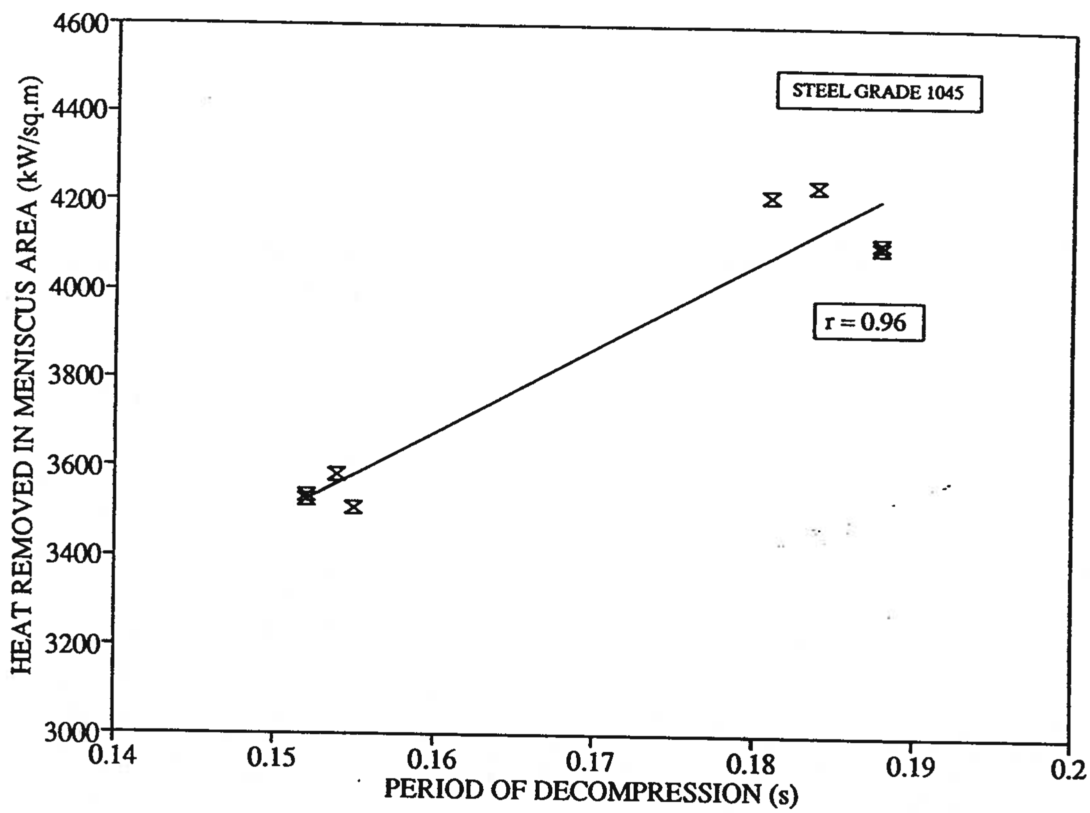

Figure 9.10 Effect of negative strip time on the mould heat transfer during the casting of 1045 grade billets at Company C.

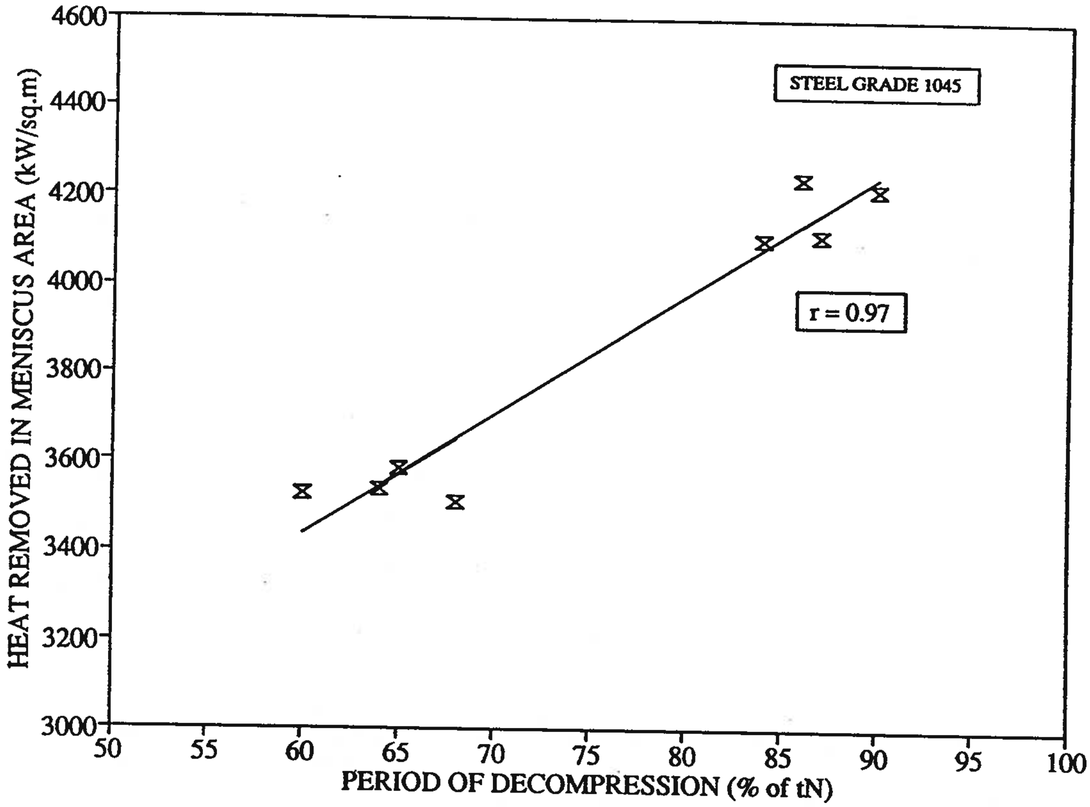

Figure 9.11 Effect of decompression period (measured as a percentage of t_N), on the mould heat transfer during the casting of 1045 grade billets.

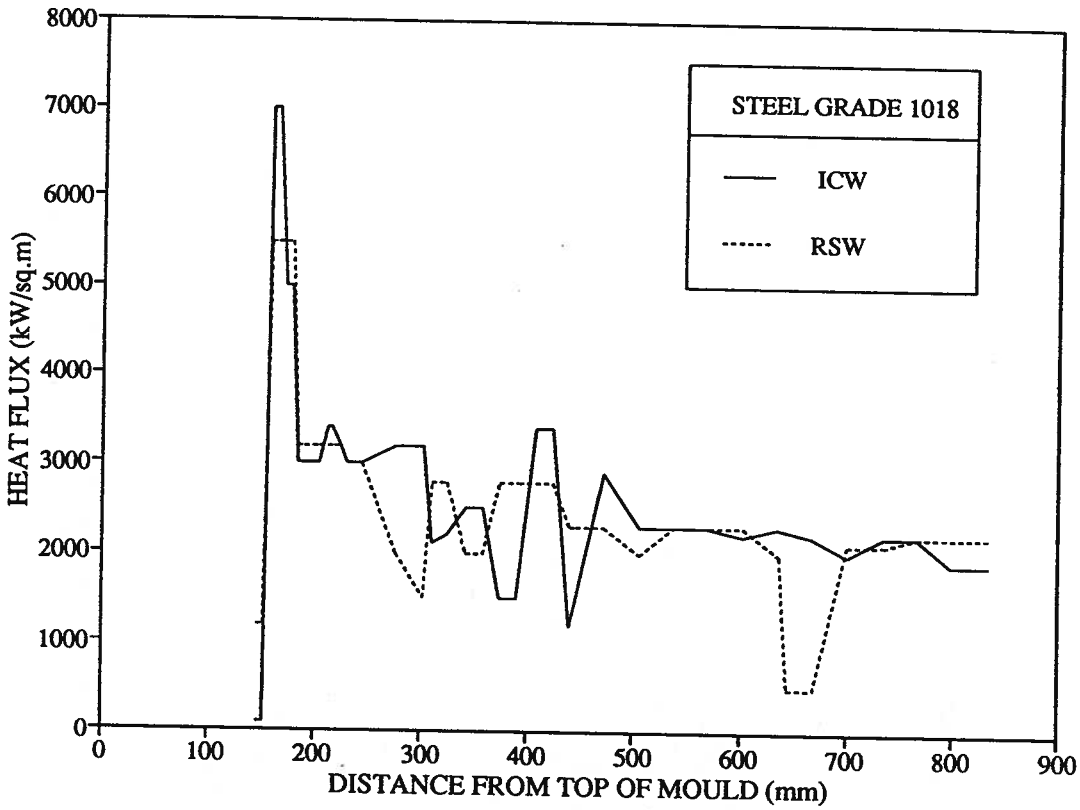

Figure 9.12 Axial heat-flux profiles on two adjacent mould walls at Company C.

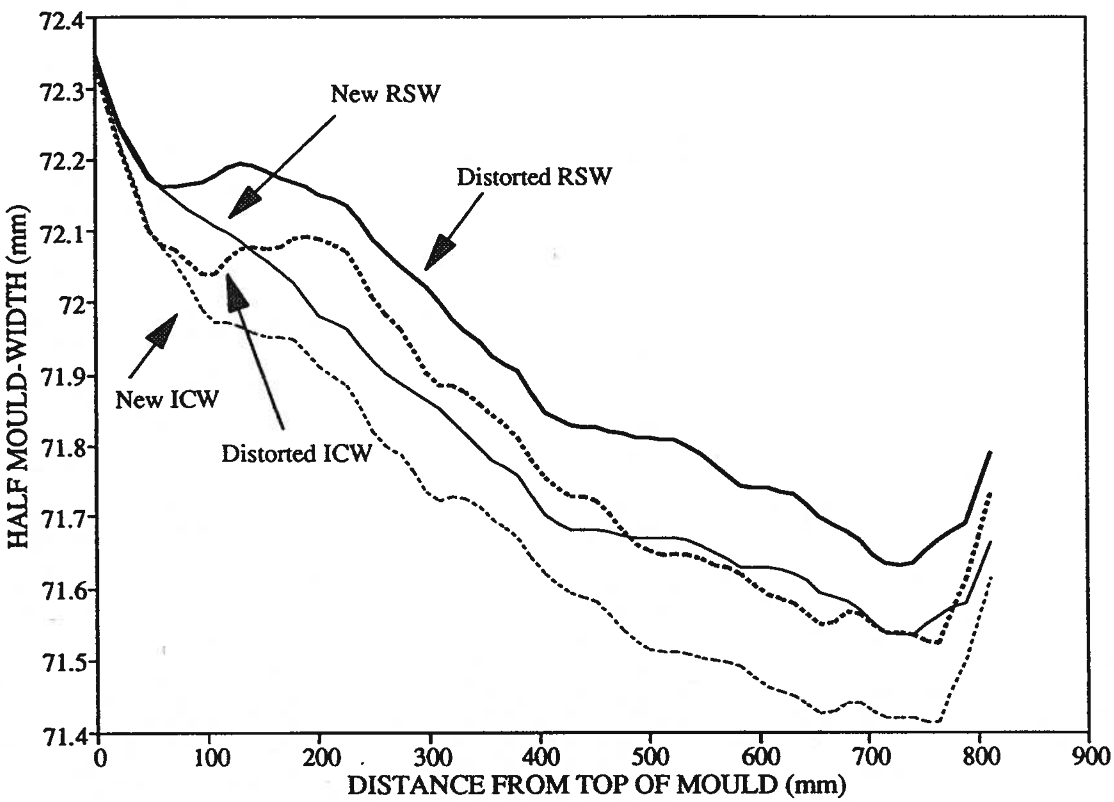

Figure 9.13 Computed mould shape during operation for two adjacent mould walls at Plant C.

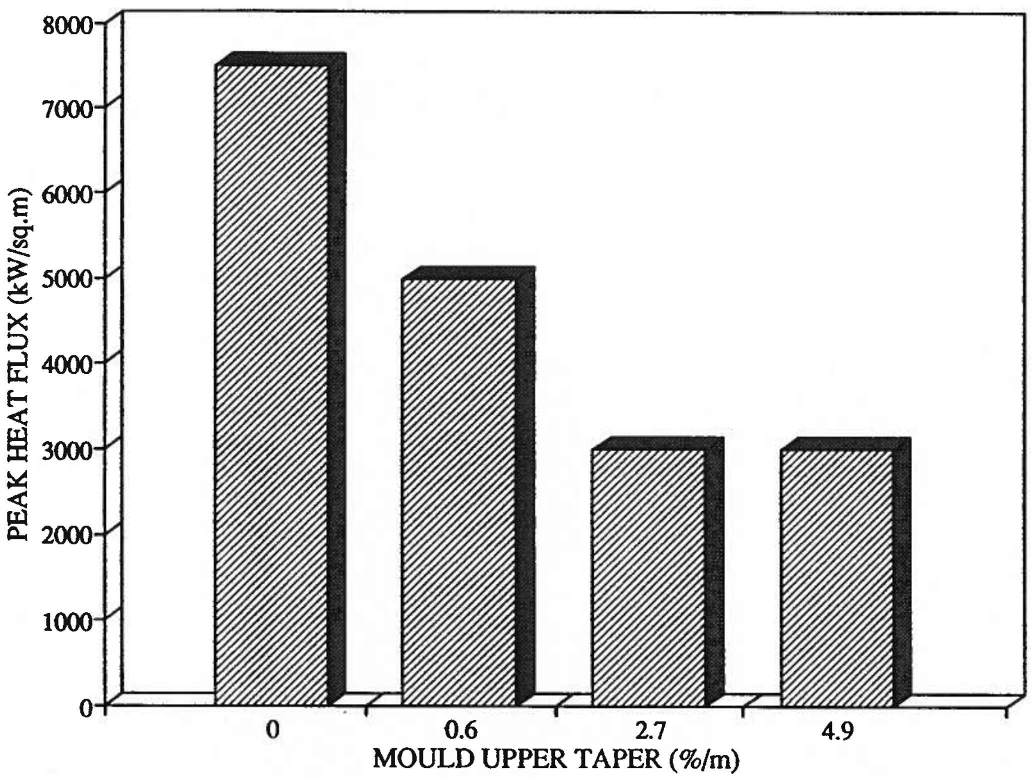

Figure 9.14 Measured peak heat flux for different initial mould tapers.

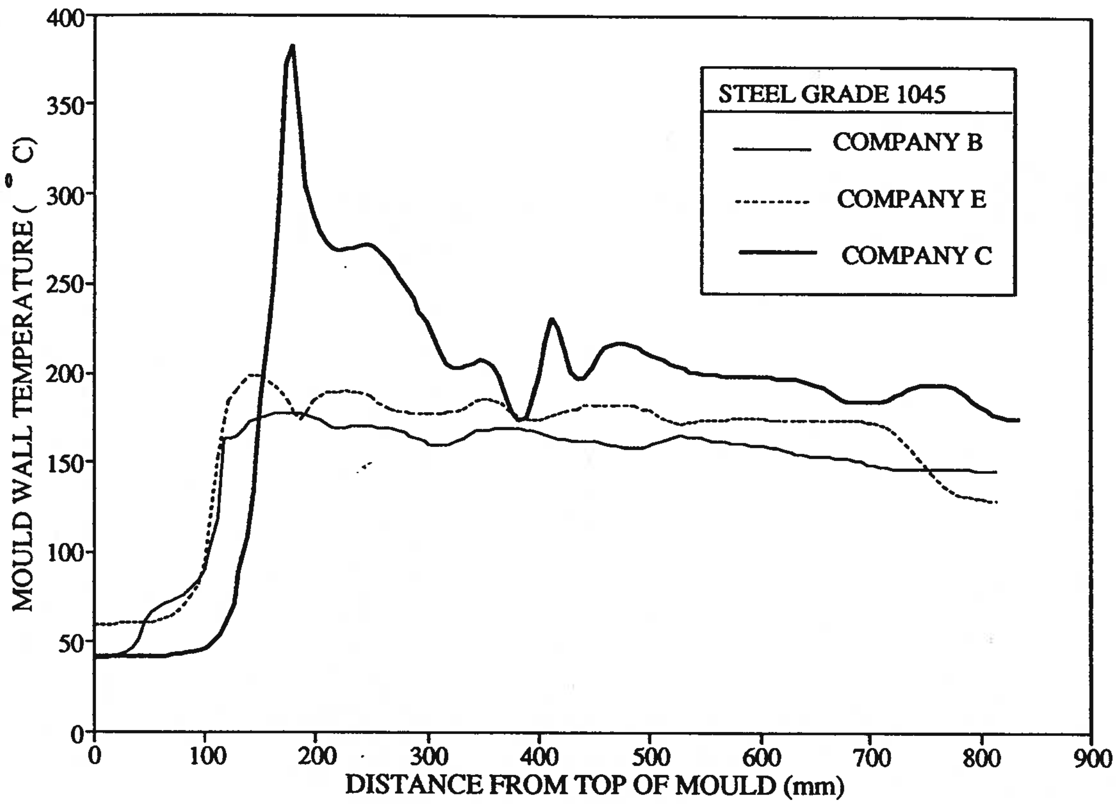

Figure 9.15 Hot face temperature of the mould wall while casting 1045 grade steel billets at Plants B, E and C.

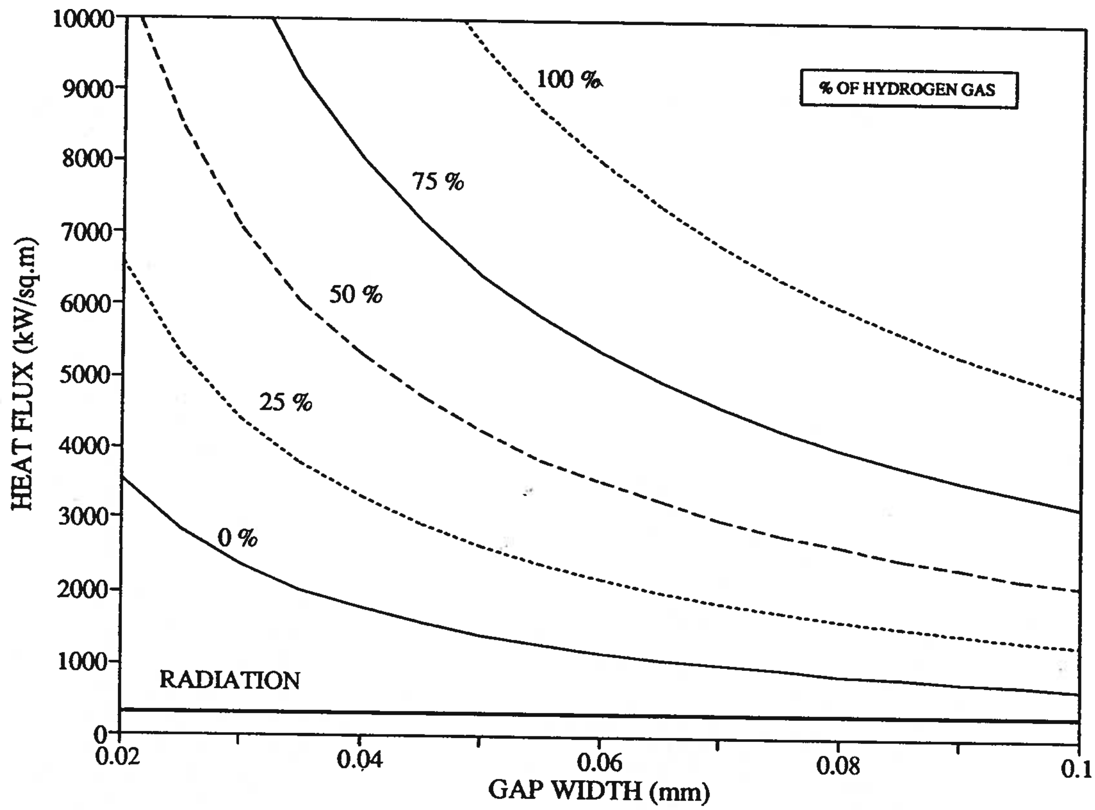

Figure 9.16 Variation in mould heat transfer on account of different amounts of Hydrogen gas in the mould-billet gap.

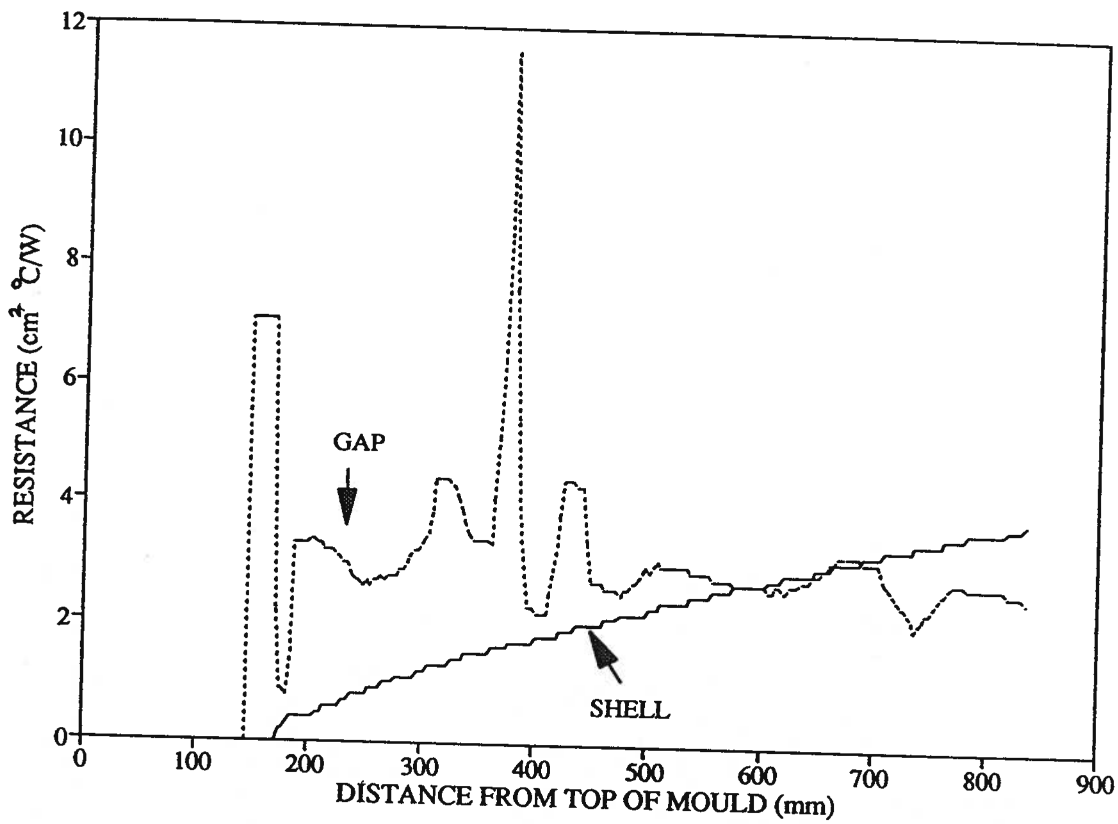

Figure 9.17 Axial profile of gap and shell thermal resistances while casting 1045 grade billets at 144 cpm of mould oscillation at Company C.

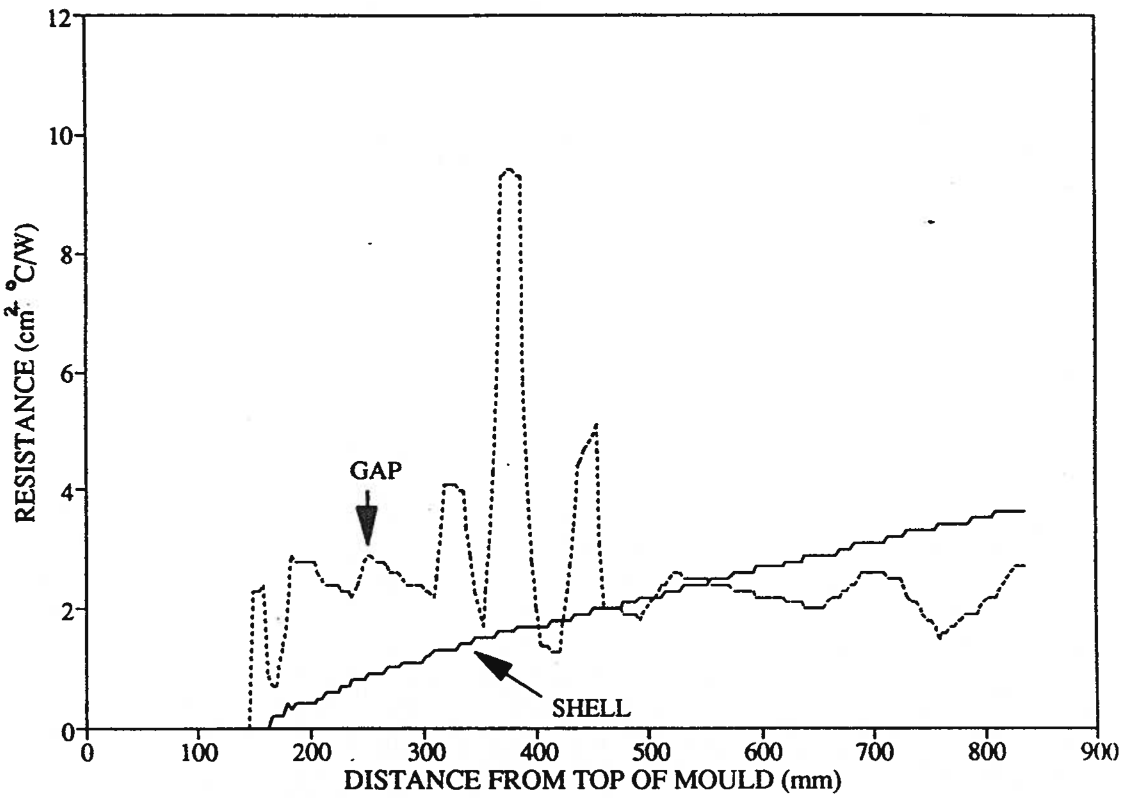

Figure 9.18 Axial profile of gap and shell thermal resistances while casting 1045 grade billets at 96 cpm of mould oscillation at Company C.

Chapter 10 : DESIGN OF MOULD TAPERS

Discussions in the previous two chapters have clearly revealed the significant effect that the pre-existing mould taper has on the heat flux in the meniscus region. It has also been shown that a steep taper in this region of the mould, designed to compensate for the mould-billet gap and thereby increase the heat transfer, actually reduces the heat flux, primarily on account of reduced mould-billet interaction. Several findings have been presented to show that enhanced mould-shell interaction leads to higher rates of heat flow in the meniscus region of the mould. A high enough heat transfer in the meniscus region, that raises the temperature of the hot face of the mould above the boiling point of the lubricating oil, causes the oil to boil, thereby, creating adverse lubrication conditions in the meniscus region. While such adverse lubrication conditions are not a cause of concern while casting billets of low carbon grades ($C < 0.60\%$), the same conditions can lead to bleeds and laps on the surface of high-carbon grade billets. This, as has been explained earlier, is on account of the large freezing range of the high carbon billets, which permits only a thin solid shell to form in the meniscus region. This thin shell is likely to develop bleeds or laps in the absence of a lubricating medium between the shell and the mould. Thus taper in the upper part of the mould needs to be designed very carefully and not necessarily from the point of view of extracting the largest amount of heat in the mould.

10.1 Conventional Design of Mould Taper

The walls of the mould are tapered inwardly so as to enhance the rate of mould heat extraction by reducing the air gap between the mould wall and the (shrinking) billet. It is not sufficient, however, to design a mould taper based solely on the shrinkage profile of the billet, because during service, the mould wall distorts and moves away from the billet (Figures 8.12 - 8.14), opening up the air gap further. Thus the design of the taper must take into account the formation of an air gap caused by both the distortion of the mould while in use and the shrinkage of the billet. Mould tapers are expressed in %/m and are based on the expression given below.

$$Taper\left(\frac{\%}{m}\right) \;=\; \frac{(M_T - M_B)}{(M_T)\,(M_L)} X\ 100 \qquad (10.1)$$

where M_T and M_B are the dimensions of the mould at the top and bottom respectively and M_L is the length of the mould in meters.

The gap between the mould and the billet is, conventionally, higher in the meniscus region of the mould than in regions below the meniscus. This is on account of the large air gap formed by the rapid initial shrinkage of the billet (high meniscus heat transfer) and the distortion of the mould wall away from the billet. To compensate for the air gap, the mould wall normally needs to be steeply tapered (between 3.0 - 5.0 %/m), for the first 100 mm (approximately) from the meniscus. With reference to the shrinkage profile and mould distortion results obtained at Company B, calculation of mould taper based on the conventional philosophy of reducing the mould-billet gap, for a 1008 grade steel, leads to a value of 2.9 %/m for the first 100 mm from the meniscus, 1.6%/m for the next 423 mm and 0.8%/m for the remaining part of the mould. It should be pointed out that an underlying assumption in this kind of calculation is that the heat-flux profile used to design the new taper is itself not altered, in any significant measure, by the new taper. The present work shows that this assumption is grossly in error and that a design aiming to enhance heat transfer in the mould by increasing the upper taper of the mould, ends up actually reducing heat transfer by decreasing mould-shell interaction.

10.2 New Approach to Design of Mould Taper

The discussion in the preceding section has shown that based on the conventional design philosophy, mould tapers would consist of a steep upper taper of about 3 - 5 %/m followed by a steeper second taper. There are at least two flaws in such a design. Firstly, an implicit assumption is that the new taper, by itself, does not alter the heat transfer in any significant manner and, secondly, the enhancement of heat transfer in the meniscus region is desirable for all grades of steel. In view of the findings of the present work, the following new points are considered important for design of mould tapers.

[1] Billets with a long freezing range (C > 0.60%) have a very thin shell near the meniscus. The surface quality of such billets is strongly affected by the absence of the mould lubricating oil near the meniscus and it is believed that bleeds and laps are a consequence of adverse friction conditions in the mould. Such grades of billets, thus, need to be cast through moulds that have hot face temperatures low enough to prevent the oil from boiling. Thus the taper in such cases must be designed to reduce heat transfer in the meniscus area.

[2] Billets with carbon < 0.60 % can be cast through moulds that have tapers, in the meniscus region, designed to enhance heat transfer. It has been shown that the absence of the mould lubricating oil and the resulting adverse friction conditions do not affect the quality of the billet surface to any significant degree.

Based on several shrinkage profiles computed during the work, an upper taper of 2.5 %/m and a lower taper between 0.6%/m to 1.0%/m is recommended for the high carbon grades (C > 0.6%). The break point and the exact value of the second taper needs to be determined from the casting speed and section size of the billet. The upper taper should extend to the top of the mould. The steep upper taper of the mould would prevent the mould wall from acquiring a negative taper during operation. The absence of negative taper has been shown to reduce mould-billet interaction and thus the heat transfer. The hot face temperature of such a mould is likely to be around 180 - 200 °C (calculations based on a mould wall thickness of 12-13 mm and a mould cooling water velocity of 10-12 m/s) which is below the boiling point of the commonly used vegetable-based lubricating oils.

Mould tapers recommended for lower carbon grade billets are an untapered mould wall (0.0%/m) in the upper region and between 1.0%/m - 2.0 %/m in the lower region with a break point of 25-30 mm from the meniscus. The exact value of the lower taper would depend on the casting speed, section size and carbon content of the steel. The mould wall should be untapered right from the top of the mould to 25-30 mm below the meniscus to ensure that even with the normal metal level fluctuations that arise during casting, the meniscus continues to reside, as per design, in an untapered region of the mould. Such a mould would, during service, distort and assume a steep negative taper leading to enhanced mould-billet interaction and, therefore, heat transfer.

The enhancement in heat transfer as obtained in a mould that is untapered in the meniscus region clearly would allow for an increase in casting speed leading to an improvement in production rates. A measure of the increase can be seen from a very simplistic calculation comparing the casting speeds for a 0.45% carbon steel at Company C and Company B. Under the conditions of low heat transfer in the parabolic mould at Company B, the casting speed is ~2.0 m/min. The heat transfer in the mould at Company C, indicative of the high heat extraction rates of a 0.0 %/m upper tapered mould, is roughly 1.5 times the value at Company B. This suggests that the casting speed at Company B, can be increased by at least 50%. The calculation assumes that the only constraint to the increase in the casting speed is the attainment of a certain shell thickness of the billet that is sufficiently thick to support the liquid steel at the exit from the mould. It needs to be pointed out that 50% increase in casting speed is a conservative estimate as the heat flux in the properly designed mould is likely to be higher than that obtained from the mould at Company C. Before the benefit of increased production rates is realised in an operating plant, modifications may have to be carried out on the positions of the billet-cutting torch and the unbending point to ensure that their locations are appropriate with the higher casting speeds.

10.3 Other Design Parameters

10.3.1 Shaping of mould walls

The tolerance levels indicated on the engineering drawings of the mould are typically +- 0.254 mm. To understand the implications of such a loose tolerance, a simple calculation is performed for a 120 X 120 mm mould having a design taper of 0.4%/m . To be correctly manufactured, the dimension of the mould wall 25.4 mm down the length of the mould, should be 119.878 mm. This decrease of 0.122 mm in the mould wall dimensions from its dimension at the top, is less than half the tolerance magnitude! The loose tolerance in use currently can lead to a taper in excess of 4- 5 %/m in the first few important cms near the top of the mould. Moulds that are explosion formed have been found to have tolerances that compare favourably with those needed and this method of manufacture is strongly recommended. Additionally it may be a good idea to change the measure of taper from %/m to %/cm at least in specifications to the manufacturer to emphasize the importance of a close tolerance over small distance. It is not unlikely that the use of the unit %/m has shifted the focus away from the dimension the mould needs to have over a shorter distance to meet the taper requirements. Thus, often, moulds have an overall taper that matches the designed one over the mould length but is grossly inadequate over shorter distances especially in the critical meniscus area.

10.3.2 Mould water pressure

Whether or not the mould cooling water boils in the cooling channel depends on the mould cold face temperature and the pressure in the water channel. A high exit pressure of the mould cooling water or "back pressure" as it is commonly referred to, permits the cold face of the mould to acquire a high temperature without causing the water to boil. In view of the large heat extraction rate now possible with the new mould design of an initial untapered meniscus region, calculations show, that the cold face temperature of the mould is likely to reach 150°C. To ensure that water does not boil under this condition the back pressure should be about 20 to 30 psi (138 to 207 KN/m^2).

10.3.3 Material of the mould

Given the high heat extraction rates achievable, the mould material should be an alloy of copper, chromium and zirconium as this has a higher half softening point than the conventional DHP copper moulds. This point has been made several times earlier [62], but assumes greater significance in light of the higher heat extraction rates being sought.

Chapter 11 : SENSOR SIGNALS AND BILLET DEFECTS

This chapter briefly introduce how mould sensors such as Thermocouples, Load Cells and LVDTs can be utilized to detect the creation of adverse casting situations and how corrective steps, if any, can be taken to move away from those conditions.

11.1 Thermocouples

Thermocouples are typically placed midway between the hot and cold faces of the mould wall and record temperature that are 100 - 150 °C lower than the mould hot face temperature. It has been shown in the course of this work that when sampled at 1 Hz., the thermocouples are capable of detecting several billet defects discussed below.

11.1.1 Off-corner Cracks

The mechanism by which off-corner cracks form in the mould has been described in an earlier chapter and has been described in some detail by Brimacombe, Samarasekera and co-workers [59]. It effectively involves bulging of the mid-face of the billet causing the shell at the mid-face to touch the mould wall. This bulging results in a hinging action at off-corner locations, and the generation of a tensile strain in the region of low-ductility adjacent to the solidification front which can lead to the generation of off-corner cracks.

In view of the fact that the bulging of the shell and its subsequent interaction with the mould is a pre-requisite for the creation of off-corner cracks, it is expected that the thermocouple(s) in the region of the mould-billet interaction would register an increase in temperature. This is clarified further in the Figure 11.1 which is a plot of the profiles of the heat-flux, the billet shrinkage and the distorted mould wall as a function of distance from the top of the mould. Also marked on the graph is the location at which the off-corner cracks are estimated to have formed. (The depth of the off-corner cracks is a measure of the solid shell thickness at the moment of crack generation and the position of the billet in the mould at that instant can thus be obtained by a consideration of the solid shell profile of the billet). As can be seen in Figure 11.1, the cracks appears to have formed at the position where the heat-flux profile rises and then falls indicating a local increase in heat transfer as may be expected with an interaction of the billet with the mould. It is interesting to note that the crack appears to have formed at the instant the billet reaches the zone of shallow second taper where, on account of the high shrinkage in the upper part of the mould, a fairly large gap (approximately 5 -6 mm) exists between the mould and the billet surface. A gap of this magnitude is conducive to the bulging of the shell.

The response of the thermocouples in the region where the crack appears to have formed can be seen in Figure 11.2 which is a plot of the mould thermocouple temperature for Company C. Also plotted on the same graph is the mould thermocouple response at Company B where off-corner cracks were not observed during the trials. The increase in temperature of the thermocouple at Company C around 400 mm from the top of the mould is indicative of the bulging of the billet. As is expected, the thermocouples at Company B do not show a similar trend.

The obvious corrective action that can be taken is a judicious decrease in the casting speed. The increase in solid shell thickness, arising from a longer residence time, **may** give sufficient strength to the solid shell to prevent bulging of the billet. A decrease in mould heat transfer can be attempted by a change in the metal level of a suitably designed "smart" mould. This topic is discussed in greater detail in a subsequent section. The ideal way to prevent off-corner cracks is to have a mould suitably tapered to compensate the formation of the air gap in the lower part of the mould.

11.1.2 Rhomboidity

Unequal heat transfer on adjacent faces of the billet, among other reasons, can lead to the formation of off-squareness in billets. This unequal heat transfer, that may or may not lead to boiling of water in the cooling water channel, can arise from an imprecisely machined mould. This is on account of the significant impact the mould profile, in particular the negative taper of the upper part, has on the heat transfer in the meniscus region.

Billet rhomboidity arising from unequal heat transfer on adjacent mould faces can be detected by thermocouples placed on neighboring mould walls. Figure 11.3 shows the hot face temperature of the mould on adjacent walls for a case in which billets were cast rhomboid at Company C. As shown in the figure, the ICW (inner curved wall) has higher mould wall temperature than the adjacent wall. (Examination of rhomboid billet samples has confirmed that the rhomboidity is always oriented in the same direction). The temperatures recorded by the thermocouples for the above case is plotted in Figure 11.4 and as can be seen the temperatures of the thermocouples on the ICW are higher than those recorded by the thermocouples on the RSW. The difference in temperature is affected by the fact that thermocouples are not embedded to the same depth on both the walls. Raw thermocouple data, thus, need to be analysed carefully.

No corrective action, short of changing the mould tube can be taken. In fact, if appropriate quality control measures are in place, such a mould would not be put in service at all.

11.1.3 Bleeds and Laps

These defects have predominantly been observed on billets that have carbon contents in excess of 0.60%. This, as has been explained in an earlier chapter, is on account of the adverse lubrication condition, that may arise in "hot" mould, to which the thin initial shell of the high carbon billet is particularly susceptible.

The onset of adverse lubrication condition can be detected both by load cells (as explained in a subsequent section), as well as by thermocouples. The key factor that controls the sustenance of the mould lubricating oil on the mould wall is the mould hot face temperature, which for appropriate lubrication should not exceed the boiling point of the oil (> 200 °C for vegetable based oil). Thus any change in the mould thermocouple measurement that amounts to an increase in the mould hot face temperature beyond the boiling point of the lubricating oil can be taken to represent adverse lubrication condition for high carbon billet.

Corrective action can be taken by increasing the mould cooling water velocity, temporarily stopping the lubricating oil flow or changing metal levels in an appropriately designed "smart" mould. All the actions suggested above will cause a reduction in the rate of mould heat transfer and restore, with the resumption of oil lubrication, appropriate lubrication condition.

11.2 Load Cells

In the study conducted load cells were placed between the mould housing and the oscillator table and signals were collected at 50 Hz. Arising out of this work it appears that friction signals can be better analysed if the load cells were located in the oscillator arms and were sampled at 500 Hz.

11.2.1 Transverse Depressions and Cracks

The mechanism for the formation of transverse depressions and cracks put forth by Brimacombe, Samarasekera has been confirmed in this work. The mechanism, discussed in detail in an earlier chapter, suggests that the tensile stresses arising out of the binding of a billet in the mould can cause the billet surface to "neck", much like the specimen used in tensile testing. This "necking" may be accompanied by the formation of transverse cracks if the binding of the billet is severe enough. (The billet may bind in the mould if the taper is too steep).

Brendzy [13] has shown that the peaks in the load cell signals during the up stroke of the mould, tend to be flat in case of normal operation but undulate when the billet binds in the mould. Figure 2.10, which is a plot of load cell signal obtained during the casting of a billet that is binding in the mould, illustrates this point.

In some cases corrective action can be taken by enhancing heat transfer in the mould by altering appropriate factors as explained in a subsequent section.

11.2.2 Adverse lubrication Conditions

In a previous work [13] adverse lubrication conditions were shown to exist when the load cells signals, during the up stroke of the mould tended to "rachet up". Similar results have been found in the present work as shown in Figure 11.5 which is a representative load cell signals corresponding to "no-lubricant" condition. It is possible to quantify the "racheting up" of the load cell response by comparing the sensor signal with load attained at the end of the downstroke of the mould.

11.2.3 Mould-Billet Interaction at the meniscus

A significant mould-billet interaction at the meniscus has been shown to lead to an increase in heat transfer in the upper part of the mould. The enhanced heat transfer is not desirable while casting high-carbon grade steel billets but is needed while casting low-carbon grade billets. To asses, on line, if sufficient mould-billet interaction is taking place, the load cell , LVDT and casting speed signals need to be analysed together. As been shown in earlier chapters, if the mould-billet interaction continues for more than 70% of the negative strip period it leads to high heat transfer in the meniscus region. A period of interaction which is less than 50% of the negative strip time will lead to low heat transfer values.

11.3 Towards a "Smart" Mould

The preceding sections have shown how sensors such as load cells and LVDTs can used to detect the onset of adverse casting conditions in the mould. The knowledge that the upper taper of the mould influences the heat transfer in the meniscus region is a powerful tool for on-line control of the process and it is possible to conceive of a "smart" mould that is so designed as to permit casting operation at two three different meniscus levels.

Thus, with a mould which is untapered till 50 mm below the normal meniscus level (meniscus level 1), and is followed by a steep taper to the bottom of the mould, it is possible to temporarily reduce the heat transfer, if necessary, by dropping the meniscus level to a region of steep taper that reduces mould-billet interaction. It may also be possible to use the mould design suggested above for casting high carbon grades where a low heat transfer in the meniscus region is desired. The meniscus level for casting high carbon steel would normally be in a zone of steep taper (meniscus level 2) which would give rise to a low heat transfer. If a high heat transfer is temporarily desired, as for instance during the binding of the billet in the mould, the meniscus level could be raised to level 1. The spray design at the bottom of the mould can be linked to the upper taper of the mould so as to allow changes in the spray water flux corresponding to changes in the meniscus level.

Other corrective actions that can be taken while casting billets through such a mould, to alter heat transfer conditions, are changes in :

[1] Mould cooling water velocity.

[2] Mould oscillation frequency.

[3] Mould lubricating oil flow rate.

[4] Billet casting speed.

The magnitude of change needed to bring about corrective action will have to be determined through several plant trials and appropriate software will need to be developed to implement the control system.

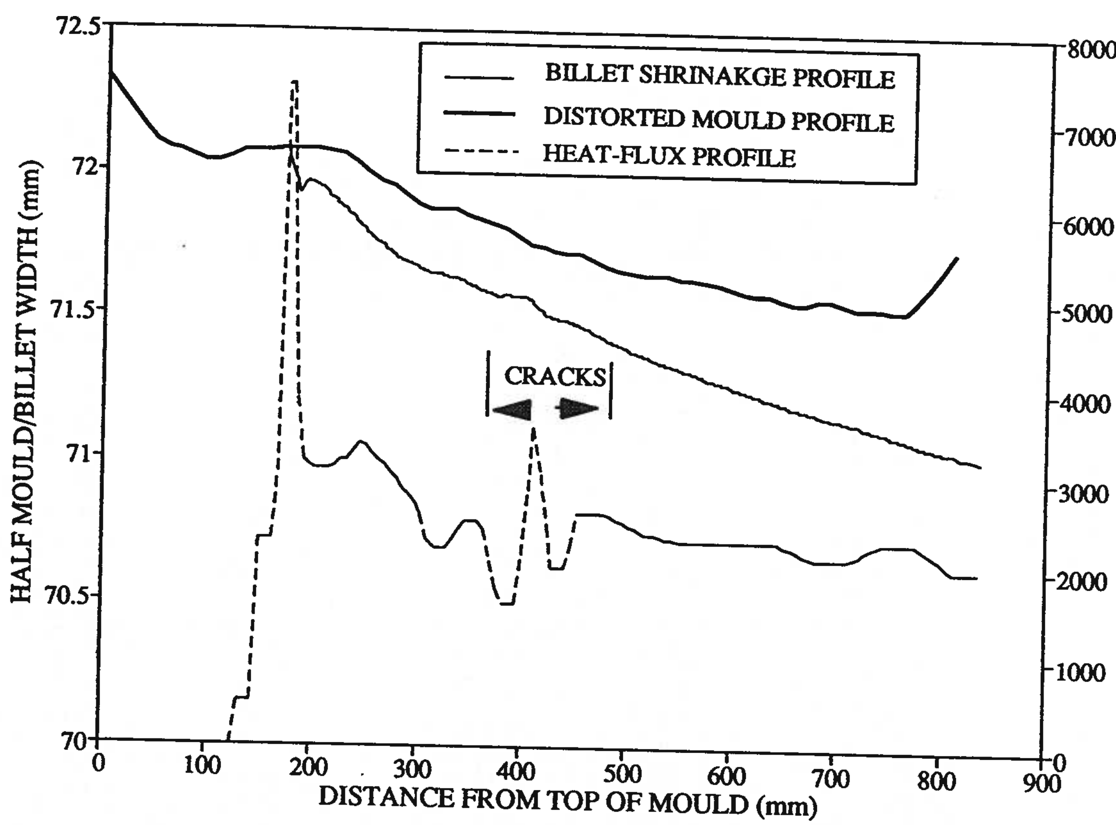

Figure 11.1 Heat Flux, billet shrinkage and mould wall profile at Company C.

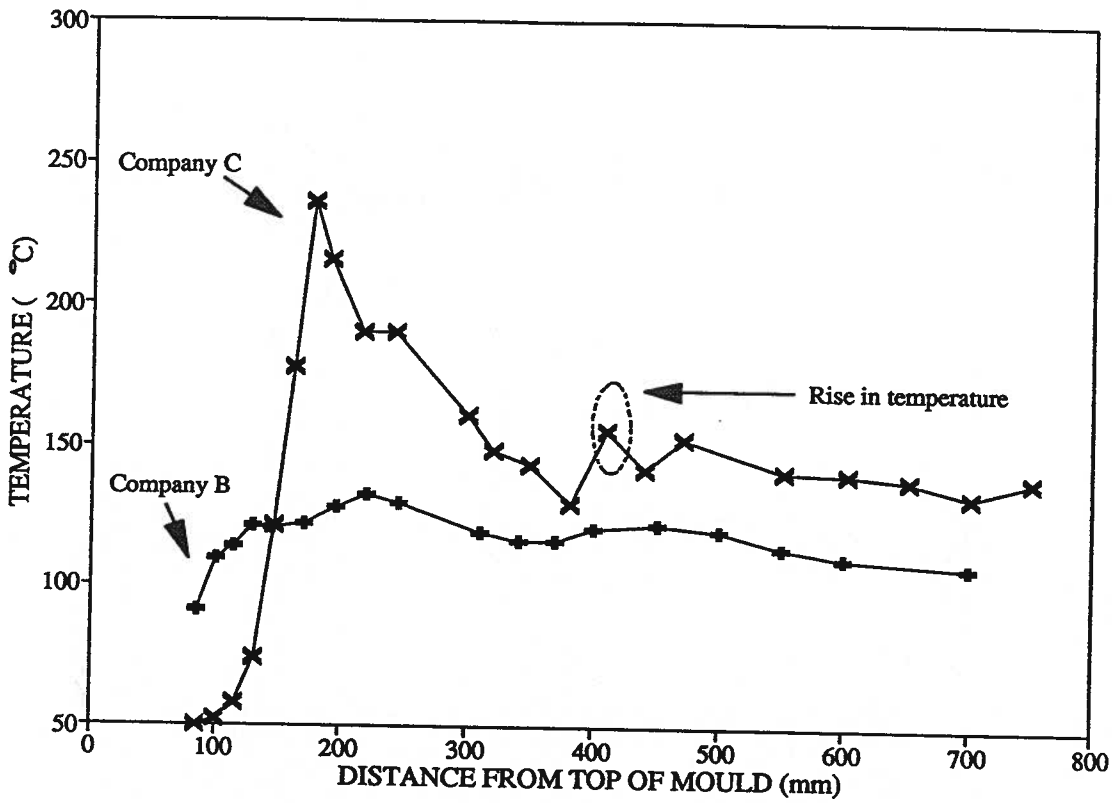

Figure 11.2 Mould thermocouple response while casting billets with off-corner cracks.

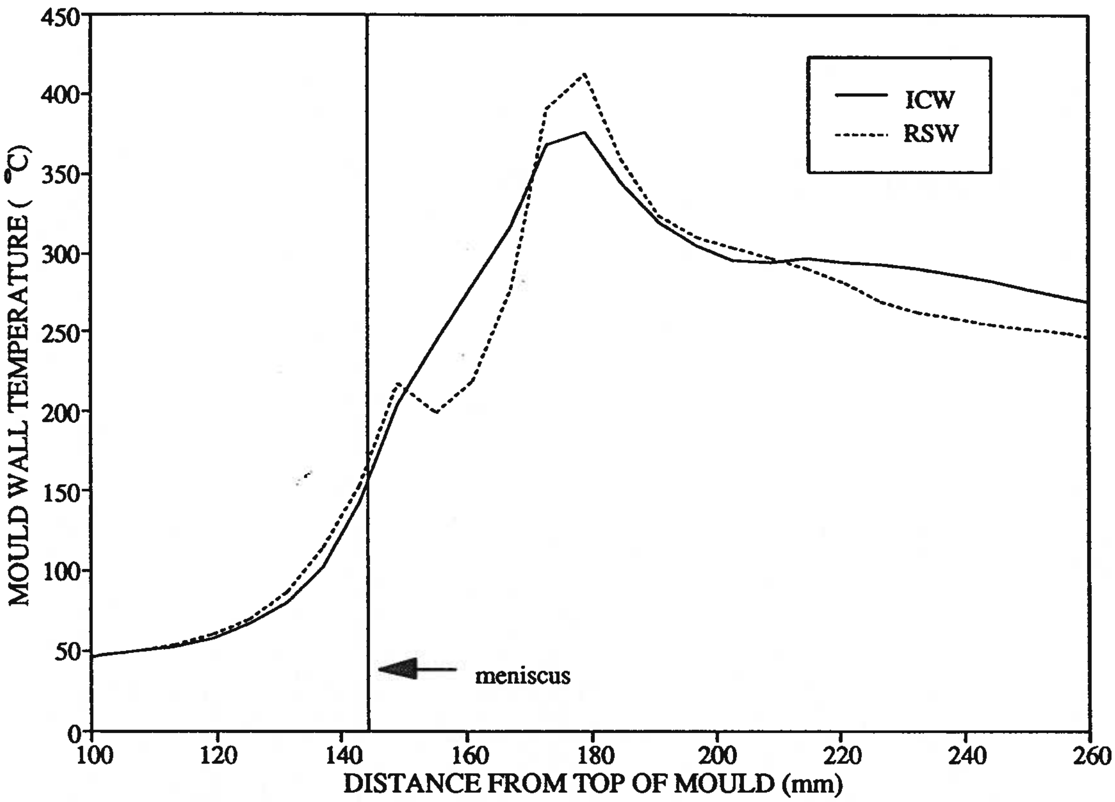

Figure 11.3 Mould hot face temperature indicating unequal heat transfer on adjacent faces.

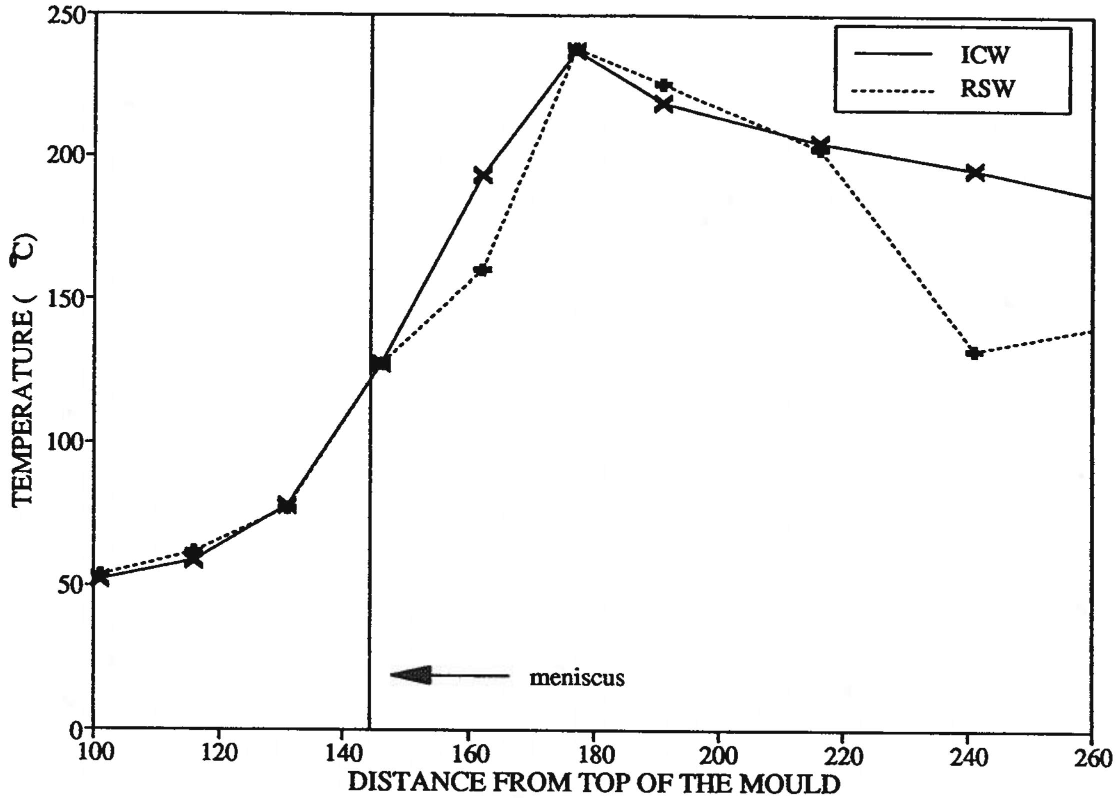

Figure 11.4 Response of mould thermocouple on adjacent mould walls indicating unequal heat transfer.

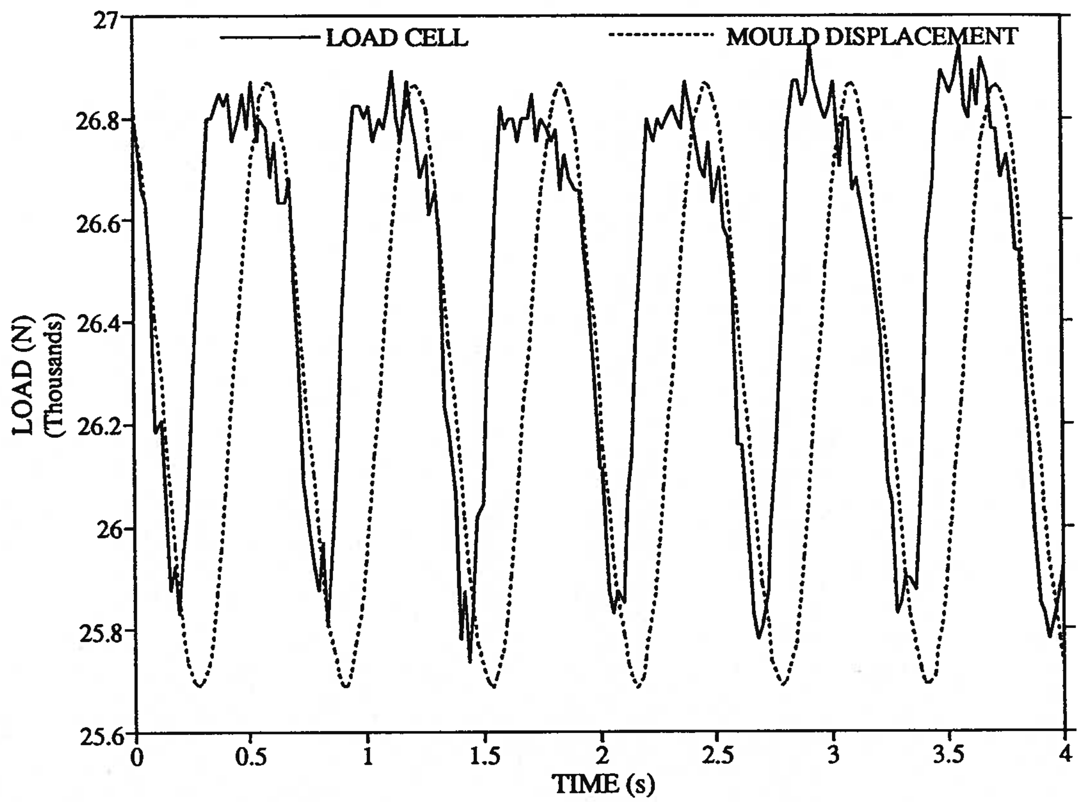

Figure 11.5 Load cell response at Company C obtained while casting billets without mould lubricating oil.

Chapter 12 : SUMMARY, CONCLUSIONS AND RECOMMENDATIONS FOR FUTURE WORK

Data on mould wall temperature and mould-billet interaction has been collected at three steel companies in elaborate plant trials organized for this purpose. Operating billet moulds were instrumented with arrays of thermocouples, several load cells and LVDTs. Water temperature at the inlet and outlet of the mould cooling water channel was measured by thermocouples. The liquid steel surface in the mould was filmed during casting to observe the behaviour of the mould lubricating oil at the meniscus. Billets samples were collected at pre-determined intervals and subsequently analysed for surface quality and internal cracks.

Thermocouple data were analysed with three mathematical models - two of the mould and one of the billet. Axial mould heat-flux profiles, obtained with a heat transfer model of the mould, were verified by comparing them with the total amount of heat extracted by the mould cooling water. The distortion of the mould was computed by a mathematical model of mould distortion that uses the temperature distribution in the mould as obtained form the first model of the mould. Shell thickness and shrinkage profiles of the billet were obtained from a mathematical model of the billet developed during the course of this work. Data on the carbon-and-temperature-dependent coefficient of expansion of steel, necessary to model the shrinkage of steel was not directly available and had to be computed from the experimental values of the lattice parameter of unit cells of alpha and gamma iron. Several curve fitting exercises had to be carried out on the experimental data available in the literature to obtain an expression for the coefficient of expansion that incorporates the effect of temperature and carbon. Model verification was done by comparison of the experimentally measured, mid-face shell thickness of the billet with the computed ones.

The load cell signals, collected at typically 50 Hz., was analysed through several small computer programs developed in this study. The signals were additionally plotted on 1524 X 1224 mm long paper to see differences, if any, in the nature of the signal for different types and flow rates of mould lubricating oils. Analysis of load cells have very strongly corroborated the mechanism of heat transfer in the mould as developed by the study of thermocouple signals.

Detailed analysis of billet quality, both in terms of surface appearance and internal cracks, was carried out. Several mathematical model predictions could be verified by measurements made on the billet.

As a result of the various analyses it has been possible to evolve a consistent theory that comprehensively explains the various factors that have been found to affect heat transfer in the mould, in particular at the meniscus. The theory has been successfully tested in a separate plant trial that has followed this research work. It has been possible to divide the mould into three different regions from the point of heat transfer. The other important conclusions from the work are as listed below.

[1] Heat transfer in the upper half of the mould primarily depends on the mould-billet interaction during the negative strip period of the mould oscillation cycle. Increased interaction leads to higher heat transfer in Zone I of the mould (Figure 9.4). The high heat transfer in Zone I raises the hot face temperature of the mould above the boiling point of the mould lubricating oil leading to the generation of hydrogen gas in the mould-billet gap. Heat transfer is significantly improved in Zone II by the higher thermal conductivity of the hydrogen gas compared to the conductivity of air. (The enhancement in heat transfer in Zone II leads to a further outward bulging of the mould wall causing an increase in the interaction of the mould and the billet, and therefore heat transfer, in Zone I). In Zone III, the presence of hydrogen

enhances the heat transfer as does a decrease in the mould-oscillation frequency that leaves fewer oscillation marks on the surface of the billet in comparison to the number of marks left by a higher frequency of mould oscillation.

[2] The design of high upper taper (> 2.5 %/m) in the upper part of the mould, prevents the mould wall from acquiring a bulged shape (or negative taper), by compensating for the differential expansion of the mould wall during operation. The absence of a negative taper results in a lower mould-billet interaction and, therefore, heat transfer.

[3] Calculations have shown that the thermal resistance of the mould-billet gap accounts for 80-85% of the total thermal resistance to heat flow in the mould. An increase in the flow rate of the mould lubricating oil leads to an enhancement in the heat transfer if the hot face temperature of the mould causes the oil to boil. No significant gain in heat transfer is obtained by increasing the flow rate of the mould lubricating oil beyond 25 ml/min as "excess" oil collects on the surface of the liquid steel and does not flow past the meniscus.

[4] The absence of the mould-lubricating oil below the meniscus of a "hot" mould and the adverse lubrication condition that arise thereby, have been found to be likely causes of bleeds and laps in the high carbon grade (C > 0.60%) steel billets. The adverse lubrication condition has been found not to affect the surface quality of medium and low carbon billets (C < 0.60%).

[5] It has been shown that despite the contraction arising from δ to γ phase change in low-carbon grades, the shrinkage of the billets of these grades is small on account of the very low heat transfer to the mould. Thus if low-carbon billets are cast through a mould designed for high-carbon grades, they are likely to bind in the mould leading to transverse depressions and cracks on the billet surface. The model predicted binding of these grades has been corroborated by an analysis of load cell signals and by an examination of the billet surface.

[6] It has been shown that mould sensors (thermocouples, load cells and LVDTs) can be used to detect the formation of some billet defects and factors that have been identified to affect heat transfer in the mould, can be altered to bring about corrective action.

[7] New mould tapers have been designed that permit a minimum of 50% increase in casting speed over the casting speed currently in vogue at several Canadian steel plants.

[8] New mould tapers have also been designed to eliminate the formation of bleeds and laps while casting high-carbon grade billets.

[9] In view of the close dimensional tolerances needed for a properly designed mould, the explosion forming technique of mould manufacture has been recommended.

[10] In view of the high heat transfer now available with an appropriately designed mould, it is important to ensure that water velocities and back pressures in the mould cooling water channel are sufficient to prevent the boiling of water.

RECOMMENDATIONS FOR FUTURE WORK

It is very clear from this research work that the heat transfer in the continuous casting mould can be controlled during operation by altering the flow rates of mould cooling water and the mould lubricating oil. Additionally by changing the level of steel in a correctly designed mould, substantial changes can be made to the shrinkage rate of the billet being cast. The necessary tools to do so have all been developed in the research work. These concepts need to be implemented in the form of a "smart" mould that is capable of sensing mould-billet interaction and taking corrective action on line.

It is possible to work towards the creation of the "smart" mould mentioned above in a series of well planned plant trials in which, based on the fundamentals developed so far, conditions are created first to adversely affect billet quality and subsequently altered to rectify the anomaly. This would not only test the theories developed so far but would build a database to be used in "programming" the "smart" mould. It is in the nature of such work to take several attempts before they are tuned to perfection and a period of five years would be a minimum necessary to carry out the above task.

With the experience acquired and the mathematical and analytical tools developed during the study of mould-strand interaction in oil-lubricated billet moulds, it should now be possible to study and understand in a relatively short period of time the friction effects in billets cast using mould powder as a lubricant.

REFERENCES

1 R. J. Dippenaar, I. V. Samarasekera and J. K. Brimacombe, ISS Transactions, 1986, Vol. 7, pp. 31-43.

2 S. Watanabe, K. Harada, N. Fujita, Y. Tamura and K. Noro, Tetsu-to-Hagane, 1972, Vol. 58, pp. 393-394.

3 Y. Aketa and K. Ushijima, Tetsu-to-Hagane Overseas (JISI of Japan), 1962, Vol. 2(4), pp. 334-343.

4 D. P. Evteev, Stahl in English, Aug. 1969, pp. 708-711.

5 A. D. Akimeinko and A. A. Skvortzov, Izov. VUZ Chernaya, Metall., 1961, (10), pp. 29-36.

6 A. Grill, K. Sorimachi and J. K. Brimacombe, Metall. Trans. B 1976, 7B(2), pp. 211-216.

7 E. G. Zetterland and J. K. Kristiansson, Scand. Journ. of Met., 1983, Vol. 12, pp. 211-216.

8 I. V. Samarasekera, Report to Stelco Edmonton Steel Works, unpublished work, 1987.

9 E. Herrmann, Handuch des Stranggiessens, Aluminium-Verlag, Dusseldorf, 1958.

10 G. J. McManus, Iron Age, Vol. 224, No 4, February 1981, pp. MP 7-9, MP 11.

11 M. Wolf, Concast Tech., Vol. 21 (3),1982, pp 7-7.

12 M. Wolf, Electr. Furn. Proc., AIME, 1983 (40), pp. 335-346.

13 L. Brendzy, M.A.Sc. Thesis, Univ. Of British Columbia, 1990.

14 Y. Takamura, S. Mizoguchi, O. Tsubakihara, T. Kuwabra and M. Saito, Nippon Steel Tech. Report, No 21, pp. 198-201, 1983.

15 F. Weinberg, Metall. Trans. B, 1979, Vol 10B, pp. 219-227.

16 B. G. Thomas, J. K. Brimacombe and I. V. Samarasekera, ISS Trans., Vol. 7, 1986, pp. 95-105.

17 I. V. Samarasekera,J. K. Brimacombe and R. Bommaraju, ISS Trans., Vol. 5, 1984, pp. 79-94.

18 I. V. Samarasekera and J. K. Brimacombe, Metall. Trans., Vol. 13B, March 1982, pp. 105-116.

19 I. V. Samarasekera and J. K. Brimacombe, Ironmaking Steelmaking, 1982, Vol. 9, pp. 1-15

20 J. K. Brimacombe, E. B. Hawbolt and F. Weinberg, ISS Trans., 1982, Vol. 1, pp. 29-40.

21 I. V. Samarasekera, Ph.d Thesis, Univ. Of British Columbia, 1980.

22 I. V. Samarasekera and J. K. Brimacombe, Canadian Metall. Quart., Vol. 18, 1979, pp. 251-266.

23 F. P. Bowden and D. Tabor, "The Friction and Lubrication of Solids", Oxford Univ. Press, 1950.

24 F. D. Dudley, "Theory and Practice of Lubrication for Engineers", New York, Wiley, 1956.

25 B. Mairy and M. Wolf, Facherichte, Vol. 20, No. r, April 1982, pp. 222-227.

26 S. N. Singh and K. E. Blazek, Iron and Steel Maker, October 1987, pp. 36-38.

27 J. Stel, J. M. Ranberg, M. C. M. Cornelissen and J. Cijsouw, 1st European Conference on Continuous Casting, Italy, 1991, pp. 2.377-2.386.

28 M. Komatsu, T. Kitagawa, K. Kawakami, 104th ISIJ meeting, September 1982, Lecture No. S927, Trans. ISIJ, 1983, 23, pp. B-86.

29 I. V. Samarasekera and J. K. Brimacombe, W. O. Philbrook Memorial Symposium Conference Proceedings, 1988, pp. 157-171.

30 I. V. Samarasekera and J. K. Brimacombe, International Metals Review, 1978, No. 6, pp. 286-300.

31 A. D. Klipov, A. I. Kolpakov, M. G. Chigrinov and E. R. Ballad, Stal in English, 1971, (2), 107-111.

32 C. R. Taylor, Metall. Trans., 1975, 6B, pp. 359-375.

33 S. N. Singh and K. E. Blazek, Open Hearth Proc., AIME, 1977, 59, pp. 264-283

34 S. Deshimaru, S. Omiya, H. Mizota, M. Yao, M. Maeda and T. Imai, Trans. ISIJ, 1984, Vol. 24, pp. B-339.

35 M. Wolf, Trans. ISIJ, 1980, Vol. 20, pp. 718-724.

36 B. Short, F. Faires and T. Horton, Concast Technology News, Vol. 26, No 3, 1987, pp. 5-5.

37 H. Yamanaka, M. Ikeda, T. Nishitani and T. Ando, Trans. ISIJ, Vol. 23, No. 10, 1983, pp. F-4.

38 M. Wolf, 103rd ISIJ meeting, April 1982, Lecture No. S149, Trans. ISIJ, 1982, 22, (7), pp. B-204.

39 G. Foussal, Rev. Metall., Vol. 4, 1984, pp. 299-307.

40 M. Komatsu, T. Kitagawa, K. Kawakami, 104th ISIJ meeting, September 1982, Lecture No. S927, Trans. ISIJ, 1983, 23, pp. B-86.

41 H. Gloor, Concast Standard News, Vol. 30, No 1, 1991, pp. 4-5.

42 H. Mizukami, M. Komatsu, T. Kitagawa and K. Kawakami, 106th ISIJ meeting, October 1983, Lecture No. S1032, Trans. ISIJ, 1984, 21, (6), pp. B-181.

43 S. Ohmiya, M. Nakato, Y. Habu, T. Emi, K. Hamagami, H. Bada and Y. Fukuhara, 104th ISIJ meeting, September 1982, Lecture No. S926, Trans. ISIJ, 1983, 23, pp. B-85.

44 J. Savage and W. H. Pritchard, JISI, Vol. 178, 1954, pp. 269-277.

45 I. M. D. Halliday, JISI, Vol 191, 1959, pp. 121-163.

46 V. A. Kobelev, Stal in English, 1967, pp. 471-473.

47 H. Jacobi, G. Komma, K. Wunnenberg, Stahl und Eisen, Vol. 102, 1982, pp. 441-449.

48 J. P. Birat, Rev. Metall., Vol 79, 1982, pp. 603-616.

49 R. Sato, Proc. 62nd NOH-BOSC, ISS-AIME, 1979, pp. 48-67.

50 V. P. Perminov, N. M. Lapotyshkin, V. E. Girskii and A. I. Chizhikov, Stal in English, 1968, Vol. 7, pp. 560-563.

51 H. Mori, Testu-to-Hagane, 1972, Vol. 58, pp. 1511-1525.

52 W. P. Young and W. T. Whitfield, Open Hearth Proc., AIME, 1968, Vol. 51, pp. 127-132.

53 K. Matsunaga, Open Hearth Proc., AIME, 1976, Vol, 59, pp. 228-248.

54 K. Ushijima, Continuous Casting of Steel, Iron Steel Inst., London, 1964, pp. 59-71.

55 Y. Aketa and K. Ushijima, Testu-to-Hagane, 1960, Vol. 46, pp. 1733-1740.

56 H. G. Baumann and W. J. Lopmann, Wire World Int., 1974, Vol. 16, pp. 149-155.

57 K. Fujinami, Funabashi Steelworks Ltd., Funabashi, Japan, unpublished research, 1977.

58 J. E. McConnell, Open Hearth Proc., AIME, 1972, Vol. 55, pp. 56-72.

59 R. Bommaraju, J. K. Brimacombe and I. V. Samarasekera, ISS Transactions, Vol. 5, 1984, pp. 95-105.

60 J. W. Donaldson, Journal of Metals, December 1965, pp. 1-6.

61 D. I. Brown, Journal of Metals, April 1965, pp. 2-8.

62 I. V. Samarasekera, D. L. Anderson and J. K. Brimacombe, Met. Trans. B, 1982, Vol. 13B, pp. 91-104.

63 J. K. Brimacombe, I. V. Samarasekera and R. Bommaraju, Steelmaking Proceedings (ISS), 1986, 69, 409-423.

64 I. A. Bakshi, A. Perri, J. K. Brimacombe, I. V. Samarasekera and R. P. Smith, U.S. Patent Application, 1991.

65 C. D. Henning and R. Parker, Trans. ASME, May 1967, pp. 146-154.

66 M. H. Burden, G. D. Funnell, A. G. Whitaker and J. M. Young, Solidification and Casting of Metals, The Metals Society London, 1979, pp. 279-286.C.

67 I. V. Samarasekera, Report to Sidbec_dosco Steel Plant, unpublished work, June 1991.

68 D. W. Peaceman and H. H. Rachford Jr., J. Soc. Indust. Appl. Math, 1955, 3, pp 28-41.

69 Handbook of Heat Transfer, W. M. Rohsenow and J. P. Hartnett, eds., McGraw Hill Book Co., 1973, pp. 13-1 to 13-75.

70 E. A. Mizikar, Trans. TMS-AIME, 1967, 239, pp. 1747-1753.

71 J. Szekely and V. Stanek, Metall. Trans., 1970, 1, pp. 119-126.

72 R. B. Mahapatra, Ph.D Thesis, Univ. of British Columbia, 1989.

73 B. G. Thomas, I. V. Samarasekera and J. K. Brimacombe, Metall. Trans, 18b, 1987, pp. 119-130.

74 H. Frederiksson and M.Thegerstrom, Scand. Journ. of Met., 1979, 8, pp. 232-240.

75 J. K. Brimacombe, I. V. Samarasekera, N. Walker, I. Bakshi, R. Bommaraju, F. Weinberg and E. B. Hawbolt, Trans. ISS, 1984, 5, pp. 95-105.

76 P. J. Wray, Proc. AIME Symp. On Modelling of Casting and Welding Processes, 1980, pp. 245-257.

77 N. Ridley and H. Stuart, Met. Sci., 1970, 4, pp. 219-222.

78 L. D. Lucas, Mem. Sci. Rev. Met., 1964, 2, pp. 1-24.

79 E. J. Fasiska and Wagenblast, Trans. Metall. Soc. AIME, Nov. 1967, 239, pp. 1818-1820.

80 I. A. Bakshi, E. Osinski, I. V. Samarasekera and J. K. Brimacombe, Intl. Symp. on Direct Rolling and Hot Charging, eds. J. J. Jonas, R. W. Pugh and S. Yue, CIM, 1988, 10, pp. 60-69.

81 J. K. Brimacombe, I. V. Samarasekera and R. Bommaraju, Proceedings of Steelmaking Conference of the Iron and Steel Society of AIME, Washington, D. C., 1986, 69, pp. 409-423.

82 D. P. Lorento, Paper presented to Globetrotters Meetings, 1988.

83 I. V. Samarasekera, Report to Stelco Edmonton Steel Works, unpublished work, 1992.